

ALFVÉN WAVE-PARTICLE ACCELERATION NEAR THE IONOSPHERE: A  
ROCKET-BORNE INVESTIGATION

by

Connor Ayen Feltman

A thesis submitted in partial fulfillment  
of the requirements for the Doctor of Philosophy  
degree in Physics in the  
Graduate College of  
The University of Iowa

December 2024

Thesis Committee: Greg. G. Howes, Thesis Supervisor,  
Craig A Kletzing (Feb. 1958 - Aug. 2023)  
David M Miles  
Allison N Jaynes  
Jasper S Halekas  
James W Labelle

Copyright by

Connor Ayen Feltman

2024

All Rights Reserved

To Craig,

A paragon of intellect, honesty and humility. It was “never a dull moment” when you were with us.

“Magnetohydrodynamics always felt like magic to me”

Randal Monroe,  
creator of xkcd comics  
Private Correspondence, Sept 30, 2022

## ACKNOWLEDGMENTS

From the day I told myself that I was going to get a Ph.D., I have been surrounded by so many people that defy my ability to adequately describe their support and commitment. Without them, I would have been lost long ago.

At the University of Iowa, I was mentored by Dr. Craig Kletzing for four years until his passing in August 2023. There are no words to give justice to how grateful I am for the time he spent teaching and guiding me. He taught me to work harder than I ever thought I could, forgive mistakes quickly, be intellectually honest and expect it from others. It would be exceedingly rare to meet someone who could rival Craig's scientific knowledge, yet rarer still to find someone who uses their knowledge to excite, encourage and support others as much as he did. I thank him for taking a chance on a graduate student and for sticking through my growing pains as a scientist (for which there were many). I hope to pay forward what was given to the next generation.

I owe deep respect and gratitude to Dr. Scott Bounds for leading the scientific mission that provided the data for this dissertation. While Craig was my scientific advisor, it was Scott who really suffered the slings and arrows of my questioning/ignorance day to day. In this way, Scott also deserves the mantle of my advisor. In those first couple years he worked to get me out of my shell by telling stories of Star Wars, Football, or whatever else was on his mind. Scott is a truly gifted experimentalist: his formidable memory, deep understanding of his craft, inspirational leadership and jovial nature have made him a role model for me as I launch my career. He may have not known it, but whenever I felt overburdened by the struggles and expectations of graduate school, I would find solace and confidence by chatting with him. In his office, I felt comfortable asking dumb questions because I knew they would genuinely be answered without judgement. He taught me the value of always keeping a cool head and how important the ability to tell a good story can be. Your patience and willingness to forgive mistakes was never unnoticed. Thank you.

I am indebted to Dr. David Miles for his responsiveness and willingness to assist in my advisor crisis. After Craig's passing, David quickly took me under his wing and found time to help me, despite having to suddenly lead one of the largest scientific projects the department had

ever managed. I will never forget how he managed to make our meetings cheerful, productive and humorous despite the circumstances.

When the dust finally settled, Dr. Gregory Howes graciously accepted me as his student to help me finish my PhD. I will never forget how quickly Greg accepted me into his research group and how he immediately gave so many hours of his time to my research. His instruction, endless patience and willingness to sit “in the trenches” with students has been precisely the experience I had dreamed of when coming to graduate school. Thank you so much.

In addition to my academic advisors, so many individuals were pivotal to this work. Many thanks to the TRACERS staff who assisted in the development of our Sounding Rocket: Jeff Dolan, Rich Dvorsky, Christian Hansen, Dr. Mathew Finlay, Dr. Suranga Ruhunusiri, Sam Hisel and Amanda Lasko. Special thanks to the TRACERS FPGA wizard Antonio Washington for painstakingly stepping through the magnetometer data with me until I could understand. Thanks to Dr. Jasper Halekas for continually demonstrating excellence and for giving me ample opportunities to be involved in TRACERS. Your graciousness when I made (many) mistakes was always noticed. I would also like to thank the extended ACES-II team, specifically Dr. Marc Lessard and Dr. Jesper Gjeorloev as well as the numerous technicians and engineers from Wallops Space Flight Facility who made our mission possible. Furthermore, I could not have done this work without my ACES-II partners in crime: Kenton Greene, Robert Broadfoot and Roger Roglans. Thank you gentlemen for keeping me sane and our conversations fun; couldn’t have asked for better colleagues to get a Ph.D. with.

Many thanks to my officemate Jeremy Faden for always bringing a smile to the workday. Our endless conversations about programming, plotting and life continually drive me to understand my own work better. Thanks to my other officemate Dr. David Hartley for offering a welcoming environment early in my career. You have continued to answer my endless questions with a level of honesty that always makes it a pleasure to talk with you. Next, I want to thank Dr. Allison Jaynes for being a refuge as an early graduate student and for providing so many project opportunities. I appreciate your continual pushes for me to be better at my job and to be a better human.

Beyond my academic colleagues, I must first thank the person who has performed the greatest service to my education - my mother. Without your unwavering dedication to my education in the face of adversity, long nights helping me study, supporting three kids after losing dad and giving ceaseless love and patience to us, this would not have happened. It took me 6 years to finish my formal education, but for you it took my whole lifetime. For this and so much more, I will be forever grateful. I must also recognize the person who planted the dream of a Ph.D. in my head long ago; my brother, Hunter. Your character and infectious curiosity have been an ideal role model for me to look up to throughout my whole life. Thank you.

Additionally, I have many lifelong friends that I wish to thank. To my friends Sanjay, Michael and Kian, you have all enriched my life with your presence and diverse experiences. I hope to continue to help you as you have helped me. To my dearest friends Riley, Daniel, Yueguang and Chris: you have all shared in the most momentous times of my life and I'm happy to be able to spend it with you. To me, you are all my family. Finally, I would like to thank my wife, Diksha. Your kindness, patience and excitement for life remind me each day why I fell in love with you. Our journey together spans two countries, two weddings and (now) two doctorates. Thank you for asking me to go on a walk with you that fateful Fall afternoon.

## ABSTRACT

The work presented in this thesis focuses on the results from the Aurora Current and Electrodynamics Structures II (ACES-II) sounding rocket mission which launched into a discrete auroral event on Nov. 20th, 2022 from Andøya, Norway. This mission was a re-flight of a similar mission launched in 2009 from Poker Flat, Alaska which suffered from the target aurora being too down-range to easily reach and some instrumental failure. ACES-II successfully launched two payloads into a post-dusk, discrete auroral arc with tight magnetic conjunction between payloads at apogee. The mission goal was to understand the input and response of the ionosphere to global field-aligned currents by determining the ionospheric Hall and Pedersen currents *is situ*. This work is still on-going, so in this manuscript we focus on a particularly interesting set of high-energy electron observations that shows evidence of Alfvénic wave-particle acceleration enhancements due to inverted-V precipitation. Five repetitive suprathermal electron bursts (STEBs) associated with low frequency ( $< 8$  Hz) Earth-ward traveling Alfvén waves are observed at 400 km altitude. The electron bursts occur both coincident and outside inverted-V electrons, with those nearest to inverted-V precipitation displaying higher peak energy and differential flux values than events further away. Our analysis provides direct evidence for theoretical and numerical predictions from the previous two decades, for which fundamental plasma experiments have only recently been capable of reproducing in highly-controlled laboratory experiments.

A study of the required background material is presented in Chapters 1, 2, 3 and 4 that covers fundamental plasma physics, auroral physics and its historical overview and finally the Alfvén wave-particle acceleration mechanism along geomagnetic field lines. A detailed description of the experimental apparatuses for the ACES-II mission are provided in Chapter 5 and how the data is processed in Chapter 6. The final Chapters 7, 8 and 9 constitute the bulk of the scientific analysis which employ both direct observations and modelling to show how significant changes in resonant source population produce equally significant changes in resultant STEB morphology that aren't explained by changes in observable wave parameters. Our observations allow us to directly associate our STEBs with observable Alfvén waves and provide estimates on the altitude range for

the resonant electron source population. By using available radar data and *in situ* measurements we conclude our accelerating waves were inertial Alfvén waves. Finally we employ modelling of local inverted-V electrons to estimate the required accelerating wave parameters to reproduce our events. We illustrate the impact that different electron populations have in their ability to resonate with Alfvén waves. To the best of this author's knowledge, this work provides the first attempt at directly showing the impact of changing source populations for STEB electrons *in situ* and adds to a ever-increasing literature highlighting the success of interpreting STEB electrons as the result of an Alfvénic wave-particle acceleration processes.

## PUBLIC ABSTRACT

Earth’s geomagnetic field interacts with the external magnetic fields carried by the solar wind, a hot plasma emanating from the sun. Normally, our terrestrial magnetic shield impedes much of the Sun’s influence from reaching the surface of Earth. However, when conditions are just right, the sun’s influence can trickle down into our atmosphere to be seen as bright and beautiful aurora. Understanding this energy cascade, which starts at the sizes of planets down to a few tens of kilometers is complex and highly variable in space and time. Despite this, commonalities exist between solar “storms” that produce predictable behavior near Earth’s electrically conductive atmosphere, called the Ionosphere. When disturbances occur in Earth’s outer magnetic field, they can propagate down to the Ionosphere as plasma waves and interact with ambient particles. When certain conditions are met, these particles literally “surf” the wave and gain energy. Just like humans surfacing an ocean wave, these electrons must have speed that’s close to the wave speed in order to be picked up and accelerated, otherwise the wave just passes by. In this manuscript, we use data from a scientific sounding rocket to show that the processes which produce aurora also produce a greater number of electrons that can surf these plasma “Alfvén” waves compared to the ambient atmospheric particles, which are not associated with aurora. This work constitutes direct evidence for theoretically and numerically modelled predictions from the previous two decades, for which fundamental plasma experiments have only recently been capable of reproducing in highly-controlled laboratory experiments.

## TABLE OF CONTENTS

List of Tables . . . . .	xiv
List of Figures . . . . .	xv
CHAPTER 1: INTRODUCTION . . . . .	1
CHAPTER 2: SPACE PLASMA FUNDAMENTALS . . . . .	11
2.1 What makes a (space) plasma? . . . . .	11
2.2 Single Particle Motion . . . . .	16
2.3 The Dipole Magnetic Field and Adiabatic Invariants . . . . .	16
2.4 Particle Drifts . . . . .	21
2.5 Magnetohydrodynamics (MHD) . . . . .	23
2.6 Generalized Ohm's Law . . . . .	24
2.7 MHD Alfvén Waves . . . . .	26
2.8 Alfvén Waves: Kinetic Theory . . . . .	30
2.9 The Dispersive Alfvén Wave (Lysak et al., 1996) . . . . .	34
CHAPTER 3: THE MAGNETOSPHERE-IONOSPHERE SYSTEM . . . . .	38
3.1 The Solar Wind . . . . .	38
3.2 The Magnetosphere . . . . .	40
3.3 The Plasmasphere . . . . .	42
3.4 The Ionosphere . . . . .	43
3.5 Reconnection and Plasma Convection . . . . .	46
3.6 The Plasma Sheet: Auroral Source Region . . . . .	48
3.7 Ionospheric Current Systems and Closure . . . . .	50
CHAPTER 4: AURORAL PLASMA . . . . .	54

4.1	Colors of the Aurora . . . . .	54
4.2	Discrete Aurora and Quasi-static Parallel Electric Fields . . . . .	56
4.3	Models of the Inverted-V: Phase Space Mapping and The Knight Relation . . . . .	68
4.4	The Evans Model . . . . .	72
4.5	Electron Acceleration through Alfvén Waves Simplified (C. A. Kletzing, 1994) . .	78
4.6	Suprathermal Electron Bursts (STEBs): History and Simulation . . . . .	84
	 CHAPTER 5: INSTRUMENTATION . . . . .	 93
5.1	ACES-II Sounding Rocket Mission . . . . .	93
5.2	Instrumentation Layout . . . . .	94
5.3	Electrostatic Analyzers - Specifications and Operational Theory . . . . .	96
5.4	Magnetic Fields - Specifications and Operational Theory . . . . .	101
5.5	Electric Fields - Specifications and Operational Theory . . . . .	103
5.6	Langmuir Probes - Specifications and Operational Theory . . . . .	105
5.7	AllSky Imagers . . . . .	110
5.8	Incoherent Scatter Radar . . . . .	111
	 CHAPTER 6: DATA AND PROCESSING . . . . .	 113
6.1	Flight . . . . .	113
6.2	Performance and Issues . . . . .	121
6.3	ESA Calibration . . . . .	121
6.4	B-Fields - Calibration and Despin . . . . .	127
6.5	E-Fields - Calibration and Despin . . . . .	134
6.6	E and B Fields - Field aligned Coordinates . . . . .	135
6.7	E and B Fields - Coning and Filtering . . . . .	137
6.8	E and B Fields - Multivariate Singular Spectrum Analysis (mSSA) Filtering . . .	140
6.9	Langmuir Probe Calibration . . . . .	146

CHAPTER 7: RESULTS AND ANALYSIS . . . . .	150
7.1 Data Overview . . . . .	150
7.2 The Dispersive Region . . . . .	152
7.3 Uniqueness of the Measurements - Criteria to Investigate a Changing Source Population . . . . .	157
7.4 Cross-Payload Interpretation . . . . .	160
7.5 Alfvén Waves on the Low Flyer . . . . .	162
7.6 Source Altitude: Time-of-Flight . . . . .	166
7.7 The effects of a changing source population: Key Observations . . . . .	176
7.8 Other Explanations - Variation in Wave Parameters and Pitch Angle . . . . .	181
7.9 Summary . . . . .	185
CHAPTER 8: MODELING . . . . .	187
8.1 Model Description . . . . .	187
8.1.1 Geomagnetic Field . . . . .	188
8.1.2 Perpendicular Scale Length . . . . .	189
8.1.3 Plasma Density, Ion mass and Skin Depth . . . . .	191
8.1.4 Ion Terms and Kinetic Corrections . . . . .	191
8.2 Fitting the Inverted-V . . . . .	196
8.3 Model Distributions and Mapping . . . . .	199
8.4 Calculating the Wave Potential $\Phi$ . . . . .	204
8.5 Results . . . . .	207
8.6 Summary . . . . .	208
CHAPTER 9: SUMMARY, CONCLUSIONS AND FUTURE WORK . . . . .	209
9.1 Summary & Conclusions . . . . .	209
9.2 Future Work . . . . .	210

APPENDIX A: DERIVING THE PLASMA WAVE EQUATION . . . . .	212
APPENDIX B: PROVE EQUATION 125 . . . . .	213
APPENDIX C: HALL AND PEDERSEN CONDUCTIVITY . . . . .	214
APPENDIX D: PROVE EQUATION 91 . . . . .	216
REFERENCES . . . . .	217

## LIST OF TABLES

Table 1. Results of the TOF analysis for four events preceding an inverted-V near 17:25:00 UTC in the High Flyer EEPAA data. The source altitudes above the payload,  $z_{src}$ , can be added to the altitude at measurement (400 km) to get true altitude. . . . . 175

## LIST OF FIGURES

Figure 1. Schematic overview of Earth's Magnetosphere, taken and edited from Kelly, 2009. Plasma flows along geomagnetic field lines produce currents between the regions of the Magnetosphere and to Earth's atmosphere at the extreme latitudes. The regions associated with nightside auroral activity are colored.	2
Figure 2. Diagram inspired from Baumjohann, 1982. The arrows indicate the direction of influence from one system to another, which are often bi-directional.	4
Figure 3. Illustration of the ACES-II sounding rocket mission. Two payloads are launched at different altitudes in an input/response style of configuration to determine the Hall/Pedersen currents within the ionosphere through a discrete auroral arc.	6
Figure 4. Image: Austin Montelius, University of Iowa (Formerly). Diagram of where Alfvén waves are created in Earth's magnetosphere due to magnetotail reconnection. Electron acceleration occurs over a range of altitudes when the waves travel towards Earth from their point of creation.	7
Figure 5. Image: Austin Montelius, University of Iowa (Formerly). Diagram showing how Alfvén Wave-particle resonance occurs, where some electrons can “surf” the wave while others are untouched.	8
Figure 6. Examples of suprathermal electron Bursts (STEBs) seen in the ACES-II High Flyer rocket data. Various shapes exist for these time-dispersed electron signature, although they generally display the highest energies arriving before the lowest energies as well as inhabit the most field-aligned pitch angle bins. The bursts are categorized based on their relation to other types of precipitation. Isolated bursts are wave-particle acceleration structures by themselves. Auroral bursts occur coincident/near auroral precipitation. Edge-type bursts occur only near the edge of auroral precipitation and may be associated with the movement of aurora (inverted-V) instead of Alfvén waves. Finally, bursts can become difficult to distinguish, especially near auroral (inverted-V) precipitation, which appear as a mix of types.	10
Figure 7. From F. Chen, 2016. 1D potential distribution inserted into a plasma.	12
Figure 8. (Left) Three types of single particle motion often found along geomagnetic field lines (M. Kivelson, 1995). (Right) Example of Earth's dipolar geomagnetic field, which is a good approximation within a few $R_E$ . The pairs A1/A2 are the geographic poles, B1/B2 are geomagnetic poles and C1/C2 are magnetic poles. Figure adapted from from ( <a href="https://en.wikipedia.org/wiki/Earth%27s_magnetic_field">https://en.wikipedia.org/wiki/Earth%27s_magnetic_field</a> ).	17

Figure 9. From <a href="https://en.wikipedia.org/wiki/L-shell">https://en.wikipedia.org/wiki/L-shell</a> . Concept of L-Shell in a dipole magnetic field. The Shells are defined by the intersection point of magnetic field lines at the magnetic equator and numbered. Auroral Field lines typically exist on L-Shells above 7. . . . .	18
Figure 10. An initial Maxwellian distribution function (left) projected into a 2D that begins in a hypothetical magnetic mirror at t=0. The circular contours represent lines of constant total velocity. (right) The same Maxwellian distribution after some time has passed. Particles with pitch angles too small to be confined by the magnetic geometry escape and are lost from the initial distribution. . . . .	20
Figure 11. Charged particle motion under the influence of orthogonal $\vec{E}$ and $\vec{B}$ fields simultaneously. Both charges move in the $\vec{E} \times \vec{B}$ direction which produces no net current. . . . .	22
Figure 12. Schematic of MHD Alfvén Wave propagation. The fluid and field lines oscillate together as if the particles were stuck to the lines of force, very much like a mechanical wave on a string. Here $\vec{E}_1$ only oscillates in the directed perpendicular to the wave i.e. no $\vec{E}_{\parallel}$ . Taken from F. Chen, 2016. . . . .	28
Figure 13. From Kelly, 2009. Three dimensional diagram of the IMF “ripples” in the spiraling outward flow of solar plasma carrying the sun’s magnetic field. . . . .	39
Figure 14. Example flux tubes from ideal MHD where the same magnetic flux passing through fluid element $S_1$ is passing through element $S_2$ at a later distance. . . . .	39
Figure 15. From Russell et al., 2016. Two dimensional cut-away of the magnetosphere. . . . .	41
Figure 16. From Kelly, 2009. Plasmasphere with lines indicating contours of plasma flow (not magnetic field). . . . .	42
Figure 17. From Kelly, 2009. Profies of neutral atmospheric temperature and Ionospheric plasma layers. . . . .	44
Figure 18. From Kelly, 2009. Daytime atmospheric composition above White Sands, New Mexico ( $32^{\circ}N, 106^{\circ}W$ ) . . . . .	44
Figure 19. From Johnson et al., 1961. (Left) Electron-neutral and (right) ion-neutral collision rates for various solar conditions vs. altitude. . . . .	45
Figure 20. From Council, 2004. Schematic showing the process of magnetic reconnection where two X-Lines are formed due to the connection between solar wind IMF and terrestrial magnetic fields. . . . .	47

Figure 21. From C. A. Kletzing et al., 2003. One pass of the POLAR satellite through the high-latitude plasma sheet over an hour long pass. The top three panels show the fit parameters with blue/black for the kappa distribution and red for the Maxwellian. The data from the left side of the figure represents the high-latitude, poleward field lines while the rightside are equatorward. . . . .	49
Figure 22. From Palmroth et al., 2021. The currents of magnetospheric origin (shown in red and blue) close their circuit through the ionosphere. A pair of currents form (1) The cross-field Pedersen currents (shown in green) that connect R1 and R2 current pairs and (2) the $\vec{E} \times \vec{B}$ Hall current (shown in yellow). . . . .	51
Figure 23. From Kelly, 2009. Ion and electron trajectories for different mobilities in a $\vec{B}$ field with a perpendicular $\vec{E}$ . . . . .	51
Figure 24. A 2D image of FACs and ionospheric currents in the connection region. In reality, Ionospheric currents close over a range of altitudes in 3D sense. . . . .	53
Figure 25. From Russell et al., 2016. This shows the energy levels of atomic oxygen associated with auroral emission. The indicated half-lifes describe the length of time before the atom de-excites to produce a photo. The long half-life of the red-line 6300Å is why this part of the aurora often looks blurry in all-sky imagers. . . . .	55
Figure 26. Photo Credit: Adrien Mauduit. Image adapted from <a href="https://auroraborealisobservatory.com/2021/03/07/best-aurora-in-3-years/">https://auroraborealisobservatory.com/2021/03/07/best-aurora-in-3-years/</a> . The colors of the aurora as it relates to the specific molecule which gets excited to emit photons. . . . .	57
Figure 27. From Frank et al., 1971. Differential number flux vs. energy from an “V” shaped structure within an auroral arc by the Injun-5 Satellite. A power law spectrum (dotted-dashed lined) and a Maxwellian distribution (dashed line) are fit to the various sections of the data. These are some of the first observations of accelerated Maxwellian distributions form parts of the discrete aurora. . . . .	59
Figure 28. Modern day view of the the electron “V” shaped structure that Frank et al., 1971 described from Injun-5 while flying through an aurora. This particular structure is extended over many latitudes and grows/deacys on the edges much like Frank et al., 1971 described. The greatest electron flux is seen in red at the lower energies, a result of the secondary emission from the higher energy primary flux (Evans, 1974). Data taken from ACES-II sounding rocket mission. . . . .	59
Figure 29. (a) One pass of S3-3 satellite measurement around 7600 km showing oppositely directed electric fields at 11:26 UT while passing the auroral oval. The parallel component appears mostly strongly when embedded in the equatorward and westward field reversals. Mozer et al., 1977 (b) Equipotential model from Temerin et al., 1981 that could produce the observed electrostatic shocks. The left panel shows the U-shaped potential which exhibits the properties of electric field reversal, but also the oppositely pointing fields that continue down to lower altitudes. . . . .	63

Figure 30. From Marklund et al., 1997 Possible configuration of a double-arc system associated with divergent electric fields at high altitudes. Here, the downward current produces a “Black Aurora” made of ion. . . . .	64
Figure 31. Probabilities of observing a shock for every 1000-km altitude (top) 3 hours magnetic local time (middle) and magnetic local time normalized by altitude (bottom). In the bottom panel the horizontal solid line represents the average probability for all MLT times of observing multiple shocks per pass, and the horizontal dashed line represents the probability of one shock per pass. Bennett et al., 1983 .	66
Figure 32. Basic view of inverted-Vs potential structure which form along Earth’s geomagnetic field to produce discrete auroral arcs in the ionosphere. An example of real data from ACES-II is shown near 400 km in both Energy vs. Time spectrogram and velocity space. . . . .	67
Figure 33. Schematic diagram of the phase space mapping in velocity space of an ambient source of plasma sheet electrons using Liouville’s theorem from the magnetosphere to the ionosphere altitudes. (Left side) Ambient plasma sheet electrons that diffuse to lower altitudes. A loss cone is added for any particles that reach 100 km to display realism. (Right Side) The same plasma sheet distribution that has a quasi-static parallel potential $V_0$ which represents an inverted-V. The mirror force acts on both distributions to spread out electrons over pitch angle. See text for details of the mapping. A example distribution of low energy, backscattered/secondary electrons is also added to the inverted-V distribution for realism. These low energy electrons have been mapped from the ionosphere to high altitude and conservatively reflect off the parallel potential (Evans, 1974). . . . .	70
Figure 34. From Evans, 1974. Black line is a model electron energy spectrum by assuming 400V potential difference and a Maxwellian of temperature 800 eV. The dotted line is an electron spectrum observed by Injun-5 satellite from Frank et al., 1971. Good agreement between the bump near $\log(E) = 3$ and the model suggests the accelerated Maxwellian picture of an Inverted-V is a good approximation. The Evans model gives the predicted values for low energy backscatter/degraded primaries which has fair agreement to this figure. The deviation at the highest energies may be due to the non-Maxwellian aspects of the underlying distribution.	73

Figure 35. Example of the Evans Model procedure. Step (1) is to determine the incoming beam accelerated by the parallel potential. Step (2) is the spread of the incoming distribution due to the mirror force. The omni-directional differential number flux $\Phi(E)$ is determined as an estimate of the incoming flux into the ionosphere. (3) The ionospheric response of degraded primaries and secondary electrons are produced isotropically and upward from the ionosphere. (4) The backscatter/secondary electrons mirror back up to the parallel potential. (5) The mirrored backscatter population is reflected by the parallel potential and descend to the ionosphere. (6) The higher-energy degraded primaries repeat the whole processes again, but with lower incoming energy . Secondary electrons are too lower energy to produce additional backscatter but they can produce more secondaries at even lower energies. The whole processes constitutes a "bounce" and the model repeats until an equilibrium is reached.	75
Figure 36. From Evans, 1974. (Left) "Universal" degraded primary electron backscatter curve. The abscissa is backscatter electron energy normalized to the incident electron energy and ordinate is in units of differential omni-directional number flux normalized by 10000/E(incident). (Right) "Universal" secondary electron backscatter curve	76
Figure 37. From Evans, 1974. Example of the Evans model applied to a Maxwellian distribution (left) $0^\circ$ and (right) $45^\circ$ with 800 eV temperature for a distribution 2000 km above the atmosphere. Excellent agreement between the general shape of this distribution and the example data we provided in Figure 28 can be seen.	77
Figure 38. The amplitude function for a $E_{\parallel}$ of an Alfvén wave pulse with symmetric bipolar electric fields moving left. The velocities of the wave and directions of the electrons are shown. For electrons in front of the wave that are slower than $V_A$ they see an accelerating electric field that accelerates them to $V_A$ . For electrons with speed greater the wave but encounter it from behind, they see a decelerating $E_{\parallel}$ which causes them to lose energy and give it to the wave, which reduces their velocity also to $V_A$ .	80
Figure 39. Illustrative diagram that shows how an ideal Alfvén wave with a sinusoidal $E_{\parallel}$ can accelerate an electron. (left) In the wave-frame the electron reflects off the wave and returns the way it came with the same velocity. (right) In the laboratory frame the electron is accelerated to the Alfvén velocity and then accelerated more to a value that corresponds to the difference between the initial electron velocity and $V_A$ so that it exits the wave with velocity $2V_A - v_e$ . Here $E_t$ is the electric field value where the particle turns around and $E_1$ is some value of $E_{\parallel}$ at an intermediary step.	82
Figure 40. From C. A. Kletzing, 1994 Evolution of a distribution for a pulse of Alfvén waves that resonantly accelerate a portion of the distribution. See text for details.	83

Figure 41. From Arnoldy et al., 1985. Electron energy vs. time spectrogram of STEBs from sounding rockets between two auroral arcs showing a time-dispersed, electron signature decaying to lower energies. Individual bursts exist $\sim 1$ sec and typically exist in the most field-aligned pitch bins. . . . .	85
Figure 42. From McFadden et al., 1986a. Sounding rocket data showing the evolution of a STEB in time, taken from the edge of an auroal arc displayed and in velocity space. The highest energy electrons in the burst is strongly field aligned. . . . .	85
Figure 43. From Chaston, Bonnell, Carlson, McFadden, Ergun, et al., 2003. FAST data that contains electric and magnetic observation of Alfvén waves (top panels) coincident with inverted-V and STEB electrons (bottom panels). Similar to studies from previous decades, FAST reports STEB electrons as field aligned and showing energy-time dispersion within a few kilometers. However, the significant improvement of temporal resolution of the dataset provided the best picture of STEB electrons at the time. . . . .	89
Figure 44. From Chaston et al., 2007. (a) Topdown view of Earth's Polar regions of the occurrence of STEBs with dispersive Alfvén waves normalized by number of FAST traversals. (b) distribution of average dispersive Alfvén wave energy from integrated Poynting flux over the area of each grid segment. . . . .	90
Figure 45. (Top) From Arnoldy et al., 1999. Electron dispersion's below an inverted-V of a few keV measured by PHAZE-II sounding rocket. Dispersion tails extend to 50 eV while some end at keV. The time to disperse is about 0.6s. An inverted-V center at 10 keV is seen. (Bottom) From L.-J. Chen et al., 2005a. Two simulated electron dispersions generated from two dispersive Alfvén waves launched at $4R_E$ using an auroral latitude plasma environment. Additional high-energy primary backscatter was added to achieve good agreement with the PHAZE-II data. . . . .	91
Figure 46. From Tanaka et al., 2005. Plots of the effect of varying accelerating wave frequency, perpendicular scale and wave amplitude in a STEB numerical simulation. Waves start at 10,000 km in the Cusp region and interact with ambient plasma at lower altitudes throughout. The STEB exhibit different peak energy and differential number flux intensity depending upon the value of the wave amplitude or perpendicular scale length. The wave frequency generally serves to widen the time-width of any particular energy channel, without meaningfully affecting STEB intensity or peak energy. . . . .	92
Figure 47. Layout of the ACES-II payloads for the High and Low Flyers. Each were equipped with a suite of instruments to measure relevant plasma parameters. See text for details. . . . .	94
Figure 48. Configuration of the payload's instrument with respect to the rail of the launcher. The $0^\circ$ mark represents where each payload is attached to the rail before launch. . . . .	95

Figure 49. Cross-sectional slice of a top-hat electrostatic analyzer. Detectable trajectories are determined by the inner hemisphere's voltage and the dimensions of the electrodes. . . . .	96
Figure 50. ACE-II anode board that shows 21 pitch-angle anode pads. Electrons are amplified by the MCP and strike these pads to be detected by the detector's electronics. . . . .	97
Figure 51. From Miles et al., 2013. Schematic of one axis of a fluxgate magnetometer. The electronics generate a driving signal of order $10^5$ Hz that saturates and unsaturates the cores. The detected deviations from expected saturation due to an external magnetic field are read in the electronics as a current that's converted into a voltage. Calibration steps convert this voltage into a magnetic field value. . . . .	102
Figure 52. Figure from (R. Roglands Dissertation), used with permission. Schematic of the double probe experiment on ACES-II. (Left) Side view of payload and (right) top-down view of payload. The rocket has some velocity $\vec{v}_{sc}$ with respect to its own reference frame. Rockets are spin-stabilized with a spin frequency of $\Omega \sim 0.5$ Hz. The DC electric field $\vec{E}_{Drift}$ can be determined by using the probes by defining baseline vectors for each probe pair, $\vec{d}_{ij} = \vec{X}_i - \vec{X}_j$ where $\vec{X}_i$ is the position of the $i^{th}$ sensor from the payload body. . . . .	104
Figure 53. A schematic of a spherical probe setup for a sounding rocket. Here $\phi(x)$ is the radial symmetric potential that transitions the probe potential at point B to the ambient plasma potential at point A. All measurements are done with respect to Point C, the chassis ground $V_C$ . . . . .	107
Figure 54. The characteristic curve for a swept LP for probe voltage on the x-axis. The measured probe current $I_p$ is the current flowing out of the probe (positive by convention) and $I_{e0}, I_{+0}$ are the electron/ ion saturation currents, respectively. The point where the applied probe voltage matches the spacecraft potential $V_{sp}$ is shown near the electron saturation region. . . . .	108
Figure 55. Example of 5570 Å green-line ASI from Skibotn, Norway on Nov. 20th, 2022 over the Norwegian coast. The image is projected to 150 km and was sampled at 17:25:40 UTC. The camera was positioned approximately 150 km east of ACES-II launch point. This southward-moving discrete arc remained quasi-stable in space and time over the 10 minutes of the mission. . . . .	111
Figure 56. Global position and range of the EISCAT radar array at the north coast of Norway. The Tromødish (see black arrow) was used in this study to characterize the plasma density and temperature <i>in situ</i> . Image taken from <a href="https://www.eiscat.rl.ac.uk/radars/ISRfactsheet.pdf">https://www.eiscat.rl.ac.uk/radars/ISRfactsheet.pdf</a> . . . . .	112
Figure 57. An image of the type of auroral arc that ACES-II may have intercepted. Seen on the night of the launch overhead the rocket range $\sim 1$ Hr after launch. Taken with an iphone 11 camera. <i>Photocredit: Connor Feltman</i> . . . . .	113

Figure 58. Trajectories of the ACES-II rockets on Nov 20th, 2022 which launched a High/Low Flyer at 17:20:00 UTC/17:21:40 UTC, respectively. AllSky imager data of the discrete arc plotted in geographic coordinates. . . . .	115
Figure 59. Time series of ground-magnetometers located above (Bjørnøya in red) and below (Tromsø in blue) our discrete arc that occurred near 17:20:00. The H-component is most associated with the auroral electrojet. The H-component for the two stations trend in opposite directions near the ACES-II launch point. Data taken from Tromsø Geophysical Observatory at <a href="https://flux.phys.uit.no/stackplot/">https://flux.phys.uit.no/stackplot/</a>	116
Figure 60. Schematic showing the projections of the geomagnetic fields to 150 km. The green box represents the plane of ILat/ILong. MATLAB's geoplot3 package was used to plot this figure. . . . .	117
Figure 61. Magnetic conjunction between the payloads expressed in ILat coordinates referenced to 150 km. $\Delta\varphi$ is the latitudinal distance between the payload footprints and ILat $\Delta t$ is the lag time. . . . .	119
Figure 62. Magnetic conjunction between the payloads expressed in ILong coordinates referenced to 150 km. $\Delta\lambda$ is the latitudinal distance between the payload footprints and ILong $\Delta t$ is the lag time. Notably, the delay time in longitude is not significantly meaningful since several longitudes are not crossed by both payloads until very large time delays occur. . . . .	119
Figure 63. Magnetic conjunction between the payloads expressed in geographic coordinates Lat/Long for a projection of the magnetic field at 100km. The dark blue line is the Low Flyer Trajectory and its associated ILat/ILong coordinates are shown in lighter blue. The Higher Flyer trajectory is shown in red with it's ILat/ILong projection shown in orange. Select times are shown as "X" marks and a green line links the positions of the payloads here. . . . .	120
Figure 64. The three primary issues ACES-II suffered during flight. . . . .	122
Figure 65. Plot showing the data pairs used in the High Flyer's EPAA detector. The principle pad represents a choice of EPAA pitch angle sector. The uncalibrated pad values for a specific principle pad are the number of datapairs in other pitch angle sectors that need to be re-binned into that specific principle pad. The diagonal reports no values since each principal pad has zero values that need to be re-binned to itself. This particular instrument had significant pitch angle mis-alignment due to the coning of the rocket. . . . .	125
Figure 66. EPAA Step number vs. $\log E_{measured}$ response curve determined using a known electron source. For each step, a calibrated energy value can be determined and was used for the energy bins of the EPAA detector. . . . .	126

- Figure 67. From Greene et al., 2024, used with permission. This data comes from the pre-flight calibrations of the Tesseract magnetometer which flew on the ACES-II Low Flyer. (left column) The S-shaped response residuals. These are derived from taking the ideal linear response of the external field and subtracting the actual response as measured by the detector. (Right column) the residuals of the actual detector response after a 5th-order polynomial was used to characterize the non-linear aspects of the detector response, and then subtract out the non-linearity. . . . . 130
- Figure 68. Fixed RingCore magnetometer frame that shows how the oscillations from the rocket spin and coning get introduced into the measurement of  $|\vec{B}|$ . Ideally, the Z-axis of the RingCore frame is perfectly aligned to  $|\vec{B}|$ . The most apparent frequency is the spin  $\omega_s$  and if rocket coning occurs  $\omega_c$  will also be seen in the spun data. This particular RingCore frame is also shown in Figure 48. Image from Kaepller, 2013, used with permission. . . . . 131
- Figure 69. From Kaepller, 2013 and used with permission, defined and inspired from Eriksson et al., 2005. The three coordinates are  $\hat{e}, \hat{p}, \hat{r}$  and are approximately eastward, field aligned and approximately northward, respectively when at low altitudes. The radial vector  $\hat{\mathbf{R}}_{sc}$  points to the spacecraft from the center of earth. . . . . 136
- Figure 70. ACES-II Low Flyer calibrated ringcore data in ENU coordinates. (Top) RingCore data with  $\vec{B}_{geo}$  subtracted, leaving only residual spintone (bottom) 0.7 Hz, Highpass, Butterworth filtered data. Clear evidence of AC  $\delta B$  fluctuations can be seen in the filtered data near 17:24:50 UTC along with residual, low amplitude spin-tone. . . . . 138
- Figure 71. ACES-II High Flyer calibrated RingCore data in ENU coordinates with a 0.7 Hz, 4-th order Butterworth Highpass filter. Only the  $B_{East}$  (top) and  $B_{North}$  components are shown. Due to the coning and excited harmonics of the payload, the depin and filtered signal are still severely contaminated at low frequencies. This motivates the use of a new type of filtering. . . . . 139
- Figure 72. Example using mSSA on the Low Flyer's RingCore  $B_E$  component, used to isolate residual spintone in the signal. (Left Column) The original waveform (Orig.), the identified harmonics  $f_n$ , example principle components  $F_2, F_3, F_4$  identifiable broadband noise and the resultant signal after reconstruction (Phys. Signal). The black lines denote where 20% of the data has been mirrored in order to avoid mSSA edge effects in the reconstructed signal. This extra data is not included in the final reconstruction. (Right Column) The FFT of each of the waveforms on the left, with red lines denoting the spin harmonics of the payloads. See texts for details. . . . . 144
- Figure 73. High Flyer RingCore  $B_E$  data. (top) 0.7 Hz, High Pass Filtered (Bottom) Same data, but after the mSSA process is applied to remove spin and coning harmonics. Physical signal is now able to be distinguished at the point labelled "After mSSA". 146

Figure 74. Calibration curve used to convert Langmuir Probe ADC values into current, I. The circuit was designed with a logarithmic respond to input current in order to response to a large range of input current values, hence the circuit response linearly to  $\ln(I_{cal})$  vs ADC. . . . . 147

Figure 75. Example showing the path the ACES-II mission took through the Tromsø EISCAT dataset. The particular parameter plotted here is the plasma density. Each available EISCAT parameter was sampled at the altitude and time corresponding to the ACES-II attitude data for comparison to *in situ* data. The ambient ion temperature indicated an average value of  $T_i = 0.1$  eV from this method, which is used to determine the ion saturation current in the Langmuir probes. . . . . 148

Figure 76. Post-processed Langmuir Probe data using the peak density of E-Region seen by both Flyers as indicated by the EISCAT data. A multiplicative factor of 1/50 is applied to both the High Flyer and Low Flyer's dataset to average out any systemic error since both instruments saw approximately the same E-Region but reported different density values. The LP circuitry was identical for both payloads. 149

Figure 77. Overview of the EPAAA electron spectra, fields data and plasma density for both payloads plotted vs ILat. (a) Averaged differential energy flux over all pitch angles. (b) 0.7 Hz highpass filtered  $\delta B_e, \delta E_r$  component pairs. No electric field measurements for the High Flyer are available. Additional filtering via mSSA was applied to the High Flyer's magnetic fields data to remove rocket coning. (c) 0.3 Hz Lowpass filtered plasma density to remove spin and wake effects. Panels (d) to (f) follow similar format for the Low Flyer. A "primary" inverted-V signature between  $72.1^\circ$  to  $72.55^\circ$  ILat is seen by both payloads. A "Dispersive" region that contained several STEB events is seen conjunctive with  $\delta B_e$  fluctuations in the High Flyer dataset. . . . . 154

Figure 78. Time-aligned data during the High Flyer's Dispersive Region. EPAAA differential energy flux (a) energy-time spectrograms at  $10^\circ$  pitch angle and (b) Pitch Angle vs time for 28 eV to 988 eV. (c) Filtered  $\delta B_e$  and  $\delta E_r$  component pairs. (d) Power spectral density of  $\delta B_e$  at 7/8 hanning overlap. Panels (e) to (h) follow similar format for the Low Flyer. Both datasets show burst-like electron signatures coincident with low-frequency magnetic fluctuations. . . . . 155

Figure 79. From Kaepller, 2013. The comparison of altitude vs. ionization profiles for two identical models, one from Kaepller, 2014 (colored) and the other from Semeter et al., 2005 for various input beams of electrons in a model nighttime ionosphere. For our work, we care about the observation that flux for electrons below 500 eV sharply falls off below 180 km. This provides a possible explanation for why we might only see the high-energy component in the Low Flyer bursts if they are STEBs. This is because the Low Flyer was at 180 km when it saw its bursts in Figure 78 so energies below 500 eV would have been stopped at higher altitudes. 156

- Figure 80. Figure 14 from L.-J. Chen et al., 2005a which used Alfvén waves to generate electron dispersions with different source distributions. An inverted-V style distribution is simulated with 5 keV energies at  $2 R_E$  with some addition of “high energy” backscattered electrons as well as “low energy” backscatter and secondary electrons. Here, “high energy” refers to electrons with energies just below the inverted-V energy but above 1 keV. Low-energy means energies below 100 eV. An Alfvén wave is passed to create dispersion traces and the wave starts at  $4 R_E$ ,  $E_{\perp} = 40$  mV/m and  $k_{\perp}c/\omega_{pe} = 1$  when the wave launches. (a) The effect of adding higher levels of high-energy backscatter electrons and (b) adding more low-energy backscatter and secondary electrons. . . . . 158
- Figure 81. Schematic showing the projections of the geomagnetic fields during the Dispersive Region for both flyers. The green box represents the plane of ILat/ILong at 150 km. A zoomed-in version of this plane is provided in the bottom panel, which connects the fluctuations seen by both rockets to an assumed  $\delta B_{\perp}$  source moving transverse to  $\bar{\mathbf{B}}_{geo}$ . To match observations, the along-arc source structure must move approximately 4.75 km/s eastward. . . . . 161
- Figure 82. Up component in ENU coordinates of rockets’ payload velocity. The High Flyer is shown in the top panel and the Low Flyer in the bottom panel. Values are converted into ENU from the ECEF velocities given in the attitude data. . . . . 163
- Figure 83. Low Flyer’s fields instruments data. (Left Column) Pre-auroral quiet region. (Middle Column) Temporally aligned data when the High Flyer was intercepting the Dispersive region. (Right Column) ILat footprint of the Dispersive Region seen by the Low Flyer 20s after the High Flyer passed above. (a-c) 0.7 Hz Highpass filtered electric and magnetic fields. (d-f) Field-aligned Poynting Flux. Positive values are Earthward. (g-i)  $\delta B_e, \delta E_r$  frequency spectra. (j-l) electric-to-magnetic field E/B ratio (black) compared to local average MHD Alfvén speed (red). . . . . 165
- Figure 84. High Flyer EEPAA differential energy flux for five STEB events which precede an inverted-V in the Dispersive Region. Panel (a) shows the energy-time counts spectrogram for  $-10 < \alpha < 10^{\circ}$  averaged bins. Black lines indicate slices in time shown in  $(v_{\parallel}, v_{\perp})$  velocity space subpanels (b), (c), (d) and (e). Examples of STEB (solid) vs. inverted-V (dot-dashed) electrons are provided in panels (d) and (e). These events coincident with inverted-V precipitation (S4, S5) show higher peak energy and flux compared to those outside. . . . . 168
- Figure 85. Example of the type of isolation used for all STEBs in our study. STEB 5 is displayed here which partially overlapped with an inverted-V on the right-hand-side. The top panel shows the isolation of the STEB and the bottom panel is the raw counts data. The cross-correlation process primarily cares about the peak counts along the diagonal of the STEB so the removal of the inverted-V on the edges will not significantly affect the TOF results. . . . . 170

Figure 86. Example of the cross-correlation technique used on STEB 5 to determine the $\Delta t$ values between all combinations of energy channels. For each possible combination, one channel is labelled $v_{fast}$ and another is labelled $v_{slow}$ . The time series are convolved and summed to produce a single correlation value. (Top panel) STEB 5 raw counts data after isolation. Green and red lines denote the $v_{slow}$ and $v_{fast}$ time series, respectively. (Second panel) The red-line $v_{fast}$ time series plotted as raw counts vs. time. (Third panel) The green-line $v_{fast}$ time series plotted as raw counts vs. time. (Bottom panel) The correlation value between our example $v_{fast}$ and $v_{slow}$ . The peak in the correlation is assumed to correspond to the arrival time delay between STEB electrons at these energies. . . . .	171
Figure 87. Time of Flight (TOF) comparison plots for STEB events S2, S3, S4, S5 using a traditional linear, single-source altitude fit and a polynomial fit from Tanaka, 2005. In every case considered here, the Pearson correlation for the polynomial fit outperforms the linear fit and events S4 and S5 clearly indicate the genuine quadratic nature of the data. The fit parameters and source altitudes are listed in Table 1. . . . .	173
Figure 88. (a) 2D Illustration of the parallel distribution function $f(\mathbf{v}_{\parallel})$ for an inverted-V/backscatter population and an ambient plasma sheet source at high altitude before IAW resonance. (b) The effect of the same IAW passing through both distributions to produce a pair of STEBs with different peak energies and number flux. (c) Peak energy and (d) Averaged differential number flux over energy for choice STEB events in Figure 84. . . . .	178
Figure 89. High Flyer Poynting Flux during the same time range as Figure 84 in the Dispersive Region. Flux values are estimated from $\delta S_{\parallel} \sim V_A \delta B_{\perp}^2 / \mu_0$ and the duration of each STEB is colored and labelled. . . . .	182
Figure 90. High Flyer EEPAA counts median pitch angle vs time since launch. Dashed black lines are provided to help distinguish S4, S5 from nearby inverted-V pixels. . . . .	185
Figure 91. (Top) The model $ \vec{\mathbf{B}}_{geo} $ for a specific L-Shell of L=8.7. (Bottom) Calculated gradient in magnetic field $\nabla  \vec{\mathbf{B}}_{geo} $ used later in magnetic mirroring. . . . .	189
Figure 92. Adapted from Lysak, 1985. As the geomagnetic field lines of Earth coalesce, the $k_{\perp}$ of the wave shrinks to maintain constant magnetic flux. . . . .	190
Figure 93. Model $\lambda_{\perp}(z), k_{\perp}(z)$ for a chosen ionospheric value of $\lambda_{\perp 0} = 3.5$ km . . . . .	190
Figure 94. Model electron plasma density for the high latitude auroral zone. Based on the work from C. A. Kletzing et al., 1998. . . . .	192
Figure 95. (Top) Ion compositions as given by equation 184. (Bottom) Effective ion mass calculated from $m_i = (n_H m_H + n_0 m_0) / n_i$ . . . . .	193

Figure 96. Model of Electron Skin Depth. An example $\lambda_{\perp}(z)$ profile is also plotted for comparison on the $k_{\perp}^2 \lambda_e^2$ term. . . . .	193
Figure 97. Model kinetic corrections to the Alfvén phase velocity vs altitude. (Top left) MHD Alfvén speed $V_A = B / \sqrt{\mu_0 \rho_m}$ (Top Right) Electron inertia term $(1 + k_{\perp}^2 \lambda_e^2)$ (Bottom left) Ion Larmor radius term $(1 + \rho_i^2 k_{\perp}^2)$ (Bottom right) Finite Frequency term $(1 - \omega^2 / \omega_{ci}^2)$ . Only the inertial term meaningfully contributes at these altitudes due to the cold electrons/ions and low frequencies involved ( $f < 10$ Hz) . . . . .	194
Figure 98. Model Alfvén wave phase velocities. (Solid Red) MHD Alfvén Velocity (Solid Blue) Inertial Alfvén Wave velocity with $f = 4$ Hz and $\lambda_{\perp 0} = 3.2$ km in the ionosphere. Example thermal velocities for a $T_e = 1$ eV and 50 eV electron plasma are provided for reference when considering resonance. . . . .	195
Figure 99. Example of fitting routine done on the ACES-II High Flyer EEPAA data to estimate the plasma parameters of the plasma sheet Maxwellian. See text for details. . . . .	197
Figure 100. Average values for the $\alpha = 10^\circ$ pitch bin for 8 sweeps of EEPAA data in the inverted-V near STEB event S5. . . . .	199
Figure 101. Slice in differential number flux used for the modelling of the ambient plasma sheet. . . . .	200
Figure 102. Plots in velocity space vs differential number flux for modelled ambient plasma sheet that likely produced with S1, S2, S3 mapped to three example altitudes. The distribution is a Maxwellian with $n = 2.2 \text{ cm}^{-3}$ and temperature $T_e = 105 \text{ eV}$ which were fitted from the Inverted-V nearest to STEB event S5. . . . .	202
Figure 103. Plots in velocity space vs differential number flux for modelled inverted-V that likely produced STEB event S4 and S5 mapped to three example altitudes. The distribution is a Maxwellian with $n = 2.2 \text{ cm}^{-3}$ , temperature $T_e = 105 \text{ eV}$ and quasi-static potential $V_0 = 232 \text{ eV}$ which were fitted from the Inverted-V nearest to STEB event S5. The mirror force causes a “banana” shape to occur in the inverted-V. . . . .	203
Figure 104. (Top Panel) Modelled Alfvén speed profile for an ionospheric perpendicular wavelength $\lambda_{\perp 0} = 3.2$ km. The value of the ionospheric perpendicular scale is chosen as an average from the heuristic fits in Chapter 7.6. (Bottom Panels) Ambient Plasma Sheet and inverted-V distributions mapped to different altitudes under the mirror force. IAW resonance bands for acceleration are shown as gray bars. At 6000 km, TOF indicates no resonance occurred so a maximum possible wave potential $\Phi_p$ is calculated. When resonance starts around 5000 km, the required $\Phi_{max}$ must have been near 268 eV. When resonance ends near 2500 km, an estimate for the minimum wave potential was $\Phi_{min} = 113$ eV to reproduce our STEB data. This plot demonstrates why STEBs S2, S3 have lower peak energies and differential number fluxes. . . . .	206

## CHAPTER 1: INTRODUCTION

The pale blue dot we call Earth is a mote of dust in space that safeguards its inhabitants from the eternal blowing of the solar wind. Our planet has a magnetic shield which deflects and deters the harmful influences of our star, creating a complex but intricately beautiful system of electromagnetic energy filled with dynamic structures. These electromagnetic systems are filled with plasmas that support electric currents, plasma waves, magnetic tension, turbulence, and particles. These fundamental elements shift, contract, expand, convect and transmit energy as they respond to the forces of the solar environment, transmitting its influence from scales as large as our planet all the way down to the size of processes in the atmosphere. It becomes necessary to separate these phenomenon in terms of their spatial scales and temporal lifetimes, allowing us to connect influences from one range of scales to another. Indeed, nowhere is this process more apparent than the production of the Aurora Borealis (Northern Lights) or Aurora Australis (Southern Lights) in Earth’s sky, the energy of which ultimately can be traced back to our star. Events such as the Aurora are the product of “Space Weather” and very much like the first peoples to survey the unknown oceans of our Planet, the study of space weather seeks to understand the patterns and behavior of the sea of electromagnetic activity that surrounds us. For any space faring civilization, it becomes imperative to understand the environments and challenges future humans may be faced with. Even close to Earth, space weather can influence satellite electronics, GPS systems, telecommunications, ground-based weather stations, electrical power grids, metal pipelines degradation and even human cancer rates. In this dissertation, we focus on the behavior of Alfvén waves near Earth’s Ionosphere, which is simply one small element that affects a particular region of this vast electrodynamic system. We will start with a broader view of Earth’s geomagnetic field and work our way down into the region of interest.

The Earth’s hot nickel-iron core spins along with the planet and produces a strong dipole-like magnetic field whose influence extends far out from the surface of the planet. This *geomagnetic field* interacts with the solar plasma from the Sun and reaches an equilibrium thereby creating

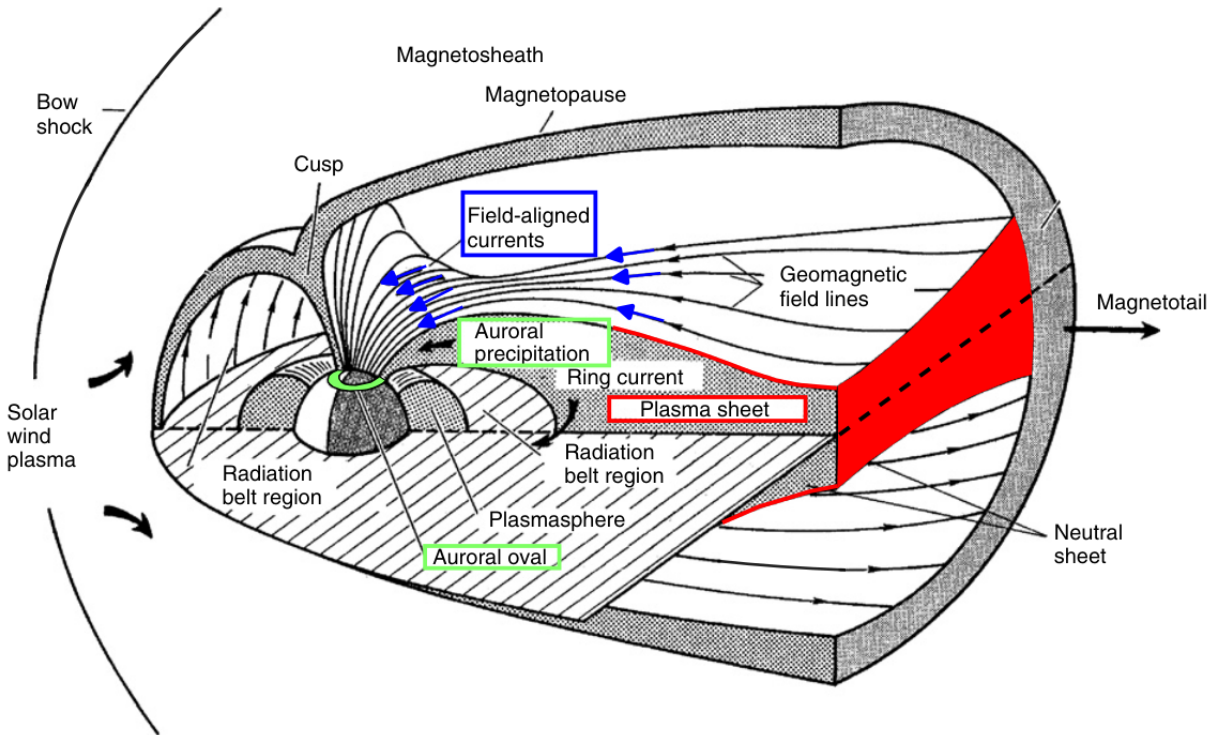


Figure 1. Schematic overview of Earth’s Magnetosphere, taken and edited from Kelly, 2009. Plasma flows along geomagnetic field lines produce currents between the regions of the Magnetosphere and to Earth’s atmosphere at the extreme latitudes. The regions associated with nightside auroral activity are colored.

Earth’s *Magnetosphere*; a region near Earth filled with plasma under the influence of Earth’s geomagnetic field. In Figure 1 we show a view of Earth’s magnetosphere and with a cut-out showing the various internal structures. From left to right, the solar wind (and solar magnetic field) impinges itself on Earth’s magnetic influence, dropping from supersonic to sub-sonic to form a bow shock  $\sim 14R_E$  Earth radii from our planet. The transition region from un-shocked to shocked plasma defines the magnetosheath and halts at the Magnetopause, which subsequently demarcates where Earth’s geomagnetic dipolar field begins to dominate. The continual influence of solar wind flow stretches out the geomagnetic field forming the Magnetotail, which spans tens of Earth radii. The coalescing magnetic fields in the dipolar geometry form two Cusp regions on the magnetic poles where plasma can flow more easily along magnetic field lines directly into the terrestrial atmosphere. Moving into the inner magnetosphere on the nightside we encounter the plasma sheet, a region of hotter plasma that forms the source region for nightside aurora by connecting energization

processes in the Magnetotail to the high latitude regions of Earth. Large-scale Field-Aligned Currents (FAC) are formed through the release of energy stored in geomagnetic fields which close their circuit through the Earth's electrically conductive atmosphere called *the Ionosphere*. To maintain electrical neutrality in the planet-scale system, upward and downward current regions at Earth's poles exist within the ionosphere that connect to FAC. These polar currents deposit their energy through collisions, ionization and waves while they cross magnetic field lines to flow through the atmosphere which heats the ionosphere in a process called *Joule Heating*. The heating occurs over a relatively short range of altitudes between  $\sim 90 - 150$  km which make up the space known as the *Current Closure Region*. This closure of currents through the atmosphere often results in electrons exciting (usually) oxygen to produce visible aurora.

These FACs and the ionospheric response to them forms the magnetosphere-ionosphere (MI) system. Here, the electrical conductivity of these regions mediates how much energy can be transferred between the coupled regions and is set by the collisions, density, temperature and ambient magnetic field of the plasma. For the magnetosphere, the conductivity along magnetic field lines is exceedingly large, whereas the conductivity in the ionosphere is low and introduces a choke-point in the transfer of energy in the MI system. From this fact, a reader might expect energy to flow only from the magnetosphere into the ionosphere, however this process is not so asymmetric and feedback between the MI system evolves through plasma waves and FACs that transfer energy between both regions. To illustrate this complexity, a schematic inspired from Baumjohann, 1982 is shown in Figure 2 which demonstrates the interconnected regions. Arrows indicate the direction of influence, which in most cases is bi-directional and implies a constantly occurring feedback process. The large scale sizes involved and speed of information transfer often cause processes to occur on the order of minutes to hours which allows many electrical processes to occur at once to reach electrical equilibrium in these systems.

Many unanswered questions remain within the MI system, such as (1) how well do the Frozen-in electric fields from the MI system map between regions (left side of Figure 2), (2) how FACs start developing and sustain themselves for long time periods (hours) or (3) how important

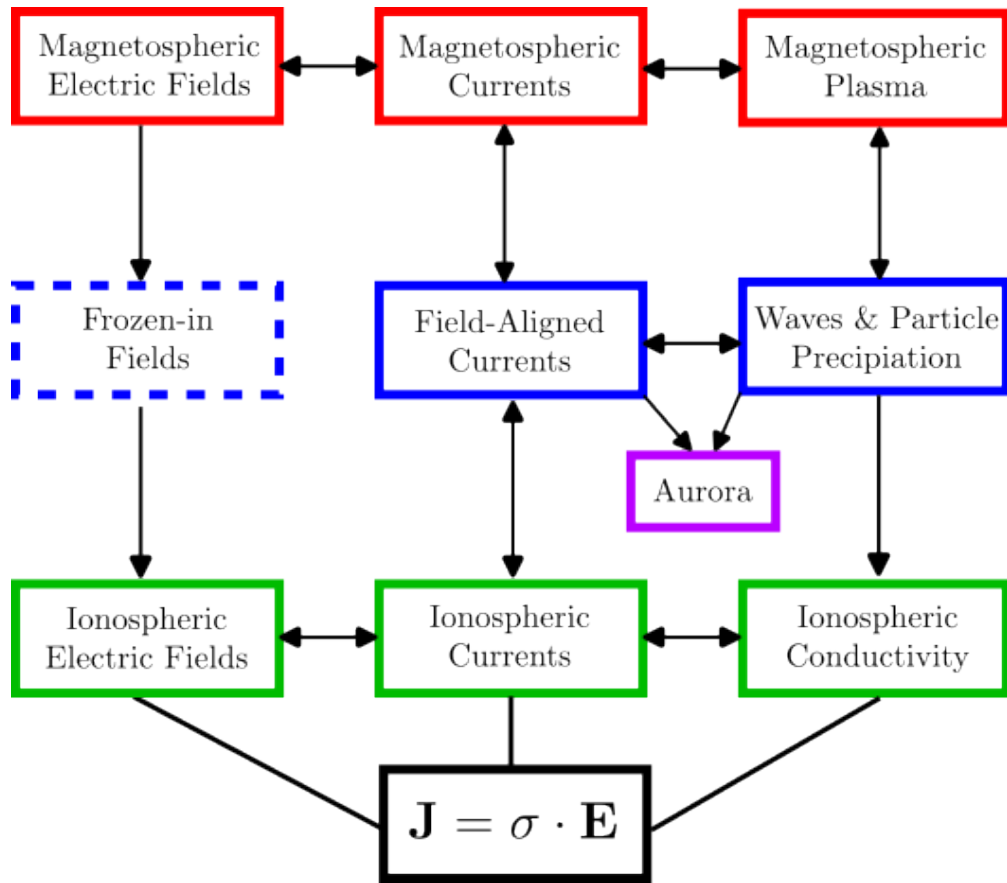


Figure 2. Diagram inspired from Baumjohann, 1982. The arrows indicate the direction of influence from one system to another, which are often bi-directional.

are the spatially small energization features seen in the aurora compared to the larger-scale ones that don't get observed as aurora? To date, it is still unknown *precisely* how current closure occurs in the ionosphere vs altitude and the impact that spatial (or temporal) gradients in conductivity have on the surrounding plasma, for which new *in situ* measurements are needed to address.

To address some of the unanswered questions stated above, the Aurora Current and Electrodynamics Structures II (ACES-II) sounding rocket mission was devised. The dynamic, fluid-like motion of the auroral plasma environment produces intrinsic challenges to its study, which is further compounded by the vast distances across altitudes covering orders of magnitude in scale. This limits the scope of observations to single-pass *in situ* measurements from satellites, rockets and balloon platforms or spatially localized ground-based instruments like Incoherent Scatter Radar, AllSky Imagers, Ionosondes and ground magnetometer arrays. Rockets have historically been successful at studying low-altitude ionospheric behavior since they are unconcerned with the large drag forces caused from Earth's dense atmosphere. The explicit goals of the mission are:

- (i) To determine the distribution of the ionospheric currents and the associated energy dissipation in a stable arc.
- (ii) Determine the relative **spatial** distribution or balance of Hall and Pedersen currents and their associated energy dissipation in the closure region.
- (iii) Estimate if current closure occurs within a uniform altitude distribution or does it vary across the arc (meridionally)?
- (iv) Evaluate where the primary energy dissipation occurs for a stable auroral arc.

The concept of the mission is shown in Figure 3. During a geomagnetic storm where a discrete auroral arc is present, a High Flyer payload was launched above the F-Region peak near 400 km in order to determine the flux of electrons entering the ionosphere below. A Low Flyer was launched to an apogee of 180km 100 seconds later along similar magnetic field lines to acquire *in situ* measurements under magnetic conjunction with the High flyer. This mission represents an

input/response style configuration that allows the Low Flyer electron, ion and magnetometer measurements to measure the Ionospheric Hall and Pedersen currents while the High Flyer estimates the total current into the arc system. Each payload was equipped with a nearly identical suite of instruments.

Achieving the goals of the ACES-II mission is still on-going work and this dissertation will instead examine a unique dataset found within the ACES-II High Flyer's High-energy electron measurements. These measurements were chosen because they relate electron wave-particle acceleration to observed low frequency plasma waves called *Alfvén waves*. Just as the processes for MI coupling can inject particles into the ionosphere, so too can Alfvén waves be excited within Earth's

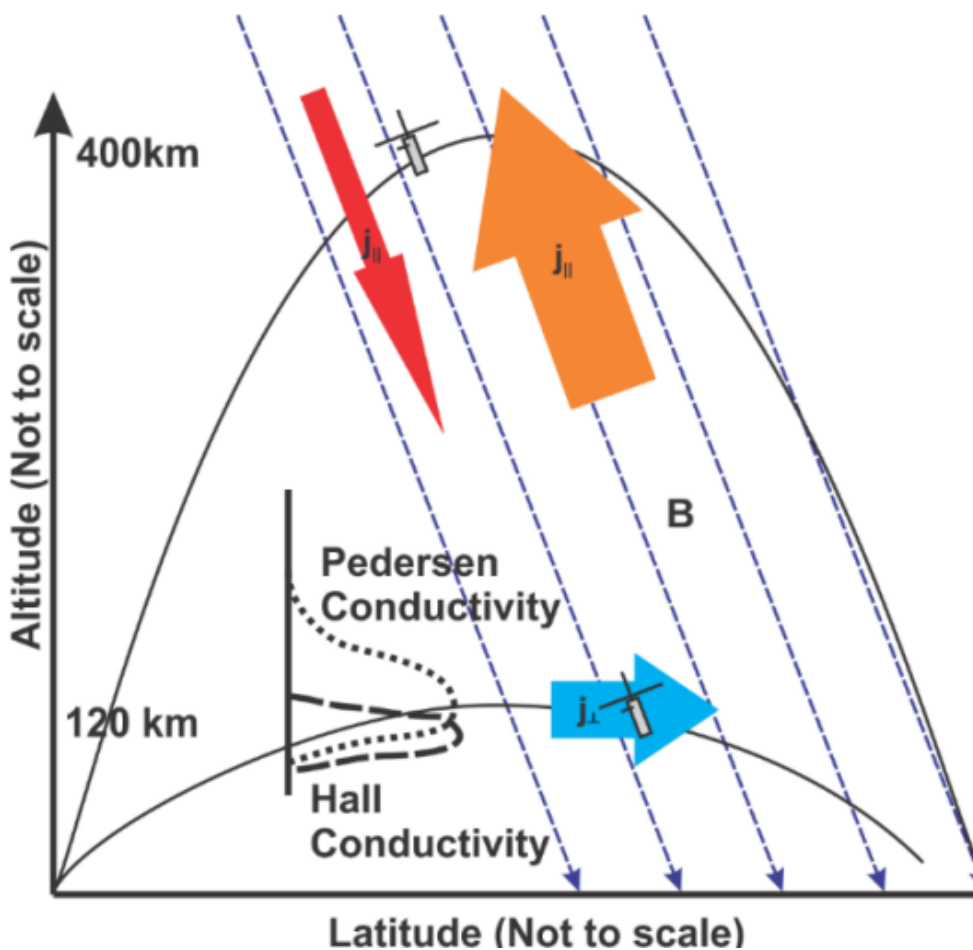


Figure 3. Illustration of the ACES-II sounding rocket mission. Two payloads are launched at different altitudes in an input/response style of configuration to determine the Hall/Pedersen currents within the ionosphere through a discrete auroral arc.

magnetosphere and propagate along geomagnetic field lines into low altitudes. Under certain conditions these waves can pick up and interact with electrons in a process called *wave-particle resonance*. The physics surrounding this process has gained significant attention in previous decades in laboratory experiments and been demonstrated under conditions relevant to auroral environments (C. A. Kletzing et al., 2010; Schroeder et al., 2016; Schroeder et al., 2017; Schroeder et al., 2021). For the work presented here, a unique set of measurements in the ACES-II data allowed for a study of these waves and provided some of the first *in situ* measurements of the wave-particle resonance interaction with different sources of naturally occurring electron distributions.

Alfvén waves themselves are fundamental plasma waves which are analogous to a wave on a string. A wave excited on one end of the string propagates because of the tension in the string and the inertia of the material that makes up the string. Similarly, an Alfvén wave is just a excitation in the magnetic field within a plasma and the magnetic tension and the inertia of the heavier, positive charge carriers causes the wave to continue propagating. The connection between a string and an Alfvén wave is more than just analogous and a formal derivation of each provides nearly identical

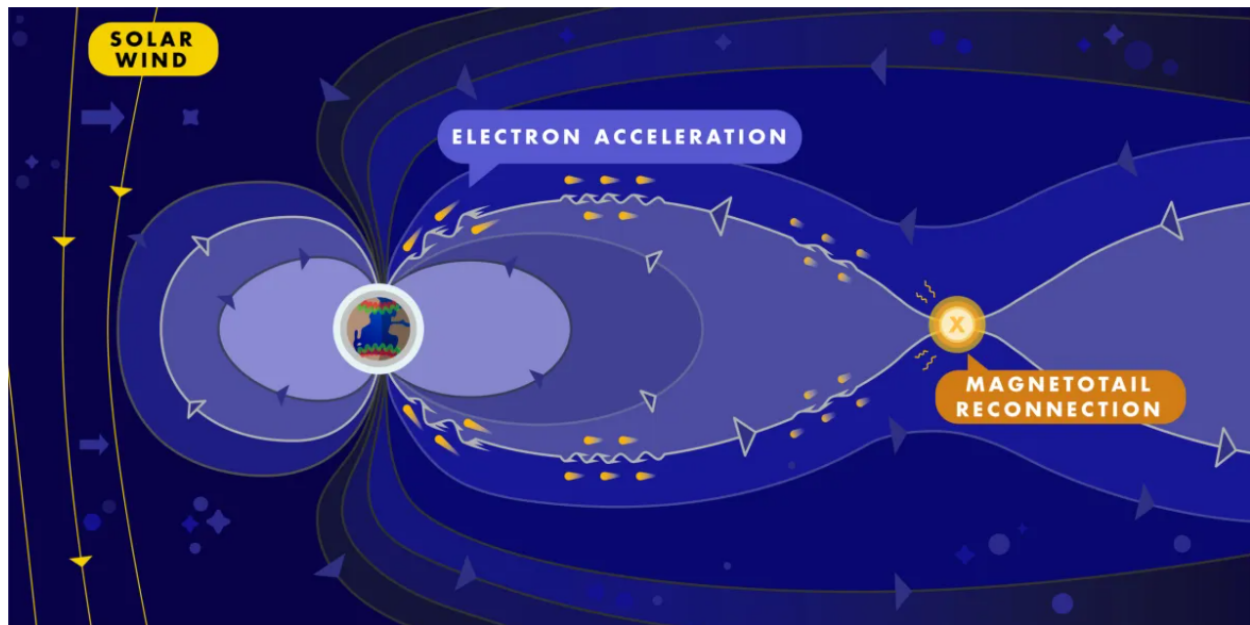


Figure 4. Image: Austin Montelius, University of Iowa (Formerly). Diagram of where Alfvén waves are created in Earth's magnetosphere due to magnetotail reconnection. Electron acceleration occurs over a range of altitudes when the waves travel towards Earth from their point of creation.

differential equations that describe their respective wave, hence the comparison is also mathematically accurate. In the Magnetosphere, Alfvén waves are excited through several processes, one of which is nightside magnetotail reconnection as shown in Figure 4. The reduction in magnetic tension via reconnection of magnetospheric geomagnetic field lines is the energy source that produces Alfvén waves that travel back to the ionosphere and interact with ambient plasma along the way.

Originally, these Alfvén waves were not considered to be part of the energization processes that create aurora. However, the discovery of an electric field parallel to the motion of the wave unlocked the possibility for electrons to “surf” the waves and gain energy (Goertz et al., 1979a; Hasegawa, 1976; Lysak et al., 1996; St  fant, 1970). In Figure 5 we show an illustration of this process. For electrons that are either too slow or too fast compared to the wave speed, the wave passes over them and no energy is transferred. But for electrons with speeds just close enough to the wave, they begin to “see” the electric field of the wave and be accelerated by it. The electrons which fall within the special band of velocities needed to resonate are within the *resonance band*

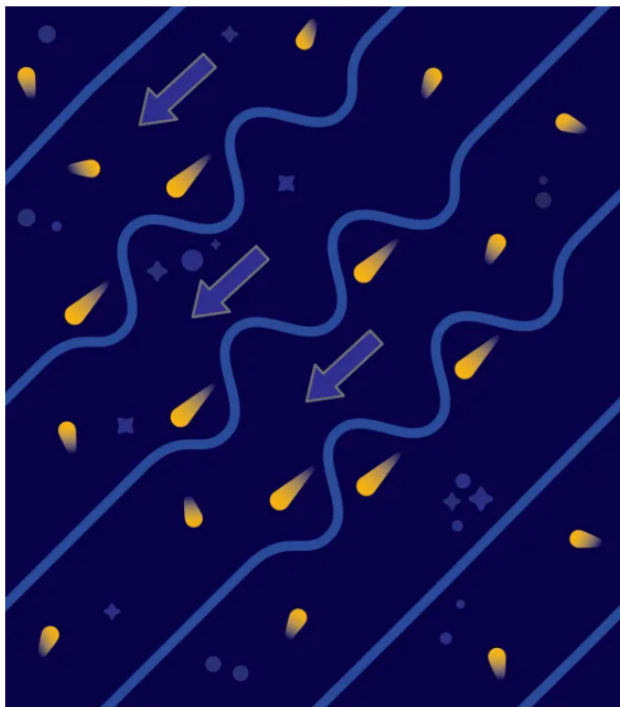


Figure 5. Image: Austin Montelius, University of Iowa (Formerly). Diagram showing how Alfv  n Wave-particle resonance occurs, where some electrons can “surf” the wave while others are untouched.

of the Alfvén wave. In any plasma, there are a spread of electron speeds and some fraction of these may fall within the resonance band of a passing Alfvén wave. When studying these waves, complexity arises due to the Alfvén wave speed changing with altitude thereby changing the speed required to resonate with the wave at different altitudes.

The primary focus of this dissertation is exploring the behavior of electrons accelerated by similar Alfvén waves when the waves interact with different electron populations. In satellite and rocket data within the low altitude auroral latitudes, suprathermal electron bursts (STEBs) are generally considered to be the signatures of the Alfvén wave-particle acceleration process. STEBs are time-dispersed features that are closely aligned to the geomagnetic field and in Figure 6 we show some examples of STEBs taken from the ACES-II high-energy electron data. Through their study, we can remotely sense the acceleration processes which happened thousands of kilometers above our payloads in order to understand which electron populations must have been present to produce these features. In particular, when STEBs are observed next to each other but exhibit different behaviors, this observation suggests the electron *source populations* for the wave themselves may be different. The question of how STEB behavior should change with differing source populations has been simulated in numerical models (L.-J. Chen et al., 2005a), but still remains a less explored question in the study of Alfvén resonance. The work contained in this dissertation provides some of the first *in situ* evidence for the enhancement of STEB energy and flux due to auroral particles.

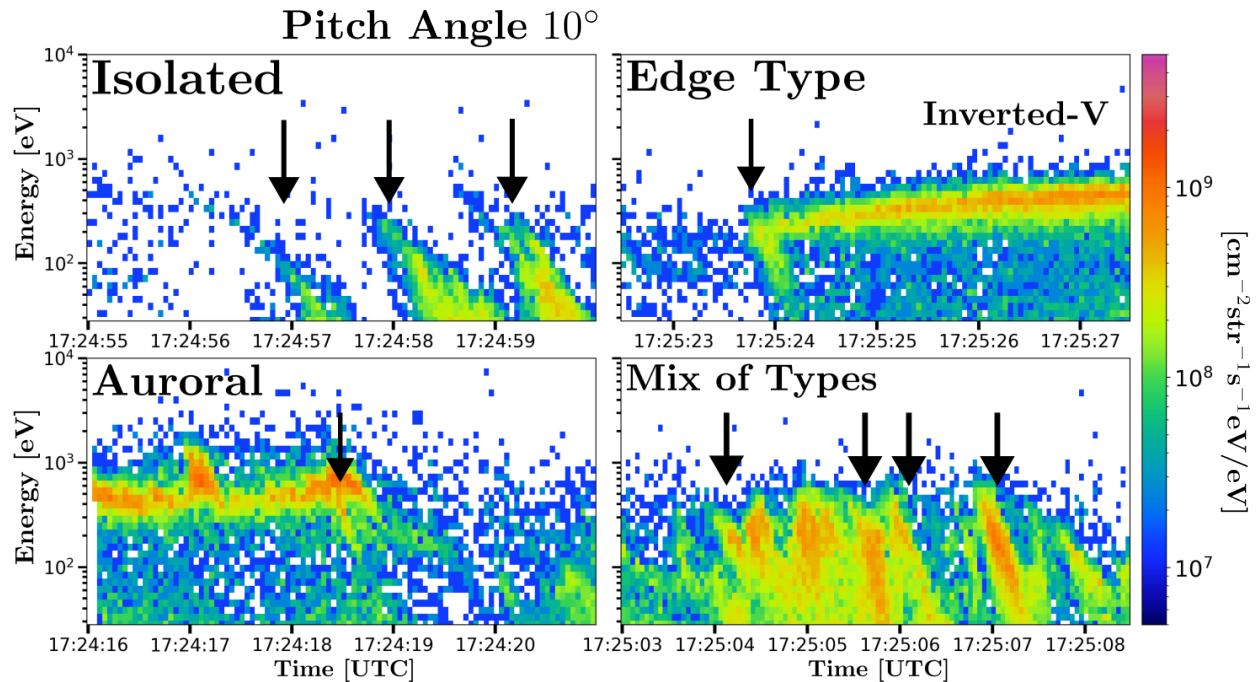


Figure 6. Examples of suprathermal electron Bursts (STEBs) seen in the ACES-II High Flyer rocket data. Various shapes exist for these time-dispersed electron signature, although they generally display the highest energies arriving before the lowest energies as well as inhabit the most field-aligned pitch angle bins. The bursts are categorized based on their relation to other types of precipitation. Isolated bursts are wave-particle acceleration structures by themselves. Auroral bursts occur coincident/near auroral precipitation. Edge-type bursts occur only near the edge of auroral precipitation and may be associated with the movement of aurora (inverted-V) instead of Alfvén waves. Finally, bursts can become difficult to distinguish, especially near auroral (inverted-V) precipitation, which appear as a mix of types.

## CHAPTER 2: SPACE PLASMA FUNDAMENTALS

(This chapter follows from F. Chen, 2016, Russell et al., 2016 and M. Kivelson, 1995.)

### 2.1 What makes a (space) plasma?

Space Plasma, like any other plasma, is a state of matter wherein a gas of charged particles responds to electric and magnetic forces in a bulk sense. Space plasmas exist around rocky planets or gas giants, as opposed to laboratory plasmas or astrophysical plasma near extra-galactic or intergalactic media. Space plasma physics is specifically concerned with this state of matter around our home planet, where scale sizes are often measured in terms of planetary radii. The range of temperatures, densities and magnetic field strengths where plasma occurs spans the greatest number of order of magnitudes compared to any other state of matter. To separate a plasma from just a low-density gas of particles, the principle of overall charge neutrality applies, often referred to as *quasi-neutrality*:

$$n \simeq n_e \simeq n_i \quad (1)$$

where  $n_e, n_i$  are the per species number density of charge particles per volume of space. This approximation holds true on a broader view, instead of a microscopic individual particle perspective. Neutral particles are also permitted in a plasma so long as the bulk behavior of the charged particles under external electromagnetic forces is retained. In addition to quasi-neutrality, three more criteria define a plasma:

$$\lambda_D \ll L \quad (\text{The Debeye Length is smaller than the scale size of the system}) \quad (2)$$

$$N_D \gg 1 \quad (\text{The number of particles in the Debeye Sheath must be large}) \quad (3)$$

$$\omega\tau > 1 \quad (\text{Collisions occur less frequently than typical plasma oscillations}) \quad (4)$$

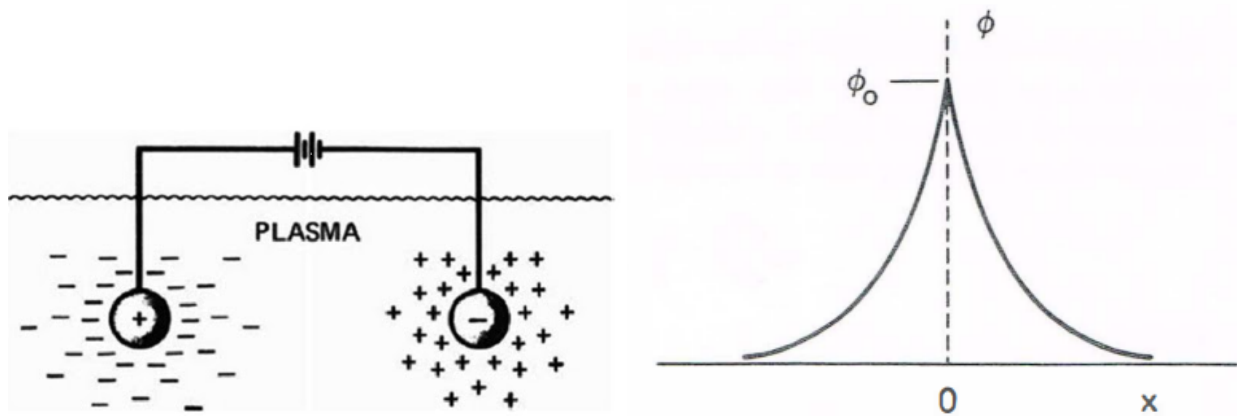


Figure 7. From F. Chen, 2016. 1D potential distribution inserted into a plasma.

To describe these criteria mathematically we must define what is meant by the Debeye length. Quasi-neutrality being a bulk property means local scale deviations from equation 1 exist which gives rise to an ambient potential energy within the gas. Charged particles constantly shift in response to these deviations in order to minimize this ambient potential. For example, consider the potential from a single electron in a plasma. The coulomb potential from this electron falls off as  $1/r$  for radial distance “r” as shown in 7. Ambient, positively charged particles called *ions* will be attracted to this potential and effectively “screen” out the electron’s influence as they form a sphere around it. The size of the sphere depends on the plasma parameters and effectively determines the sphere of influence the electric field from the electron has. The space of charged particles that surrounds the electron is called a *Debeye Sheath*. If the system were electrostatic, the electron’s electric field would be totally screened out by ions that reach equilibrium positions. However, thermal motions of the electrons or ions allow some of the point particle’s E-Field to “bleed” further into the plasma than otherwise allowed by electrostatics. The collective average of the non-screened out potentials that exists throughout the plasma is called *the Plasma Potential*. For any sheath, the “edge” occurs when the energy of the screened potential approximately equals the thermal energy of the particles,  $k_B T/e$ . The scale factor that describes the size of the sheath is called the *Debeye Length*, which can be calculated for our 1D system.

Consider the potential shown in Figure 7 which represents a single dimension of the spher-

ical potential  $\phi(\vec{r})$  from a charged particle. We assume the that the ratio of  $m_+/m_i$  is effectively infinite so we treat ions as basically stationary and form a background positive charge. Essentially, ion interia is so large they don't move much on time scales of experiment. Possion's equation is then:

$$\epsilon_0 \nabla^2 \phi = -e(n_i - n_e) \quad (5)$$

Within the sphere of charge particles the ion plasma density varies with distance, but when very far away the ion density is uniformly defined  $n_i = n_\infty$ . To understand how the density of electrons in a plasma  $n_e$  should behave, we appeal to the statistical mechanical definition of the electron distribution function. A gas in thermal equilibrium with  $T \simeq T_i \simeq T_e$  has the most probable velocity distribution described by a the *Maxwellian* velocity distribution:

$$f_M(\vec{v}) = n \left( \frac{m}{2\pi k_B T} \right)^{1/2} \exp \left( -\frac{m(\vec{v} \cdot \vec{v})}{k_B T} \right) \quad (6)$$

For particle velocity  $\vec{v}$ , temperature  $T$ , plasma density  $n$  and mass  $m$ . The distribution function  $f_M du$  gives the number of particles per  $[m^3]$  with velocity between  $u$  and  $u + du$ . The electron density itself comes from the *first moment of the distribution*:

$$n = \int f(\vec{v}) d^3 \vec{v} \quad (7)$$

This distribution under the influence of the electrostatic potential  $\phi$  is modified so the term in the exponential is  $(-\frac{1}{2}m\vec{v} \cdot \vec{v} + q\phi(\vec{r})) / k_B T$ . The first moment of this modified distribution function is

$$n_e = \int f_M(\vec{v}) \exp \left( \frac{q\phi(\vec{r})}{k_B T} \right) d^3 \vec{v} = n(\vec{r}) \exp \left( \frac{q\phi(\vec{r})}{k_B T} \right) \quad (8)$$

At  $\vec{r} = \infty$  we have  $n_e = n_\infty, \phi(\vec{r}) = 0$ , which gives us *the Boltzmann Relation* for  $q=e$ :

$$n_e = n_\infty \exp \left( \frac{e\phi}{k_B T_e} \right) \quad (9)$$

By inserting equation 9 into equation 5, we now get a solvable differential equation:

$$\varepsilon_0 \nabla^2 \phi = en_\infty \left( \exp\left(\frac{e\phi}{k_B T_e}\right) - 1 \right) \quad (10)$$

If we assume the thermal energy of the plasma surpasses the electrical potential energy i.e.  $|e\phi/k_B T| \ll 1$ , then we can taylor expand the exponential to approximate equation 10 as:

$$\nabla^2 \phi = \frac{1}{r} \frac{\partial^2}{\partial r^2} (r\phi) = \left( \frac{e^2 n_\infty}{\varepsilon_0 k_B T_e} \right) \phi \quad (11)$$

For which appropriate solutions to (11) are:

$$\phi(r) = \phi_0 \exp(-r/\lambda_D) \quad (12)$$

Where the scale factor  $\lambda_D$  is the *Debye length* defined as:

$$\lambda_D \equiv \left( \frac{\varepsilon_0 k_B T_e}{ne^2} \right)^{1/2} \quad (13)$$

A sphere one Debeye Length in radius defines the Debeye Sheath for any particle/region. Fundamentally, this parameters tells us a few important things about all plasmas:

1. Plasma particles (generally electrons due to their mobility) try to screen out potentials that differ from the plasma potential.
2. Electric Fields penetrating a plasma drop to  $1/e$  ( $\sim 37\%$ ) of their magnitude after a distance of  $\lambda_D$ , and continue to decrease exponentially for every successive  $\lambda_D$  until the plasma potential is reached.
3. The Debye length is dependent upon the plasma parameters, not on the potential inserted into the plasma.
4. Changes in temperature or density of the plasma affect the size of the Debeye sheath greater

than changes in  $\phi_0$ . (Relevant for Langmuir Probes in Chapter 5.)

We can now discuss the plasma criterion stated in equations 2, 3, 4. The first plasma criterion is set by the scale length “L” of any system in question for any geometry. If the Debeye length is of-order or greater than L, the plasma is unable to come to an equilibrium plasma potential. This situation would not be quasineutral and charge imbalance would occur, breaking the  $e\phi/kT$  assumption. This requires that  $\lambda_D \ll L$  for a plasma to be considered an electrical gas instead of individual particles. The second criteria comes from *the Plasma Parameter*  $N_D$ , which refers to the number of particles within a Debeye Sheath. Mathematically, a *Debeye Sphere* with a radius of  $\lambda_D$  and charged particle density “n” must have many particles:

$$N_D = n \frac{4}{3} \pi \lambda_D^3 \gg 1 \quad (14)$$

We require this in order for the Debeye Seath itself to be statistically meaningful. The final criterion deals with the typical frequency of plasma oscillations  $\omega$  and the mean time between collisions  $\tau$ . If the particles in the gas collide more often than the fastest oscillations in the plasma, then virtually no bulk plasma characteristics can be observed. An example of this is the exhaust from a jet airplane which has many charged particles but collides too often with neutral atoms to be a plasma. Thus we require,

$$\omega_{plasma} > \frac{1}{\tau} \quad (15)$$

## 2.2 Single Particle Motion

While the behaviors of plasmas are generally bulk motions of lots of particles, the trajectories of individual particles can illustrate the behavior of the gas. In this section we will develop some of the tools to discuss the single particle motion effects of a plasma. For any magnetic field  $\vec{B}$ , electric field  $\vec{E}$ , particle velocity  $\vec{v}$  and charge  $q$ , the *Lorentz Force*  $\vec{F}$  on that particle is

$$\vec{F} = m \frac{d\vec{v}}{dt} = q (\vec{E} + \vec{v} \times \vec{B}) \quad (16)$$

To start, we isolate the behaviour of the magnetic influence by assuming no electric field  $\vec{B} = B_0 \hat{b}$ ,  $\vec{E} = 0$ . For this setup, the particle begin to circularly gyrate in the plane perpendicular to  $\hat{b}$ . The oscillation frequency is called the *cyclotron frequency* or *Larmor Frequency* and is defined by

$$\Omega_s = \frac{qB}{m_s} \quad r_c = \frac{v_\perp}{\Omega_s} \quad (17)$$

where  $q$  is particle charge,  $B$  is the field perpendicular to the particle's orbit,  $m_s$  is mass of the species. Due to charge dependence, oppositely charged particles gyrate in opposite directions. The radius of the gyration is the *Larmor Radius*  $r_c$  which depends upon the particle velocity perpendicular to the magnetic field  $v_\perp$ . Unless otherwise acted upon, charged particles are constrained to these gyrating orbits in the plane perpendicular to  $\vec{B}$  but otherwise are free to move parallel to  $\vec{B}$ . For particles with a velocity component parallel to  $\vec{B}$  the particle motion becomes a helix, as shown in on the first panel on the left column of Figure 8. The “Bounce” motion described in Figure 8 originates from the conservation of the first adiabatic invariant, which we will discuss next.

## 2.3 The Dipole Magnetic Field and Adiabatic Invariants

Within a few  $R_E$  of Earth's surface, the dipole model of the geomagnetic field is a good approximation. Here, Earth's crustal fields, magnetic anomalies from mineral deposits, multipole moment contributions and the (assumed) core dynamo are negligible. The right side of Figure 8

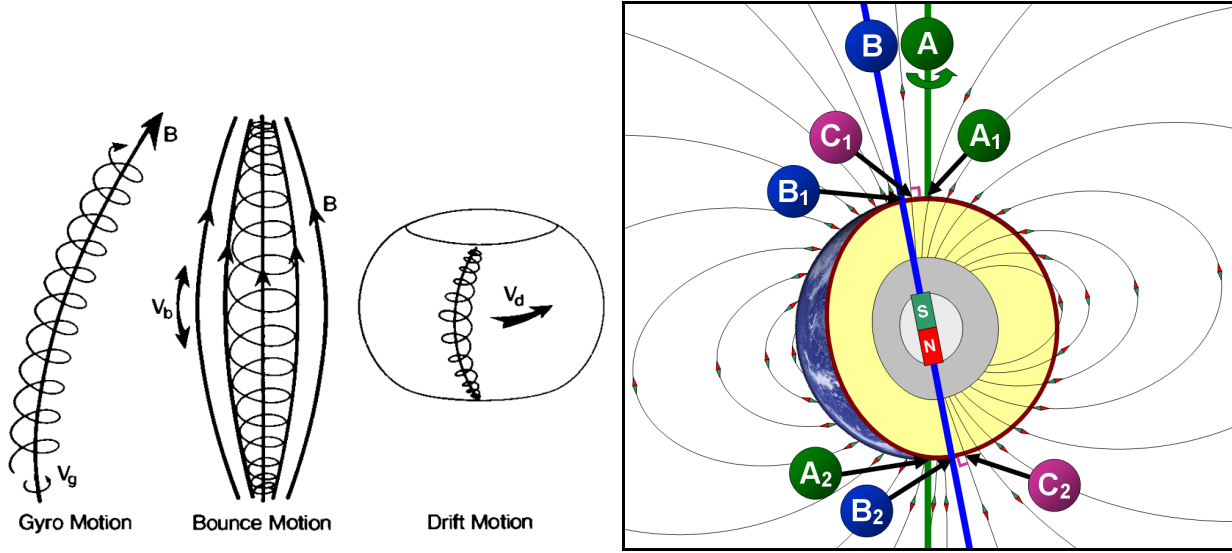


Figure 8. (Left) Three types of single particle motion often found along geomagnetic field lines (M. Kivelson, 1995). (Right) Example of Earth’s dipolar geomagnetic field, which is a good approximation within a few  $R_E$ . The pairs A1/A2 are the geographic poles, B1/B2 are geomagnetic poles and C1/C2 are magnetic poles. Figure adapted from from ([https://en.wikipedia.org/wiki/Earth%27s\\_magnetic\\_field](https://en.wikipedia.org/wiki/Earth%27s_magnetic_field)).

shows the poles of Earth, where the geographic poles are defined by the rotation axis of Earth (A1/A2), the geomagnetic poles (B1/B2) are Earth’s magnetic poles from a dipolar contribution (perfectly antipodal points) and (C1/C2) are the magnetic poles which are the sum of all contributions to the magnetic field (non-antipodal). The Earth’s northern magnetic pole as of 2024 is approximately  $11^\circ$  off-axis from its geographic pole. In spherical coordinates  $(r, \Phi, \lambda)$  the dipole vector field is given as

$$\vec{B}_{dip} = \frac{\mu_0 M}{4\pi r^3} (-2 \sin \lambda \hat{r} + \cos \lambda \hat{\lambda}) \quad (18)$$

where  $M$  is the magnetic moment,  $r$  is radial distance from the center of the sphere,  $\lambda$  and  $\Phi$  are magnetic latitude and longitude. The vector magnitude is

$$|B_{dip}| = \frac{\mu_0 M}{4\pi r^3} \sqrt{1 + 3 \sin^2 \lambda} \quad (19)$$

We can define the concept of individual “field lines” in the dipole geometry where a set of magnetic fields at the surface of Earth is chosen and traced out to higher altitudes, as was done by McIlwain,

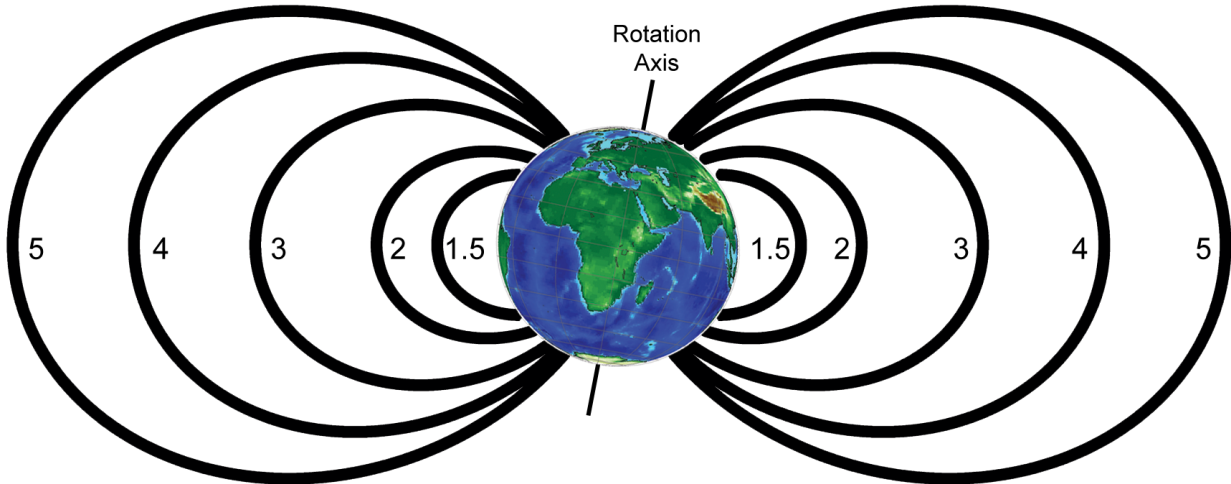


Figure 9. From <https://en.wikipedia.org/wiki/L-shell>. Concept of L-Shell in a dipole magnetic field. The Shells are defined by the intersection point of magnetic field lines at the magnetic equator and numbered. Auroral Field lines typically exist on L-Shells above 7.

1961. From this, the *L-Shell* is a dimensionless parameter that describes the “shell” of a specific set of field lines at the magnetic equator all the way to the poles. This is visualized in Figure 9, but can be described mathematically as

$$r = L \cos^2 \lambda \quad (20)$$

where  $r$  is the radial distance (in  $R_E$ ) to a point on the field line,  $\lambda$  is geomagnetic latitude and  $L$  is the L-Shell parameter.

The bounce motion of particles occurs on the dipole field lines of the geomagnetic field across many L-Shell values. Here particles follow field lines to the high latitude regions of Earth and mostly reflect, returning the way they came. In aggregate this motion traps particles within this magnetic geometry, a phenomenon that’s responsible for *the Van Allen Radiation Belts* which are mainly large fluxes of two large-scale donut-shaped collections containing highly energetic (100’s of keV to MeV) electrons and protons surrounding Earth. To understand why these particles are trapped we must look at the *adiabatic invariants* of the plasma, which are pseudo-conserved quantities that remain constant under certain conditions.

If the magnetic field experienced by a particle changes in space and time slowly compared to the gyroperiod (and there are no collisions), then a quantity called the *first adiabatic invariant*

is conserved throughout the particle's motion:

$$\mu = \frac{\frac{1}{2}mv_{\perp}^2}{B} \quad (21)$$

where  $v_{\perp}$  is the perpendicular velocity relative to the local magnetic field. For example, particles entering the polar regions of Earth experience growth in their  $v_{\perp}$  as the magnetic field lines converge and increase  $B$ . The change in  $v_{\perp}$  is always to keep  $\mu$  constant, so  $v_{\perp}$  would necessarily increase. Equation 21 allows us to setup and compare two points along a geomagnetic field line. The change in  $v_{\perp}$  is represented by a force, called *the mirror force* given by

$$F_{\text{mirror}} = -\mu \frac{\partial \vec{B}}{\partial \vec{S}} \quad (22)$$

where  $d\vec{S}$  is a line segment along the magnetic field  $\vec{B}$ . As a particle enters regions of growing magnetic field strength ( $d\vec{B}/d\vec{S} > 0$ ) the mirror force will continually convert a parallel energy into perpendicular energy until all the energy becomes perpendicular or the particle is lost from the plasma. If mirror force converts all parallel energy to perpendicular, this forces particles back into regions of ( $d\vec{B}/d\vec{S} < 0$ ), thereby starting the process over but now converting perpendicular energy back into parallel. The point where this energy flip occurs is called *the mirror point*. For Earth, the mirror points for particles exist near the magnetic poles and particles are continuously reflected from these conjugate points, often several times a second.

To better analyze Earth's magnetic mirror we introduce the concept of the *pitch angle*  $\alpha$ , which is the angle between a particle's total velocity  $\vec{v}$  and the direction of the B-Field vector  $\vec{B}$ . If we assume the first adiabatic invariant in equation 21, the total particle velocity  $|v|$  is constant. Using  $v_{\perp} = |v| \sin(\alpha)$  our conservation relation for two points along a geomagnetic field line becomes:

$$\frac{\sin^2(\alpha_1)}{B_1} = \frac{\sin^2(\alpha_2)}{B_2} \quad (23)$$

Notably, when  $\alpha_2 = 90^\circ$  the particle is at its mirror point since this implies all velocity is in the perpendicular direction. The pitch angle of the particle at the position of  $B_1$  is then defined in terms

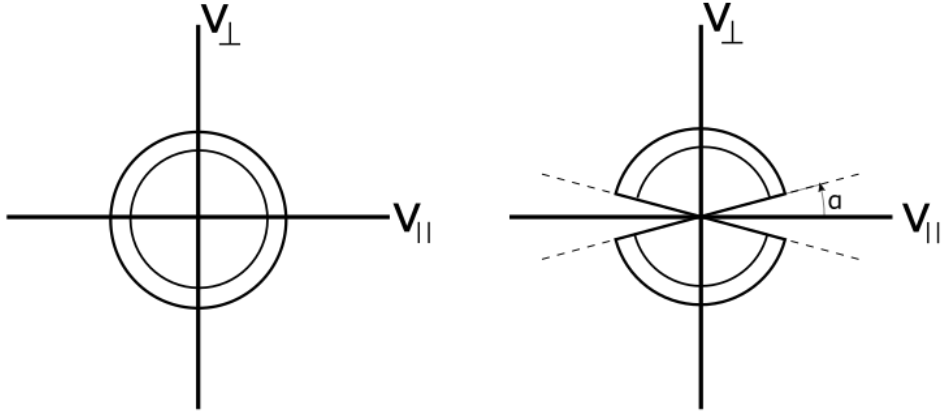


Figure 10. An initial Maxwellian distribution function (left) projected into a 2D that begins in a hypothetical magnetic mirror at  $t=0$ . The circular contours represent lines of constant total velocity. (right) The same Maxwellian distribution after some time has passed. Particles with pitch angles too small to be confined by the magnetic geometry escape and are lost from the initial distribution.

of the magnetic field value where the particle mirrors:

$$\sin(\alpha_1) = \sqrt{\frac{B_1}{B_2}} \equiv \frac{1}{\sqrt{r_{mirror}}}, \quad r_{mirror} = \frac{B_{max}}{B_{min}} \quad (24)$$

This definition implies particles with pitch angle  $\alpha < \alpha_1$  will not be reflected at  $B_2$  and particles with  $\alpha > \alpha_1$  would be mirrored before reaching  $B_2$ . This process is conservative and is a method to trap particles within cleverly designed magnetic field geometries. The Van Allen radiation belts are then those particles with pitch angles that trap them between Earth's magnetic mirror points. However, if collisions or the walls of a device allow particles to escape from the magnetic containment then they are considered lost from the distribution and the set of all particles which have no mirror points contained within a system are considered to be in *the loss cone*. The loss cone is defined for each spatial point in the mirroring plasma as the set of velocities with pitch angles that have trajectories that escape the plasma. Figure 10 shows an example Maxwellian distribution that has developed a loss cone of particles in a hypothetical mirroring configuration. Particles with pitch angles too small (large initial  $V_{||}$  compared to  $V_{\perp}$ ) go beyond the size of the mirror geometry and become lost from the initial distribution.

## 2.4 Particle Drifts

The *drift motion* in Figure 8 is derived through an analysis of particle forces in magnetic field gradient's. Here we will consider the impact that *external*  $\vec{E}$  have on a plasma, and more generally any externally applied force. Writing the equation of motion of a charged particle for generalized force  $\vec{F}$  we get

$$m \frac{\partial \vec{v}}{\partial t} = q \vec{v} \times \vec{B} + \vec{F} \quad (25)$$

where  $\vec{F}$  can be the electrostatic force  $q\vec{E}$  or any additional constant force that acts perpendicular to  $\vec{B}$ . If we take the cross product of equation 25 with  $\vec{B}$  we get:

$$\begin{aligned} m \frac{\partial \vec{v}}{\partial t} \times \vec{B} &= q (\vec{v} \times \vec{B}) \times \vec{B} + \vec{F} \times \vec{B} \\ &= q \vec{v} B^2 - q \vec{B} (\vec{v} \cdot \vec{B}) + \vec{F} \times \vec{B} \end{aligned}$$

The perpendicular component on the right side of this equation has  $\vec{v}_\perp \cdot \vec{B} = 0$ . Additionally, the  $\partial \vec{v} / \partial t$  term just results in the known circular/Larmor motion. Setting this Larmor term to zero leaves only the generalized *drift* motion on a single particle's guiding center perpendicular to  $\vec{B}$ :

$$\vec{v}_d = \frac{\vec{F} \times \vec{B}}{qB^2} \quad (26)$$

With equation 26 in hand, we can understand the drift motion of plasma particles for any force as long as  $\vec{F} \perp \vec{B}$ . Two examples of  $\vec{F}$  are: (1) the **gradient** in  $B_{dip}$  which causes drifts due to changes in  $r_L$  over a gyroperiod and (2) the curvature of  $B_{dip}$  which causes a centrifugal force to occur on the particles which induces a drift perpendicular to  $\vec{B}$  along the radius of curvature  $\vec{R}_c$ . Using equation 26 for the curvature drift we can combine both of these drifts into one process since they act in the same direction, called the *gradient-curvature* drift:

$$\vec{v}_B = \frac{m}{2qB} (v_\perp^2 + 2v_\parallel^2) \frac{\vec{B} \times \nabla B}{B^2} \quad (27)$$

This drift is dependent upon the charge of the particle, and thus can give rise to currents. The large-scale *Ring Current* shown in Fig. 1 is a result of this drift.

Now, if we consider the impact of an external electric field's force ( $q\vec{E}$ ) we can replace  $\vec{F}$  in equation 26 to get the  $E$  cross  $B$  drift ( $\vec{E} \times \vec{B}$  drift):

$$\vec{v}_{E \times B} = \frac{\vec{E} \times \vec{B}}{B^2} \quad (28)$$

Here the charge dependence of our expression has cancelled implying both ions and electrons move together and no net currents are produced. The physical picture is that the particle gains/loses energy from  $\vec{E}$  during gyration, thereby affecting its  $v_{\perp}$  which shrinks/expands  $r_L$ . Even though electrons would drift with smaller gyroradii than ions, their gyrofrequency is exactly large enough so they both drift at the same speed. Figure 11 shows this helical motion in the plane perpendicular to  $\vec{B}$  for a constant  $\vec{E}$ .

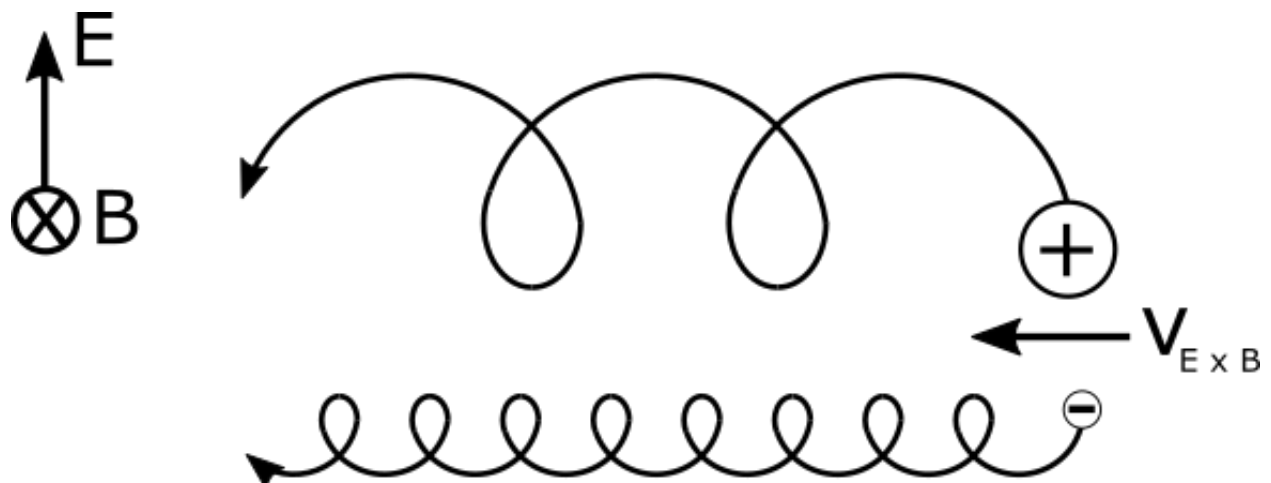


Figure 11. Charged particle motion under the influence of orthogonal  $\vec{E}$  and  $\vec{B}$  fields simultaneously. Both charges move in the  $\vec{E} \times \vec{B}$  direction which produces no net current.

## 2.5 Magnetohydrodynamics (MHD)

(This work follows from M. Kivelson, 1995 and F. Chen, 2016.)

The treatment of plasmas as conducting fluids dates back to Swedish physicist Hannes Alfvén (1908-1995) who won the Nobel Prize in physics for his work on Magnetohydrodynamics (MHD); a combination of classical fluid theory, thermodynamics and electromagnetism. The theory applies the principles of fluid theory (conservation of mass, linear momentum, energy) to a conducting fluid for multiple charged species instead of single particle motions. An interesting result from the analysis of these new equations was the prediction of a class of plasma waves that now bear his name, Alfvén waves. Here we provide a bare-bones overview of the MHD equations in order to motivate our discussion of The Kinetic Theory of plasma later on. The full set of 16 MHD equations are:

$$\sigma = n_i q_i + n_e q_e \quad (29)$$

$$\vec{J} = n_i q_i \vec{v}_i + n_e q_e \vec{v}_e \quad (30)$$

$$\epsilon_0 \nabla \cdot \vec{E} = n_i q_i + n_e q_e \quad (31)$$

$$\nabla \times \vec{B} = - \frac{\partial \vec{B}}{\partial t} \quad (32)$$

$$\nabla \cdot \vec{B} = 0 \quad (33)$$

$$\mu_0^{-1} \nabla \times \vec{B} = n_i q_i \vec{v}_i + n_e q_e \vec{v}_e + \epsilon_0 \frac{\partial \vec{E}}{\partial t} \quad (34)$$

$$\frac{\partial n_j}{\partial t} = \nabla \cdot (n_j \vec{v}_j) = 0 \quad (35)$$

$$m_j n_j \left[ \frac{\partial \vec{v}_j}{\partial t} + (\vec{v}_j \cdot \nabla) \vec{v}_j \right] = q_j n_j \left( \vec{E} + \vec{v}_j \times \vec{B} \right) - \nabla \cdot \vec{P}_j - \frac{mn(\vec{v} - \vec{u}_0)}{\tau} \quad (36)$$

$$p_j = C_j n_j^{\gamma_j} \quad (37)$$

$$\frac{d}{dt} \left( \frac{p}{\rho^\gamma} \right) = 0 \quad (38)$$

where the “j” subscript in equations 35,36,37 refers to either species j=i,e,  $\vec{v}_j$  is the average velocity

of the fluid element for the species. If a neutral fluid is also considered then  $\tau$  in equation 36 is the collisional mean free time between charged and neutral species,  $\vec{u}_0$  is the velocity of a neutral fluid. The pressure tensor  $\vec{\mathbf{P}}$  in equation 36 typically is approximated as an isotropic Maxwellian gas:

$$\vec{\mathbf{P}} = \begin{pmatrix} p & 0 & 0 \\ 0 & p & 0 \\ 0 & 0 & p \end{pmatrix} \implies \nabla \cdot \vec{\mathbf{P}} = \nabla p \quad (39)$$

for  $p = nk_B T$ .

The most important assumption in MHD theory is that the plasma is “localized” i.e. the rate of change of any plasma property depends on the properties of the plasma in the region where the rate of change is determined. Collisions often satisfy this criteria since they tend to “average out” or erase previous history of individual particles, but space plasma often is considered collisionless. Magnetic field lines partially constrain the motion of plasma, but not parallel to  $\vec{\mathbf{B}}$ . For motions perpendicular to  $\vec{\mathbf{B}}$  *the fluid theory is a good approximation*. Additional assumptions that were used to derive (29) - (37) are:

1. Equation 36 implicitly assumes a Maxwellian Distribution (implicitly collisional) to get the average thermal velocity. Distributions with similar thermal velocities would similarly be well described by MHD.
2. Equation 37 requires low thermal conductivity, which is more likely  $\perp \vec{\mathbf{B}}$  than  $\parallel \vec{\mathbf{B}}$ .
3. The displacement current in equation 34 is generally ignored for most applications if quasi-neutrality applies and the characteristic velocities of the plasma are much less than the speed of light.

## 2.6 Generalized Ohm's Law

An equation with deep importance to MHD theory is the *Generalized Ohm's Law*. For brevity, the general outline for the derivation is provided but not shown (see M. Kivelson, 1995 for

details):

1. Multiply the momentum equation (36) by  $q_s/m_s$  and sum over all species
2. Ignore collisions relating to neutral-charged species
3. Assume quasi-neutrality  $(\sigma \sim 0, \nabla \cdot \vec{J} \sim 0)$
4. Assume  $m_e/m_i \ll 1$
5. Treat all bulk ions movement to be approximately the same ( $\vec{u}_i \simeq \vec{u}$ )
6. Linearize the result by ignoring terms quadratic in  $\vec{u}$  and  $\vec{J}$

The result is an Ohm's Law of the form:

$$\vec{E} + \vec{u} \times \vec{B} = \frac{\vec{J}}{\sigma} - \frac{1}{n_e e} \nabla \cdot \vec{P}_e + \frac{\vec{J} \times \vec{B}}{n_e e} + \frac{m_e}{n_e e^2} \frac{\partial \vec{J}}{\partial t}, \quad \sigma \equiv \frac{n_e e^2}{m_e \bar{v}_{ei}} \quad (40)$$

Physically, the terms in the parenthesis for equation 40 are resistive term  $\vec{J}/\sigma$ , inertia term  $(\partial \vec{J}/\partial t)$ , electron pressure  $(\nabla \cdot \vec{P}_e)$ , Hall Term  $(\vec{J} \times \vec{B})$ . As is often the case, the conductivity for near-collisionless plasmas is considered extremely high (effectively infinite) which are commonly observed in magnetospheric regions. The terms in parenthesis in equation must compensate in order to be physical and often assumed to tend towards zero. This defines *Ideal MHD*, for when  $\sigma \rightarrow \infty$  we have the *Ideal Ohm's Law*:

$$\vec{E} + \vec{u} \times \vec{B} = 0 \quad (41)$$

An additional result of equation 41 is the *Frozen-In* theorem which states that magnetic lines of force (field lines) are “frozen-in” to the motion of the conducting fluid, thus the evolution of the magnetic field is determined/caused by the motion

## 2.7 MHD Alfvén Waves

(This work follows from Stasiewicz et al., 2000 and F. Chen, 2016.)

The term “Wave Zoo” is apt at describing the myriad of oscillatory excitation’s a plasma can undergo. Here we will only cover the MHD *Shear Alfvén Wave* mode due to its relevance to this dissertation. Alfvén waves are low-frequency ion oscillations in a background magnetic field. The background magnetic tension provides the restoring force for perturbations and the ion mass provides the inertia to sustain the oscillation. The term “shear” comes from the radial wave  $\vec{E}_1$  perturbation and subsequent azimuthal  $\vec{v}_1$  fluid oscillation in the plane perpendicular to an external  $\vec{B}_0$ . The simplest derivation assumes a static background magnetic field  $\vec{B}_0$  that permits oscillations/perturbations in  $\vec{B}_1, \vec{E}_1$  and  $\vec{J}_1$  such that

$$\vec{B} = \vec{B}_0 + \vec{B}_1, \quad \vec{E} = \vec{E}_0 + \vec{E}_1, \quad \vec{J} = \vec{J}_0 + \vec{J}_1 \quad (42)$$

where "0" subscript parts are constant terms and the perturbation components,  $\vec{X}_1$ , are assumed to be plane waves with some phase  $\delta$ :

$$\vec{X}_1 = \overline{X}_1 e^{i(\vec{k} \cdot \vec{r} - \omega t + \delta)} = \overline{X}_1 e^{i\delta} e^{i(\vec{k} \cdot \vec{r} - \omega t)} \equiv \overline{X}_1 e^{i(\vec{k} \cdot \vec{r} - \omega t)}. \quad (43)$$

For complex vector amplitude  $\overline{X}$  that has been defined with the phase information. The wave is assumed field-aligned ( $\vec{k} \parallel \vec{B}$ ) and let  $\vec{E}_1$  exist perpendicular to  $\vec{B}_0$ . Without loss of generality, we take  $\vec{B}$  to be in  $\hat{z}$  direction and  $\vec{E}_1$  to be in  $\hat{x}$ . We assume in the  $\vec{E} \times \vec{B}$  direction, no current will arise but a motion  $\vec{v}_1$  is present. In the  $\vec{E}_1$  direction, a momentary  $\vec{j}_1$  is permitted so we let  $\vec{v}_1, \vec{B}_1$  to be in the  $\hat{y}$  direction and  $\vec{j}_1$  in  $\hat{x}$  direction. From taking the curl of Ampere’s Law , inserting Faraday’s Law and using our perturbation expressions from equation 42, we get:

$$\nabla \times (\nabla \times \vec{E}_1) = -\vec{k} (\vec{k} \cdot \vec{E}_1) + k^2 \vec{E}_1 = \frac{\partial}{\partial t} \left( \mu_0 \vec{J} + \epsilon_0 \mu_0 \frac{\partial \vec{E}}{\partial t} \right) = \frac{\omega^2}{c^2} \vec{E}_1 + \frac{i\omega}{\epsilon_0 c^2} \vec{J}_1 \quad (44)$$

Since  $\vec{k} \parallel \vec{B}$ , the only term in equation 44 that's non-zero is the  $\hat{x}$  direction based on our assumptions of the direction of  $\vec{J}_1$  and  $\vec{E}_1$ :

$$\epsilon_0 (\omega^2 - c^2 k^2) E_1 = -i\omega J_1 = -i\omega n_0 e (v_{ix} - v_{ex}) \quad (45)$$

We now need expressions for  $v_{ix}$  and  $v_{ex}$ . Here we make an important assumption: the thermal motion of ions/electrons is negligible. This allows us to write the collisionless momentum equation for ions without pressure effects. We also “Linearize” equation 36 by ignoring terms quadratic in any perturbation component. This gives the Lorentz Force as:

$$m_i \frac{\partial \vec{v}_{i1}}{\partial t} = q_i (\vec{E}_1 + \vec{v}_{i1} \times \vec{B}_0) \quad (46)$$

Separating this expression in each perpendicular direction gives us two equations that couple  $v_{i1x}$  and  $v_{i1y}$ , which can be solved to give

$$v_{ix1} = \frac{ie}{m_i \omega} \left( 1 - \frac{\Omega_c^2}{\omega^2} \right)^{-1} E_1 \quad (47)$$

The same can be done for electrons, except their gyro frequency is much greater than the wave frequency ( $\omega_c \gg \omega$ ), so in this limit we get:

$$v_{ex1} = \frac{ie}{m_e \omega} \frac{\omega^2}{\omega_c^2} E_1 \rightarrow 0 \quad (48)$$

which shows that the electrons move fast enough to respond to the wave but the ions do not by comparison. Instead, electrons just have their  $\vec{E} \times \vec{B}$  motion in the  $\hat{y}$  direction. Inserting equation 47 and 48 into equation 45 and defining the *Ion plasma frequency* as  $\Omega_p \equiv (ne^2/\epsilon_0 m_i)^{1/2}$  we have:

$$\omega^2 - c^2 k^2 = \Omega_p^2 \left( 1 - \frac{\Omega_c^2}{\omega^2} \right)^{-1} \quad (49)$$

We assume Hydromagnetic waves have frequencies well below ion cyclotron resonance  $\omega^2 \ll \Omega_c^2$ ,

which gives us the *MHD Alfvén wave Dispersion relation*

$$\left(\frac{\omega}{k}\right)^2 = \frac{c^2}{1 + c^2 / (\rho \mu_0 / B_0^2)} \quad (50)$$

where  $\rho = n_0 m_i$ . Notably,  $m_i$  is the effective mass of ions the wave is interacting with and should be modified by a weighted sum. For non-relativistic waves, the term  $c / (B_0 / \sqrt{\rho \mu_0}) \gg 1$ , thus the *non-relativistic MHD phase velocity* becomes

$$\frac{\omega}{k} = \frac{B_0}{\sqrt{\mu_0 \rho}} \equiv V_A \quad (51)$$

where  $V_A$  is the *Alfvén velocity* for the *Alfvén wave*. Notably, the Alfvén wave does not perturb the plasma density or plasma pressure ( $\vec{n}_1, \vec{p}_1 = 0$ ). If the density of the plasma is low enough and the magnetic field large enough, then  $V_A$  can approach the speed of light and must be modified in the usual way:

$$V'_A = \frac{V_A}{\sqrt{1 + V_A^2/c^2}} \quad (52)$$

We have describe the wave mathematically, but how do we physically interpret it? In Figure 12

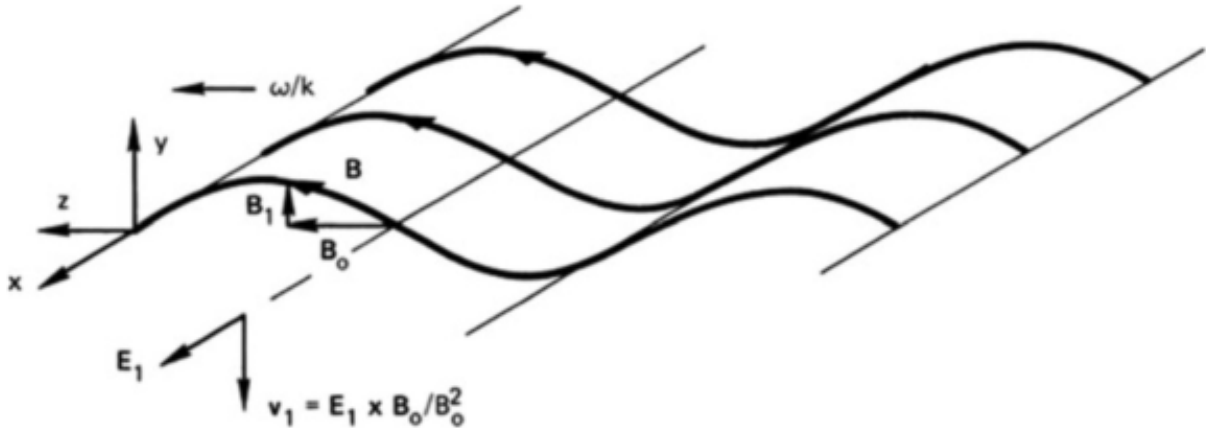


Figure 12. Schematic of MHD Alfvén Wave propagation. The fluid and field lines oscillate together as if the particles were stuck to the lines of force, very much like a mechanical wave on a string. Here  $\vec{E}_1$  only oscillates in the directed perpendicular to the wave i.e. no  $\vec{E}_{\parallel}$ . Taken from F. Chen, 2016.

we show a schematic of an Alfvén wave from F. Chen, 2016. Consider the the point labeled  $\vec{\mathbf{B}}_0$  and  $\vec{\mathbf{B}}_1$  for an instant in time. A presumed  $\vec{\mathbf{E}}_1$  occurs here, giving rise to an  $\vec{\mathbf{E}}_1 \times \vec{\mathbf{B}}_0 / B_0^2$  drift on the fluid. This drift moves ions and electrons at the same velocity in the  $\hat{\mathbf{y}}$  direction, opposite to  $\vec{\mathbf{B}}_1$ . As time briefly passes,  $\vec{\mathbf{B}}_1$  will also briefly begin to move in the  $-\hat{\mathbf{y}}$  direction. Now, the perturbation flow of the plasma  $\vec{\mathbf{v}}_1$  and the perturbation magnetic field  $\vec{\mathbf{B}}_1$  follow each other. In this region of  $\vec{\mathbf{B}}_1 = B_1 \hat{\mathbf{y}}$ , the  $\vec{\mathbf{E}}_1$  term flips to  $-\hat{\mathbf{x}}$  but the inertia of  $\vec{\mathbf{E}}_1 \times \vec{\mathbf{B}}_0$  motion causes the plasma to enter this space. Now the  $\vec{\mathbf{E}}_1 \times \vec{\mathbf{B}}_0$  is in the upward  $\hat{\mathbf{y}}$  direction, so the plasma starts to decelerate and oscillate back the way it came. Once again the plasma over-corrects and its inertia carries it into a region where the  $\vec{\mathbf{E}}_1 \times \vec{\mathbf{B}}_0$  points downward which starts to decelerate its motion. This process continues *ad Infinitum* until the wave fully passes. This picture is mathematically identical to a mass-loaded string where particles are stuck to the lines of force ( $\vec{\mathbf{B}}_1$  in this case) and oscillate up and down with a restoring force trying to bring things to equilibrium. A natural question is: What prevents  $\vec{\mathbf{E}}_1$  from being shorted out by the plasma? The answer is that the inertia of Ions prevents them from responding to the wave  $\vec{\mathbf{E}}_1$  as fast as electrons. Thus, ions lag behind electrons producing a  $\vec{\mathbf{J}}_1$  that's parallel to  $\vec{\mathbf{E}}_1$ . The  $\vec{\mathbf{J}}_1 \times \vec{\mathbf{B}}_0$  force from this is in the same direction as the  $\vec{\mathbf{E}} \times \vec{\mathbf{B}}$  drift ( $\vec{\mathbf{v}}_1$ ) but it's necessarily out of phase by  $90^\circ$  due to ion overshoot. In summary, the key assumptions used in this derivation are:

1. The wave travels parallel to the non-perturbation magnetic field  $\vec{\mathbf{B}}_0$  ( $\vec{\mathbf{k}} \parallel \vec{\mathbf{B}}$ )
2. Thermal Motions of the ions are negligible so the MHD ion momentum equation becomes the Lorentz force.
3. The Electron gyro frequency is much greater than the wave frequency ( $\omega_c \gg \omega$ )
4. Hydromagnetic waves have frequencies well below the ion cyclotron resonance ( $\omega^2 \ll \Omega_c^2$ )
5. The Alfvén velocity is much less than the speed of light ( $V_A \ll c$ )

## 2.8 Alfvén Waves: Kinetic Theory

(This section follows from Lysak et al., 1996, Stasiewicz et al., 2000 and F. Chen, 2016.)

Observations of naturally produced Alfvén waves and electron features in spacecraft data in the decades surround the 1980s hinted at the possibility that an electric field parallel to the background magnetic field could be supported by these low-frequency plasma waves. However, the idealizations of MHD do not permit  $\vec{E}_1 \parallel \vec{B}_0$  via equation 41. The work by St  fant, 1970 showed that the inclusion of the ion gyroradius at the electron temperature  $(T_e/m_i)^{1/2}/\Omega_c$  turned typical Alfv  n waves into a new class of dispersive plasma waves called *Dispersive Alfv  n Waves* (DAWs). Dispersive meaning that the wave frequency depends on its wavelength. Further work by Hasegawa, 1976 and Goertz et al., 1979a showed that the ion thermal gyroradius  $(T_i/m_i)^{1/2}/\Omega_c$  as well as the collisionless electron skin depth  $\lambda_e = c/\omega_{pe}$  also produced an  $\vec{E}_{\parallel}$  in these new waves. Finally, Lysak et al., 1996 derived the first dispersive Alfv  n wave dispersion relation along auroral field lines to show these play a significant factor in particle acceleration processes. Here we will provide the relevant equations from kinetic theory and derive the dispersion relation for DAW that are germane to the work in this dissertation.

Thus far we have concerned ourselves with Alfv  n waves in plasma where the thermal motions of ions and cyclotron resonance is negligible. We've accomplished this by linearizing the fluid equations of motion by assuming low frequency waves in a cold plasma so that the majority of the terms in the MHD momentum equation (equation 36) are left out. Instead of using the fluid of equations 29 to 37, we use *The Kinetic Theory of gases* to derive our DAWs. We start with the evolution of *particle distribution function* for a gas,  $f(\vec{x}, \vec{v})$ . The concepts of  $f(\vec{x}, \vec{v})$  come from statistical mechanics and it describes the probability of finding a particle between  $\vec{x} + d\vec{x}$  and  $\vec{v} + d\vec{v}$ . This function has a zero time-derivative if collisions are ignored (Louville's Theorem):

$$\frac{df(\vec{x}, \vec{v})}{dt} = 0 \quad (53)$$

We expand the total derivative of equation 53 to:

$$\frac{\partial f}{\partial t} + \vec{v} \cdot \nabla f + \frac{q}{m} (\vec{E} + \vec{v} \times \vec{B}) \cdot \frac{\partial f}{\partial \vec{v}} = 0 \quad (54)$$

for which we have inserted the Lorentz Force into the generalized force  $\vec{F}$  that occurs during the derivation. This is called the *Vlassov-Maxwell* equation without collisions. To include collisions requires making equation 54 inhomogeneous by adding a term on the right hand side. We can linearize this equation in terms of  $\vec{E}$ ,  $\vec{v}$ ,  $\vec{B}$ , and  $f(\vec{x}, \vec{v})$ . Doing so allows us to derive various plasma waves under different conditions. For the moment, we ignore any  $\vec{B}$  terms and linearize equation 54. We will introduce the perturbation distribution  $f_{1,s}$  for species s and solve our linearized equation:

$$f_{1,s} = -\frac{iq}{m_s} \frac{1}{\omega - \vec{v} \cdot \vec{k}} \left( \vec{E}_1 \cdot \frac{\partial f_{0,s}}{\partial \vec{v}} \right) \quad (55)$$

In general, the perturbation plasma density  $n_{1,s}$  is first moment of the perturbation distribution function  $f_{1,s}$ :

$$n_{1,s} = \int f_{1,s} dv^3 \quad (56)$$

$$= -\frac{iq}{m_s} \vec{E}_1 \cdot \int \frac{1}{\omega - \vec{v} \cdot \vec{k}} \left( \frac{\partial f_{0,s}}{\partial \vec{v}} \right) dv^3 \quad (57)$$

It is often the case that the unperturbed distribution function  $f_{0,s}$  has the form of a Maxwellian with an average thermal speed per species  $v_{th,s}$ . The form of this Maxwellian has shape  $f_0 \propto n_0 \exp(-v^2/v_{th}^2)$ . Inserting this expression in equation 56 starts to look messy, so it is useful to define the *plasma dispersion function*  $Z(\zeta)$  to simplify:

$$Z(\zeta_s) = \frac{1}{\pi^{1/2}} \int_{-\infty}^{\infty} \frac{e^{-t^2}}{t - \zeta_s} dt \quad (58)$$

where

$$t \equiv v_s/v_{th,s} \quad \zeta_s \equiv (\omega/k)/v_{th,s} \quad (59)$$

and the phase speed of the wave is  $\omega/k$ , and “t” is just the particle speed normalized by the thermal velocity of the unperturbed distribution. Analyzing equation 56 further requires additional mathematics which we will present now.

In general, the wave frequency  $\omega$  is complex valued such that  $\omega = \omega + i\gamma$ , where  $\gamma$  is called the *damping factor* of the wave. If  $\gamma < 0$  then the wave will decay over time and if  $\gamma > 0$  the wave grows over time. This can be seen by the equation of a general plane wave:

$$\exp\left\{i\left(\vec{k} \cdot \vec{x} - i(\omega + i\gamma)t\right)\right\} = e^{\gamma t} \exp\left\{i\left(\vec{k} \cdot \vec{x} - i\omega t\right)\right\} \quad (60)$$

Thus, evaluating equation 58 is then equivalent to a 1D contour integral with a single pole at  $\zeta$ . Performing an exact calculation of this integral is non-trivial and can be simplified considerably by approximating  $\zeta_s$  under different assumptions. For the case when the phase speed of the wave is small compared to the plasma thermal velocity (small  $\zeta$ ):

$$Z(\zeta) \approx i\pi^{1/2}e^{-\zeta^2} - 2\zeta \left[1 - \frac{2\zeta^2}{3} + \frac{4\zeta^4}{15} - \frac{8\zeta^6}{105} + \dots\right] \quad ; \quad \omega/k \leq v_{th} \quad (61)$$

Conversely, when the phase speed of the wave is much larger than the thermal speed (Large  $\zeta$ ):

$$Z(\zeta) \approx i\pi^{1/2}\sigma e^{-\zeta^2} - \zeta^{-1} \left[1 + \frac{1}{2\zeta^2} + \frac{3}{4\zeta^4} + \frac{15}{8\zeta^8} + \dots\right] \quad ; \quad \omega/k \gg v_{th} \quad (62)$$

where  $\zeta = x + iy$  and the asymptotic expansion requires  $x > 0$ . The  $\sigma$  term is

$$\sigma = \begin{cases} 0 & y > 1/|x| \\ 1 & |y| < 1/|x| \\ 2 & y < -1/|x| \end{cases} \quad (63)$$

We have omitted the details of these expansions. It is through equation 61 and 62 that motivate the definition of two regimes of DAW: (1) The *Inertial Alfvén Wave* occurs when the phase velocity of

the wave is significantly above the plasma thermal speed ( $\omega/k \gg v_{th}$ ) and (2) The *Kinetic Alfvén Wave* occurs when the phase velocity is of-order or less than the thermal velocity ( $\omega/k \leq v_{th}$ ). These conditions can be rephrased in terms of the commonly used *Plasma Beta*, which relates the magnetic pressure in the plasma to the thermal plasma pressure:

$$\beta \equiv \frac{\text{Thermal Plasma Pressure}}{\text{Magnetic Pressure}} = \frac{nk_B T}{B_0^2/2\mu_0} \quad (64)$$

where “n” is the plasma density, plasma temperature T and background magnetic field B. Defining the thermal velocity as  $v_{th,s} = \sqrt{2k_B T_s / m_s}$  and using the MHD Alfvén speed  $V_A = B / \sqrt{\mu_0 \rho_m}$ , we can refine our definition for electrons:

$$\begin{aligned} \beta_e &= \frac{n_e k_B T_e}{B_0^2/2\mu_0} \\ &= \left( \frac{\mu_0 n_e}{B_0^2} \right) \left( \frac{2T_e}{1} \frac{m_i m_e}{m_i m_e} \right) \\ &= \left( \frac{v_{the}}{V_A} \right)^2 \left( \frac{m_e}{m_i} \right) \end{aligned}$$

Which gives:

$$\frac{v_{th,e}}{V_A} = \left( \frac{\beta_e}{(m_e/m_i)} \right)^{1/2} \quad (65)$$

Thus, when the phase velocity of the wave  $\omega/k$  is approximately close to  $V_A$ , we describe the inertial Alfvén wave regime when  $\beta_e < m_e/m_i$  and the kinetic regime when  $\beta_e > m_e/m_i$

To actually derive the dispersion relations for these Alfvén waves requires we introduce a finite DC magnetic field  $\vec{B}_0$  and perturbation  $\vec{B}_1$  in the linearized Vlassov analysis. Unfortunately, this analysis gets becomes complicated very quickly. The work by Lysak et al., 1996 was entirely dedicated to finding approximations to these dispersion relations as applied to auroral geomagnetic field lines. In order to follow in the footsteps of Stasiewicz et al., 2000 we need to understand the *plasma wave equation* in a conductive medium. Before moving on, a final note about  $\vec{E}_1$  in

equation 56: By including the linearized Possion's equation

$$i\vec{k} \cdot \vec{E}_1 = \frac{1}{\epsilon_0} \sum_s n_{1,s} \quad (66)$$

in the analysis of equation 56, the expressions for collisionless damping in a plasma called *Landau Damping* arise after proper treatment of the contour integral, wherein energy exchange between the electromagnetic wave and particles can damp/grow a plasma wave.

## 2.9 The Dispersive Alfvén Wave (Lysak et al., 1996)

As shown in Appendix A, the response of a plasma to a linear wave is described by the plasma wave equation:

$$\vec{n} \times (\vec{n} \times \vec{E}) + \vec{\epsilon} \cdot \vec{E} = 0 \quad ; \quad \vec{\epsilon} \equiv \epsilon_0 \left( \vec{I} + \frac{i}{\epsilon_0 \omega} \vec{\sigma} \right) \quad (67)$$

with wave index of refraction vector  $\vec{n} = \frac{c}{\omega} \vec{k}$  and the *dielectric tensor*  $\vec{\epsilon}$ , which depends upon the frequency of the wave  $\omega$  and the conductivity tesnor  $\vec{\sigma}$ . The solutions to equation 67 will give the DAW dispersion relations since. In general, the dielectric tensor has the form

$$\vec{\epsilon} = \begin{pmatrix} \epsilon_{xx} & \epsilon_{xy} & \epsilon_{xz} \\ \epsilon_{yx} & \epsilon_{yy} & \epsilon_{yz} \\ \epsilon_{zx} & \epsilon_{zy} & \epsilon_{zz} \end{pmatrix} \quad (68)$$

If we define a propagation direction such that  $\vec{n} = n_\perp \hat{x} + n_\parallel \hat{z}$  where we the wave vector is in the x-z plane and  $\hat{z}$  is in the direction of  $\vec{B}_{geo}$ , then we can expand equation 67 as

$$\vec{M} \cdot \vec{E} = \begin{bmatrix} \epsilon_{xx} - n_\parallel^2 & \epsilon_{xy} & \epsilon_{xz} + n_\parallel n_\perp \\ -\epsilon_{xy} & \epsilon_{yy} - n_\perp^2 & \epsilon_{yz} \\ \epsilon_{xz} + n_\parallel n_\perp & -\epsilon_{yz} & \epsilon_{zz} - n_\perp^2 \end{bmatrix} \cdot \begin{bmatrix} E_x \\ E_y \\ E_z \end{bmatrix} = 0 \quad (69)$$

This is a set of three homogeneous equations, for which the existence of solutions requires  $\det(\vec{\mathbf{M}}) = 0$ . For the specific case where  $T_{\parallel} = T_{\perp}$  and no zero-order plasma drifts  $\vec{v}_{0j}$ , we can derive  $\vec{\epsilon}$  and its components (F. Chen, 2016):

$$\epsilon_{xx} = 1 + \sum_s \frac{\omega_p^2}{\omega^2} \frac{e^{-b}}{b} \zeta_0 \sum_{-\infty}^{\infty} n^2 I_n(b) Z(\zeta_n) \quad (70)$$

$$\epsilon_{yy} = 1 + \sum_s \frac{\omega_p^2}{\omega^2} \frac{e^{-b}}{b} \zeta_0 \sum_{-\infty}^{\infty} \{n^2 I_n(b) + 2b^2 [I_n(b) - I'_n(b)] Z(\zeta_n)\} \quad (71)$$

$$\epsilon_{xy} = -\epsilon_{yx} = i \sum_s \pm \frac{\omega_p^2}{\omega^2} e^{-b} \zeta_0 \sum_{-\infty}^{\infty} [I_n(b) - I'_n(b)] Z(\zeta_n) \quad (72)$$

$$\epsilon_{xz} = \epsilon_{zx} = \sum_s \frac{\omega_p^2}{\omega^2} \frac{e^{-b}}{(2b)^{1/2}} \zeta_0 \sum_{-\infty}^{\infty} n I_n(b) Z'(\zeta_n) \quad (73)$$

$$\epsilon_{yx} = -\epsilon_{zy} = -i \sum_s \pm \frac{\omega_p^2}{\omega^2} \left(\frac{b}{2}\right)^{1/2} e^{-b} \zeta_0 \sum_{-\infty}^{\infty} [I_n(b) - I'_n(b)] Z'(\zeta_n) \quad (74)$$

$$\epsilon_{zz} = 1 - \sum_s \frac{\omega_p^2}{\omega^2} e^{-b} \zeta_0 \sum_{-\infty}^{\infty} I_n(b) \zeta_n Z'(\zeta_n) \quad (75)$$

where  $Z(\zeta)$  is the plasma dispersion function from equations 61 and 62,  $I_n(b)$  is the n-th order Bessel function of imaginary argument “b”. The other symbols are

$$\omega_{ps}^2 = n_{0s} Z_s^2 e^2 / \epsilon_0 m_s \quad (76)$$

$$\zeta_{ns} = (\omega + n\omega_{c,s}) / k_z v_{th,s} \quad (77)$$

$$\zeta_{0s} = \omega / k_z v_{th,s} \quad (78)$$

$$\omega_{cs} = |Z_s e B_0 / m_s| \quad (79)$$

$$v_{th,s}^2 = 2k_B T_s / m_s \quad (80)$$

$$b_s = \frac{1}{2} k_{\perp}^2 r_{L,s} = k_x^2 k_B T_s / m_s \omega_{c,s}^2 \quad (81)$$

where  $\omega_{ps}$  is the species-dependent plasma frequency with number of charges “Z”. The per species cyclotron frequency is  $\omega_{c,s}$  and Larmor Radius  $r_{L,s}$ . In equations 70 to 75 the first summation is over species s for which  $\omega_p, b, \zeta_0$  and  $\zeta_n$  all depend. The  $\pm$  sign in equation 72 and 74 represents

sign of the charge. The set set of summations is over harmonic number n in the Bessel functions. The primed variables indicate differentiation with respect to the argument.

These equations must be simplified to be usable and we will not reproduce the works of Lysak et al., 1996 to show this. Instead, we note that Lysak et al., 1996 solved the various terms in equation 69 by assuming a low-frequency, long parallel wavelength wave with small electron masses to derive the full dispersion elation for linear DAW with arbitrary electron velocity, large ion gyroradius and finite frequency effects:

$$Z'(\zeta) \left[ \left( 1 - \frac{\omega^2}{\omega_{ci}^2} \right) \left( 1 + k_\perp^2 \rho_i^2 \right) \frac{V_A^2}{v_{th,s}^2} - \zeta^2 \right] = k_\perp^2 \lambda_e^2 \quad (82)$$

From this, the dispersion relations of the Kinetic Alfvén Wave (KAW) or the Inertial Alfvén Wave (IAW) can be determined.

In the cold electron plasma, inertial limit ( $\beta_e < m_e/m_i$ ),  $\zeta$  is large and we approximate the derivative of the plasma dispersion function as  $Z'(\zeta) \rightarrow \zeta^{-2}$ . This gives the generalized *Inertial Alfvén Wave* dispersion relation:

$$\left( \frac{\omega}{k_\parallel} \right)^2 = V_A^2 \frac{(1 - \omega^2/\omega_{ci}^2)(1 + k_\perp^2 \rho_i^2)}{(1 + k_\perp^2 \lambda_e^2)} \quad (83)$$

In the opposite, hot plasma limit where  $\zeta$  is small, then we get the *Kinetic Alfvén Wave* dispersion relation:

$$\left( \frac{\omega}{k_\parallel} \right)^2 = V_A^2 \left( 1 + k_\perp^2 (\rho_s^2 + \rho_i^2) - \frac{\omega^2}{\omega_{ci}^2} (1 + k_\perp^2 \rho_i^2) \right) \quad (84)$$

By using the first row of equation 69 we can determine the generalized parallel electric field for the DAW:

$$\frac{E_\parallel}{E_\perp} = \frac{k_\parallel}{k_\perp} \left( 1 - \frac{\omega^2}{k_\parallel^2 V_A^2} \frac{1}{(1 - \omega^2/\omega_{ci}^2)(1 + k_\perp^2 \rho_i^2)} \right) \quad (85)$$

In the cold plasma, low-frequency IAW limit the associated parallel electric field is:

$$E_\parallel = \frac{k_\parallel}{k_\perp} \frac{(k_\perp \lambda_e)^2}{1 + (k_\perp \lambda_e)^2} E_\perp \quad (86)$$

And for the hot plasma, low frequency KAW limit:

$$E_{\parallel} = -\frac{k_{\parallel}k_{\perp}\rho_s^2}{1+k_{\perp}^2\rho_i^2}E_{\perp} \quad (87)$$

where  $\rho_s = c_s/\omega_{ci}$  and the speed of sound is  $c_s = (T_e/m_i)^{1/2}$ . The above equations represent the most useful forms of the new class of Alfvén Wave derived from Kinetic Theory. These waves are truly “Dispersive” due to the wave frequency’s dependence upon the wavelength. It is these waves which permit electron and ion acceleration parallel to the background geomagnetic fields, which is the primary focus of this dissertation. In particular, the Inertial Alfvén wave is abundant in the cold plasma of the auroral ionosphere and has interesting interactions with the plasma there which will be covered in Chapter 4, 7 and 8.

## CHAPTER 3: THE MAGNETOSPHERE-IONOSPHERE SYSTEM

(The content of this section follows from Kelly, 2009; M. Kivelson, 1995; Russell et al., 2016)

Here we develop some of the concepts relating to the various structures within Earth's geo-magnetic field. The different regions of the near-Earth plasma environment are distinguishable and can be characterized by the bulk properties of the plasmas that exist there. The plasma characteristics such as average temperature, density, large-scale currents, magnetic field strength, mobility, ion species content, magnetic topology, peak particle energies all serve to uniquely identify these regions. In this chapter we discuss the ideas of the inner and outer magnetosphere which are germane to our work: Magnetic Reconnection, the ionosphere and the plasma sheet.

### 3.1 The Solar Wind

Our local star spews out hot plasma ejected from its photosphere and million-degree solar corona called the Solar Wind (SW). This plasma carries with it the solar magnetic fields which permeates throughout our entire solar system. This Interplanetary Magnetic Field (IMF) has one end or “footprint” at the sun that co-rotates with the 27 period of our star. Far away from the sun, the IMF begins to lag behind the star’s rotation, developing a spiral nature that appears similar to the 3D picture shown in Figure 13 near the Earth.

The IMF is “frozen in” to the expanding solar plasma and describable as tubes of magnetic flux that carry momentum and energy away from the star. This theorem is derived from ideal MHD via  $\vec{E} + \vec{u} \times \vec{B} = 0$  and it implies that if a magnetic field initially connects two elements of a conducting fluid, say  $S_1$  and  $S_2$  as shown in Figure 14, then the same magnetic field will continue to connect these elements as the fluid moves (Russell et al., 2016). Put another way, the cross-sectional surface  $S_1$  that expands over a distance to a new size  $S_2$  will contain the same amount of magnetic flux regardless of how the fluid moves, i.e.  $\Phi_B = \vec{B} \cdot \vec{S} = const.$  and  $\partial\Phi_B/\partial t = 0$ . The speed of the SW that emanates from our star is very fast ( $> 10^6$  mi/hr or 250 km/s to 750 km/s)

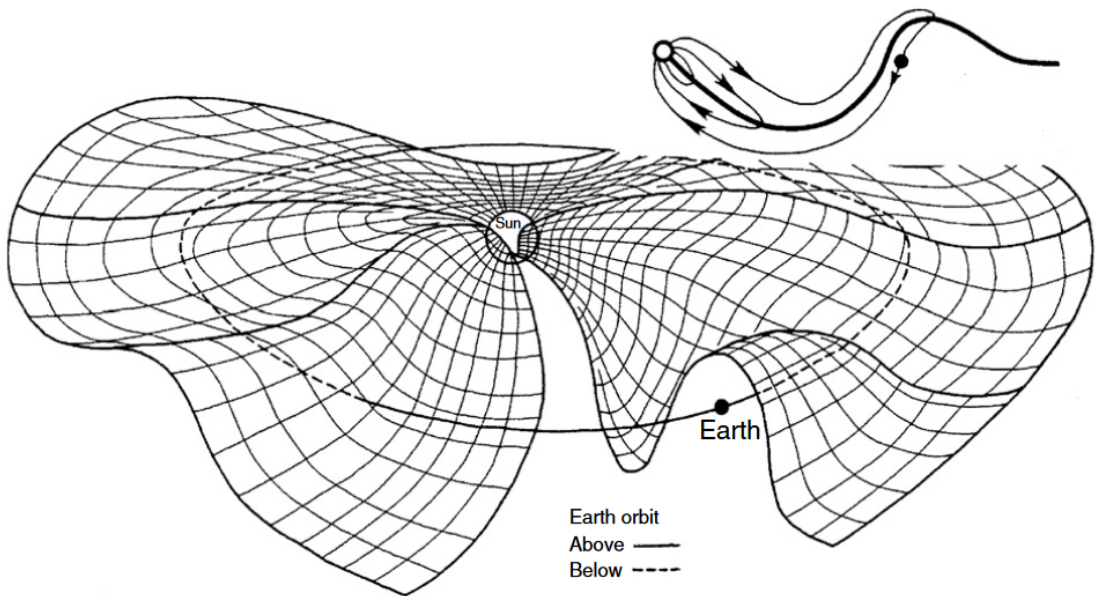


Figure 13. From Kelly, 2009. Three dimensional diagram of the IMF “ripples” in the spiraling outward flow of solar plasma carrying the sun’s magnetic field.

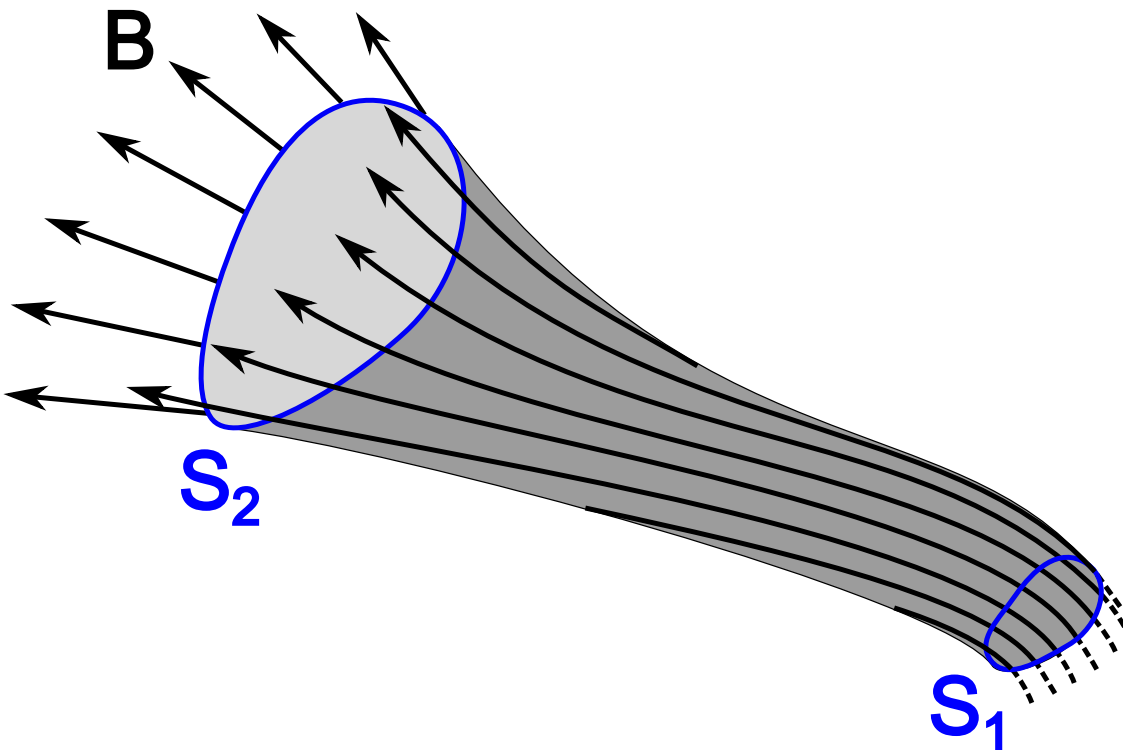


Figure 14. Example flux tubes from ideal MHD where the same magnetic flux passing through fluid element  $S_2$  is passing through element  $S_1$  at a later distance.

and accelerates to faster than the local speed of sound within tens of solar radii before flattening out to a constant flow. This flow is supersonic by the time it reaches Earth, which acts analogously to an obstacle that impedes the flow of a river stream.

### 3.2 The Magnetosphere

As the solar plasma and IMF distribute themselves throughout the solar system, some fraction reaches Earth at a distance of  $R = 1 \text{ AU} = 1.5 \times 10^8 \text{ km}$  from the sun. As the SW crashes into the Earth, it interacts with the terrestrial geomagnetic field and flows around the planetary obstacle. This causes a pileup of plasma in front of the geomagnetic field where the SW speed drops to subsonic velocities forming a shock region called the *Bow Shock*. For Earth, the Bow Shock forms  $10 - 15 R_E$  from the planet (See Figure 15) and is the outer boundary where new SW plasma enters the shock. The turbulent transition region inside the shock is called the *magnetosheath* and contains plasma with greater energy densities (higher temperature and plasma densities) than the SW. The point where the influence of the IMF stops and the terrestrial geomagnetic field starts to dominate is the same place where the magnetosheath stops and forms a thin inner boundary called the *magnetopause*. The magnetopause occurs where the magnetic pressure from Earth's field matches the dynamic pressure of the SW. Here, the IMF is draped around the geomagnetic field and the momentum flux of the SW compresses the dipole-like magnetic field of Earth on the sunward side and significantly elongating  $\vec{\mathbf{B}}_{geo}$  on the nightside. Typically the dayside magnetopause occurs near  $10 R_E$  although intensification of the solar dynamic pressure introduces spatial variability. The stretched out *magnetotail* can reach distances  $> 100 R_E$  and is shaped as a cylinder-like tube that “flaps” in the solar wind.

Inside the magnetopause is the *magnetosphere* where the plasma is primarily of terrestrial origin, with some allowances for SW plasma to enter. Here geomagnetic field lines have two footprints in the lower-to-medium latitudes on Earth with the exceptions of the ultra-high latitude magnetic poles which contain field lines that extend far out into the magnetosphere. The polar *Cusp* regions exists on the north and south magnetic poles and contain the field lines which intersect with

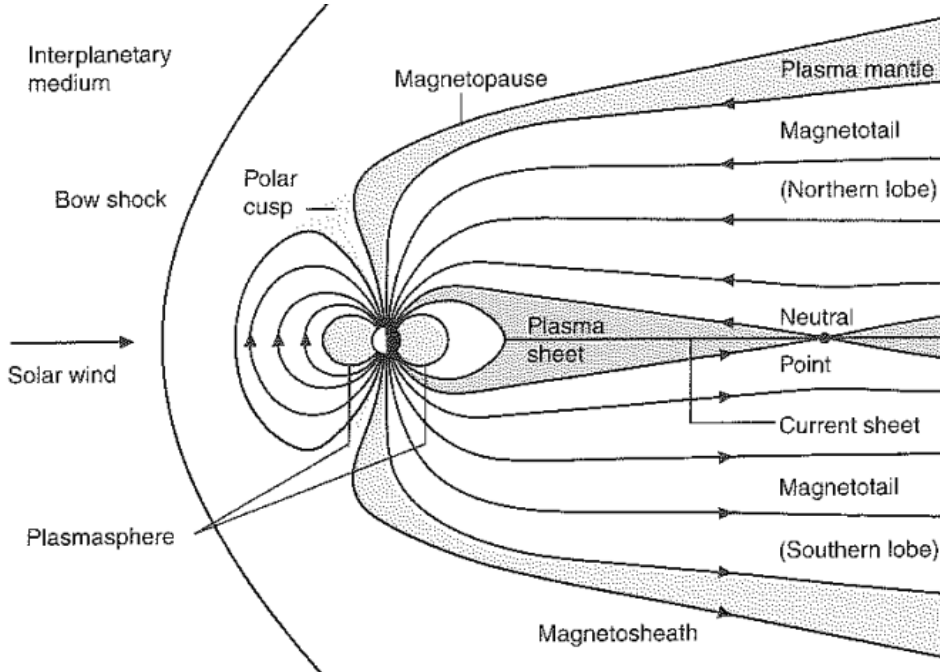


Figure 15. From Russell et al., 2016. Two dimensional cut-away of the magnetosphere.

the magnetopause. Beneath these field lines on in the magnetotail lies the *plasma mantle*, which is the boundary layer where low-density SW plasma is seen (Russell et al., 2016). The mantle forms the outer edge of the *tail lobes* which are defined by the direction of the geomagnetic field termed the *Northern Lobe* or *Southern Lobe*; regions that contain low ( $< 0.02 \text{ cm}^{-3}$ ) SW plasma. The SW plasma flows over these lobes and generally is carried along with the magnetic fields out into the magnetotail and rarely do particles flow upstream to Earth. The reversal of the geomagnetic field in the magnetotail occurs at point where these lobes would meet called the *neutral point*. The *plasma sheet* is a much warmer ( $T_e \geq 100 \text{ eV}$ ) and denser ( $\geq 0.5 \text{ cm}^{-3}$ ) plasma that fills the geomagnetic field lines near the neutral point. Here, the large-scale magnetopause currents that form along the tail return their current through the center magnetotail by crossing out of the page in Figure 3.2. Next we will discuss the plasma that inhabits the near-Earth environment: The plasmasphere and Ionosphere.

### 3.3 The Plasmasphere

If we imagine evacuating all the plasma in the entire magnetosphere, then over a few weeks-to-months the inner magnetospheric field lines would again fill up (Russell et al., 2016). The initial source of this plasma is the creation of charged particles from Earth's neutral atmosphere due to Solar radiation and cosmic sources. The magnetic field lines that are "closed" (two footprints on Earth) exist at the low-to-mid latitudes and these fill up first. The high latitude field lines would take longer to fill up since these flux tubes cover significantly larger areas of space. Since this plasma comes from a wholly terrestrial source, it will be very cold with temperatures on the order of  $1\text{eV}$  and will co-rotate with the planet it came from. This region of cold plasma that forms a "cloak" around our plasma is called the *plasmasphere* and it extends typically between  $3 - 5R_E$  as shown in Figure 16. When traveling from Earth, the plasma density decays exponentially and reaches near  $10^3\text{cm}^{-3}$  at the upper boundary of the plasmasphere called the *plasmapause*, where a sudden drop-out of density occurs down to magnetospheric levels. The reason for this boundary comes from magnetic reconnection, which is discussed later. The co-rotation of an electrical cloak of particles that decay in density over radial distance induces an inward co-rotating electric field.

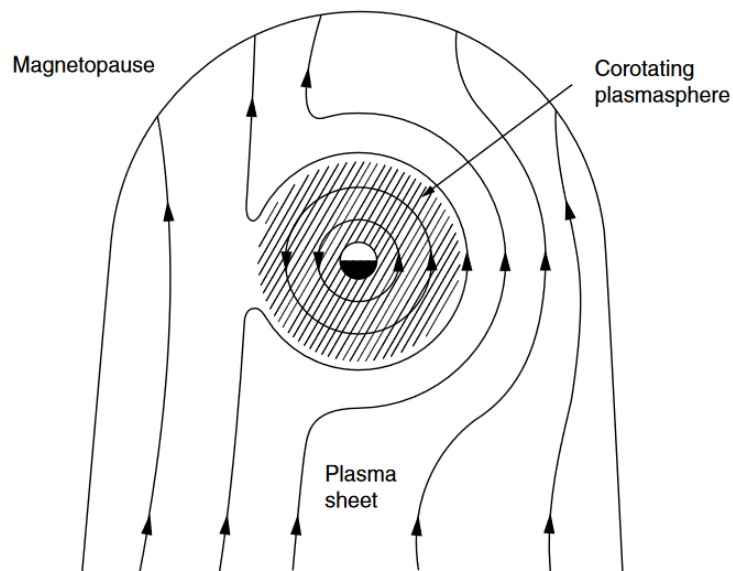


Figure 16. From Kelly, 2009. Plasmasphere with lines indicating contours of plasma flow (not magnetic field).

### 3.4 The Ionosphere

Moving on from the high altitude structures which are measured in Earth radii, we now briefly turn our attention to the near-Earth conductive atmosphere. The thin layers of our neutral atmosphere that get their neutrality broken through the absorption of solar radiation forms a conductive shell around the Earth called the *Ionosphere*. The altitudes where this radiation is absorbed stratify the created plasma largely into three different layers called the *D, E and F* regions. The boundaries of these layers are indefinite, but are distinct in the types of ions that exist, plasma densities and how electromagnetic radiation is affected when passing through them. Because of their dependence upon solar radiation, these regions morph in thickness and individuality throughout the day-night cycle. In a big-picture sense, the properties of the layers are (NOAA Center For Environmental Information, 2006):

- *D-Region* Between 75km to 95km with relatively weak ionization. Responsible for medium to lower-high frequency radio wave absorption. Contains typical atmospheric ionized populations of  $O_2^+$ ,  $NO^+$ .
- *E-Region* Thicker layer between 95 and 150km. Extreme latitude Magnetospheric Currents close their circuit through this region. Ions are mostly  $O2^+$ .
- *F-Region* Between 150km to 500km. Highest density of electrons. Can be split into two regions called, F1 and F2. F1 ions are mainly  $NO^+$  and F2 ions predominantly  $O^+$ .
- *Topside-Region* Above 500km. Mostly  $H^+$ ,  $He^+$  and  $O^+$  ions.

These layers and the ambient temperature of the plasma are given in Figure 17. In Figure 18 we show the various ion and neutral species densities in an altitude profile composed of several satellite and rocket datasets above the mid-latitude point in White Sands, New Mexico for daytime conditions. Neutral turbulence and collisions tend to dominate below 75 km which prevents bulk plasma behavior.

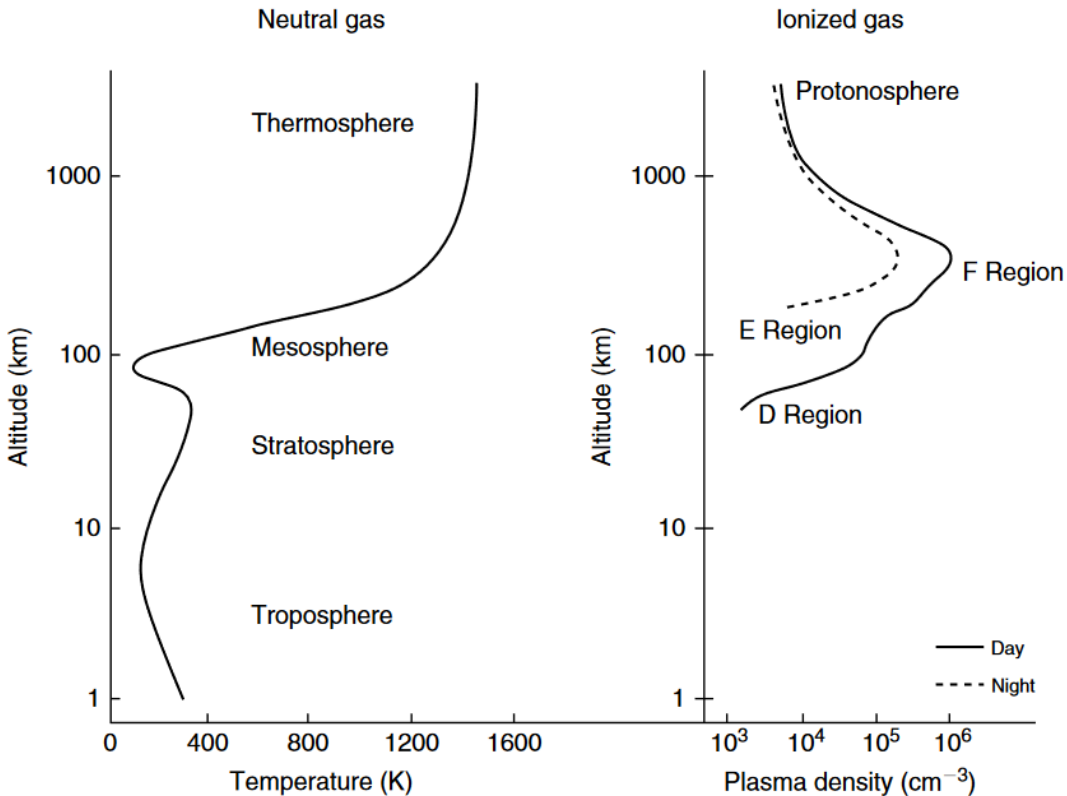


Figure 17. From Kelly, 2009. Profiles of neutral atmospheric temperature and Ionospheric plasma layers.

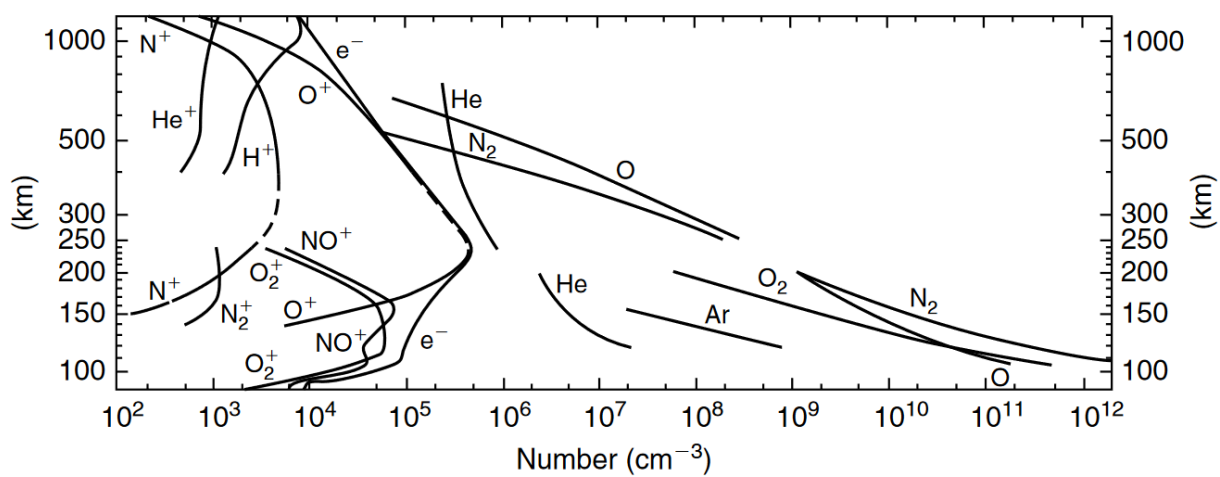
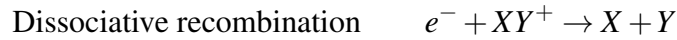


Figure 18. From Kelly, 2009. Daytime atmospheric composition above White Sands, New Mexico ( $32^\circ\text{N}, 106^\circ\text{W}$ )

Naturally, the dayside of Earth exhibits the highest plasma densities due to the greatest amount of solar radiation present. Once these photons diminish on the dusk side of Earth, a continual decrease in the plasma density for all altitudes occur into the night. Here the D layer of the ionosphere disappears and the two F-region peaks tend to merge into a single F layer. The E-Region also remains but with diminished plasma density. The two major ion loss mechanisms which facilitate this process are:



where X, Y are some atoms. The dissociation of molecular oxygen  $O_2^+ + e^- \rightarrow O + O$  and nitrogen  $N_2^+ + e^- \rightarrow N + N$  are particularly relevant here (Russell et al., 2016). Because the ion loss processes are sufficiently long compared to the rotation of our planet, the ionosphere doesn't entirely disappear through the night. Finally, the collisions of the plasma in the ionosphere plays a key role in determining where the precipitation from magnetospheric sources will stop. For ions and electrons below 120 km, collisions with neutral particles become exponentially more prevalent and relaxes at higher altitudes. Above 1000 km both species experience very little collisions.

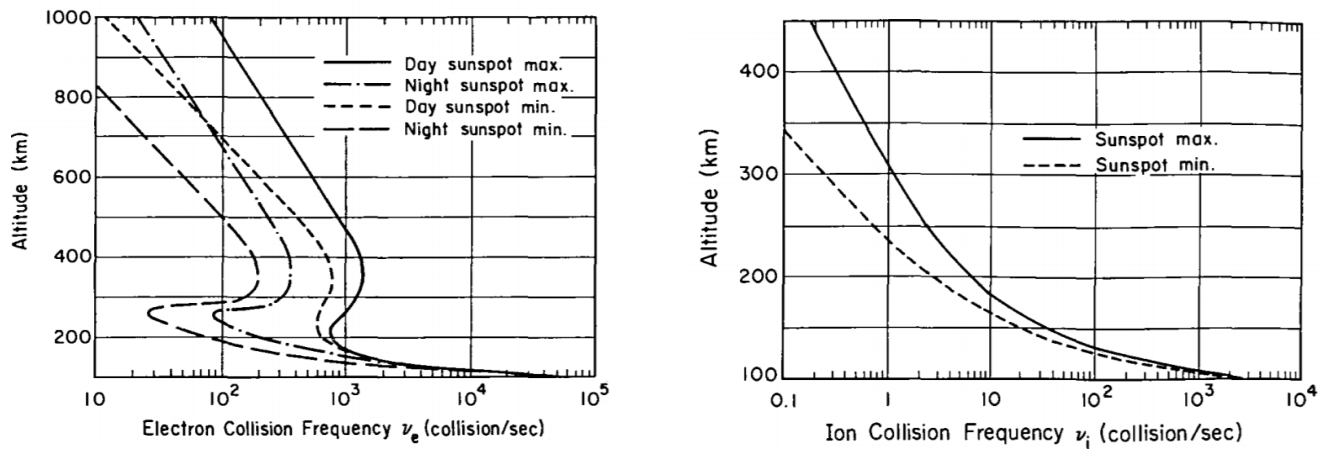


Figure 19. From Johnson et al., 1961. (Left) Electron-neutral and (right) ion-neutral collision rates for various solar conditions vs. altitude.

### 3.5 Reconnection and Plasma Convection

Zooming back out to the magnetosphere, we now discuss the dynamic coupling process between the Solar Wind and Earth’s geomagnetic field called *Magnetic Reconnection*. In undisturbed conditions, the IMF flux tubes drape over the magnetosphere and mostly flow around the Earth. However, when the IMF is oriented anti-parallel (or “southward”) to the magnetopause  $\vec{B}_{geo}$  the frozen-in condition of MHD can momentarily break on the day-side, creating a “X-line” pattern on the Lower Latitude Boundary Layer (LLBL). The anti-parallel case is shown on the left in Figure 20. This re-configures the magnetic topologies between the IMF and  $\vec{B}_{geo}$ , where the once closed geomagnetic field line is broken into two field lines, each with only one footprint on the Earth and the other in the SW plasma. This process does not require a particularly strong SW magnetic field since the IMF has a value near 5 nT at 1 AU, although greater incoming IMF flux does enhance the process.

The newly created field lines on the sun-side of Earth are pulled along or “convected” over the polar cap due to the continual motion of the SW. These field lines are stretched out into the magnetotail and eventually can become so stretched they begin to compress into the center of the magnetotail. Here, another pair of X-Lines are formed (X-Line 2 in Figure 20) in the plasma sheet allowing the release of this magnetic tension through another magnetic reconnection processes. The Earth-ward pair of field lines created by this X-Line 2 “snap” back towards the Earth to reform the dipole-like magnetic field. Because the dayside magnetopause is relatively constant, we know these newly minted night-side X-Lines must convect back towards the dayside to replenish the field lines there. Conversely, the X-Line 2 points that are anti-Earthward can form a *plasmoid* or ”plasma-magnetic entity”. This lava lamp-like closed magnetic torus structure can peel off from the magnetotail and be carried out into the solar wind.

There are some significant consequences of this process. First, it is this processes which defines the outer boundary of the high latitude Plasmasphere (Russell et al., 2016) since the convection of field lines over the magnetic poles creates an electric field that pushes low-energy plasma back towards the Earth. Second, the snapping back of magnetic field lines which quickly pass

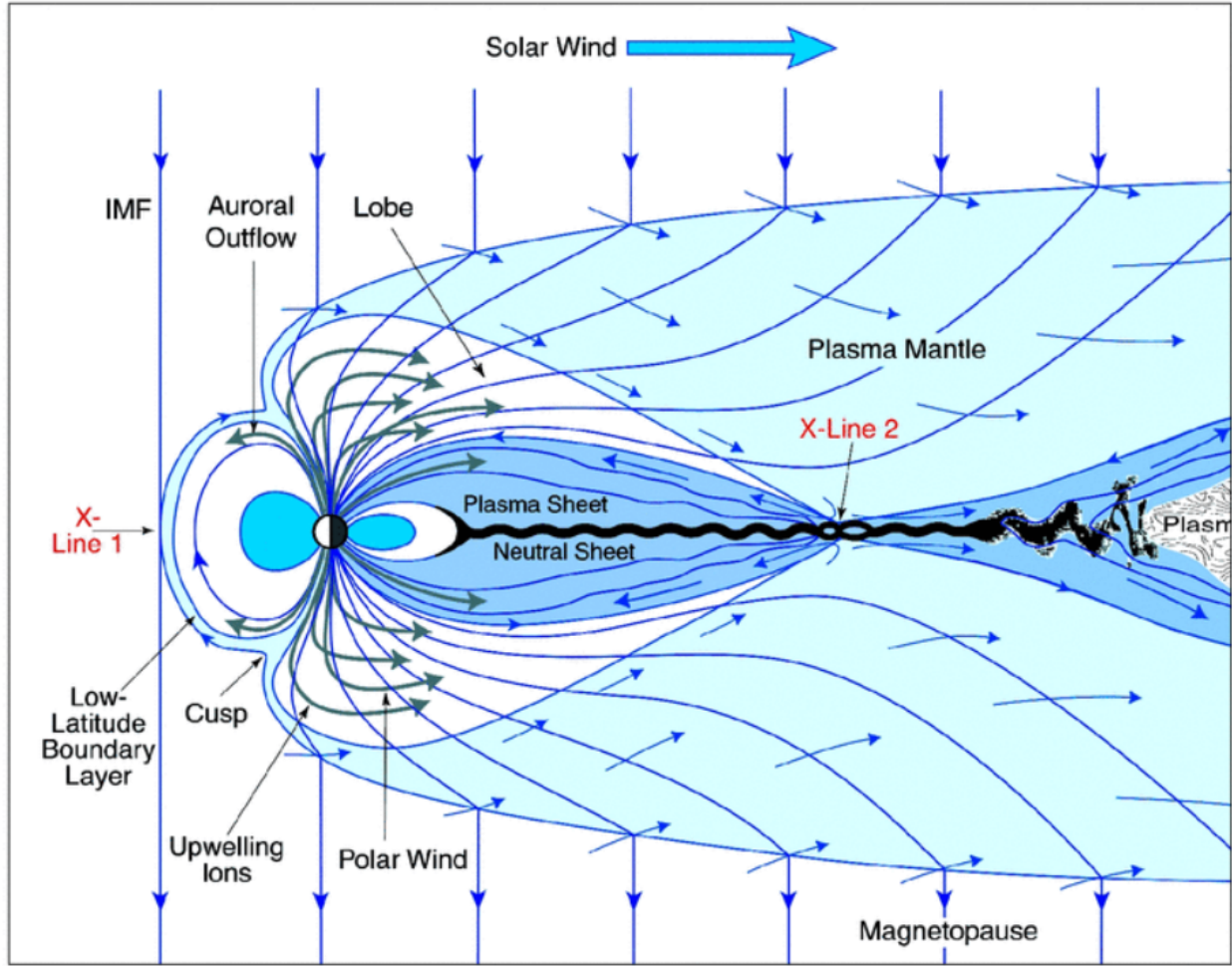


Figure 20. From Council, 2004. Schematic showing the process of magnetic reconnection where two X-Lines are formed due to the connection between solar wind IMF and terrestrial magnetic fields.

through the plasma sheet form the conceptual basis for the production of the nightside aurora. During the snapback, an electric field parallel to the background magnetic field develops which accelerates plasma sheet electrons into and ions out-of the ionosphere to close the many magnetospheric currents setup during the reconnection process. This electric field is covered in more detail in Chapter 4.2.

### 3.6 The Plasma Sheet: Auroral Source Region

Due to its relevance with this dissertation and aurora in general, we very briefly cover a few properties of the high latitude plasma sheet in more detail. The plasma sheet itself provides the plasma pressure to balance the magnetotail lobe's magnetic pressure and exists between 3-10  $R_E$  from Earth. The plasma here is often described as a kappa distribution rather than a Maxwellian, although both can be appropriate at times (Dors et al., 1999; Kaepller, 2014). The particles here flow along field lines and mirror at various altitudes while traveling Earthward, forming a sharp loss cone between pitch angles  $\alpha = 0^\circ$  to  $30^\circ$  for the particles that map to the auroral acceleration region. The diffusion of particles into the atmosphere is sometimes invoked as the explanation for the diffuse background glow aurora (C. A. Kletzing et al., 1999). In Figure 21, we show the results of a plasma sheet crossing of the POLAR spacecraft from C. A. Kletzing et al., 2003, where a kappa and Maxwellian distribution fit was performed to estimate the temperature and density. For the magnetic field lines that define the poleward edge of the plasma sheet, the density was  $0.01 \text{ cm}^{-3}$  to  $0.03 \text{ cm}^{-3}$  on the equatorward boundary. The average electron mean energy was between 400 eV to 900 eV on these same boundaries, respectively. The kappa distribution fit these results twice as often as a Maxwellian.

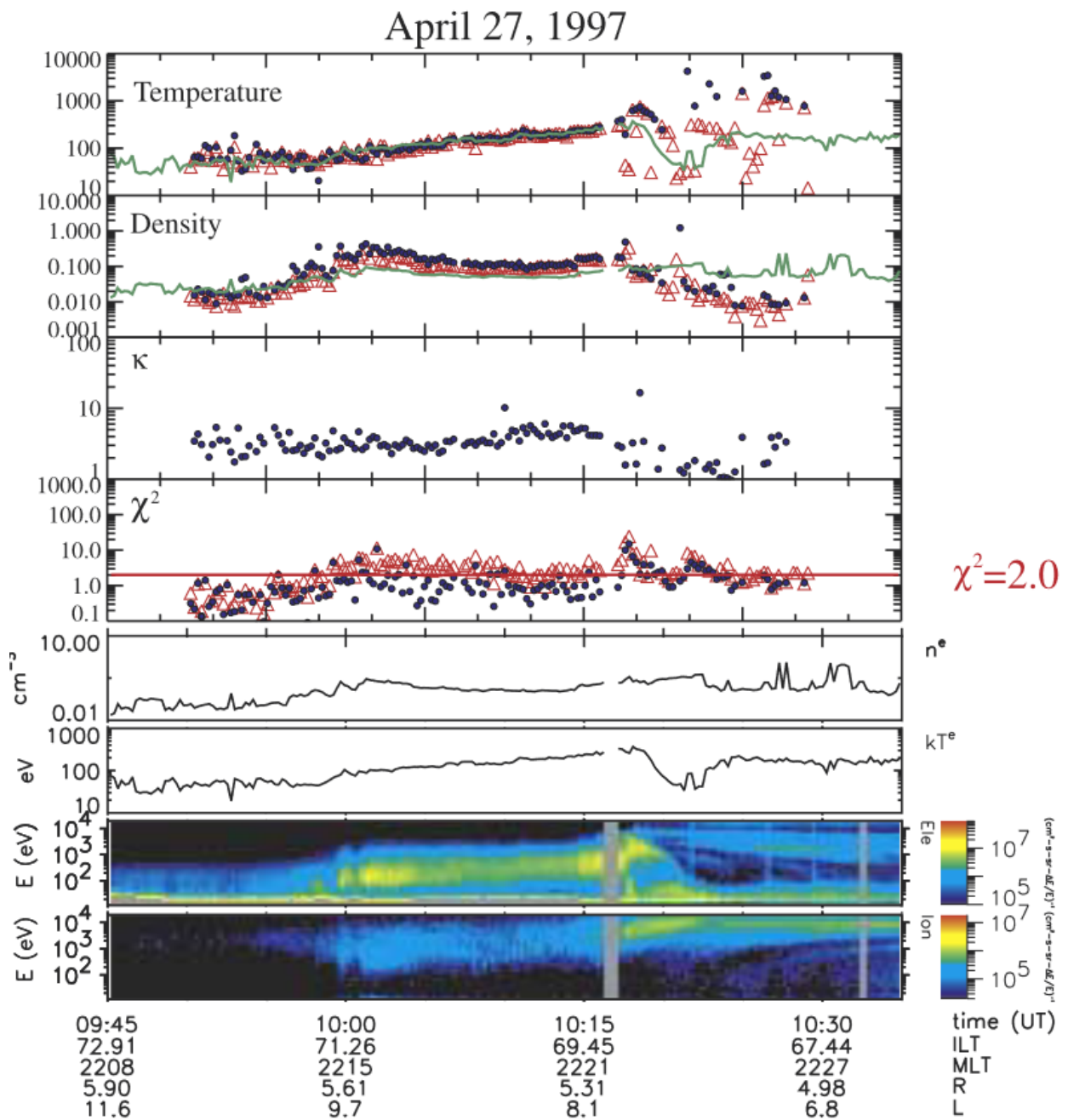


Figure 21. From C. A. Kletzing et al., 2003. One pass of the POLAR satellite through the high-latitude plasma sheet over an hour long pass. The top three panels show the fit parameters with blue/black for the kappa distribution and red for the Maxwellian. The data from the left side of the figure represents the high-latitude, poleward field lines while the rightside are equatorward.

### 3.7 Ionospheric Current Systems and Closure

Among the last remaining concepts to cover is the closure of magnetospheric currents through the ionosphere called the *electroject*. In Figure 22 are shown blue and red arrows representing Field-Aligned Currents (FACs) that flow along the geomagnetic field lines of Earth into the polar regions, both into and out-of the ionosphere. These are denoted by Region 1 (R1) currents that form the two poleward flows and Region 2 (R2) that form the equatorward pair. These currents are most prominent during geomagnetically active times when magnetospheric currents are forced to close part of their circuit through the ionosphere. The ionosphere behaves much like a resistor in the FAC system and these large-scale in-flowing currents cross geomagnetic field lines within a narrow band of altitudes to pass through this resistive atmosphere, depositing some energy along the way. The optical signature of this process is the vibrant aurora.

Here we provide some concepts and mathematical tools to describe this current closure. At high altitudes ( $> 1000$  km), electron-neutral and ion-neutral collisions are low, as indicated by Figure 19. This means FAC particles are still largely fixed to magnetic or *magnetized*. When collisions become significant at lower altitudes the particle *mobility*  $\kappa_s$  changes and is described by the ratio of the gyrofrequency and collision frequency:

$$\kappa_s = \frac{\omega_{c,s}}{v_s} = \frac{|q_s|B}{m_s v_s} \quad (88)$$

Where  $q_s$  is electric charge for species “s”,  $B$  is the field perpendicular to the particle’s orbit,  $m_s$  is species mass and  $v_s$  is the species collision frequency. For any particle, when  $\kappa_s \ll 1$  it moves unobstructed along  $\vec{B}$  and when  $\kappa \gg 1$  collides so often that gyromotions become irrelevant. At  $\kappa_s \sim 1$  the particle motion is affected just enough to occasionally displace the particle but not enough to prevent it from (on average) completing a gyro-orbit before colliding again. In a region where  $\kappa_s \sim 1$  and an external electric field  $\vec{E}$  perpendicular to the background magnetic field is present, it introduces a method of producing a  $\vec{J}$  perpendicular to  $\vec{B}$ .

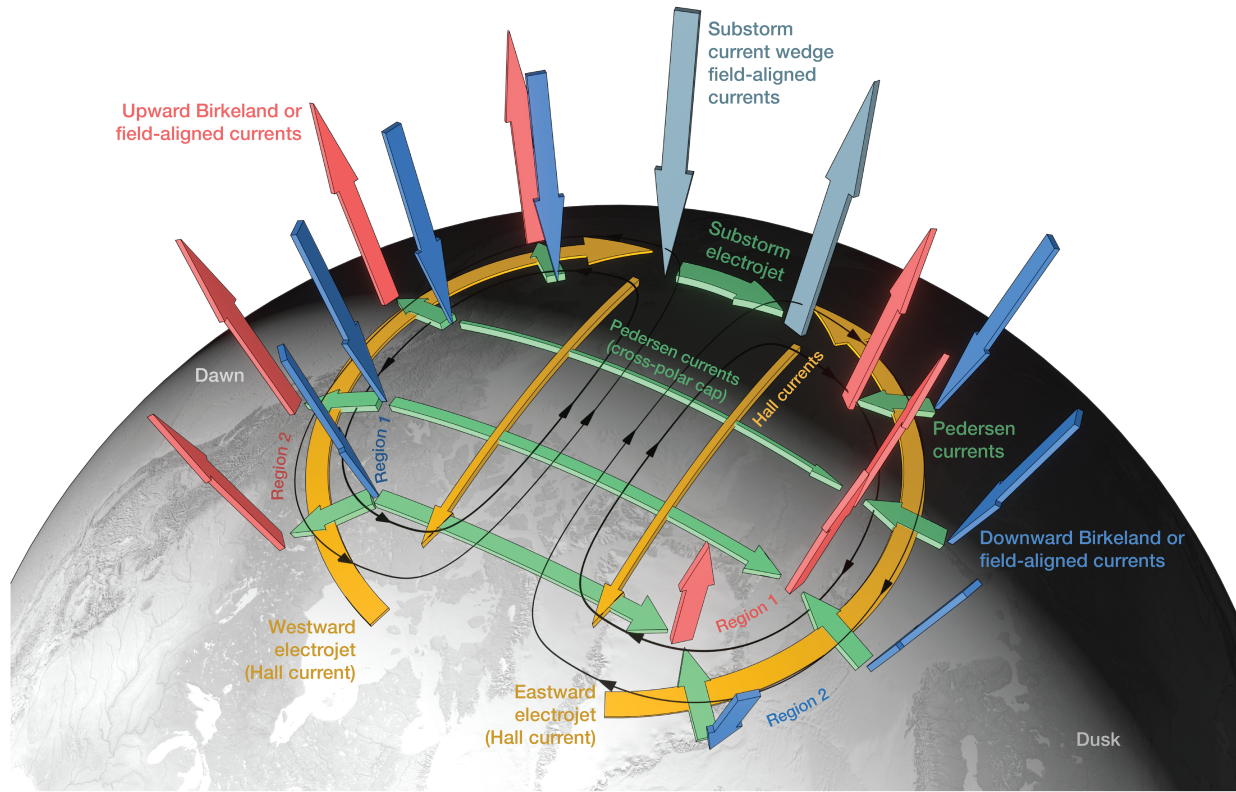


Figure 22. From Palmroth et al., 2021. The currents of magnetospheric origin (shown in red and blue) close their circuit through the ionosphere. A pair of currents form (1) The cross-field Pedersen currents (shown in green) that connect R1 and R2 current pairs and (2) the  $\vec{E} \times \vec{B}$  Hall current (shown in yellow).

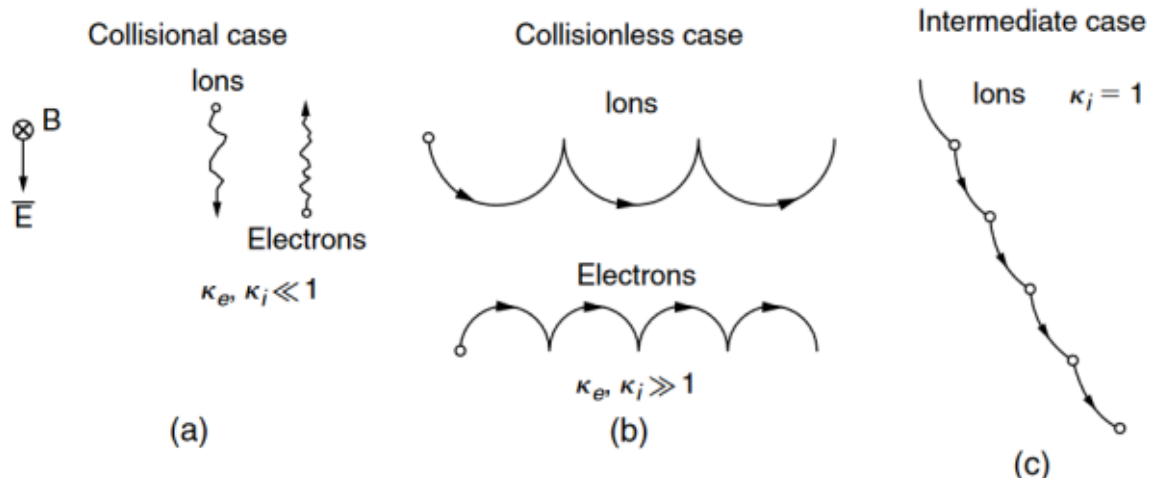


Figure 23. From Kelly, 2009. Ion and electron trajectories for different mobilities in a  $\vec{B}$  field with a perpendicular  $\vec{E}$ .

During FACs, there exists a large-scale perpendicular electric field  $\vec{E}_\perp$  that maps down from the high altitude magnetosphere onto the high latitude ionosphere. The origin of this  $\vec{E}_\perp$  is covered in Chapter 4.2. Within the ionosphere, this  $\vec{E}_\perp$  causes ions and electrons to move perpendicular to the geomagnetic field  $\vec{B}_{geo}$  in the  $\vec{E}_\perp \times \vec{B}_{geo}$  direction. At high altitudes, no  $\vec{J}_\perp$  is produced since both electrons and ions drift the same amount. However, at the altitudes where the mobilities of the ions reach  $\kappa_s \sim 1$ , the ions are demagnetized and briefly accelerated by  $\vec{E}_\perp$  in a picture similar to Figure 23(c). Electrons will also collide, but since ion inertia is greater their displacement carries them further in the direction of  $\vec{E}_\perp$ . This differential motion between the charge carriers permits a current flowing in the direction of  $\vec{E}_\perp$  called the *Pedersen Current*. As a consequence, the  $\vec{E}_\perp \times \vec{B}_{geo}$  drift of the plasma breaks neutrality due to the reduction in ion motion in the drift direction, resulting in a net current carried by electrons called the *Hall Current*. The conversion between FAC current into Hall/Pedersen current occurs over a range of altitudes between 90 km to 150 km called *the current closure region* and is mediated by the conductivity of the ionosphere.

Since Earth's atmosphere does not exhibit an ever-increasing build-up of charge, the FAC flowing into the polar regions must satisfy current continuity. Mathematically, this means for the region of FAC current closure,  $\partial\rho/\partial t = 0$ . Explicitly written, the current continuity equation is

$$\frac{\partial\rho}{\partial t} + \frac{\partial\vec{j}_\parallel}{\partial z} + \nabla_\perp \cdot \vec{J}_\perp = 0 \quad (89)$$

where  $\vec{j}_\parallel$  are the in-flowing/out-flowing FACs and  $\vec{J}_\perp$  are the cross-field Hall/Pedersen currents as shown in the red box in Fig 24. To isolate  $\vec{j}_\parallel$  we integrate equation 89 over the z-axis and apply  $\partial\rho/\partial t = 0$  to get a relationship between FACs and ionospheric currents:

$$\vec{j}_\parallel = -\nabla_\perp \cdot \vec{j}_\Sigma \quad (90)$$

where  $\vec{j}_\Sigma$  represents the height-averaged cross-field currents. Essentially, we have assumed the cross-field currents can be represented as a thin slab with uniform *height-integrated Hall/Pedersen conductivities*  $\Sigma_H, \Sigma_p$ , respectively. By assuming  $\Sigma_p, \Sigma_H$  are spatially varying only in x-y plane and

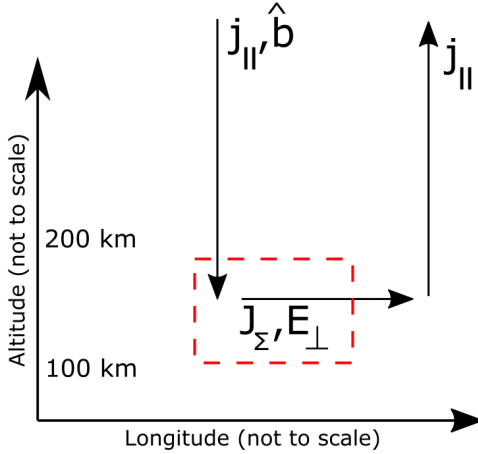


Figure 24. A 2D image of FACs and ionospheric currents in the connection region. In reality, Ionospheric currents close over a range of altitudes in 3D sense.

using Faraday's Law  $\nabla \times \vec{E} = -\partial \vec{B}/\partial t = 0$  we can show equation 90 becomes

$$\vec{j}_{\parallel} = -\Sigma_P (\nabla \cdot \vec{E}_{\perp}) - \vec{E}_{\perp} \cdot (\nabla \Sigma_P) + \hat{b} \cdot [\nabla \Sigma_H \times \vec{E}_{\perp}] \quad (91)$$

A full derivation can be found in Appendix D. The study of terms in equation 91 are central to the science goals of the sounding rocket mission described in Chapter 5.1.

How the ionosphere responds to the Pedersen current determines how much FAC energy is deposited in the atmosphere. This processes is called *Joule Heating* and its identical to the reason a resistor gets warm in a common circuitry. The alignment between the ionosphere currents  $\vec{J}_{\perp}$  and the external  $\vec{E}$  determine whether the ionosphere acts like a resistive element or is the supplier of the energy in the magnetosphere-ionosphere system:

$$\vec{J} \cdot \vec{E} > 0 \implies \text{Load-like (Joule Heating)}$$

$$\vec{J} \cdot \vec{E} < 0 \implies \text{Generator-like}$$

In the study of energy transfer in the MI system, Joule heating plays an important role in cataloging where the energy of FACs go.

## CHAPTER 4: AURORAL PLASMA

There exists a rich history of discovery and debate surrounding the electrodynamics of the magnetosphere-Ionosphere regions, particularly focused on the electrodynamics that produce aurora. Within the vast literature of the high latitude aurora, there exists some essential elements and structures found in spacecraft data that are generally agreed upon and recognized, even if the underlying processes which create them are not fully understood. The work in this thesis primarily deals with these more common auroral signatures that have been seen by the vast majority of spacecraft missions into these regions. In this chapter, we will describe these common elements and detail some of their substructure as well as discuss useful models to understand them.

### 4.1 Colors of the Aurora

At a high level, the aurora is simply energetic particles striking Earth's atmosphere which excites terrestrial atoms/molecules enough to produce light when de-excitation occurs. These particles are a part of the FAC system of currents described in Chapter 3.7 which form due to the cascade of solar energy from sun down eventually down to the ionosphere. This section is dedicated to the introducing the finer aspects of the aurora itself. Much of the content here comes from the aurora content in Chapter 11 of Russell et al., 2016.

The beautiful fluid-like nature of aurora in photographs is a clear demonstration of the dynamic processes which create these dazzling light displays. However, commonalities exist in the magnetosphere-ionosphere system which consistently produce aurora forms that can be classified, organized and understood in terms of the different processes which drive their respective auroras. Most aurora do not come directly from solar particles and instead have a terrestrial source which exists within Earth's magnetosphere (C. A. Kletzing et al., 2003). Specifically, accelerated electrons striking Earth's atmosphere produce the photons which power the visual aspect of the aurora (McIlwain, 1960).

As part of the FAC/ionospheric current system, these FAC electrons are eventually stopped

by collisions in the atmosphere which excite neutral atoms which eventually emit photons. In this way, the composition of Earth's atmosphere below 500 km is what determines the colors of the aurora, and the stratification of the auroral colors to specific altitudes is simply a reflection of the types of molecules that exist at those altitudes. In Figure 26 we show the composition of the Thermosphere which become excited due to electron precipitation. In particular, the excitation of monatomic oxygen  $O$  produces the majority of photons that compose the auroral green and red lines of 5570Å and 6300Å. The redline occurs between 200 km to 300 km while the green-line emission occurs at lower altitudes near 150 km. The altitude of color emission is related to the energy of the incoming electrons, where higher energy electrons penetrate deeper within the ionosphere before deflecting significantly due to collisions. For extreme solar events which can induce electrons of high energy into the ionosphere, excited diatomic nitrogen  $N_2^+$  can produce blue-line aurora of 4700Å near 100 km and  $N_2$  can produce crimson, which results in a purple-pink auroral layer at low altitudes due to color mixing.

The de-excitation times of aurora also shapes their behavior. In Figure 25 we show the de-excitation half-lives of atomic oxygen which shows the green-line half-life near 0.8s while the red-line decay time of 111 s. This substantial difference in decay time results in a murky, diffuse-like

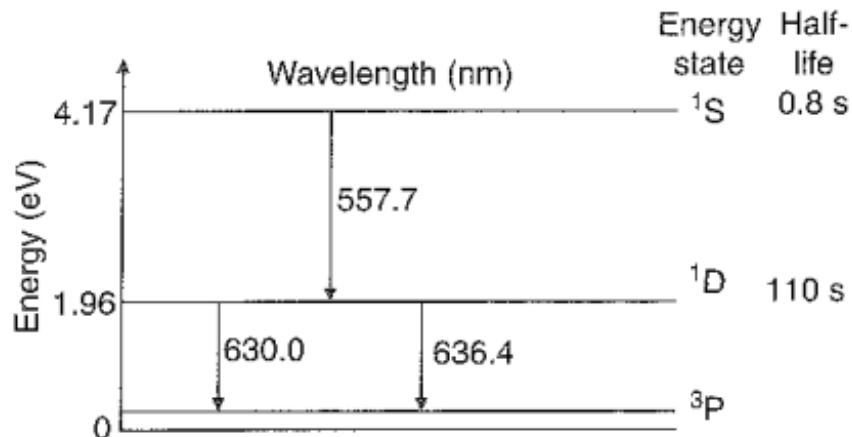


Figure 25. From Russell et al., 2016. This shows the energy levels of atomic oxygen associated with auroral emission. The indicated half-lives describe the length of time before the atom de-excites to produce a photo. The long half-life of the red-line 6300Å is why this part of the aurora often looks blurry in all-sky imagers.

shape for red aurora since excited oxygen atoms have long periods to move around before releasing a photon. Green aurora appear bright and spatial localized since their photons are released almost immediately after excitation and all within the same region of the incoming electron precipitation. Because the typical energy range of incoming electrons ( $\sim 1$  keV) generally excites the green-line oxygen band most often and it releases its photons quickly means aurora are generally seen as green bands dancing across the sky.

## 4.2 Discrete Aurora and Quasi-static Parallel Electric Fields

Aurora can be categorized into many different types of shapes, generally based upon the type of mechanism which produced them. Just to name a few, there are diffuse, discrete, theta, pulsating and Alfvénic aurora and many more. For the thesis work here, we're most interested in the discrete aurora or “auroral arcs” category due to its geometrical simplicity and quasi-static characteristics. Discrete aurora exhibit a few common characteristics. Firstly, “discrete arcs” exhibit long longitudinal extents, spanning hundreds of kilometers compared to their much shorter latitudinal lengths of tens of kilometers. Second, these aurora appear at the typical auroral latitudes around  $70^\circ$  for the northern hemisphere and  $20^\circ$  in the southern Hemisphere. They are very common and often seen early in the night, during the beginning phases of a geomagnetic substorm. Finally, these aurora are quasi-static, existing in approximately the same location in the sky on the order of minutes but drifting to different (usually equatorward) latitudes on the order of hours.

In order to discuss the mechanisms which drive discrete aurora, we provide historical context. Some of the first *in situ* measurements of discrete aurora came from sounding rockets out of Fort Churchill, Canada (McIlwain, 1960). This study flew directly into a “bright active auroral arc” and measured particle flux and atmospheric absorption of total flux to estimate the energy spectrum of the precipitating particles. The data showed a significant electron flux in the 10 keV or less energy range for which McIlwain, 1960 concluded that electrons were the particles responsible for the visible aurora. This was based on (a) ions flux indicated smaller amounts of energy deposition at 100-to-120-km than electrons and (b) the energy-to-light efficiency calculated for ions was too

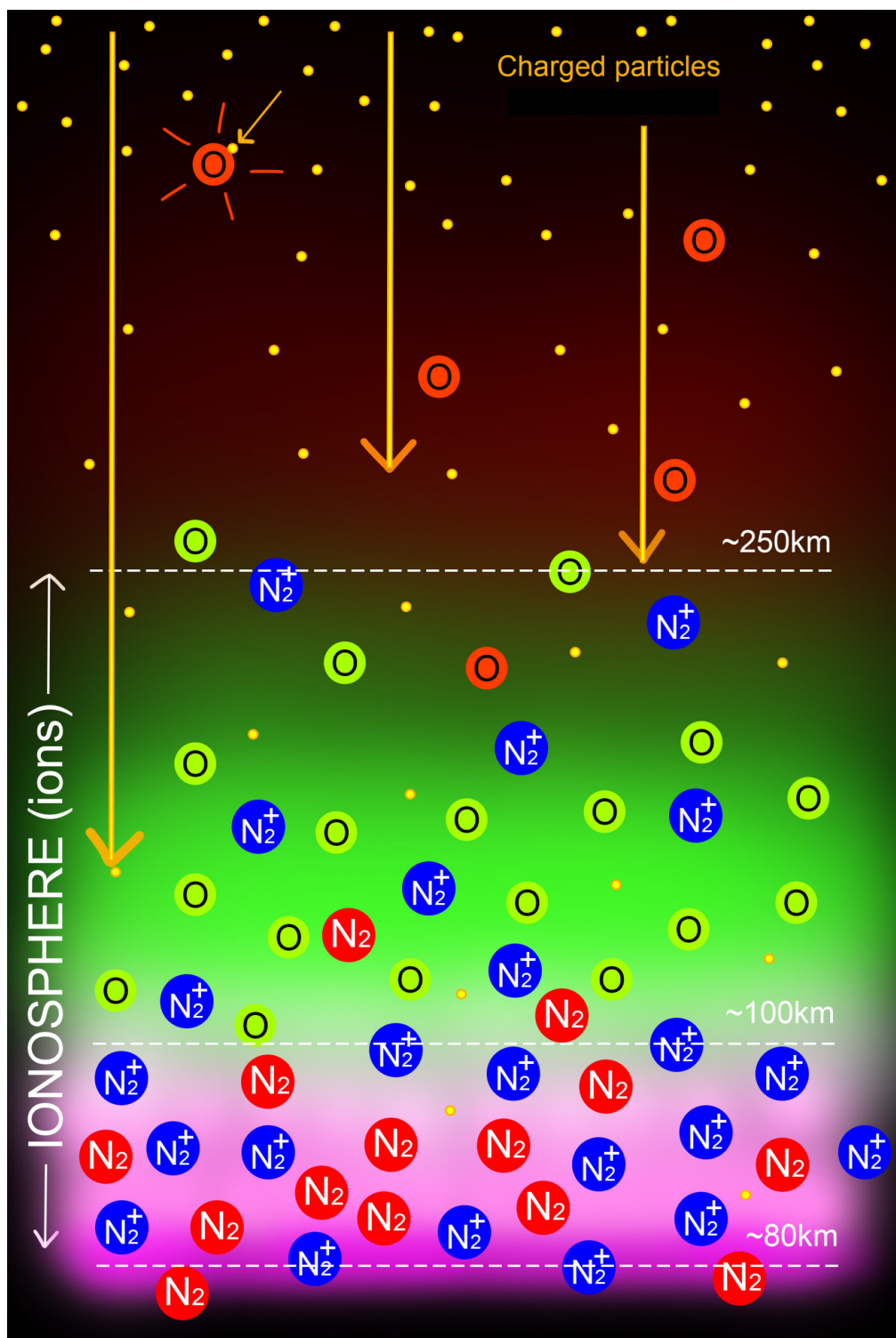


Figure 26. Photo Credit: Adrien Mauduit. Image adapted from <https://auroraborealisobservatory.com/2021/03/07/best-aurora-in-3-years/>. The colors of the aurora as it relates to the specific molecule which gets excited to emit photons.

low. Combined with the low ion flux, this implied ions shouldn't be able to contribute enough energy to the total observed luminosity to produce the visible signature of aurora. A key observation of their electron distribution was that the electron auroral-signature couldn't be represented as a Maxwell-Boltzmann distribution. Instead they showed the auroral electrons as a nearly monoenergetic beam, which they concluded wouldn't occur if some statistical process was involved in accelerating the electrons. The authors proposed electric fields as a possible mechanism to explain this.

The idea of a parallel electric field for auroral particles continued to provide a simple explanation for future auroral studies in the follow decades, despite considerable resistance to the idea. Another rocket by Evans, 1968 corroborated the existence of the near monoenergetic flux of auroral electrons near 3.8 keV and debated the possibility of a parallel E-Field. The Injun 5 satellite data in Frank et al., 1971 displayed some of the first evidence of a "V" substructure in the Energy-time spectrograms for auroral precipitation at much higher temporal/energy resolutions than previously published. This "V" substructure was a well-defined increase of the electron energy for peak differential flux intensities with time to a maximum energy (usually keV levels) followed by a subsequent decrease of this energy and flux. In Figure 27 we show an example of the electron differential number flux vs. energy slice within this "V" substructure, where a power law has been fit to the low energy portion of the data and a Maxwellian distribution to the high energy roll-off. In Figure 28 we show a modern-day example of the "V" shaped structure they are referring to from the ACES-II sounding rocket mission. Figure 27 two common observations seen in discrete aurora: (1) An acceleration Maxwellian-like "beam" at high energy and (2) An intense flux of low-energy, power-law distribution of electrons at low energies which outnumber a thermal Maxwellian.

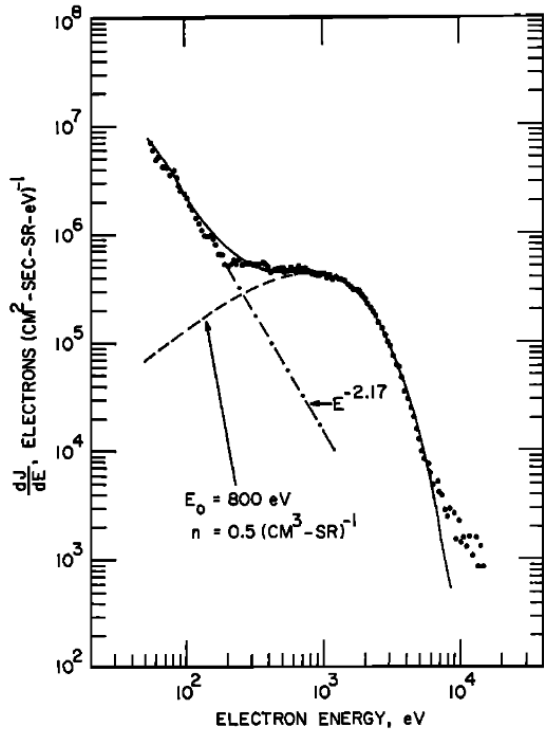


Figure 27. From Frank et al., 1971. Differential number flux vs. energy from an “V” shaped structure within an auroral arc by the Injun-5 Satellite. A power law spectrum (dotted-dashed line) and a Maxwellian distribution (dashed line) are fit to the various sections of the data. These are some of the first observations of accelerated Maxwellian distributions form parts of the discrete aurora.

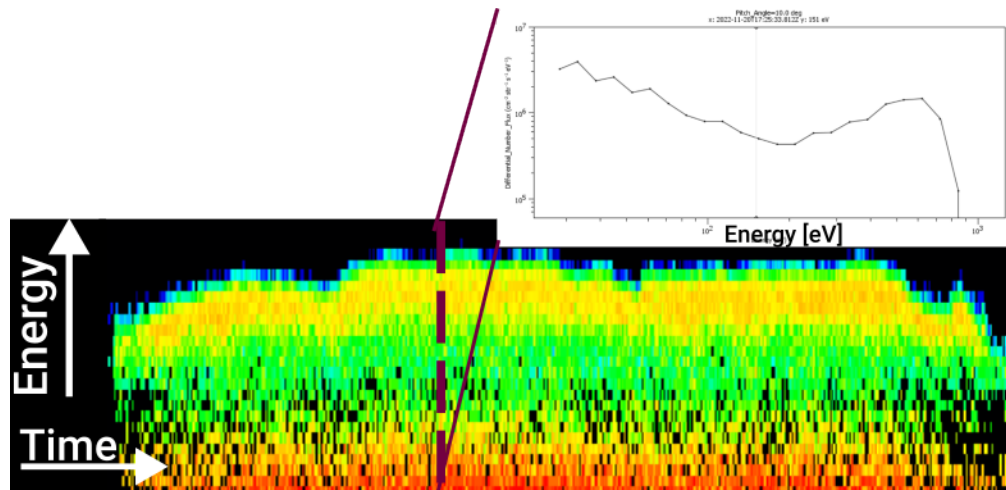


Figure 28. Modern day view of the the electron “V” shaped structure that Frank et al., 1971 described from Injun-5 while flying through an aurora. This particular structure is extended over many latitudes and grows/deacys on the edges much like Frank et al., 1971 described. The greatest electron flux is seen in red at the lower energies, a result of the secondary emission from the higher energy primary flux (Evans, 1974). Data taken from ACES-II sounding rocket mission.

It was these observations that help generate sharp criticism of the idea of a quasi-static parallel electric field as an explanation for aurora. The paper by O'Brien, 1970 dismissed the idea of a parallel electric field to  $\vec{B}$  based on the observation of the low-energy, power-law flux of electrons coincident with high energy auroral electrons. They argued if the high-energy, Maxwellian part of the auroral distribution is supposed to be the accelerated auroral electrons, then the existence of the intense, low-energy power-law electrons is not consistent with the idea that a DC electric field accelerated all auroral electrons. The second criticism from the community was that Earth's geomagnetic field lines at high altitude should have a nearly infinite conductivity parallel  $\sigma_{\parallel}$  to  $\vec{B}_{geo}$ , which is not capable of sustaining a voltage drop to accelerate electrons. The first criticism was addressed by Evans, 1974 who used a new model of secondary electron production from incident electrons by Banks et al., 1974 to show how incoming, keV electrons can produce significant levels of secondary and backscattered electrons in the atmosphere due to collisions. These secondary/backscattered populations will either (a) be lost to the collisional atmosphere or (b) be reflected upward via the mirror force back into the region of an (assumed) parallel electric field where they will be reflected back towards the ionosphere to start the process over again. As described by Evans, 1974, these trapped secondaries/backscatter electrons will reflect, scatter and produce more electrons every "bounce" until equilibrium is reached, producing significant flux of electrons at all energies below the primary monoenergetic beam. This model will be discussed in detail in Chapter 4.4 in this thesis.

Next, the second criticism about the prohibition of  $E_{\parallel}$  by MHD theory is discussed. The argument against parallel fields is similar to the following: Consider a FAC into the ionosphere where  $\vec{J}$  is parallel to  $\vec{B}_{geo}$ . Start with Ohm's law in Chapter 2.5:

$$\vec{J} = \sigma \vec{E} \tag{92}$$

where we have assumed the electron pressure, Hall terms and inertia terms are zero and that the fluid velocity is primarily along  $\vec{B}_{geo}$  ( $\vec{u} \times \vec{B} = 0$ ). At higher altitudes above the collisional iono-

sphere current continuity ( $\nabla \cdot \vec{\mathbf{J}} = 0$ ) should apply and the only variation in the conductivity  $\sigma$  for the altitude, z-direction is considered. This is because at high altitude the perpendicular current  $\vec{\mathbf{J}}_{\perp}$  is virtually zero due to extremely low cross-field conductivities. Using  $\vec{\mathbf{E}}$  from equation 92 into current continuity we get

$$\nabla \cdot \vec{\mathbf{J}} = \nabla \cdot (\sigma_{\parallel}(z) E_{\parallel}(z)) = 0 \quad (93)$$

When expanded using the chain rule we get

$$E_{\parallel} \frac{\partial \sigma_{\parallel}}{\partial z} + \sigma_{\parallel} \frac{\partial E_{\parallel}}{\partial z} = 0 \quad (94)$$

Rearranging this gives

$$\frac{1}{\sigma_{\parallel}} \frac{\partial \sigma_{\parallel}}{\partial z} = - \frac{1}{E_{\parallel}} \frac{\partial E_{\parallel}}{\partial z} \implies \frac{\partial}{\partial z} \ln \sigma_{\parallel} = - \frac{\partial}{\partial z} \ln E_{\parallel} \quad (95)$$

This last statement implies the equality

$$\ln(\sigma_{\parallel}) = - \ln E_{\parallel} \implies \ln \sigma_{\parallel} E_{\parallel} = 0 \quad (96)$$

This last statement gives us the final relationship

$$\sigma_{\parallel} E_{\parallel} = 1 \quad (97)$$

Under the idealized MHD conditions we must set  $\sigma_{\parallel} \rightarrow \infty$  which suggests  $E_{\parallel} \rightarrow 0$ . On the basis of the previous assumptions and of ideal MHD, this prohibits a parallel electric field. These assumptions are not entirely unreasonable since the high altitude magnetospheric plasma is virtually collisionless ( $v \sim 0$ ) and  $\sigma \propto 1/v$ . However, the continued success of the quasi-static parallel electric field in describing several observations throughout the late 1970s, 1980s and beyond made it increasingly difficult to dismiss it on the grounds of MHD alone (Bennett et al., 1983; Goertz et al., 1979b; Kaufmann et al., 1976; C. Kletzing et al., 1983; C. A. Kletzing et al., 1996; Knight,

1973; Lyons, 1981; Mozer et al., 1977; Sharp et al., 1979; Temerin et al., 1981; Torbert et al., 1978). This lead to the term “anomalous resistivity” to appear in literature as a “catch-all” description of unknown processes that could sustain the  $E_{\parallel}$  required to produce the aurora (Hudson et al., 1978; Lysak et al., 1981). Today, the “V” type structures described by Frank et al., 1971 are called *inverted-Vs* and are still widely observed by rockets and satellites at high latitudes.

Among the vast literature on this topic we wish to address a few concepts which we will encounter in later chapters. What does the high altitude electric field associated with the inverted-V look like and where does it form? In the mid-70s to early 80’s, parallel electric fields began to be recognized for their equipotential geometries and their spatially confined nature which were associated with an oppositely pointing electric field configuration. For this reason the term “electrostatic shock” arose to describe the suddenly oppositely directed, large-magnitude electric fields seen by satellites at high altitude. For example, the Small Secondary Satellite 3 (S3-3) launched in 1976 was the first satellite to make in situ measurements of these shocks throughout its 260 km to 8000 km altitude range. Panel (a) in Fig 29 shows the typical form of an electrostatic shock, which was taken from the satellite’s DC electric field instrument as the satellite passed through auroral precipitation. Large amplitude electric perturbations on the order of 100s mV/m are seen near 12:26 UTC in both perpendicular directions as well as a nearly unidirectional, upward  $E_{\parallel}$ . Here, the sudden  $E_{\perp}$  constitutes the “shock” portion of the electric field despite not being a traditional shock such as the magnetospheric bow shock. The authors of the study (Mozer et al., 1977) performed a statistical study on these shocks for over 100 high latitude passes that included shocks and found: (a)  $|E| \geq 120$  mV/m seen on about half of the high-latitude passes, on time scales less than 10 sec (b) Significant FACs ( $> 10^{-6}$  A/m<sup>2</sup>) occur in the same region as the shocks,. (c) beams of electrons are observed within the regions of large electric field and (d)  $\sim 3$  kV potential drops in the parallel part of the shock structure can be seen, which is consistent with the potential required to accelerate auroral electrons to observed energies.

An illustration of the possible geometry to reproduce the results in panel (a) are shown in panel (b) of 29, with a “U-Shaped” that consists of oppositely directed  $E_{\perp}$  with an  $E_{\parallel}$  embedded

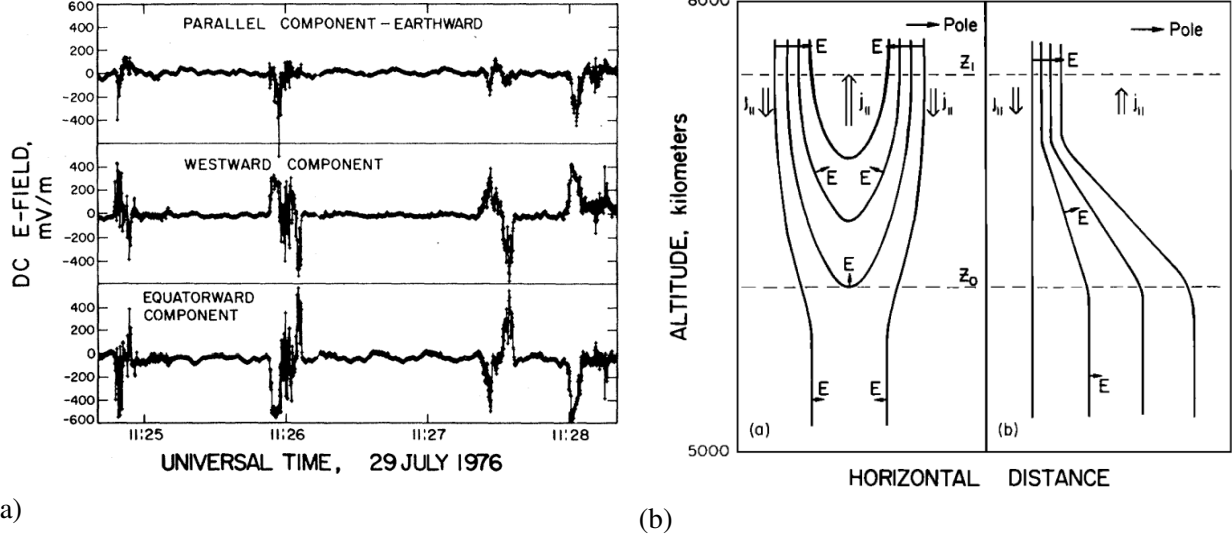


Figure 29. (a) One pass of S3-3 satellite measurement around 7600 km showing oppositely directed electric fields at 11:26 UT while passing the auroral oval. The parallel component appears mostly strongly when embedded in the equatorward and westward field reversals. Mozer et al., 1977 (b) Equipotential model from Temerin et al., 1981 that could produce the observed electrostatic shocks. The left panel shows the U-shaped potential which exhibits the properties of electric field reversal, but also the oppositely pointing fields that continue down to lower altitudes.

between them due to the bending of the contour lines. An alternative representation called the “S-Shaped” potential is shown on the right side of Figure 29. In either case, the  $E_{\perp}$  fields map to lower altitudes while the parallel component is confined to thousands of kilometers above the Earth. Today, the mechanism that can exactly produce these potentials self consistently is still an open question. For example, the work by Borovsky, 1993 posits 22 theories that deal with the thickness and generation of auroral arcs based on various potentials at high altitude. Additional satellites, such as the Freja mission provided additional insight by adding complexity to the U-Shaped potentials, as shown in Figure 30 which displays how multiple discrete arcs forming in succession may be caused from divergent electric fields at high altitude that form an upward/downward current system. The U-Shaped geometry is typically what is used to explain the “V” shape of the inverted-V in auroral electron distributions and is often the most observed discrete auroral feature.

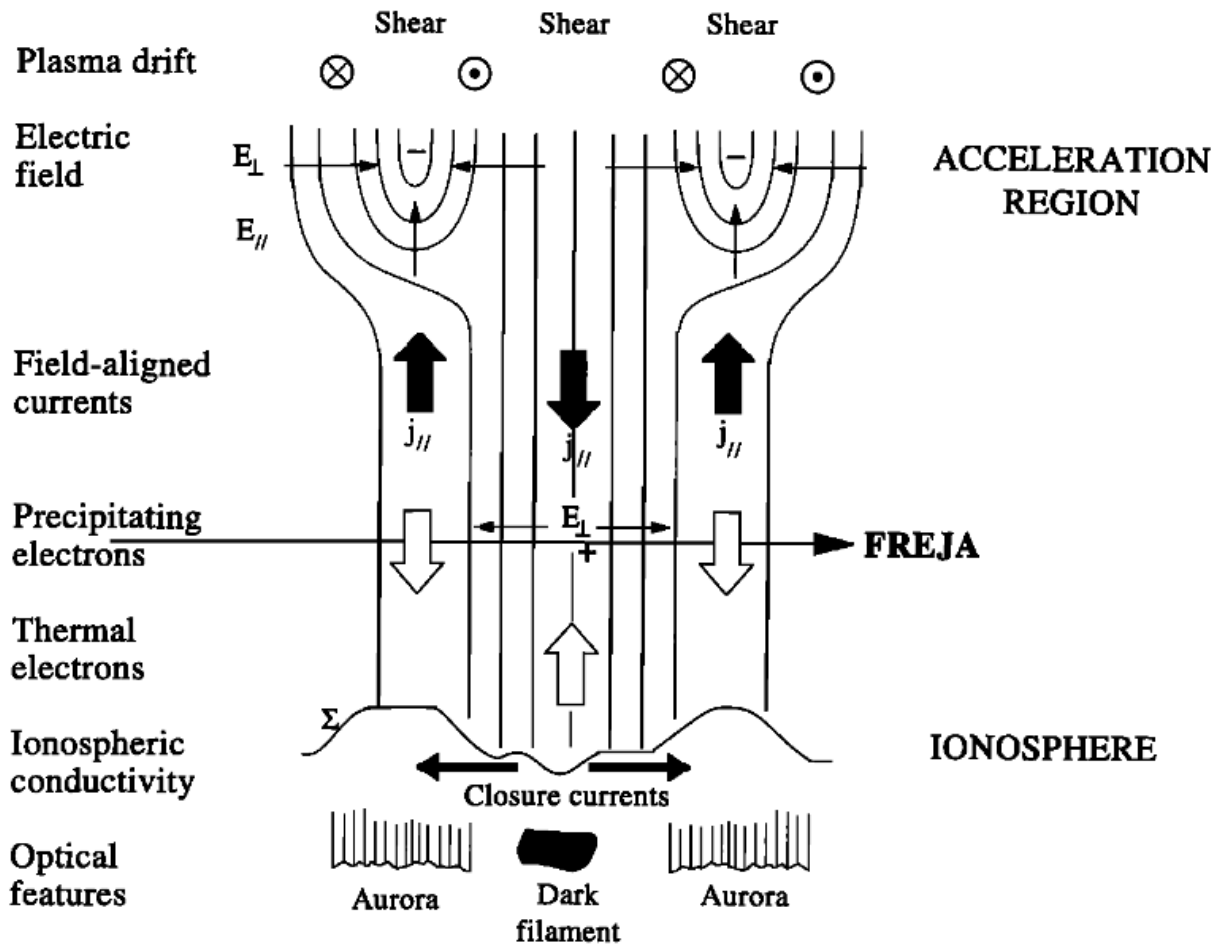


Figure 30. From Marklund et al., 1997 Possible configuration of a double-arc system associated with divergent electric fields at high altitudes. Here, the downward current produces a “Black Aurora” made of ion.

The height occurrence of these electrostatic shocks has also been studied. The statistical survey by Bennett et al., 1983 used three years of S3-3 which gathered electric field data over a large range of altitudes in the polar regions. The study included 2375 auroral zone crossings of which 1248 included electrostatic shocks, defined by any small scale variation in the electric field of magnitude 90 mV/m or greater. Using quiescent periods (times of E-field variations  $< 10$  mV/m) as a control to separate regions of shocks from one another, the authors produced a probability histogram of encountering a shock as shown in Fig. 31. Among the many results of this paper, three stand out for our discussion. The first is that the probability of observing a shock increases sharply between 0 and 5000 km altitude. After 5000-km altitude the probability increases at a

slower rate. The second point is that electrostatic shocks occurred almost exclusively in or near the latitudes associated with the auroral oval. Few shocks were found inside the polar cap, and low altitude shocks were observed only during periods of high  $K_p$ . The final point was the significant probability of observing a shock given any satellite pass, which is  $\sim 0.3$  for multiple shocks in a pass and  $\sim 0.5$  for a single shock. This rather high probability of shocks led these features to be definitively connected to the aurora acceleration mechanism, as evidenced by the work of C. Kletzing et al., 1983. Furthermore, these electrostatic shocks produced parallel electric fields extended over thousands of kilometers, which could produce electrons at keV energy levels after acceleration, precisely resembling the aurora.

In summary, the key ideas for discrete auroral physics formed over the last 50 years has been presented. The fundamental process consists of magnetospheric electrons being accelerated through a quasi-static parallel potential at altitudes between 2000 - 12000 km to later be observed as “inverted-V” distributions. The high altitude electric fields typically exhibit a U-Shaped electrostatic potential where the converging perpendicular field lines bend to form some component parallel to the background geomagnetic field. The direction of these potentials determines whether electrons or ions are accelerated and the upward  $E_{||}$  can accelerate electrons to produce aurora whereas the downward pointing parallel E-Fields tend not to. These define an upward current (electrons down) or a downward current (ions down) system. When the electrons strike the atmosphere, not only do they produce aurora but also a zoo of secondary and backscattered emission which can be magnetically mirrored back up the field line into the parallel potential to restart the processes. This processes addresses one of the major criticisms of the parallel potential explanation of inverted-Vs. An outstanding problem in this field is how the parallel potential drop can be maintained and/or what produces a conductivity gradient along the magnetic field, for which many theories exist. The basic picture of inverted-V precipitation at the ionosphere is illustrated in Figure 32.

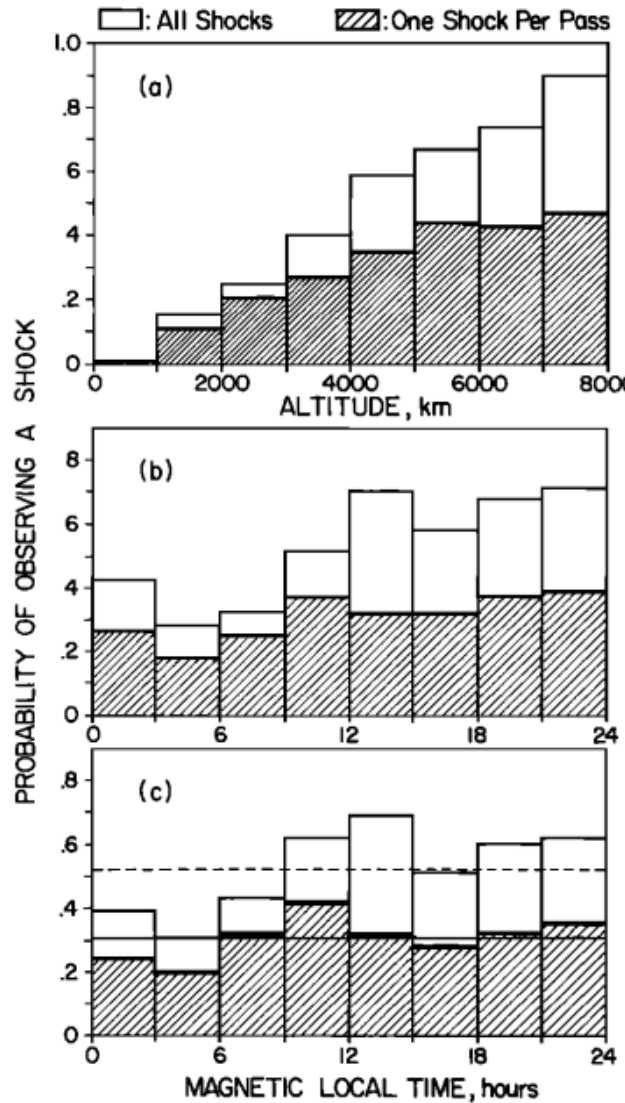


Figure 31. Probabilities of observing a shock for every 1000-km altitude (top) 3 hours magnetic local time (middle) and magnetic local time normalized by altitude (bottom). In the bottom panel the horizontal solid line represents the average probability for all MLT times of observing multiple shocks per pass, and the horizontal dashed line represents the probability of one shock per pass. Bennett et al., 1983

# Inverted-V

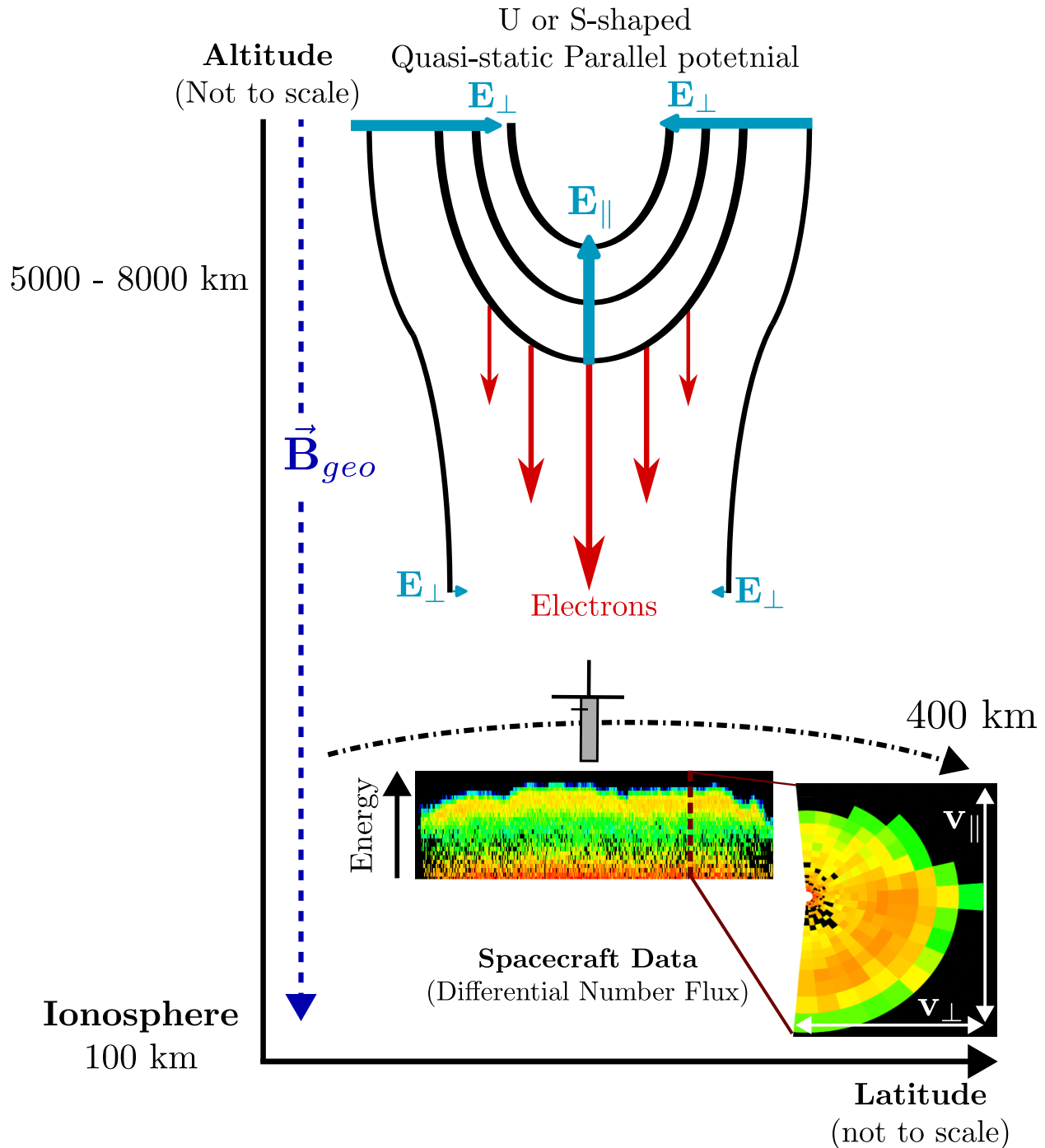


Figure 32. Basic view of inverted-Vs potential structure which form along Earth's geomagnetic field to produce discrete auroral arcs in the ionosphere. An example of real data from ACES-II is shown near 400 km in both Energy vs. Time spectrogram and velocity space.

### 4.3 Models of the Inverted-V: Phase Space Mapping and The Knight Relation

If permitted to assume the existence of a parallel electric field along a geomagnetic field line, such as a U-Shaped potential described in the previous section, then several predictions can be made to (mathematically) to describe the resulting FAC currents. Among the first to do this was the work by Knight, 1973 who provided a steady state, one-dimensional model to estimate the electron current along a field line from the auroral zone to the plasma sheet when a potential difference exist between its ends. The work resulted in a current-voltage relationship. Realistic parameters for the model were inserted and they found potential differences of the order of 10 kV were required to sustain auroral FACs, which are quite reasonable given the thousands of kilometers this potential would be spread over resulting in a lower required parallel electric field. In this section we wish to develop some tools that will be used in later sections via the work by Knight, 1973 and others.

Here we consider a geomagnetic field line from the high latitude auroral zone which has one footprint in the ionosphere and the other in the plasma sheet. Along this field line exists both cold, ionospheric origin plasma and hot plasma sheet electrons with more cold plasma nearer to the ionosphere and more hot plasma at higher altitudes. Focusing on the left side of Figure 33 we show the differential number flux of an example plasma sheet population with  $n = 2.2\text{cm}^{-3}$  and  $T = 105 \text{ eV}$  at various altitudes where point A represents the plasma sheet at  $> 2R_E$  and point D is the ionosphere near 150 km. The plasma sheet distributions are assumed Maxwellian for simplicity and are given as (previously given in Chapter 2) :

$$f(v_{\parallel}, v_{\perp}) = n \left( \frac{em}{2\pi T_{[eV]}} \right)^{3/2} \exp \left\{ -\frac{e(v_{\parallel}^2 + v_{\perp}^2)}{2T_{[eV]}} \right\} \quad (98)$$

where  $T_{[eV]}$  is the characteristic temperature of the distribution in eV,  $n$  is the plasma density in  $\text{m}^{-3}$ ,  $m$  is the mass of the plasma species and  $v_{\perp}, v_{\parallel}$  are the velocity components in velocity space and  $f$  is the distribution function in units  $\text{m}^{-6}\text{s}^3$ . This distribution is assumed to start at point A and map under conservative forces down to lower altitudes via Liouville's theorem. Strictly speaking, Liouville's theorem describes the rate of change of the distribution function in phase space under

the action of conservative forces as being zero, which can be written as

$$\frac{df(\vec{x}, \vec{v})}{dt} = 0 \quad (\text{Conservative Forces}) \quad (99)$$

In the case where collisions are negligible, equation 99 applies, which is generally satisfied for altitudes above 1000 km from the ionosphere. This expression allows us to map the value of the distribution in the magnetosphere to a point in the ionosphere so long as we know how the velocities transform i.e.  $f(v_{\perp M}, v_{\parallel M}) = f(v_{\perp I}, v_{\parallel I})$ . In the case of no parallel potential, the only force considered in this analysis is the mirror force for which the velocity transformation is given by the conservation of the first adiabatic invariant in equation 21 and conservation of energy:

$$\frac{m_e v_{\perp M}^2}{2B_M^2} = \frac{m_e v_{\perp I}^2}{2B_I^2} \quad (100)$$

$$v_{\perp M}^2 + v_{\parallel M}^2 = v_{\perp I}^2 + \quad (101)$$

If we define the ratio of our magnetic fields as  $\tau = B_I/B_M$ , we can write the above expressions for the new velocity components as

$$v_{\perp I} = v_{\perp M} \sqrt{\tau} \quad (102)$$

$$v_{\parallel I} = \sqrt{v_{\parallel M}^2 - \left(1 - \frac{1}{\tau}\right) v_{\perp I}^2} \quad (103)$$

By implementing an arbitrary loss-cone at 100 km we can represent a more realistic distribution along our magnetic field line, as shown on the left side of Figure 33.

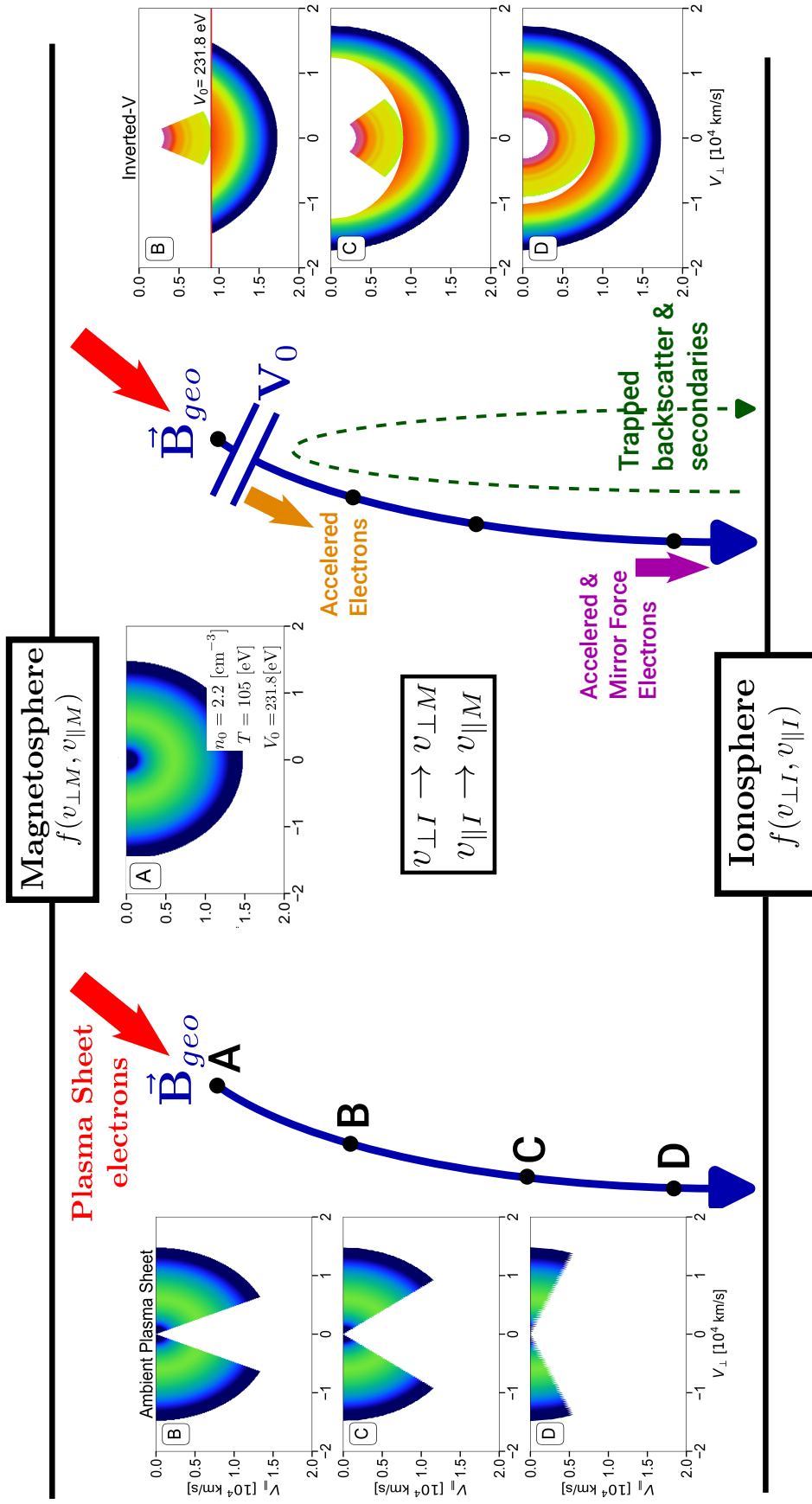


Figure 33. Schematic diagram of the phase space mapping in velocity space of an ambient source of plasma sheet electrons using Liouville's theorem from the magnetosphere to the ionosphere. (Left side) Ambient plasma sheet electrons that diffuse to lower altitudes. A loss cone is added for any particles that reach 100 km to display realism. (Right Side) The same plasma sheet distribution that has a quasi-static parallel potential  $V_0$  which represents an inverted-V. The mirror force acts on both distributions to spread out electrons over pitch angle. See text for details of the mapping. A example distribution of low energy, backscattered/secondary electrons is also added to the inverted-V distribution for realism. These low energy electrons have been mapped from the ionosphere to high altitude and conservatively reflect off the parallel potential (Evans, 1974).

If we now introduce a parallel potential distributed along the field line with total potential  $V_0$  in electron volts we can directly the above analysis. This situation is shown on the right side of Figure 33. First, assume the same Maxwellian distribution impinges upon the top of the parallel potential and we only consider the part of the distribution which has a velocity component towards the ionosphere, essentially half a Maxwellian like before. The distribution that exits the parallel potential (point B on the right side of fig 33) is assumed to be the same half-Maxwellian distribution where all velocity components have been shifted by  $\frac{2V_0}{m_e}$  in parallel velocity space. From this we re-write our previous velocity mappings as

$$v_{\perp I} = v_{\perp M} \sqrt{\tau} \quad (104)$$

$$v_{\parallel I} = \sqrt{v_{\parallel M}^2 + \frac{2V_0}{m_e} - \left(1 - \frac{1}{\tau}\right) v_{\perp I}^2} \quad (105)$$

The movement of electron distributions along a geomagnetic field line constitutes a current, for which the work by Knight, 1973 becomes relevant. Using the (now) accelerated Maxwell distribution

$$f(v_{\parallel}, v_{\perp}) = n \left( \frac{m}{2\pi e T_{[eV]}} \right)^{3/2} \exp \left\{ -\frac{(v_{\parallel}^2 + v_{\perp}^2) + V_0}{2e T_{[eV]}} \right\} \quad (106)$$

the current along a field line can be determined through the integral overall all velocity space between the subtraction of the distributions at their respective altitudes:

$$j_{\parallel} = -e \int v_{\parallel} (f_I - f_M) d^3 v \quad (107)$$

We won't show the details of this integral, and just quote the result:

$$j_{\parallel} = j_{\parallel 0} \tau \left[ 1 - (1 - \tau) \exp \left\{ -\frac{V_0}{T_{[eV]} (\tau - 1)} \right\} \right] \quad (108)$$

where  $j_{\parallel 0}$  corresponds to the result of the same integral applied only to equation 100 for the plasma sheet that can diffuse to the ionosphere. In the limit that the term inside the exponent is small, the

often-quoted linear relationship is derived:

$$j \approx j_0 (1 + V_0/T_{[eV]}) \quad (109)$$

This is called *the knight relation* and offers a simple relationship between the FAC on the field line and the electrostatic potential. We have glossed over the details of the low-energy backscatter/secondary population on the right side of Figure 33, which we'll cover now.

#### 4.4 The Evans Model

(The content of this section comes from Evans, 1974; Kaepller, 2013; Russell et al., 2016)

The success of the model by Evans, 1974 (herein referred to as “Evans Model”) comes from its accuracy and universality in describing the additional lower-energy electrons that accompany inverted-V distributions in the ionosphere. The theory which forms the basis for the model was first developed by Banks et al., 1974 which was uniquely tuned to a 10 keV beam of incoming electrons. The Evans model extends the predictions of the Banks et al., 1974 by re-scaling its results to any incoming electron beam. The remarkable success of the Evans model when compared to *in situ* data is shown in 34, where the solid black line is the predicted curve from the model and the black dots are the directional flux values taken from the Injun-5 measurements as shown in Figure 27. Thus far we have only stated the key concepts of the model without developing the core ideas mathematically. Here we provide a more thorough description of the physics involved in order to rely on these concepts in Chapter 7 and 8.

At its core, the Evans Model describes the expected number of low-energy electrons at various energies below the inverted-V potential due to an incoming beam of high-energy electrons. The model starts by assuming the existence of an anti-parallel electric field along the magnetic field at altitudes above the collisional atmosphere. Electron distributions passing through will acquire  $eV_0$  proportional to the potential drop (called “primaries”) which will interact with the topside

ionosphere. These primaries lose some energy through scattering with ambient neutrals and can be pitch-angle scattered if they are not immediately lost to the atmosphere in this process. These are referred to as “degraded primaries” or “primary backscatter” electrons. Thus degraded primaries constitute a fraction of the incoming electron beam which starts to move back up the field line via the mirror force. When these reach the region of the upward quasi-static potential they necessarily have insufficient energy to overcome the potential drop and reflect back towards the ionosphere. Degraded primaries have energies just below/near the inverted-V potential and emanate isotropically from the ionosphere throughout an inverted-V. In addition to degraded primaries, lower energy particles called “secondaries” are a new source of electrons produced through ionization of

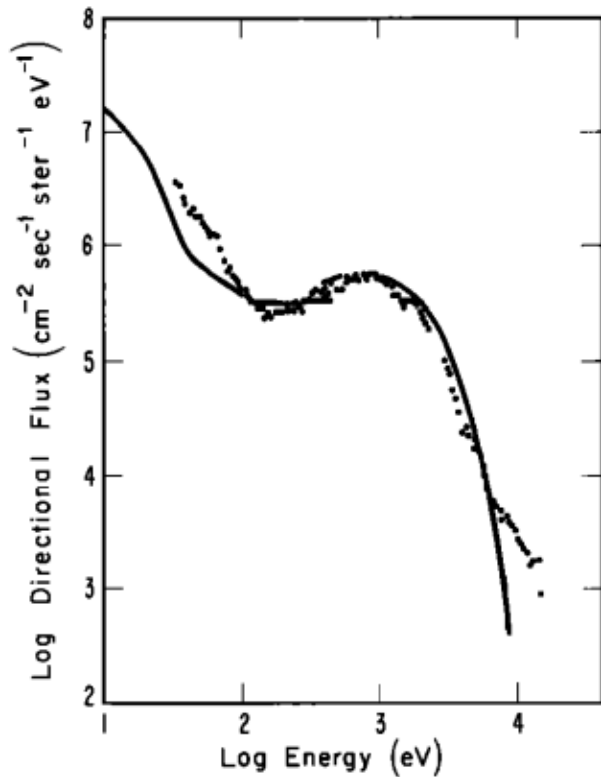


Figure 34. From Evans, 1974. Black line is a model electron energy spectrum by assuming 400V potential difference and a Maxwellian of temperature 800 eV. The dotted line is an electron spectrum observed by Injun-5 satellite from Frank et al., 1971. Good agreement between the bump near  $\log(E) = 3$  and the model suggests the accelerated Maxwellian picture of an Inverted-V is a good approximation. The Evans model gives the predicted values for low energy backscatter/degraded primaries which has fair agreement to this figure. The deviation at the highest energies may be due to the non-Maxwellian aspects of the underlying distribution.

neutral particle. Every time a source of energetic electrons strike the atmosphere a combination of degraded primaries and secondaries is produced isotropically which become trapped between their lower mirror point and upward parallel potential. In Figure 35 we show the mechanics of this process. Step (1) shows the initial beam of electrons accelerated from the inverted-V which are assumed to come from a magnetospheric Maxwellian distribution. The pitch angles of the initial distribution have an altered post-accelerated pitch angle given by

$$\alpha_m = \sin^{-1} [E/(E + V_0)]^{1/2} \quad (110)$$

where  $\alpha_m$  is the half-angle, E is the original energy of the electron before acceleration and  $V_0$  is the accelerating potential. This describes the width of exiting cone from the U-shaped potential. In step (2) of Figure 35 the distribution widens in pitch angle due to the magnetic mirror force and strikes the ionosphere. In order to discuss the response of the ionosphere in Step (3) we must introduce the universal backscatter curves presented by Evans, 1974 and some definitions. The plasma distribution function  $f(v_\perp, v_\parallel)$  can be related to the *differential number flux*  $j_N$  through the conversion:

$$j_N(E, \alpha) = \frac{2E}{m^2} f(v_\perp, v_\parallel) \quad (\text{Differential Number Flux}) \quad (111)$$

where E is energy, m is electron mass and the differential flux for a given energy and pitch angle is in units of [(# of electrons)  $m^{-2}s^{-1}str^{-1}eV^{-1}$ ]. The differential number flux describes the number of electrons passing through an imaginary surface per surface area per second per steradian angle per unit of energy. The *Differential Omni-Directional Number Flux* is needed for the model and is given:

$$\Phi(E) = \int j_N(E, \alpha) d\Omega \quad (112)$$

in units of [ $cm^{-2}s^{-1}eV^{-1}$ ] which gives the total flux passing through a unit sphere

The Evans model uses the flux in equation 112 striking the ionosphere with the “Universal” response curves to quantify the production of ionospheric degraded primaries/secondaries. In Figure 36 we show the functions given by Evans, 1974 which describe the flux of degraded primaries

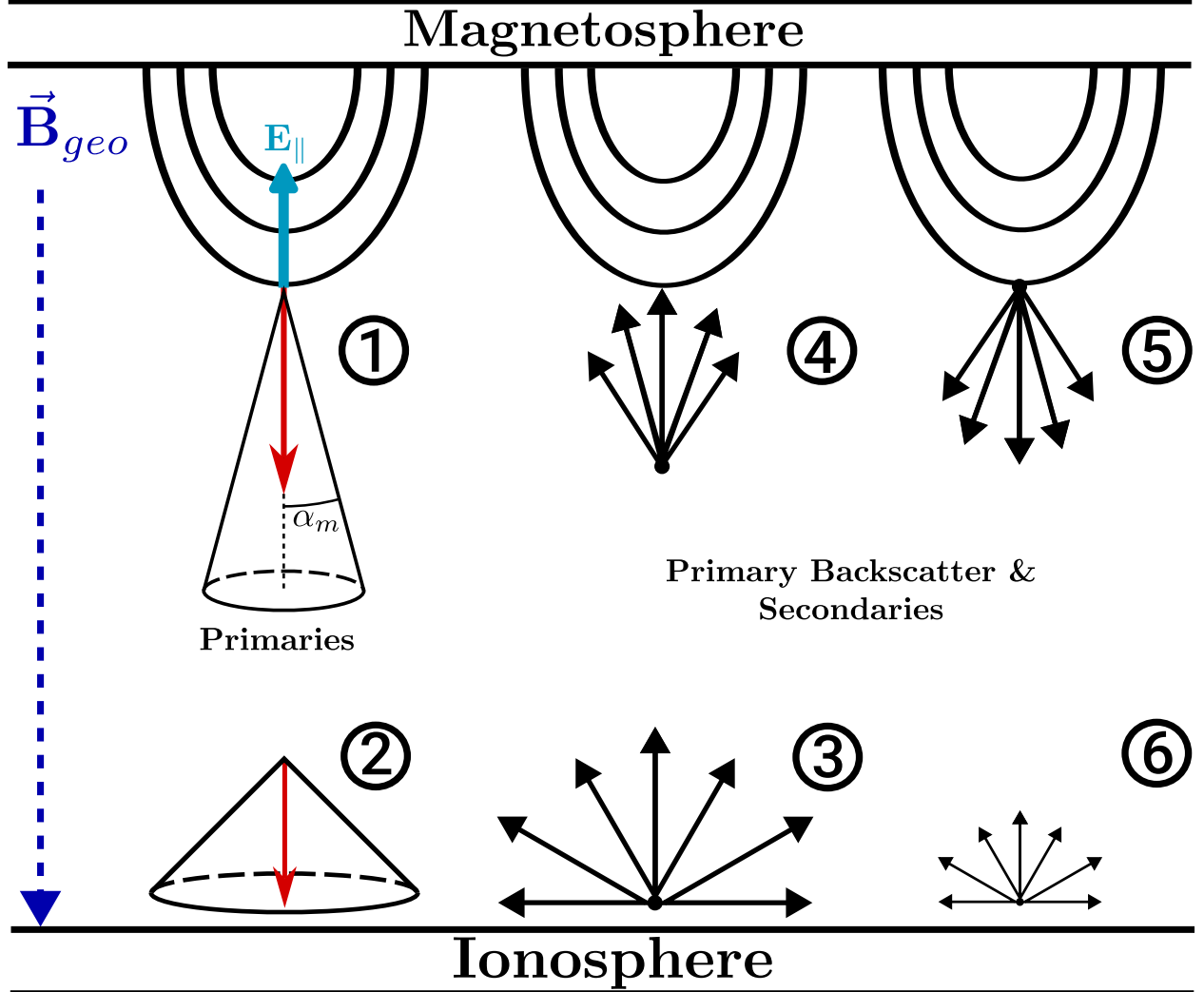


Figure 35. Example of the Evans Model procedure. Step (1) is to determine the incoming beam accelerated by the parallel potential. Step (2) is the spread of the incoming distribution due to the mirror force. The omni-directional differential number flux  $\Phi(E)$  is determined as an estimate of the incoming flux into the ionosphere. (3) The ionospheric response of degraded primaries and secondary electrons are produced isotropically and upward from the ionosphere. (4) The backscatter/secondary electrons mirror back up to the parallel potential. (5) The mirrored backscatter population is reflected by the parallel potential and descend to the ionosphere. (6) The higher-energy degraded primaries repeat the whole processes again, but with lower incoming energy . Secondary electrons are too lower energy to produce additional backscatter but they can produce more secondaries at even lower energies. The whole processes constitutes a "bounce" and the model repeats until an equilibrium is reached.

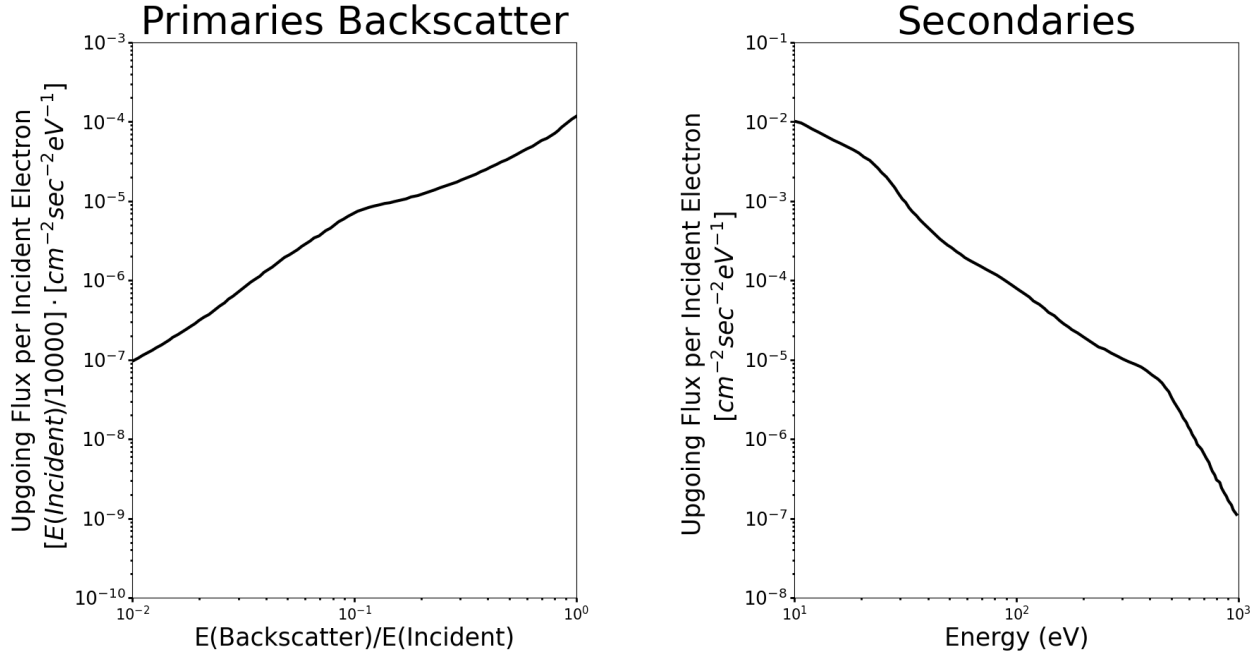


Figure 36. From Evans, 1974. (Left) “Universal” degraded primary electron backscatter curve. The abscissa is backscatter electron energy normalized to the incident electron energy and ordinate is in units of differential omni-directional number flux normalized by 10000/E(incident). (Right) “Universal” secondary electron backscatter curve

(left) created for incoming electrons and the flux of secondary electrons (right) also produced. The curves are used to describe the amount of isotropic up-going omni-directional differential number flux is produced for incoming electrons. The degraded primary curve depends upon the energy of the incident electrons, hence its x-axis is scaled by the incident energy as well as its y-axis. However, the secondary electrons produced are so low-energy that they do not generate additional electrons every “bounce” between the electrostatic potential, thus this curve only cares about the incoming flux of electrons at a particular energy.

To use these curves, the incident omni-directional differential number flux (equation 112) is first calculated giving  $\Phi(E)$ . Next, the upward directed flux produced from the incident beam  $\Phi_{up}$  is determined by integrating over the secondary and degraded primary/backscatter response curves via

$$\Phi_{up}(E) = \int [B(E, E') + S(E, E')] \Phi_{beam}(E') dE' \quad (113)$$

where  $E'$  is the energy grid corresponding to the differential number flux of the primary beam,

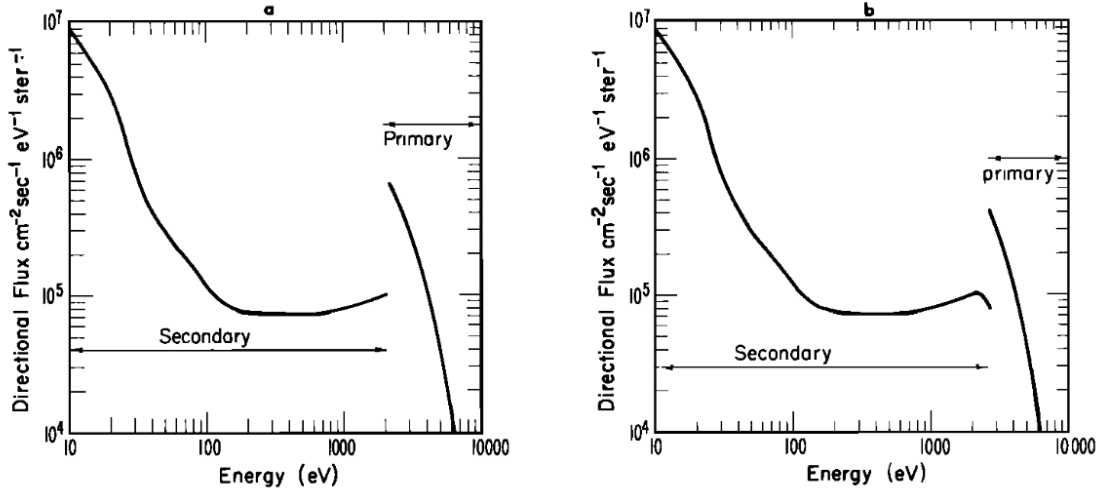


Figure 37. From Evans, 1974. Example of the Evans model applied to a Maxwellian distribution (left)  $0^\circ$  and (right)  $45^\circ$  with 800 eV temperature for a distribution 2000 km above the atmosphere. Excellent agreement between the general shape of this distribution and the example data we provided in Figure 28 can be seen.

$B(E,E')$  and  $S(E,E')$  are the backscatter and secondary response curves. The upward flux is also omni-directional differential number flux in units of  $[cm^{-2}s^{-1}eV^{-1}]$  and assumed isotropic. Step (3) of Figure 35 is determining the ionospheric  $\Phi_{up}(E)$  from the first iteration. This up-going population will mirror until the parallel potential is reached and be reflect back down to the ionosphere to repeat the process again in step (4), (5) and (6) except with lower incident flux and energies. The higher-energy degraded primaries can create both additional backscatter/degraded primaries as well as secondaries on each bounce. Secondary electrons are too lower energy to produce additional backscatter but they can produce more secondaries at even lower energies.

As a final demonstration, we show the energy spectrum from Evans, 1974 for a modelled  $0^\circ$  and  $45^\circ$  pitch angle precipitating distribution above the atmosphere in Figure 37. The electron source distribution was assumed to be a 800-eV plasma accelerated through a 2000V potential drop located at 2000 km. The essential shape is the same as shown in the example data from Figure 28, minus the discontinuity between the inverted-V and start of the secondary/backscatter emission for which Evans, 1974 noted is smoothed in actual measurement due to the energy bins of the detector.

## 4.5 Electron Acceleration through Alfvén Waves Simplified (C. A. Kletzing, 1994)

Central to the ideas of this thesis are the concepts of *wave-particle* acceleration along Earth's geomagnetic field at high latitude. The solar-terrestrial processes that accelerate particles into the ionosphere also excite plasma waves in the environments of the aurora in great abundance which can pick up particles and accelerate them to low altitudes. This occurs due to the parallel electric fields from the Alfvén waves which were presented in Chapter 2.8. These unlock new possibilities for acceleration mechanisms in Earth's space environment. In this section we will cover the fundamental concepts of the Alfvén wave-particle resonance under idealized conditions and show how these highly non-linear processes motivate the need for simulation work to accurately describe them.

The seminal work by C. A. Kletzing, 1994 offered a tangible and easy-to-digest model for the acceleration of electrons for dispersive Alfvén waves. The model starts by assuming all wave and environmental parameters held constant. The wave then propagates through a homogeneous distribution of electrons distributed over a magnetic field line. For the example given by C. A. Kletzing, 1994, they used the Inertial Alfvén Waves (IAW) the phase velocity in the low-frequency, low ion Larmor radius limit

$$\frac{\omega}{k_{\parallel}} = \frac{V_A}{\sqrt{1 + k_{\perp}^2 c^2 / \omega_{pe}^2}} \quad (114)$$

for MHD Alfvén velocity  $V_A = B / \sqrt{\mu_0 \rho_m}$ , for ion mass density  $\rho_m = \sum n_i m_i$ , speed of light  $c$ , perpendicular scale length  $k_{\perp} = 2\pi/\lambda_{\perp}$  and electron plasma frequency  $\omega_{pe} = \sqrt{n e^2 / \epsilon_0 m_e}$ . The corresponding electric field parallel to the propagation of the wave is:

$$E_{\parallel} = \frac{k_{\parallel}}{k_{\perp}} \frac{(k_{\perp} \lambda_e)^2}{1 + (k_{\perp} \lambda_e)^2} E_{\perp} \quad (115)$$

for parallel scale length  $k_{\parallel} = 2\pi/\lambda_{\parallel}$  and perpendicular electric field wave amplitude  $E_{\perp}$ . In our idealized case, the parameters  $\lambda_{\perp}, \lambda_{\parallel}, n, B, \rho_m$  are fixed while the wave perturbation fields  $E_{\perp}, B_{\perp}$  are considered plane waves  $E_{\perp}, B_{\perp} \propto \sin(kx + \omega t)$ . Based on this, the wave travels at a constant

velocity with sinusoidal parallel electric field  $E_{\parallel}$  that has an amplitude modified by the wave terms in equation 115.

Already, the complexity of imagining the oscillations in the  $E_{\perp}, B_{\perp}$  directions as well as the shape of  $E_{\parallel}$  can be challenging. Additionally, we must now introduce the parallel wave potential  $\Phi_w$ . Because the perpendicular  $E_{\perp}, B_{\perp}$  components do not directly contribute to the resonance process, we will drop them in our illustrations of  $\vec{E}_{\parallel}$ , but we remind the reader to always keep them in mind. To explain wave-particle resonance, there are two important perspectives to take: (1) the frame of reference moving with the wave  $V_A$  and (2) the laboratory frame where measurements are generally taken. We show the wave frame in Figure 38 along with the process of wave-particle acceleration and deceleration. The axes are unit-less for y-axis and spatial altitude for x-axis. The amplitude of a bipolar  $E_{\parallel}$  is drawn along with an associated wave potential derived from

$$\Phi_w = - \int \vec{E} \cdot d\vec{r} \quad (116)$$

which contains a peak in the wave potential  $\Phi_{max}$  where the electric field switch directions. For electrons with parallel velocities slower than  $V_A$ , the wave catches up and these particles start to see an accelerating wave potential (left side of Figure 38). In the wave-frame (primed), the velocity of the electron can be related to the laboratory frame (unprimed) via

$$v'_e = v_e - V_A \quad (117)$$

From here, two possibilities can occur, either (a) the electron wave-frame velocity is too larger because  $v_e \ll V_A$  and the wave will simply passes over the electron, causing it to briefly accelerate and then decelerate, resulting in no energization or (b) the wave-frame velocity is less than or equal to the peak wave potential:

$$v'_e \leq \sqrt{2e\Phi_{max}/m_e} \quad (118)$$

In this case, the electron is picked up by the wave because it is moving just fast enough to not

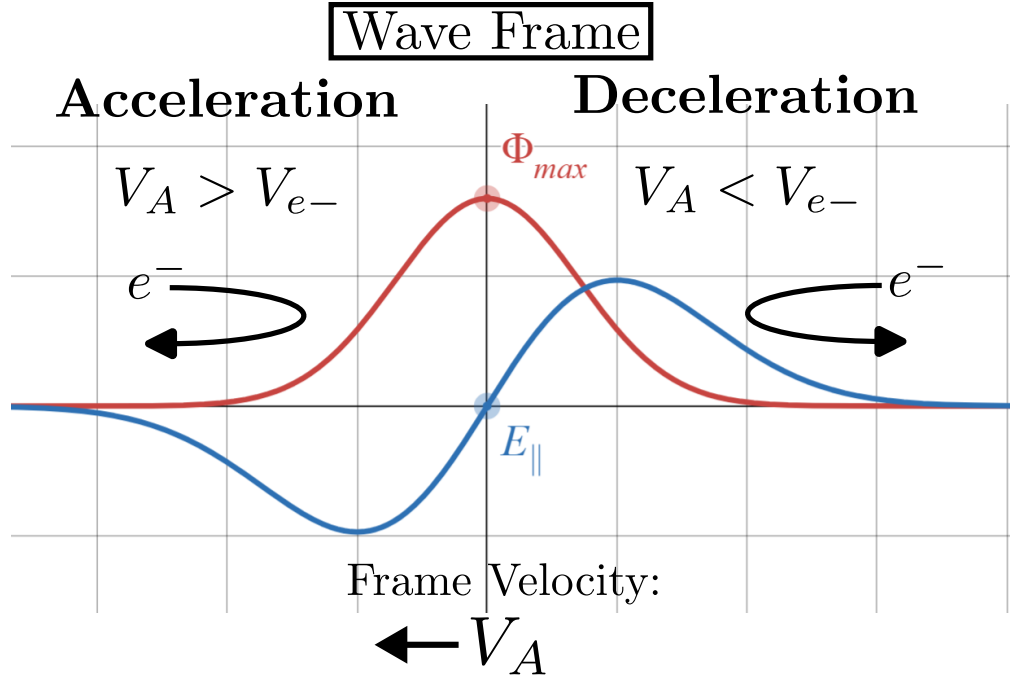


Figure 38. The amplitude function for a  $E_{\parallel}$  of an Alfvén wave pulse with symmetric bipolar electric fields moving left. The velocities of the wave and directions of the electrons are shown. For electrons in front of the wave that are slower than  $V_A$  they see an accelerating electric field that accelerates them to  $V_A$ . For electrons with speed greater than the wave but encounter it from behind, they see a decelerating  $E_{\parallel}$  which causes them to lose energy and give it to the wave, which reduces their velocity also to  $V_A$ .

overcome the peak wave potential. In the wave frame, the electron is reflected out the front of the wave with a new velocity equal to its wave-frame velocity:  $v_{reflected} = +|v'_e|$ . This process is called a “Fermi-bounce”. What this looks like in the laboratory frame is that the electron gets accelerated up to  $V_A$  plus the magnitude of the difference between the initial velocity of the electron in the laboratory frame and  $V_A$ :

$$v_e = V_A + |V_A - v_e| = 2V_A - v_e \quad (119)$$

Finally, the change in kinetic energy of the electron in the laboratory frame can be calculated:

$$\Delta KE = KE_f - KE_0 = \frac{1}{2}m_e(2V_A - v_e)^2 - \frac{1}{2}m_e v_e^2 = m_e V_A (2V_A - v_e) \quad (120)$$

As the wave passes through more electron distributions, a portion of these distributions are snipped

off for all electron velocities which fall within the *accelerating resonance band*:

$$\frac{\omega}{k_{\parallel}} - \sqrt{2e\Phi_{max}/m_e} < v_{e,\parallel} < \frac{\omega}{k_{\parallel}} \quad (121)$$

for local Alfvén velocity  $V_A$ . The process is identical in the case of deceleration, except now the electrons must not be too fast otherwise they will pass through the bipolar field without any energy gain/loss. The full *resonance condition* for Alfvén waves with parallel electric fields can be given as

$$\frac{\omega}{k_{\parallel}} - \sqrt{2e\Phi_{max}/m_e} < v_{e,\parallel} < \frac{\omega}{k_{\parallel}} + \sqrt{2e\Phi_{max}/m_e} \quad (122)$$

or just

$$|V_A - v_e| < \sqrt{2e\Phi_{max}/m_e} \quad (123)$$

A figure that helps to visualize this process in the wave-frame vs Lab frame is given in Figure 39. By using these we can estimate the maximum possible kinetic energy gain for a wave-particle resonance via equation 122:

$$\Delta KE_{max} = \frac{m_e}{2} V_A^2 + m V_A \sqrt{2e\Phi_{max}/m} + e\Phi_{max} \quad (124)$$

The beauty of this description is how the entire process is just electrostatic acceleration, albeit in a moving reference frame. These illustrations presented here do a good job of representing the fundamental processes. However, the assumptions of constant wave/environmental parameters on our accelerating waves are virtually never physically realized. This is because the geomagnetic field  $\vec{B}_{geo}$  changes over altitude, as does every other wave parameter with the exception of wave frequency. Since these parameters themselves are non-linear this makes the phase velocity in equation 114 highly non-linear and solutions to the wave-particle resonance over altitude non-analytic. This motivates numerical solutions.

To account for this non-analytic solution, C. A. Kletzing, 1994 presented a numerical simulation of the resonance process in a homogeneous electron plasma with parameters described in

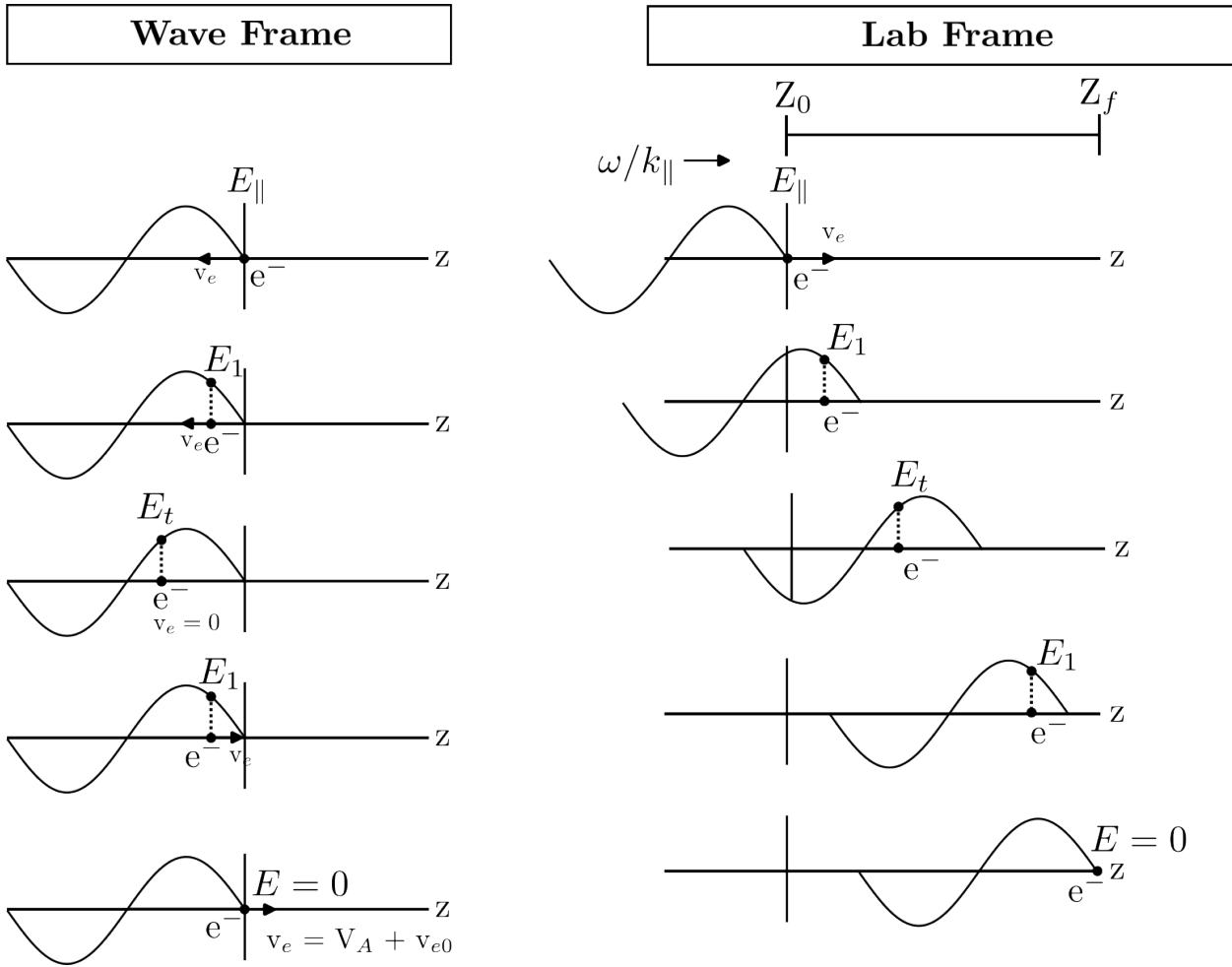


Figure 39. Illustrative diagram that shows how an ideal Alfvén wave with a sinusoidal  $E_{\parallel}$  can accelerate an electron. (left) In the wave-frame the electron reflects off the wave and returns the way it came with the same velocity. (right) In the laboratory frame the electron is accelerated to the Alfvén velocity and then accelerated more to a value that corresponds to the difference between the initial electron velocity and  $V_A$  so that it exits the wave with velocity  $2V_A - v_e$ . Here  $E_t$  is the electric field value where the particle turns around and  $E_1$  is some value of  $E_{\parallel}$  at an intermediary step.

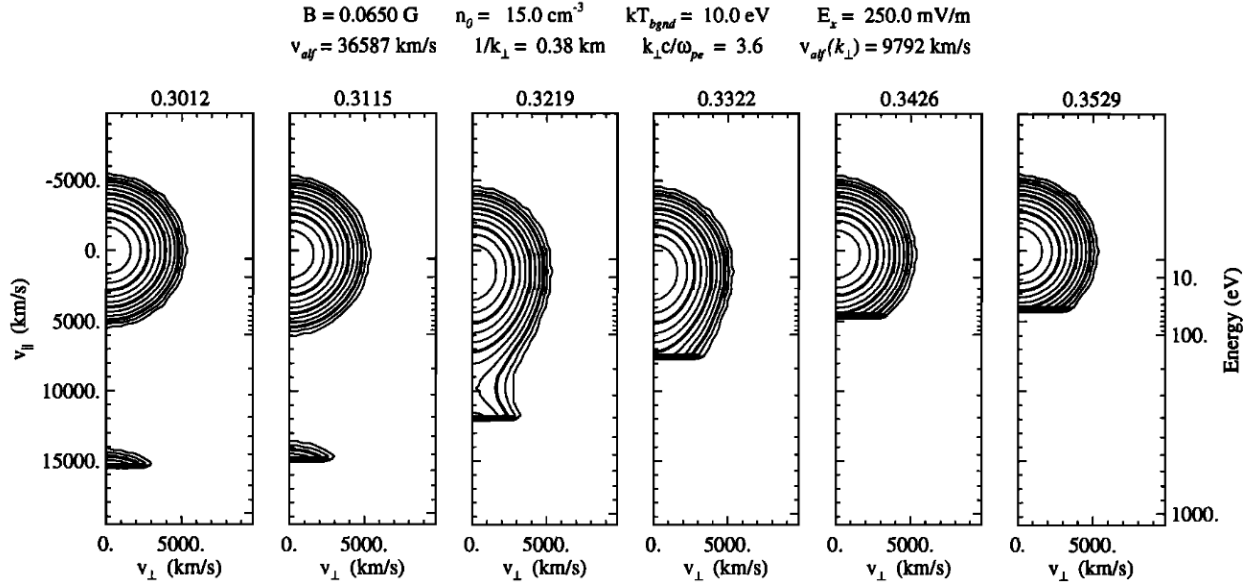


Figure 40. From C. A. Kletzing, 1994 Evolution of a distribution for a pulse of Alfvén waves that resonantly accelerate a portion of the distribution. See text for details.

Figure 40. Here, the phase velocity is allowed to change but not  $k_{\perp}$ . This alters  $V_A$  in the resonance condition in equation 122. The panels here show a fixed altitude as various distributions that interacted with the wave pass by. The first panel in Figure 40 shows the unaccelerated distribution as well as the beginning of a high-energy burst of electrons. The successive panels shown different snippets in time where the high-energy burst decreases in energy. Eventually, the distributions which had portions “snipped-off” due to resonance arrive in the final panels without portions of their distribution which correspond to the electrons lost due to resonance. A key observation from C. A. Kletzing, 1994 is that accelerated electrons necessarily outrun the wave and arrive ahead of the pulse while decelerated electrons can either arrive with the wave or behind it. In the next section we will explore these electron bursts in more detail and explore the most germane numerical models that have been performed to replicate them.

## 4.6 Suprathermal Electron Bursts (STEBs): History and Simulation

In practice, the concepts of idealized wave-particle acceleration and deceleration from the previous section do apply to the auroral environment, however the identification of this process in spacecraft data greatly depends upon the altitude of observation as well as the time/energy resolution of the instrumentation. Some of the first *in situ* measurements of this process occurred in the 1970s, which were described in satellite data as “Fast and irregular Flux time-varying fluctuations at energies below the monoenergetic peak” (Lin et al., 1979) and “localized strongly field-aligned fluxes observed at energies below the inverted-V peak that result from thermal electrons [at the altitudes of the quasi-static acceleration]” (Burch et al., 1979). The work by Johnstone et al., 1982 on the ISIS 2 satellite used the term “Suprathermal Electron Burst” (STEB) to describe an “increase in intensity of suprathermal electrons ( $E < 500$  eV) by more than an order of magnitude with a duration of a few seconds, an angular distribution that is field-aligned over a wide energy range, and an increase in the intensity at all pitch angles”. The “bursts” were considered irregular features that occurred nearby any type of aurora. Throughout the 1980s as the temporal resolution and sampling speeds of electron detectors improved, these STEBs began to commonly appear in spacecraft data with approximately similar forms, all displaying some form of time dispersion to lower energies, field-aligned nature and proximity to auroral arcs (Arnoldy et al., 1985; McFadden et al., 1986a, 1986b; McFadden et al., 1987; Robinson et al., 1989). In Figure 41 we show data of the STEBs observed by sounding rockets which estimated the bursts to have latitudinal space scales on the order of kilometers in the ionosphere. Figure 42 shows high resolution observations at the edge of a discrete auroral arc through a STEB, showing the time evolution of the burst in velocity space as it decays to lower energies over a distance of 2.3 km.

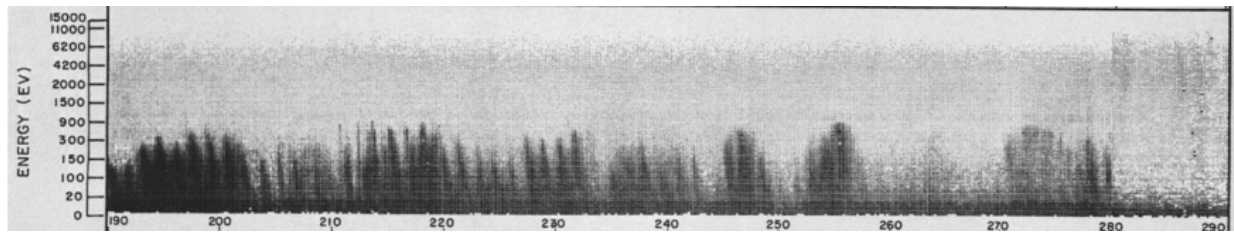


Figure 41. From Arnoldy et al., 1985. Electron energy vs. time spectrogram of STEBs from sounding rockets between two auroral arcs showing a time-dispersed, electron signature decaying to lower energies. Individual bursts exist  $\sim 1$  sec and typically exist in the most field-aligned pitch bins.

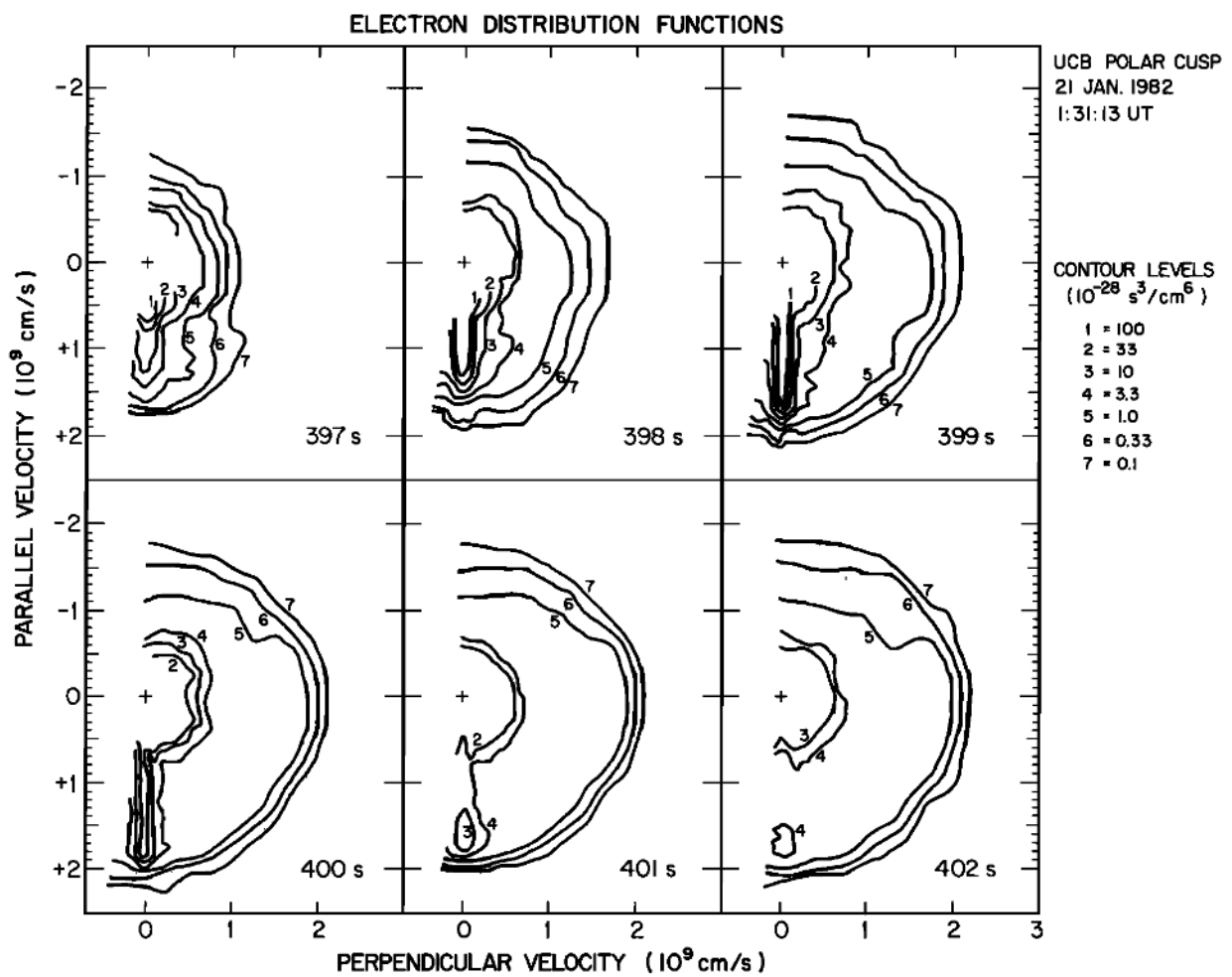


Figure 42. From McFadden et al., 1986a. Sounding rocket data showing the evolution of a STEB in time, taken from the edge of an auroral arc displayed and in velocity space. The highest energy electrons in the burst is strongly field aligned.

The 1990s saw continued advancements in instrumentation as well as breakthroughs in the connection between STEB electrons and Alfvén Waves. Based on the STEB observations of the previous decades and the theoretical developments in kinetic Alfvén Waves with electric fields parallel to background geomagnetic fields (Goertz et al., 1979a; Hasegawa, 1976; Lysak et al., 1996; Stasiewicz et al., 2000; Stéfant, 1970), C. A. Kletzing, 1994 posited one of the first models predicting electron dispersions behaving similar to STEB electrons. This model was covered in detail in Chapter 4.5 and presented, clearly and concisely, the fundamental mechanisms required for electron acceleration through inertial Alfvén waves to produce STEBs. Throughout this period, spacecraft missions continued to characterize the behavior of STEBs as we have described (Arnoldy et al., 1999; Ivchenko et al., 1999; C. A. Kletzing et al., 1994; Lynch et al., 1999; Nagatsuma et al., 1996), however in 1996 the launch of the Fast Auroral SnapshotT Explorer (FAST) satellite which produced some of the most detailed, high-resolution and scientifically successful studies. This was due to FAST's scientific dedication solely to the study of auroral phenomena between 350 km to 35000 km at temporal resolutions almost two orders of magnitude faster than previous missions, allowing for ultra-high speed “snapshots” of electron distributions and electric/magnetic fields. Through the FAST dataset, many properties of STEB were confirmed but the high resolution datasets allowed for a rich history of simulation work that solidified dispersive Alfvén waves with parallel electric fields as one of the dominant explanation for STEB electron dispersions. Notably, FAST data allowed several theoretical ideas to be tested and simulated such as the Ionospheric Alfvén Resonator (Lysak, 1991) and Ionospheric Feedback Instability (Atkinson, 1970). While these two theories are useful in the study of Alfvén waves at the Ionosphere, they played no part in the work for this dissertation and will not be discussed further.

Here we will discuss some of the foundational observations and simulation work in the study of STEBs and Alfvén waves that occurred near the turn of the century. In Figure 43 we show a panel of FAST data from Chaston, Bonnell, Carlson, McFadden, Ergun, et al., 2003 which displays some of the highest time-resolved view of STEBs that was available. The top panels show the component-pair electric and magnetic field data displaying evidence of a low-frequency Alfvén

burst that's coincident with STEB electron and inverted-V precipitation (bottom panels). The view of STEBs in Figure 43 is virtually identical to how they are still observed today more than twenty years later (as of this writing), an indication of the quality of the dataset. The statistical study on FAST data by Chaston et al., 2007 confirmed connection between STEB particles and auroal arcs and showed a preference for their creation to the noon and midnight MLT sectors, in agreement with a magnetic reconnection interpretation as the source of the Alfvén waves themselves (figure 44). In particular, this study showed how dispersive Alfvén waves provided a significant, but not dominant, means for electron acceleration to form aurora with a greater contribution during geomagnetic active times rather than quiet times. Some of the earliest simulation work was successful in replicating the results of spacecraft by using the full form of the non-linear wave-particle resonance process. In Figure 45 we show in the top panel the STEBs formed beneath a 10 keV aurora seen by the PHAZE-II sounding rocket in Arnoldy et al., 1999 while in the bottom panel we show the dispersive Alfvén wave simulation by L.-J. Chen et al., 2005a that successfully replicated the data's fundamental features.

These simulations proved useful in understanding how STEB behavior changed based upon the accelerating wave parameters. Figure 46 shows three Figures from Tanaka et al., 2005 that detail the response of a plasma along Cusp field lines to variations in the accelerating wave frequency, perpendicular scale or wave amplitude. Similar simulation work around this time period was successful in using the dispersive Alfvén wave to investigate STEBs formed in the dayside and nightside aurora, the cusp as well as explaining the smaller features such as the lack of electrons which follows STEBs, their often-seen repetition time and the oscillations in the cold-core of the plasma to the wave (Andersson et al., 2002; Chaston, Bonnell, Carlson, Berthomier, et al., 2002; L.-J. Chen et al., 2005b; C. A. Kletzing et al., 2001; Su et al., 2004; Watt et al., 2005, 2006). These studies served to complete the picture of STEB electrons: They are resonantly accelerated particles that come from Alfvén waves that are produced through magnetic reconnection largely near the noon or midnight MLT sectors.

After the significant advances in the early 2000s, work on the Alfvén wave-particle acceler-

ation refocused its efforts from trying to explain the origin of STEBs to other larger-scale features or characteristic oddities. Alfvénic aurora are a optical feature where the aurora is formed entirely of STEB electrons without any discrete arcs. This was the focus of the CASCADES-II sounding rocket by Lynch et al., 2012 combined *in situ* data with allsky imagers to show a clear connection between the latitudes of the Alfvénic Aurora and the poleward boundary intensification region. This region is a set of latitudes which map directly to the most recent reconnection events in the magnetotail (Lyons, 1999). The “rayed curtain” of Alfvénic aurora they observed moved at 8.5 km/s along-arc with a 8 Hz periodicity. Similar results were reported by the e-POP instrument on the CASSIOPE satellite by Wu et al., 2021. In particular, Wu et al., 2021 observed some of the first instances of “inverse dispersion” where the lowest energy STEB particles are observed before the highest energies. The authors proposed the explanation for this was that the position of the satellite was too close to the acceleration region for the high energy electrons to overtake the low energies and reproduce the typical STEBs seen at rocket altitudes. The work by Cameron et al., 2016 showed how not all time-dispersed electrons correlate to suprathermal bursts accelerated by Alfvén waves. A sudden movement of a quasi-static inverted-V potential could inject new electrons in the acceleration region at different altitudes and thereby accelerate them to different energies. This is called an “edge-type” dispersion, which we show in Figure 6. Optically, STEBs have been invoked to explain the smaller scale ( $< 10$  km) features seen in auroral rays and Alfvénic aurora that vary much more quickly in time than the larger scale inverted-V signatures associated with quasi-static potential drops (Liang et al., 2019; Lynch et al., 2012).

Today, the connection between dispersed electron signatures and Alfvén waves is placed upon firm theoretical, numerical and observational grounds. Their origin and source mechanisms are largely established in numerical environments and observation. Open questions still exist as to the role STEBs play in Joule Heating of the Ionosphere. Indeed, the focus of this dissertation is to characterize the impact that the resonant source population of electrons for Alfvén wave acceleration has on the resultant STEB peak energy and differential number flux. This will be the focus of Chapters 7.2 and 8.

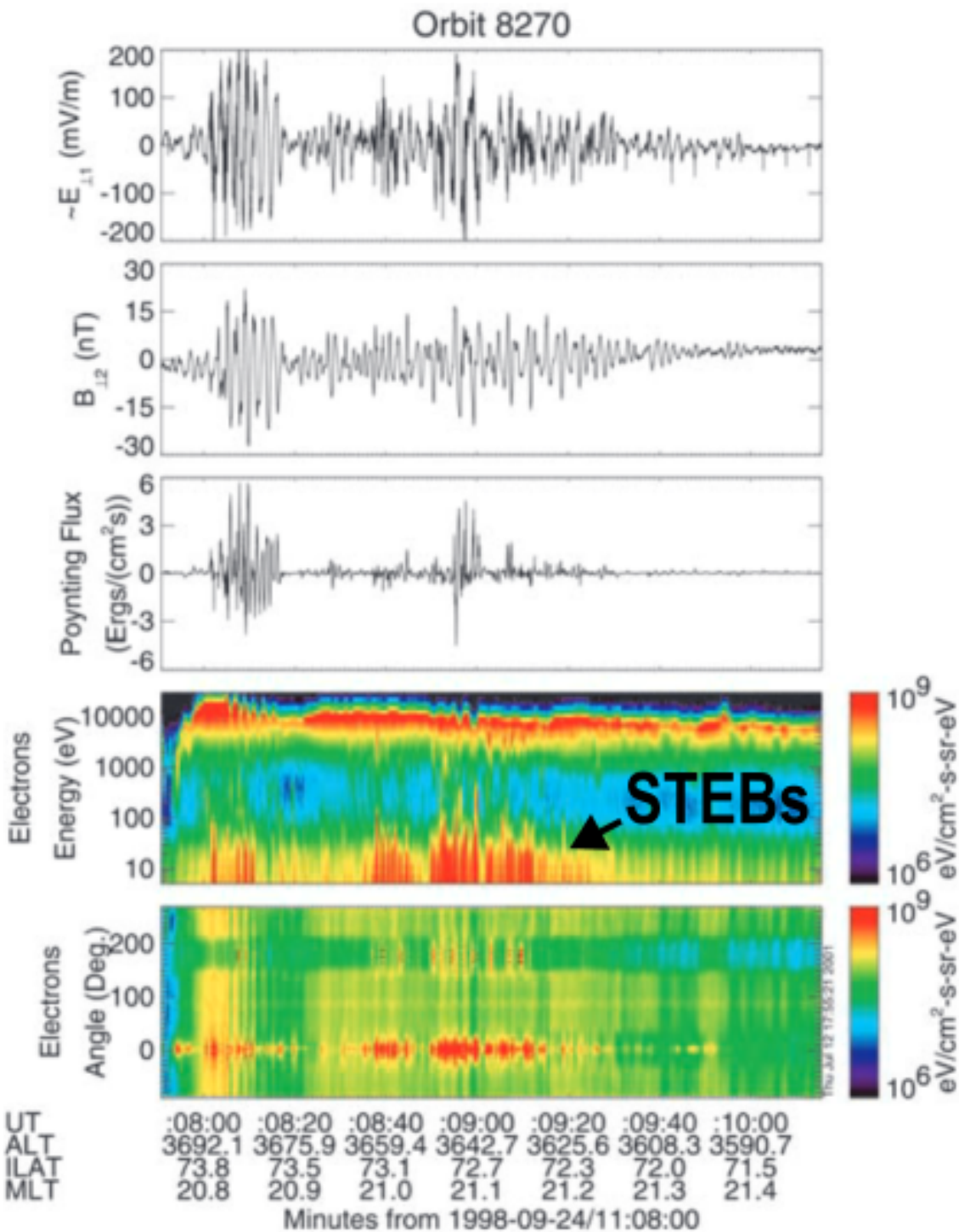


Figure 43. From Chaston, Bonnell, Carlson, McFadden, Ergun, et al., 2003. FAST data that contains electric and magnetic observation of Alfvén waves (top panels) coincident with inverted-V and STEB electrons (bottom panels). Similar to studies from previous decades, FAST reports STEB electrons as field aligned and showing energy-time dispersion within a few kilometers. However, the significant improvement of temporal resolution of the dataset provided the best picture of STEB electrons at the time.

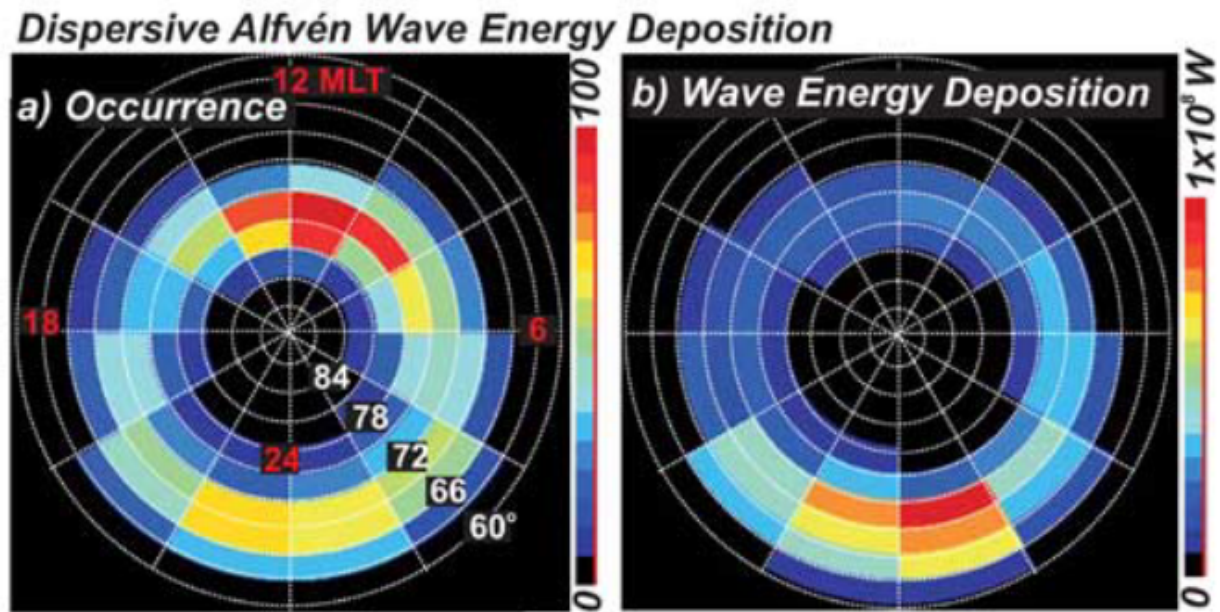


Figure 44. From Chaston et al., 2007. (a) Topdown view of Earth's Polar regions of the occurrence of STEBs with dispersive Alfvén waves normalized by number of FAST traversals. (b) distribution of average dispersive Alfvén wave energy from integrated Poynting flux over the area of each grid segment.

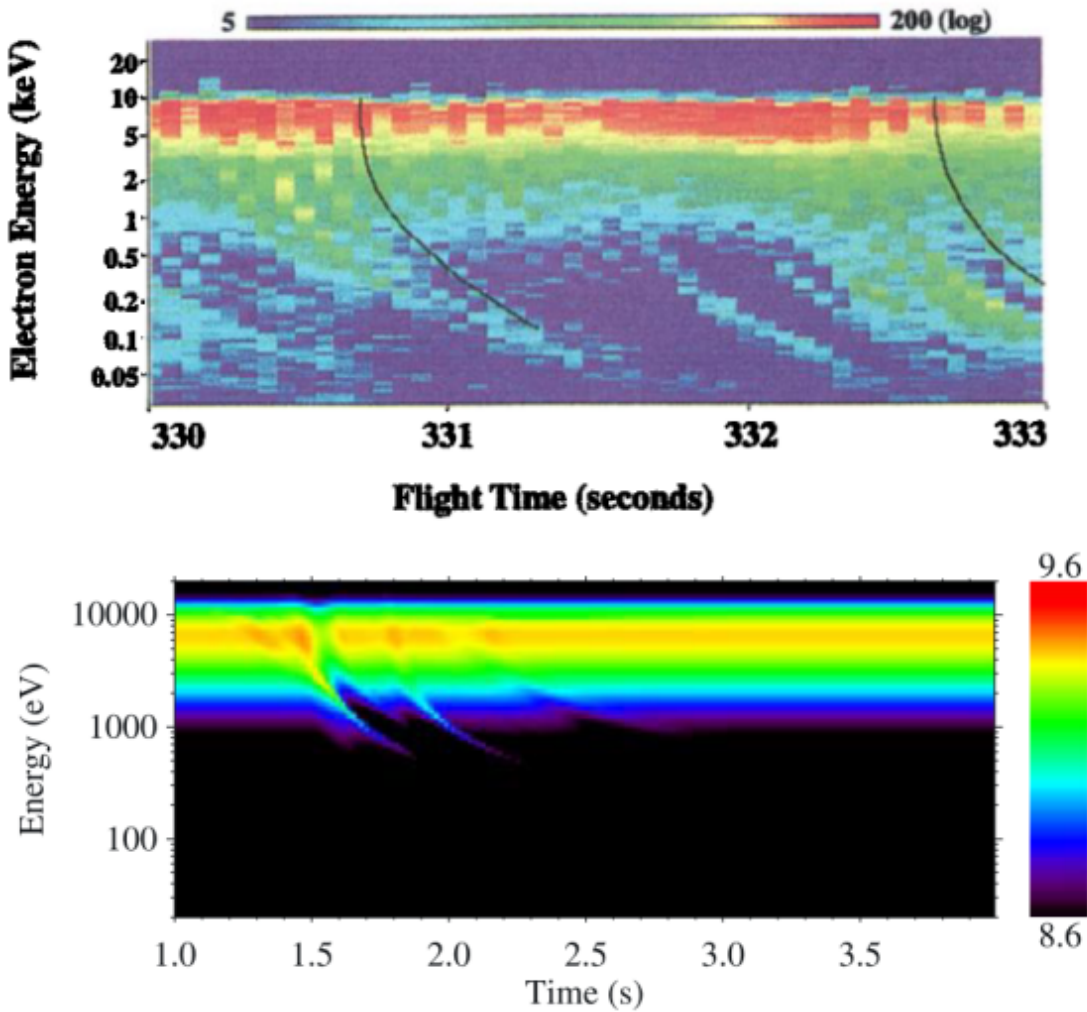


Figure 45. (Top) From Arnoldy et al., 1999. Electron dispersion's below an inverted-V of a few keV measured by PHAZE-II sounding rocket. Dispersion tails extend to 50 eV while some end at keV. The time to disperse is about 0.6s. An inverted-V center at 10 keV is seen. (Bottom) From L.-J. Chen et al., 2005a. Two simulated electron dispersions generated from two dispersive Alfvén waves launched at  $4R_E$  using an auroral latitude plasma environment. Additional high-energy primary backscatter was added to achieve good agreement with the PHAZE-II data.

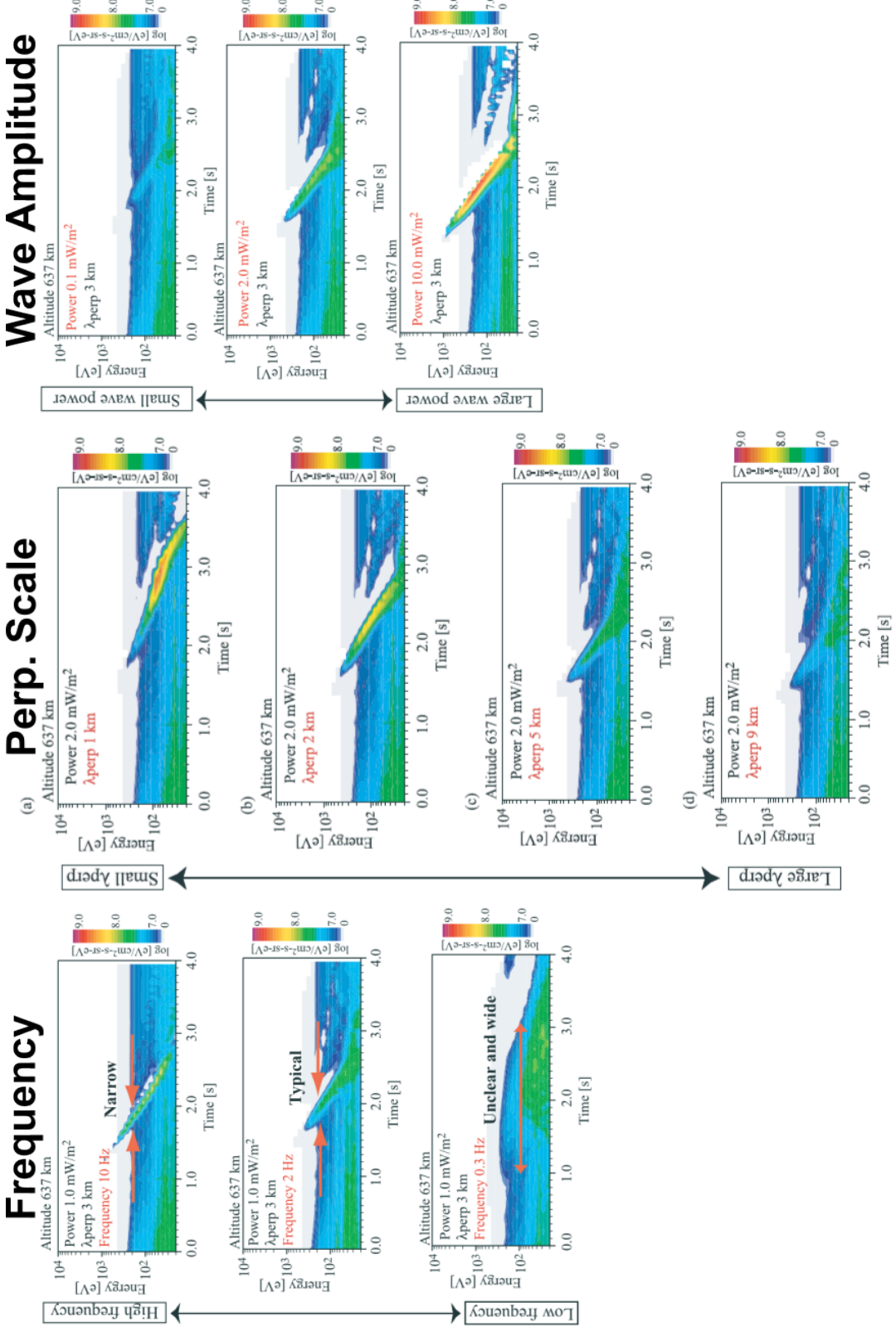


Figure 46. From Tanaka et al., 2005. Plots of the effect of varying accelerating wave frequency, perpendicular scale and wave amplitude in a STEB numerical simulation. Waves start at 10,000 km in the Cusp region and interact with ambient plasma at lower altitudes throughout. The STEB exhibit different peak energy and differential number flux intensity depending upon the value of the wave amplitude or perpendicular scale length. The wave frequency generally serves to widen the time-width of any particular energy channel, without meaningfully affecting STEB intensity or peak energy.

## CHAPTER 5: INSTRUMENTATION

In this section, we discuss the ACES-II Sounding rocket mission, which is the primary source of experimental data for this thesis. We will cover the specific instrumentation used and how the data products were processed/calibrated. Specifically, we will discuss the high-energy electrostatic analyzers, electric and magnetic fields, Langmuir probes and any supporting data from external sources (AllSky imagers, Incoherent Scatter Radar).

### 5.1 ACES-II Sounding Rocket Mission

The Aurora Current and Electrodynamics Structures II (ACES-II) mission successfully launched two payloads 100 seconds apart from Andøya, Norway on Nov.20th, 2022 into a northward post-dusk discrete auroral arc during calm geomagnetic conditions. The High and Low Flyers were each equipped with a nearly identical suite of instruments and followed similar latitude/longitude trajectories in order to achieve magnetic conjunction at their respective apogees. The explicit goals of the mission and subsidiary questions were:

1. **Main Goal** To determine the distribution of the ionospheric currents and the associated energy dissipation in a stable arc.
2. (Subsidiary Goal) What is the relative **spatial** distribution or balance of Hall and Pedersen currents and their associated energy dissipation in the closure region?
3. (Subsidiary Goal) Does current closure occur with a uniform altitude distribution or does it vary across the arc (meridionally)?
4. (Subsidiary Goal) Where does the primary energy dissipation occur for a stable auroral arc?

As of this writing, work is still on-going to investigate these questions thus they are not addressed in this thesis. Despite this, we provide the goals here to emphasise the relevance of the mission, namely that *in situ* measurements of Hall/Pedersen currents in the ionosphere are valuable measurements for determining how the MI coupling processes evolve. Furthermore, multi-payload

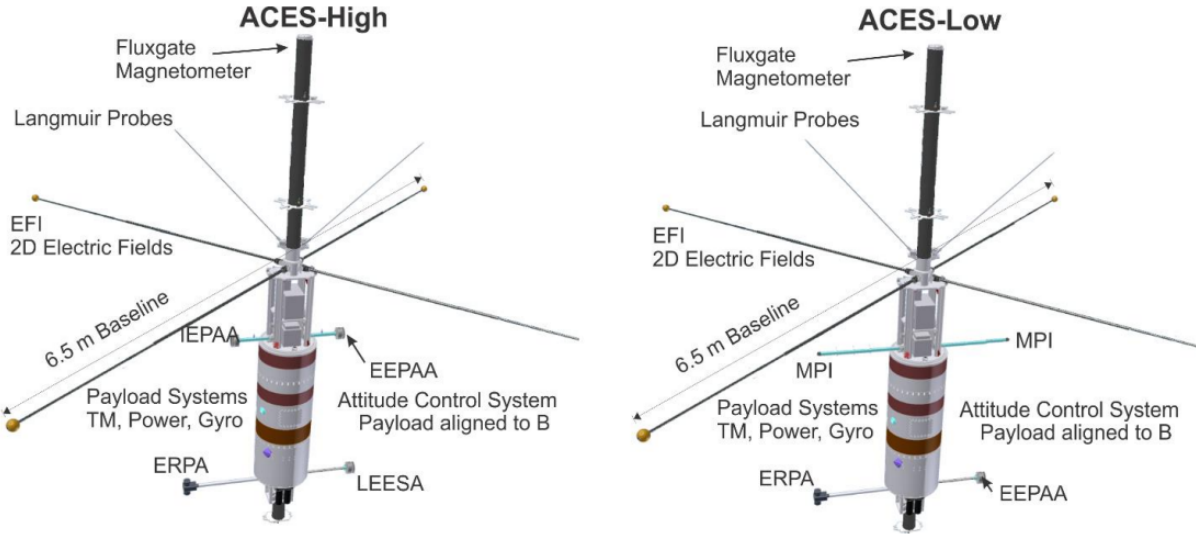


Figure 47. Layout of the ACES-II payloads for the High and Low Flyers. Each were equipped with a suite of instruments to measure relevant plasma parameters. See text for details.

rockets provide greater insight than single-payload missions for studying the evolution of quasi-static structures such as inverted-Vs.

## 5.2 Instrumentation Layout

Each payload was equipped with a full suite of plasma instruments that included: (1) a high-energy electron and a high-energy ion electrostatic analyzer (EEPAA/IEPAA), (2) fluxgate magnetometer (MAG) (3) cruciform electric field array (EFI), (4) a pair of fixed and swept Langmuir Probes (LP) for plasma density and temperature and (5) a retarding potential electron analyzer (ERPA). The High Flyer also flew a low-energy version of its electron electrostatic analyzer (LEESA) and the Low Flyer carried two miniature plasma imagers (MPI) to detect ion drifts magnitude and direction. Furthermore, a new style of small-sized, low-current high performance magnetometer called the tesseract made its maiden voyage on ACES-II Low Flyer, details are reported in Greene et al., 2024. Figure 47 illustrates the layout of the instruments on both the ACES-II High and Low payloads. The electrostatic analyzers, fluxgate magnetometers and Langmuir Probes were developed at the University of Iowa. The University of California Berkeley provided the cruciform EFI array and University of Calgary developed the MPI instruments. The University of New

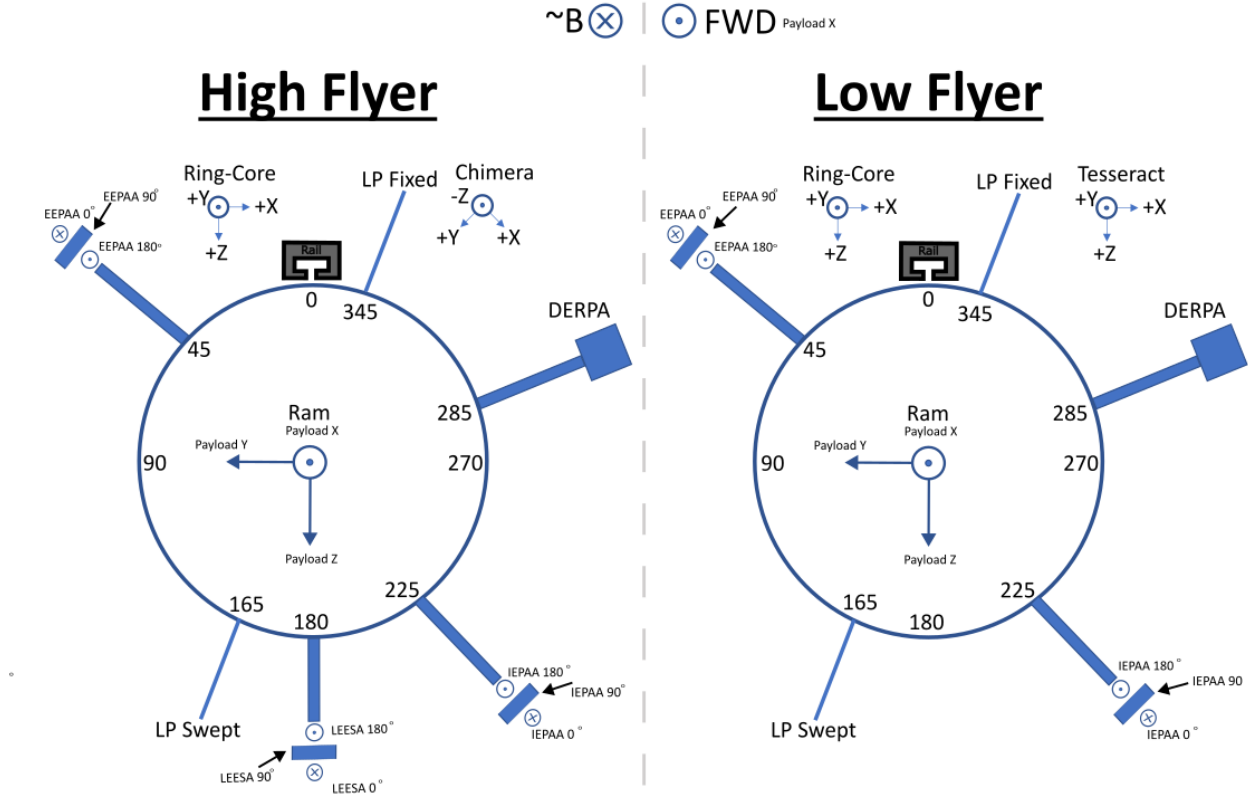


Figure 48. Configuration of the payload's instrument with respect to the rail of the launcher. The  $0^\circ$  mark represents where each payload is attached to the rail before launch.

Hampshire provided the DERPA analyzers. Wallops Spaceflight Facility provided the payloads and processed the attitude control system (ACS) data. No additional ACS magnetometers for the payload guidance to  $\vec{B}_{geo}$  were outfitted, instead rocket trajectories were optimized beforehand for maximum alignment to  $\vec{B}_{geo}$  at apogee. The coordinates with respect to the payload launcher's rail are given in Figure 48 as well as the individual coordinate systems used for the magnetometers and ESAs. For this thesis work, only the data from the EEPAA, IEPAA, MAG, EFI and LP instruments were used, so we will cover their data processing next.

### 5.3 Electrostatic Analyzers - Specifications and Operational Theory

For auroral electrons, the Electron Energy and Pitch Angle Analyzer (EEPAA) was a top-hat style electrostatic analyzer (ESA) modelled after the design style originally from Carlson et al., 1982. Figure 49 shows a slice in the input aperture for the device. For ACES-II, the EEPAA measured 8.2 eV to 13.7 keV electron distributions in 49 energy steps at  $\Delta E/E = 18\%$  FWHM resolution. The EEPAA had 21 pitch angle bins at  $10^\circ$  azimuthal resolution ranging from  $-10^\circ$  to  $190^\circ$  and a full sweep of all pitch angles and energies was performed every 50 ms with 1 ms per energy step. Here we will discuss the basic working principle behind top-hat ESAs and show how the velocity space plasma distribution function  $f(\vec{v}_\perp, \vec{v}_\parallel)$  can be calculated or derived.

The detector functions by using two concentric hemispherical electrodes of different radii, a signal amplification Microchannel Plate (MCP) and many collection anodes that radially fan out, as shown in Figure 50. The outer electrode is grounded to the rocket payload chassis and a bias voltage is applied to the inner electrode that will set the acceptance energy of the incoming particle.

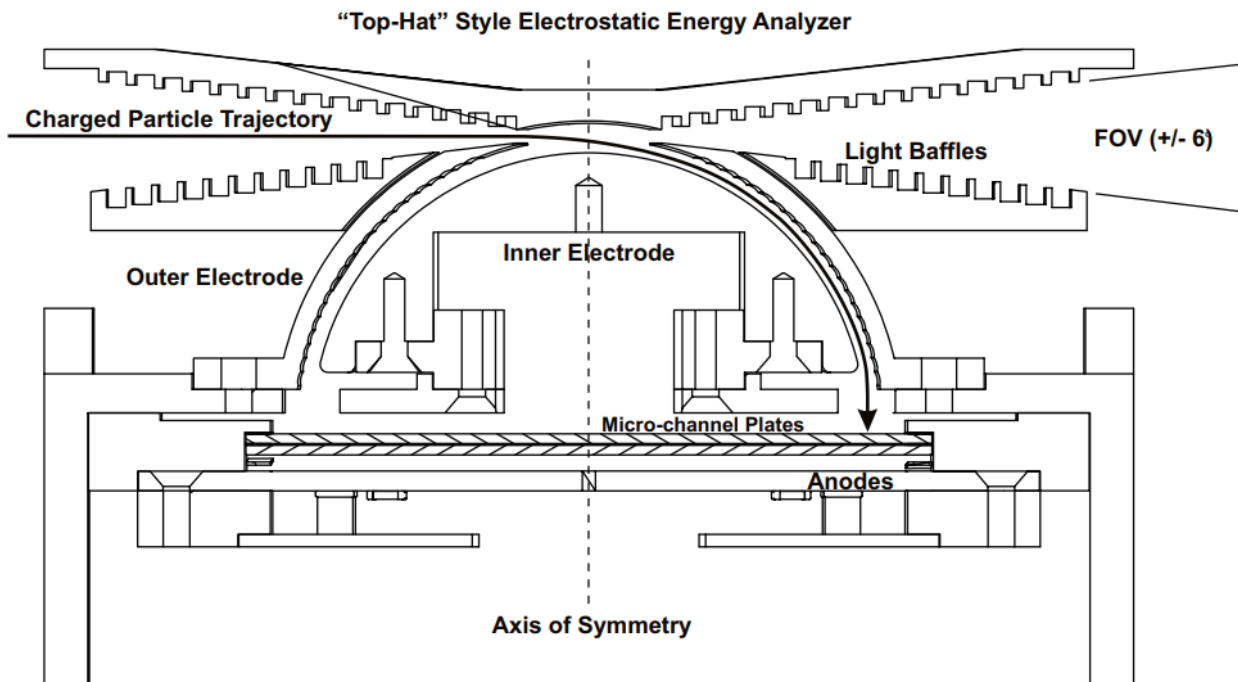


Figure 49. Cross-sectional slice of a top-hat electrostatic analyzer. Detectable trajectories are determined by the inner hemisphere's voltage and the dimensions of the electrodes.

Depending on the polarity of the inner electrode voltage, electrons or ions can be measured. The electric field between the inner and outer hemispheres can be approximated as purely radial  $\vec{E}$ , with origin centered on the inner hemisphere. The path particles follow is essentially a centripetally accelerated one, with particles having radius too small colliding with the inner hemisphere, and too big hitting the outer one. Only those particles that travel between the hemispheres, strike the MCP and become amplified to the anode are detected as a single count value. The incoming particle energy determines this path and is related through the centripetal force from the electric field:

$$E_{permitted} \approx -\frac{qV_{set}}{2} \frac{r_{particle}}{\Delta r} \quad r_{in} < r_{particle} < r_{out} \quad (125)$$

where  $r_{out}$  is the radius of the outer hemisphere,  $r_{in}$  is the radius of the inner hemisphere,  $\Delta r$  is the radial spacing between the hemispheres,  $q$  is particle charge,  $V_{set}$  is the applied bias voltage to the

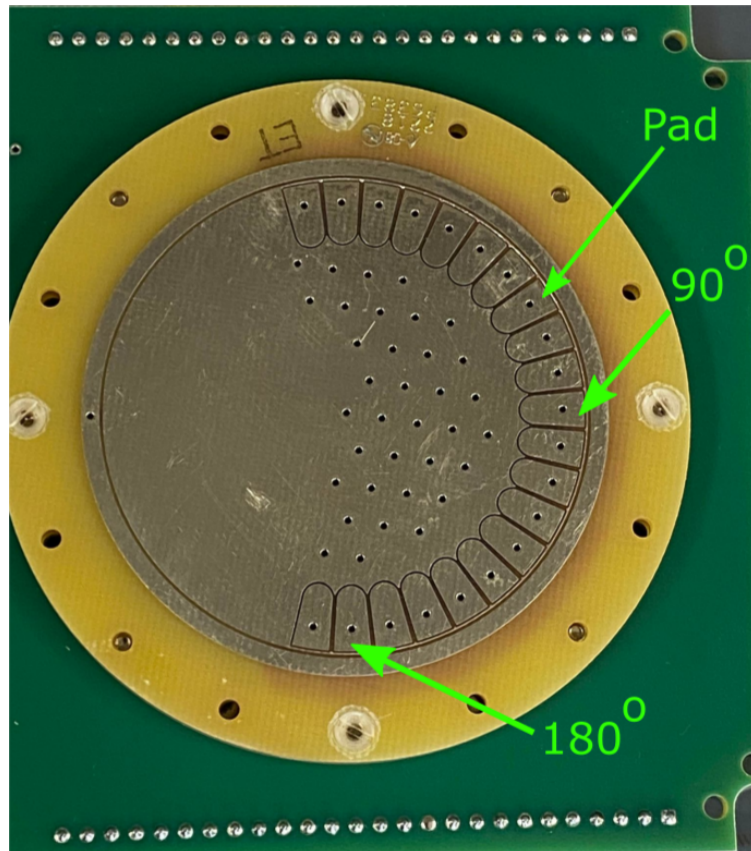


Figure 50. ACE-II anode board that shows 21 pitch-angle anode pads. Electrons are amplified by the MCP and strike these pads to be detected by the detector's electronics.

inner electrode and  $r_{particle}$  is the centripetal radius of the electron, which must be between  $r_{in}$  and  $r_{out}$  to be detected. Notably, mass identification is not possible for ions due to the cancellation of mass while deriving this equation. A derivation of this relationship is found in Appendix B.

By using equation 125 the nominal energy resolution of the detector is defined from the azimuthal acceptance of electrons for a constant  $V_{set}$ :

$$\frac{E(r_{out}) - E(r_{in})}{E_c} = \frac{\Delta r}{r_c} \equiv \gamma = \frac{\Delta E}{E_c} \quad (126)$$

where  $r_c$  is the radius exactly between  $r_{out}, r_{in}$  for an electron at the central permitted energy  $E_c$  and  $\gamma$  is the energy resolution. Equation 126 shows  $\gamma$  is fixed by the physical dimensions of the detector. This is an idealization and corrections are often made e.g. azimuthal contamination can occur when the amplified signal strike multiple anodes, a processes that is corrected through calibration.

By measuring the number of counts  $N$  within an accumulation time,  $\Delta t$  for particles with energy  $E$  using a detector with geometric factor  $g$ , an estimate of the particle distribution function  $f(\vec{v}_\perp, \vec{v}_\parallel)$  can be made. In general, the phase space distribution function is given by:

$$f = \frac{dN}{d^3 v d^3 x} \quad (127)$$

If we choose a preferred axis of measurement we can change to spherical coordinates via  $dx = vdt$  and  $v dv = d(v^2)/2$  so that

$$f = \frac{dN}{(v^2 dv)(d\Omega dA)(vdt)} \quad (128)$$

$$= \frac{m^2}{2E} \frac{dN}{dEd\Omega dAdt} \quad (129)$$

$$= \frac{m^2}{2E} j_N \quad (130)$$

where the differential number flux is defined by  $j_N = dN/dAd\Omega dEdt$  in units of  $[\text{cm}^{-2} \text{str}^{-1} \text{s}^{-1} \text{eV}^{-1}]$ .

A related quantity is the *differential energy flux* given by  $j_E = j_N E$  for incoming particle energy  $E$ . By assuming  $j_N$  is constant with respect to all its differentials, we can relate it to the measured counts via

$$N = \int_{A-\Delta A/2}^{A+\Delta A/2} \cdots \int_{t-\Delta t/2}^{t+\Delta t/2} j_N dA d\Omega dE dt = j_N \Delta A \Delta \Omega \Delta E \Delta t \quad (131)$$

so that we can write

$$j_E = E j_N = \frac{N}{\Delta A \Delta \Omega \Delta t} \frac{E}{\Delta E} \quad (132)$$

in units of  $[\text{cm}^{-2} \text{str}^{-1} \text{s}^{-1} \text{eV/eV}]$ . This assumption is perhaps questionable for large  $\Delta t$  or  $\Delta E$ .

In practice, some corrections to equation 132 must be made. The collection interval is modified by the *deadtime* of the circuitry i.e. for every count pulse detected by the circuit, there is a small  $\Delta t_{\text{Dead}}$  before the detector can observe another particle. Furthermore, the quantum efficiency of the MCPs can be as poor as 50% and must be factored into the counts via  $N = \varepsilon N'$  where  $N'$  is the true counts and  $\varepsilon$  is the conversation efficiency. Finally, we include the energy resolution  $\Delta E = \gamma E$  from equation 126 so that equation 132 becomes

$$j_E (\vec{v}_\perp, \vec{v}_\parallel) = \frac{N'}{g(\Delta T - N' \Delta t_{\text{Dead}})} \quad (133)$$

where we have defined the *geometric factor* as  $g = \varepsilon / (\gamma \Delta A \Delta \Omega)$  and  $\Delta T$  is the single-step collection interval per energy. Formally, the geometric factor is analogous to the physical collection area of the detector and is given by

$$G(E, \Omega) = \frac{1}{E_0^2} \int E dE \int dA \int d\Omega R(E, \Omega) \approx \left[ \frac{\Delta E}{E_0} \Delta A \Delta \Omega \right]_{\text{sensor}} \quad (134)$$

where  $E_0$  is the average electron energy and  $R(E, \Omega)$  is the instrument response function which ensures only those electrons from the plasma distribution which are detected are used in this calculation (see Collinson et al., 2012 for more details). This expression is dependent upon energy, but is simplified by virtue of the energy-independence of the energy resolution via equation 126. The geometric factor is often determined through a calibration using a known source of  $j_N$  and

measuring  $N$  directly for a known  $\Delta t_{Dead}$  and  $\Delta T$ . Thus, we can write our distribution function as

$$f(\vec{v}_\perp, \vec{v}_\parallel) = \frac{1}{2} \left( \frac{m}{E} \right)^2 j_E(\vec{v}_\perp, \vec{v}_\parallel) \quad (135)$$

for which some choice of particle mass must be made for ions. Note that the 21 anode pads in Figure 50 define the detected pitch angles of the detector.

$$f(E, \alpha) = \frac{m_e^2}{2E} j_N \quad (136)$$

$$j_N = \frac{N}{\Delta A \Delta \Omega \Delta E \Delta t} \quad (137)$$

## 5.4 Magnetic Fields - Specifications and Operational Theory

A total of four Fluxgate magnetometers were flown on the ACES-II mission: two traditional fluxgate RingCores (MAG), a new “Tesseract” fluxgate design and a hybrid Fluxgate-searchcoil named “CHIMERA”. The primary scientific magnetometers used in this thesis were the traditional RingCores, with one flown on each payload. For additional information on the success of the Tesseract design, we refer the interested reader to Greene et al., 2024. The MAG instruments were made using a copper-nickel alloy developed at the University of Iowa and sampled the 3-axis geomagnetic field at 128 Hz with 50 pT resolution. These were mounted in the nose of the payload.

A fluxgate essentially works by starting with a magnetically permeable ferromagnetic material and driving it into/out-of magnetic saturation using an AC signal (see Figure 51). This material is the “primary” core that is often shaped into a ring (hence “RingCore”) and will measure a single axis of an external magnetic field  $\vec{B}_{ext}$ . By driving the core in an out of saturation, the fully expanded Faraday’s Law will provide the expected induced voltage in the core:

$$V_i = NA\mu_0\mu_r \frac{dH(t)}{dt} + N\mu_0\mu_r H \frac{dA(t)}{dt} + N\mu_0 AH \frac{d\mu_r}{dt} \quad (138)$$

where  $N$  is the number of turns of wire,  $A$  is the cross-sectional area of the coil of wire,  $\mu_0$  is the magnetic permeability of free space, and  $\mu_r$  is the magnetic permeability of the ferromagnetic core. In our case, only the term with  $N\mu_0 AH \frac{d\mu_r}{dt}$  is non-zero since the cores are being driven through their hysteresis curves. Notably, the first term  $\frac{\partial H(t)}{\partial t}$  is the basis for a search coil magnetometer and  $\frac{\partial A(t)}{\partial t}$  is usually an error term from sensor rotation in the external field.

External magnetic fields can be measured via a negative feedback loop when the core is continuously magnetically saturated and unsaturated. The core is driven into/out-of magnetic saturation at the drive frequency  $f_{drive}$ . A “sensing winding” is placed around the core to measure the induced voltage due to the changing magnetic flux in the core. The circular geometry of the core minimizes the cross-coupling between the driving input signal and the induced output signal. The induced voltage in the sense winding via equation (138) is measured, amplified, filtered and

integrated to produce a quasi-dc voltage, which is related to H. Negative magnetic field is achieved by converting the measured H field into a current (V/I) and driving it back into the sense winding to null the magnetic flux there. This creates a zero magnetic field within the sense winding. By placing three cores in an orthogonal configuration the a 3D vector measurement of the DC magnetic field can be obtained. Considerable work must be done to properly calibrate a magnetometer strapped to a rocket, which will be covered in Chapter 6.2.

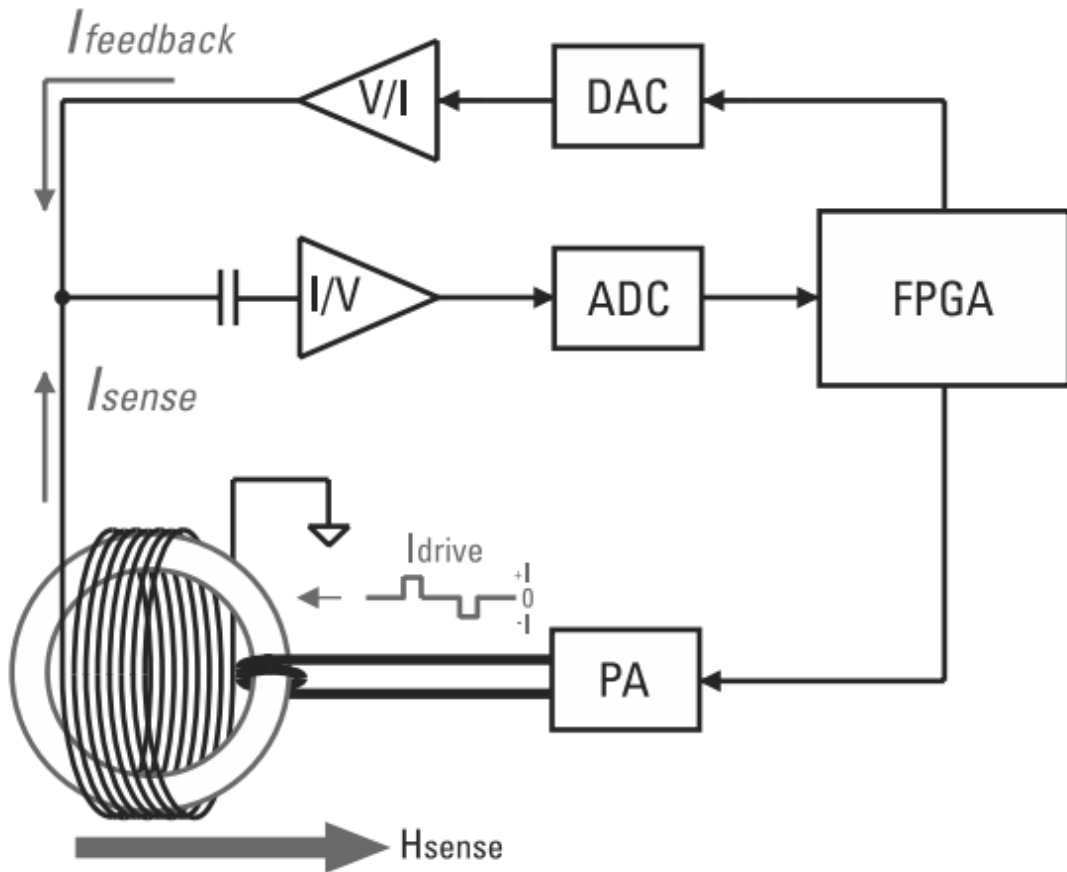


Figure 51. From Miles et al., 2013. Schematic of one axis of a fluxgate magnetometer. The electronics generate a driving signal of order  $10^5$  Hz that saturates and unsaturates the cores. The detected deviations from expected saturation due to an external magnetic field are read in the electronics as a current that's converted into a voltage. Calibration steps convert this voltage into a magnetic field value.

## 5.5 Electric Fields - Specifications and Operational Theory

The ACES-II mission employed a 6.25 m tip-to-tip cruciform array double probe Electric Fields Instrument (EFI) similar to Bonnell et al., 2008 for the THEMIS mission to measure the DC and AC electric field. It measured the spin-plane components of the field at a 4 kHz sample rate with  $50 \mu\text{V/m}$  resolution over a voltage range of  $\pm 20 V_{pp}$ . The probes themselves are Aluminum spheres with a conductive coating (Aerodag) which are placed on the tips of booms that extend off the payload. Measuring the electric field using a double probe technique involves the differential voltage measurement ( $\Delta\Phi$ ) between two probes, separated by some distance  $d$  (called the “baseline”). The electrodes are connected to a voltmeter a distance apart and the difference in the measured probe potentials  $\Delta\Phi$  provides electric field via:

$$\Delta\Phi = -\vec{\mathbf{E}} \cdot \vec{\mathbf{d}} \quad (139)$$

where  $\vec{\mathbf{E}}$  is the electric field and  $\vec{\mathbf{d}}$  is the vector distances between the spheres. Formally, this expression is the result of a line integral on the equation  $\vec{\mathbf{E}} = -\nabla\Phi$  and averages the value of  $\vec{\mathbf{E}}$  over the distance of the probe separation. Thus, the double probe technique only resolves DC electric fields that are spatially much larger than the baseline  $\vec{\mathbf{d}}$ . The error in the probe scales inversely to the distance between the probes:  $\delta E \sim \delta V/d$  for a given probe measurement error  $\delta V$ . A balance must be struck between minimum resolvable E-Field structure and sensitivity of the instrument. Theoretically, equation 139 is all that is required to determine  $\vec{\mathbf{E}}$ , however several sources of error and calibration exist that must be accounted for to ensure a good measurement. This will be covered in Chapter 6.5.

For the configuration on ACES-II we show an example setup in Figure 52 where a pair of double probes V1-V2 and V3-V4 constitute two measurements of  $\vec{\mathbf{E}}$  in the spin plane of the rocket. This setup only provides two components of  $\vec{\mathbf{E}}$  since a third, orthogonal cruciform axis was not used. The third dimension can be derived as a pseudo coordinates using the assumption that  $\vec{\mathbf{E}} \cdot \vec{\mathbf{B}} = 0$  using the direction of the geomagnetic field vector  $\vec{\mathbf{B}}$ .

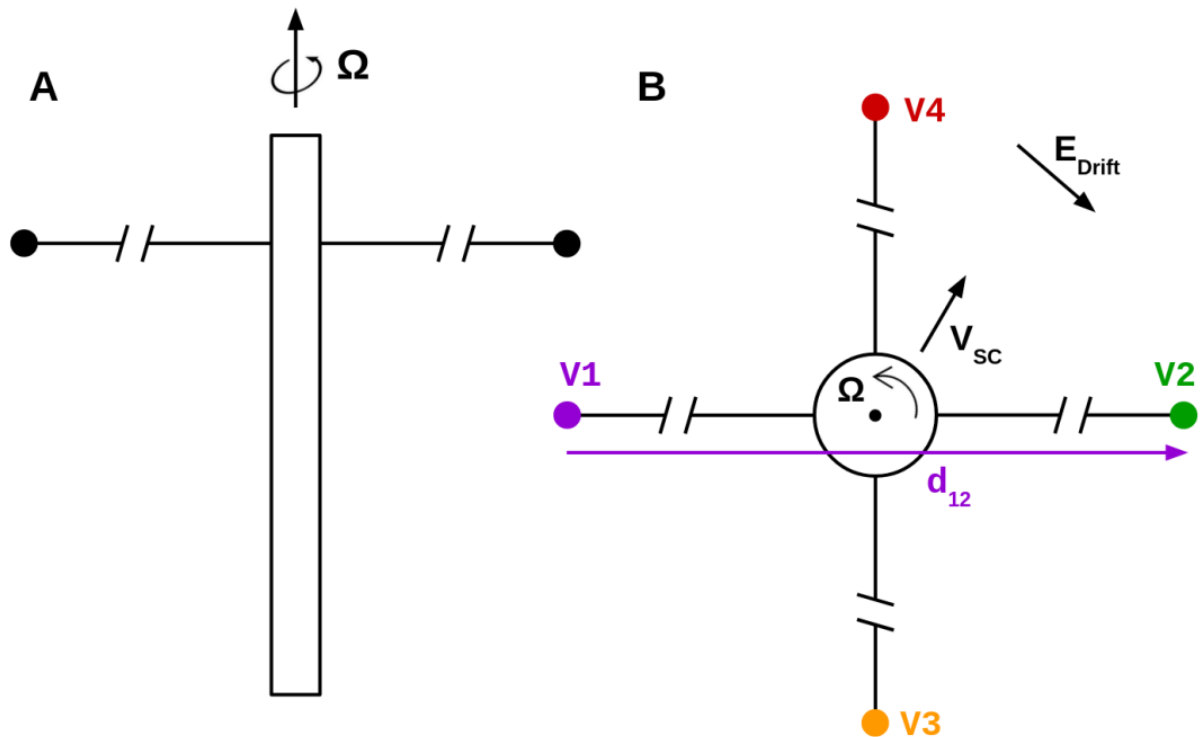


Figure 52. Figure from (R. Roglands Disseration), used with permission. Schematic of the double probe experiment on ACES-II. (Left) Side view of payload and (right) top-down view of payload. The rocket has some velocity  $\vec{v}_{sc}$  with respect to its own reference frame. Rockets are spin-stabilized with a spin frequency of  $\Omega \sim 0.5$  Hz. The DC electric field  $\vec{E}_{Drift}$  can be determined by using the probes by defining baseline vectors for each probe pair,  $\vec{d}_{ij} = \vec{X}_i - \vec{X}_j$  where  $\vec{X}_i$  is the position of the  $i^{th}$  sensor from the payload body.

## 5.6 Langmuir Probes - Specifications and Operational Theory

The ACES-II mission featured two Langmuir Probe (LP) instruments, each near the nose of the payload and deployed at 45° along booms of 1 meter in length. Each probe consisted of a sphere with surface area 20 cm<sup>2</sup>. The *Fixed Langmuir Probe* was negatively biased to -5V with respect to payload body and sampled the ambient ion plasma density at 1 kHz. The *swept Langmuir probe* measured the current intake from 101 different voltage steps between -4.68V to 2.08V with respect to payload chassis. Unfortunately, the gain within the detector circuit for the swept Langmuir probe was set too high on both payloads, preventing determination of the characteristic curves required to determine plasma density and temperature. For this reason we will only present data from the fixed LP instrument, which had no such issue. In general, the theory behind Langmuir Probes is extensive and we will only present the theoretical background required to interpret our data for spherical probes.

Langmuir probes have provided a reliable means to estimate a plasma's temperature and charge density for over a century since the development of their theory by Irving Langmuir and others in the early 1920s. The key plasma phenomenon that LPs operates upon is the ability of plasma to try to stay neutral. Plasmas are highly conductive mediums that quickly screen out external electric fields by surrounding the source of the potential in a cloud of charge with a semi-definite shape called the Debeye Sheath (see chapter 2.1 for details). The interplay between the Debeye sheath, the ambient plasma potential and the voltage applied to the probe determines the characteristic voltage vs current curves from Langmuir Probe data. In the simplest case, we insert our spherical probe into our quasi-neutral plasma with no applied voltage. Electrons and ions will strike the probe at different rates owing to their different thermal speeds, given by

$$v_{th} = \sqrt{\frac{2k_B T}{m\pi}} \quad (140)$$

for species mass T and mass m. The mass dependence implies electrons move much faster on average than ions by  $v_{th-}/v_{th+} \sim (m_+/m_-)^{1/2}$  for the same temperature. Consequently, the probe

will charge negative as more electrons strike it until an equilibrium is reached where a sheath of ions forms around the probe. This sheath screens out the negative probe potential which then falls off with distance the potential reaches the ambient *plasma potential*  $V_{pl}$ . The plasma potential comes from the imbalance of charge motion that usually favors losing electrons. This gives rise to a positive space charge that creates a potential throughout the plasma, often measured as a few volts on sounding rockets. Sounding rockets immersed within a plasma also charge negative for the same reasons Langmuir Probes do. This negative potential is called *the payload potential* and affects the chassis ground voltage for instrumentation.

By sweeping the voltage applied to the probe well below, near or above the payload potential we can define some regions of measured probe current that obey simple relations that allow us to estimate the plasma parameters. In order to analyze the system, we must define some voltages using Fig. 53 as a guide:

- Reference potential (e.g. Chassis ground):

$$V_C$$

- Potential difference between the outer edge of the Debye sheath and reference (i.e. the plasma potential):

$$V_{pl} \equiv V_A - V_C$$

- Potential difference between probe surface and Debye sheath edge:

$$V \equiv V_B - V_A$$

- Potential difference between probe surface and reference voltage (probe voltage):

$$V_p \equiv V_B - V_C = V + V_{sp}$$

The *Ion Saturation Region* occurs when the probe voltage is sufficiently negative to overcome the plasma potential and the (typically) negative payload potential. This results in a flood

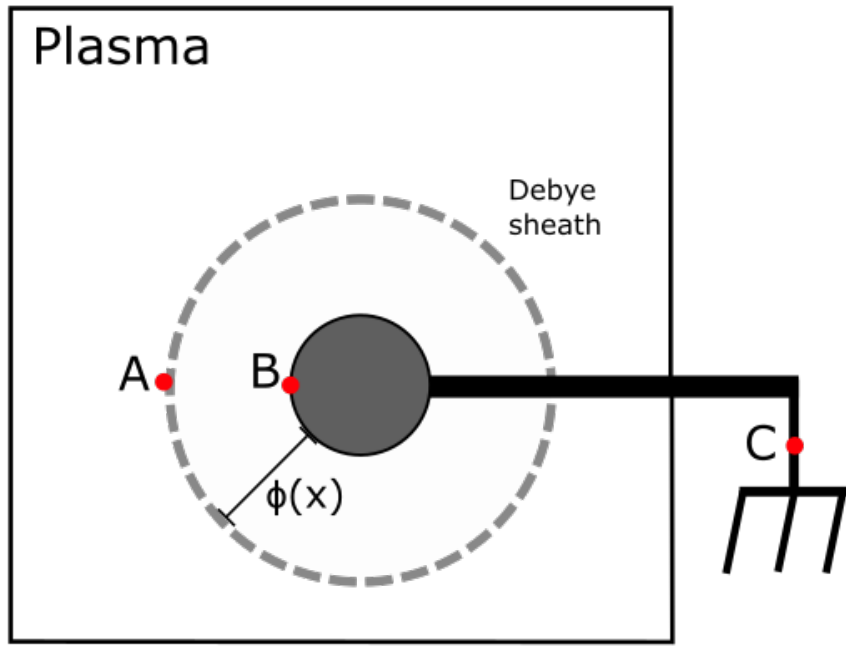


Figure 53. A schematic of a spherical probe setup for a sounding rocket. Here  $\phi(x)$  is the radial symmetric potential that transitions the probe potential at point B to the ambient plasma potential at point A. All measurements are done with respect to Point C, the chassis ground  $V_C$ .

of ion current that precludes any electron contribution. The probe's electric field influence is still bound within a sheath, except now any ions within its influence tend towards the probe which sets up a “sink” that collects a roughly constant amount of ions. The saturation value of this sink is called the *Ion Saturation Current*  $I_{+0}$  and it’s value is calculated by considering the flux of ions passing through a surface:

$$\Gamma_+ = \frac{1}{4} n_{+0} \bar{v}_+ \quad (141)$$

where  $\Gamma$  is particle flux in  $\text{s}^{-1} \text{ m}^{-2}$ ,  $n_{+0}$  is the ion plasma density and  $\bar{v}_+$  is the average ion velocity. For our isotropic and homogeneous plasma, the average ion velocity is given by the thermal velocity so that the ion saturation current into the probe is then

$$I_{+0} = \frac{1}{4} n_{+0} e \bar{v}_+ S = \frac{1}{4} n_0 e \bar{v}_+ A_{probe} \quad (142)$$

where  $A_{probe}$  is the surface area of the probe and  $e$  is elementary charge. By using equation 142

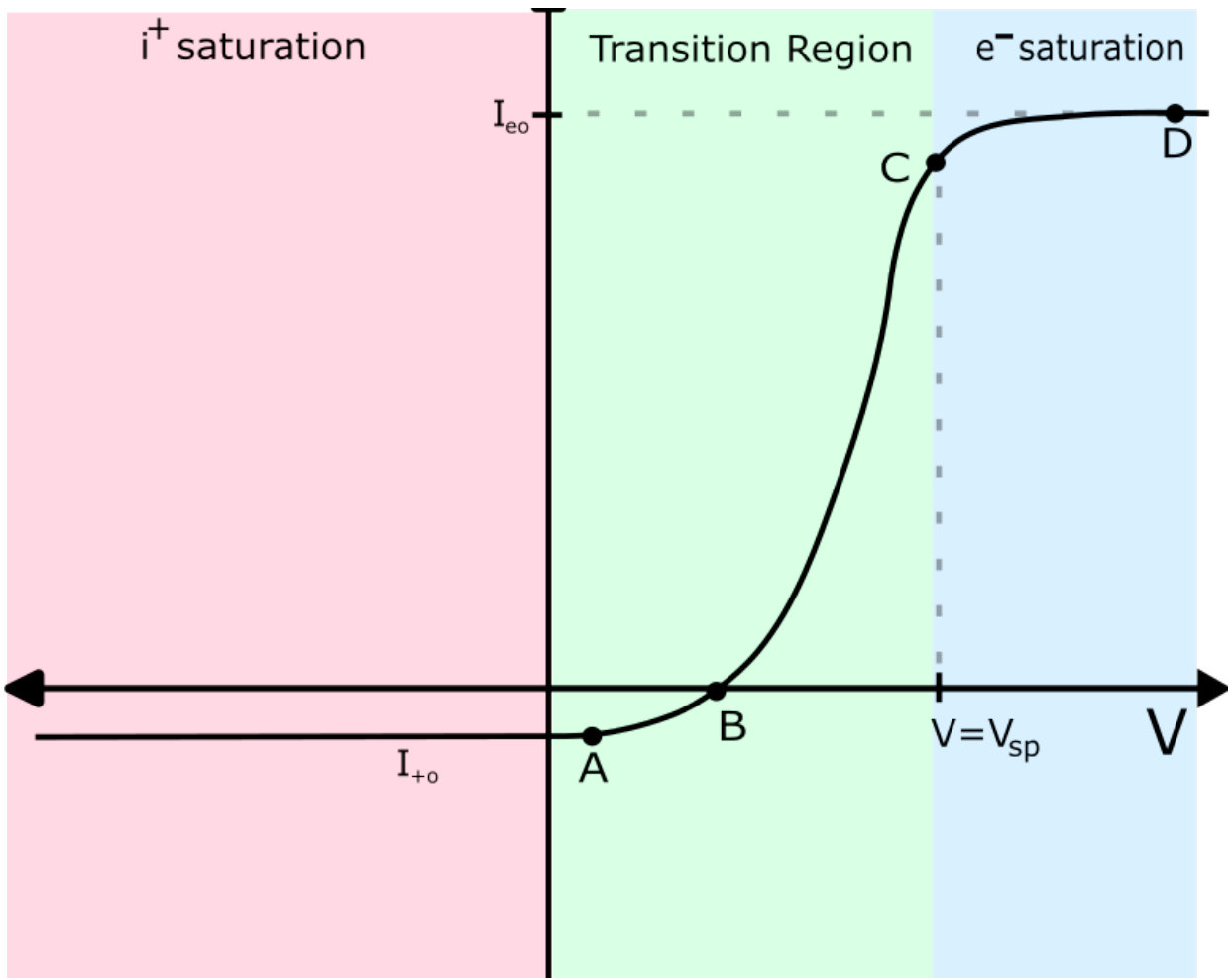


Figure 54. The characteristic curve for a swept LP for probe voltage on the x-axis. The measured probe current  $I_p$  is the current flowing out of the probe (positive by convention) and  $I_{e0}, I_{+0}$  are the electron/ ion saturation currents, respectively. The point where the applied probe voltage matches the spacecraft potential  $V_{sp}$  is shown near the electron saturation region.

and the measured probe current  $I_{+0}$  for our fixed Langmuir probes we can estimate the ion plasma density,  $n_{+0}$ .

A similar case occurs for the electron saturation region (blue region in figure 54) except now the probe applies larger positive voltages until it overcomes the negative payload potential. The inflection point occurs when the ever-more-positive probe voltage matches the negative spacecraft potential  $V_{sp}$ , at which point the payload becomes positive with respect to the plasma thereby inviting a cascade of electrons that saturates the probe and precludes ions. Again,  $V_{sp}$  is usually a couple of volts and changes throughout the flight. The formula for  $I_{-0}$  is identical to equation 142, although a more rigorous analysis can reveal a weak dependence upon the probe potential  $V_p$  :

$$I = I_{e0} \left( 1 + \frac{eV_p}{k_B T_e} \right); \quad I_{e0} = \frac{1}{4} n_0 e \bar{v}_e A \quad (143)$$

For further reading, we recommend the works by Hershkowitz, 2013 and Merlino, 2007.

Finally, the *Transition Region* occurs between the electron and ion saturation regions, wherein the probe voltage selects which ions/electrons are permissible for detection based on the thermal spread of their underlying distributions. Naturally, this region depends upon the temperatures of the ions and electrons since this determines what fraction of particles can overcome the negative payload potential. An analytical approach of this region which relies on maxwellian distributions will result in an exponential response of the plasma. Deeper analysis of this region is not given since we don't report any characteristic curves from our data, but we will list the complete set of equations for each region here:

$$I_p = \begin{cases} -I_{+0} & ; V_p \ll 0 \\ I_{e0} \exp \left\{ \left[ \frac{eV_p}{k_B T_e} \right] \right\} - I_{+0} & ; V_p < 0 \\ I_{e0} \left( 1 + \frac{eV_p}{k_B T_e} \right) & ; V_p \geq 0 \end{cases} \quad (144)$$

For saturation currents:

$$I_{+0} = \frac{1}{4} n_0 e \bar{v}_+ A$$
$$I_{e0} = \frac{1}{4} n_0 e \bar{v}_e A$$

Our data only contains knowledge on the ion plasma density, however under quasi-neutrality ( $n_{+0} \approx n_{e0} = n_0$ ) we can estimate the electron density. However, the estimate on electron density is tempered with EISCAT radar data since quasi-neutrality is often broken locally on smaller scales pertinent to our rocket. This will be discussed in Chapter 6.2

## 5.7 AllSky Imagers

The Allsky Imagers (ASI) data were provided from the University of Oslo's (UiO) Svalbard array. The data is managed, calibrated and processed by Dr. Lasse Clausen from UiO and made available at <http://tid.uio.no/plasma/aurora/tech.html>. The imagers are routinely aligned to astronomical stars and planets to ensure the validity of the camera's coordinate system (geopgraphic/geomagnetic azimuth, elevation, latitude/longitude etc) for its pixels. In each imager, two cameras with a 20° cutoff elevation angle measure specific wavelengths of light that are associated with particular altitudes. The brightness of each image pixel is measured by recording the number of photons per pixel as a 16-Bit value and converting into Rayleighs using a provided calibration constant K (in this case, K = 1 R/count). Calibration was done using data from a quartz tungsten halogen lamp calibration lamp at some distance from a diffuse screen. Only one ASI was germane to the ACES-II launch, located at Skibotn, Norway approximately 160 km east from the payload's launch point at Andøya. It acquired images of green-line 5570 Å at 150 km and red-line 6300Å at 250 km aurora with a 30 second integration time over the Norwegian Coast. An example of the 5570 Å green line at 17:25:40 UTC is given in Figure 55. The altitude values for the ASI wavelengths determine the spatial coverage for each pixel in the ASI, for which a calibration step involving aligning the ASI timestamps and ACES-II auroral crossing given by the high-energy

**17:25:40**

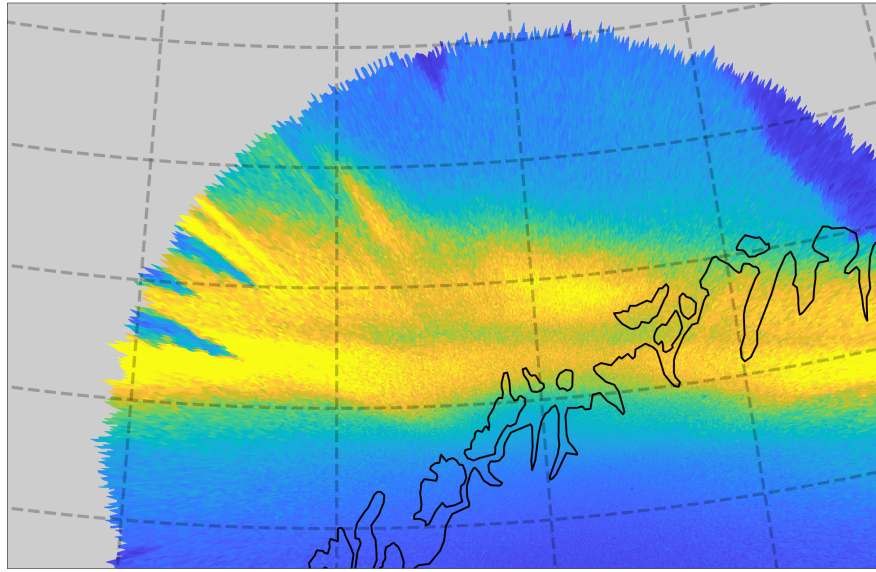


Figure 55. Example of 5570 Å green-line ASI from Skibotn, Norway on Nov. 20th, 2022 over the Norwegian coast. The image is projected to 150 km and was sampled at 17:25:40 UTC. The camera was positioned approximately 150 km east of ACES-II launch point. This southward-moving discrete arc remained quasi-stable in space and time over the 10 minutes of the mission.

electron data is performed. The approximate altitude/time when the two payloads crossed their respective aurora are used to estimate the altitude the ASIs should project to. For this work, the previously mentioned 150 km and 250 km values were sufficiently accurate for when the payloads crossed the discrete arc.

## 5.8 Incoherent Scatter Radar

The European Incoherent Scatter Scientific Association (EISCAT) radar array was a ground-based asset available to ACES-II during the night of the launch on Nov 20th, 2022. The Norwegian-based arrays consists of three dishes located at Tromsø, Kiruna and Sodankylä, which are shown in Figure 56. For this work the UHF Tromsø dish was primarily used due to it's proximity to our flight and largest coverage of the mission flight path. A black arrow in Figure 56 denotes this dish, which was angled approximately Northward at  $\sim 85^\circ$  elevation. It transmitted a frequency of 0.93 GHz, sampling the electron plasma density  $n_e$ , ion temperature  $T_i$ , temperature ratio  $T_e/T_i$ , heavy

ion composition ( $n_{O2+} + n_{NO+} + n_{N2+})/n_e$  and oxygen composition  $n_{O+}/n_e$  among other things. An altitude profile up to 700 km vs time for each of these variables is provided and full sweeps occurred approximately every 60 seconds. Given the significant delay between radar sweeps, no work was done to determine the precise alignment between our spatio-temporal sounding rocket measurements and the EISCAT data. Instead, broad aurora-like features were identifiable within the radar data by eye and during the approximate times indicated by the ASIs and the payload instruments. Some of the values from EISCAT are used to aid Langmuir Probe calibrations, determine weighted ion mass density  $\rho_m = n_i m_i$  and to gauge the quiescent ionospheric plasma temperatures vs altitude in Chapter 8. None of the calculations involving the use of this data strongly depended upon the accuracy of our chosen EISCAT values, up to an order of magnitude.



Figure 56. Global position and range of the EISCAT radar array at the north coast of Norway. The Tromødish (see black arrow) was used in this study to characterize the plasma density and temperature *in situ*. Image taken from  
<https://www.eiscat.rl.ac.uk/radar/ISRfactsheet.pdf>

## CHAPTER 6: DATA AND PROCESSING

This Chapter presents the overview of the ACES-II flight and the various calibrations steps to process data to scientific quality. Most Figures are taken from Feltman et al., 2024.

### 6.1 Flight

The mission was successful in launching two payloads into a discrete auroral arc from Andøya, Norway during its two week launch window in mid November, 2022. A phone image of an auroral arc similar to what ACES-II intercepted is shown in Figure 57. The High Flyer (ACES-II 36.359) launched at 17:20:00 UTC and Low Flyer (ACES-II 36.364) at 17:21:40 UTC reaching corresponding apogees of 407 km at 17:25:30 UT and 188 km at 17:25:39 UT, collecting



Figure 57. An image of the type of auroral arc that ACES-II may have intercepted. Seen on the night of the launch overhead the rocket range ~ 1 Hr after launch. Taken with an iphone 11 camera. *Photocredit: Connor Feltman*

*in situ* data for a total of 10.22 minutes and 7.31 minutes respectively. Figure 58 shows the altitude vs geographic/geomagnetic latitude of the rocket trajectories along with an assumed 79° inclined geomagnetic field. In Figure 58(b) the Skibotn ASI 557.7 nm green-line and 630.0 nm red-line are projected over the Norwegian coast. The Tromsø Geophysical Observatory ground magnetometer array for Bjørnøya (in red) and Tromsø (in blue) are shown in Figure 59. These locations are chosen since the typical discrete electrojet forms below the latitudes of the red line and above the blue line. Deviations in the H-Component (northward) are suggestive of the presences of an electrojet. The K<sub>p</sub> index for the night was 2+ and the ASI indicated that ACES-II intercepted the first visually identifiable discrete arc throughout the night. The MLT of launch was approximately 18, which would place the arc in the “West of Bulge” section (Gjerloev et al., 2000) of the substorm.

As stated, tight magnetic conjunction is required for the mission to ensure both flyers are along a similar set of fields lines at apogee. This allows the High Flyer to see the input into the ionosphere while the Low Flyer estimates the ionospheric response. Magnetic alignment between payloads is expressed by converting geographic data into a set of ionospheric invariant coordinates (ILat, ILong). These are calculated by using the CHAOS-7 geomagnetic field model (Finlay et al., 2020) to determine the latitude/longitude coordinates of the geomagnetic field at a chosen reference altitude,  $Z_{ref}$ , for all points in the flight. Essentially, this process is called “ray tracing” which usually involves complex curved geometries to map magnetic field lines to specific altitudes on Earth from satellite distances. Here our altitudes are so low that Earth’s Field line is assumed to be a straight line in 3D space at any point along our rockets’ trajectories. Conceptually, the ILat/ILong coordinates are shown in Figure 60 where these new coordinates are just geographic coordinates at a new altitudes found using  $\vec{B}_{geo}$  at all points in space/time for our rocket’s attitude data. For any given time ( $T_r$ ), altitude (Alt), latitude ( $\phi$ ) and longitude ( $\lambda$ ) we can determine a  $\hat{b} = \vec{B}_{geo}/|\vec{B}_{geo}|$  unit vector using python’s chaosmagpy library. This gives  $\vec{B}_{geo}$  in East, North, Up (ENU) coordinates. There is no physical transformation between magnetic coordinates (in nT) to spatial coordinates (Lat/Long), so we instead parameterize a line (in physical space) with slope given by  $\hat{b}$ . In general, for 3D slope vector  $\vec{v}$  and 3D initial position  $\vec{x}_0$ , a line is parameterized by

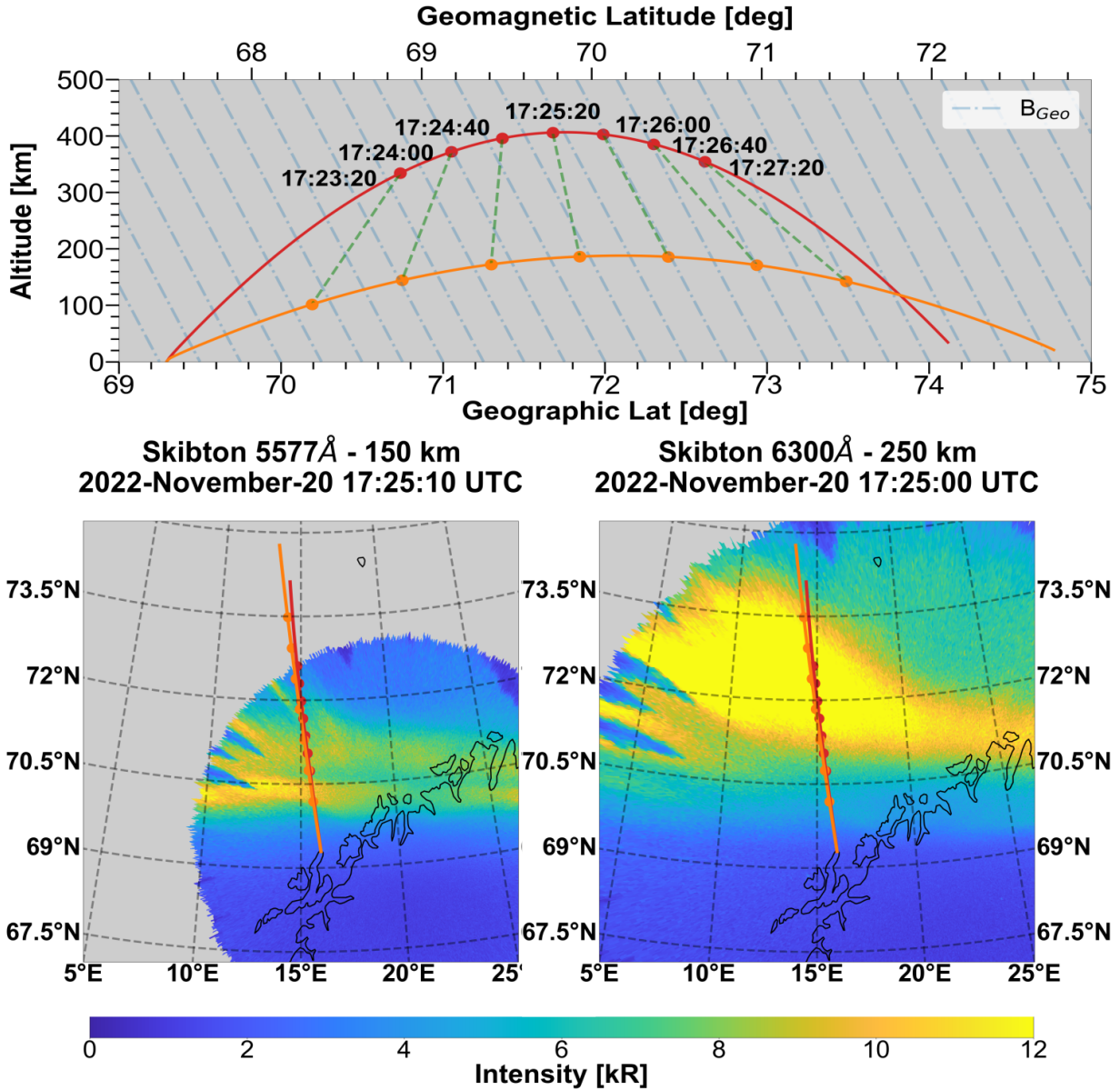


Figure 58. Trajectories of the ACES-II rockets on Nov 20th, 2022 which launched a High/Low Flyer at 17:20:00 UTC/17:21:40 UTC, respectively. AllSky imager data of the discrete arc plotted in geographic coordinates.

a single variable (call it “t”):

$$\vec{x} = \vec{v}t + \vec{x}_0 \quad (145)$$

We are interested in determining when this parameterized line intersects with the plane a new altitude,  $\vec{x} = (\text{ILat}, \text{ILong}, Z_{ref})$  for all points in the flight. To start, we calculate the parameter t that

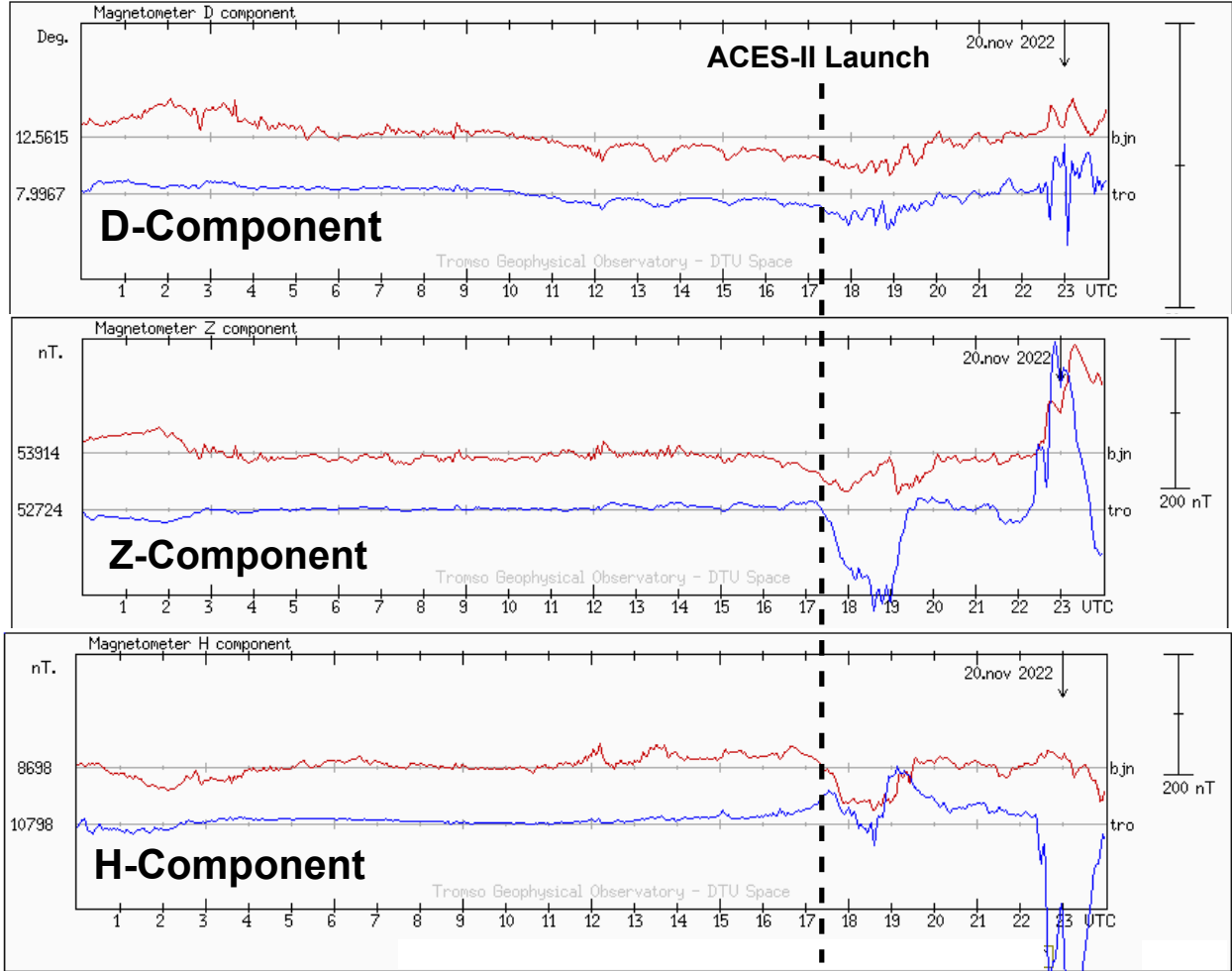


Figure 59. Time series of ground-magnetometers located above (Bjørnøya in red) and below (Trømsø in blue) our discrete arc that occurred near 17:20:00. The H-component is most associated with the auroral electrojet. The H-component for the two stations trend in opposite directions near the ACES-II launch point. Data taken from Trømsø Geophysical Observatory at <https://flux.phys.uit.no/stackplot/>

corresponds to when the altitude component of  $\vec{x}$  reaches our target altitude. In ENU coordinates this is

$$t = \frac{Z_{ref} - Alt}{b_U} \quad (146)$$

where  $\hat{b}_U$  is the Up component of  $\hat{b}$ . From this we can determine the other components

$$\vec{x}_E = x_{0E} + tb_E$$

$$\vec{x}_N = x_{0N} + tb_N$$

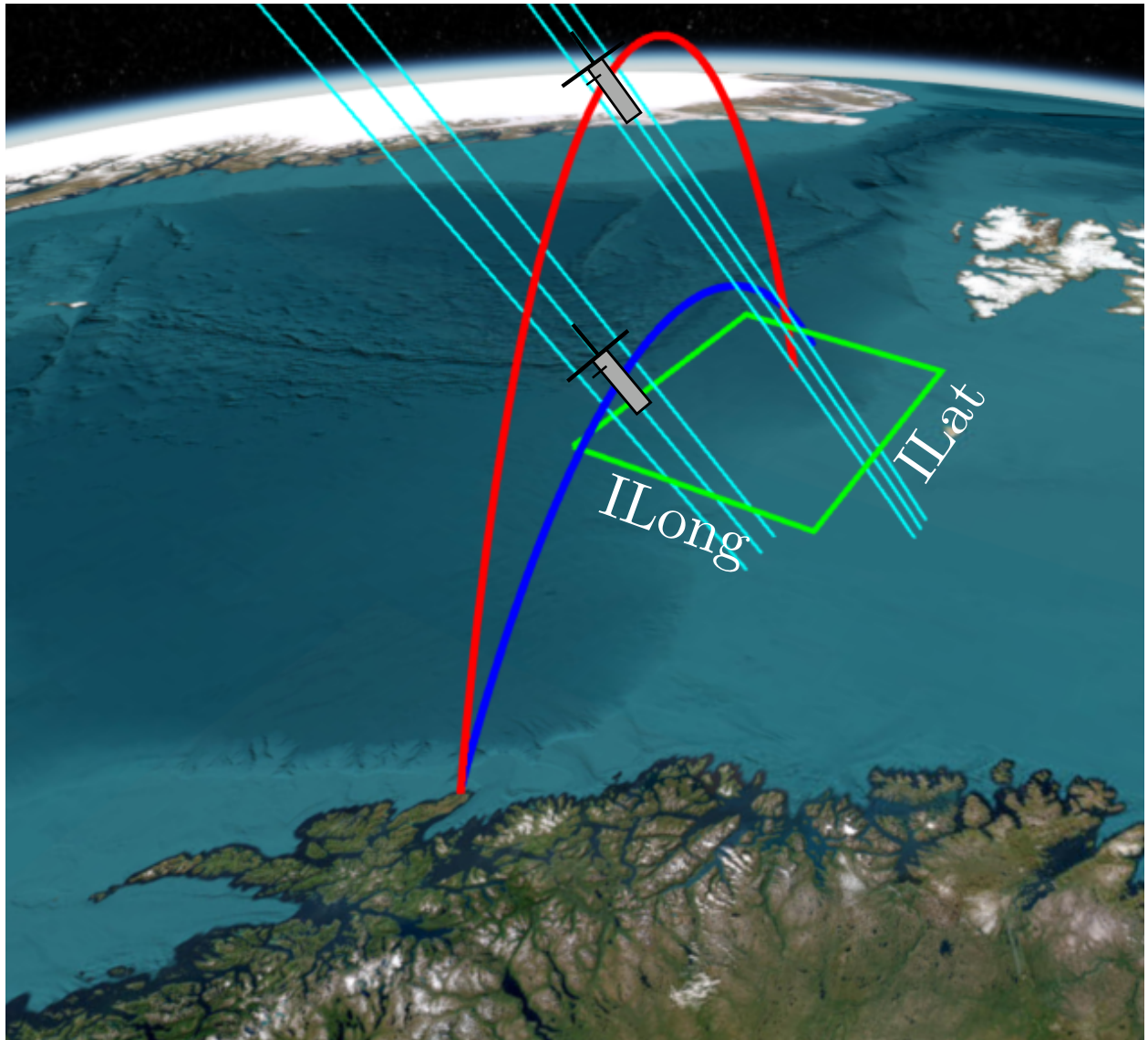


Figure 60. Schematic showing the projections of the geomagnetic fields to 150 km. The green box represents the plane of ILat/ILong. MATLAB's geoplot3 package was used to plot this figure.

All spatial values are given in kilometers using the conversion between latitude/longitude:

$$1^\circ\text{Lat} = (111.319488) \text{ km} \quad (147)$$

$$1^\circ\text{Long} = (111.319488) \cos(\text{Lat}) \text{ km} \quad (148)$$

This procedure assumes that Earth's curvature is negligible by determining the planar intersection of the  $\hat{\mathbf{b}}$  vector. Accounting for this effect would introduce negligible corrections at these altitudes.

For this thesis, we use a reference altitude of 150 km for our coordinates since this is a conservative estimate for the E-Region of the ionosphere. The result of this coordinate transformation is that rockets at the same ILat/ILong are considered to be on the same geomagnetic field line, an approximation that holds better when closer to Earth. Furthermore, this coordinate system aligns data based on the static geophysical magnetic field, which should line-up slow-moving auroral forms seen by both payloads. Attempting to align data with geographic or geomagnetic coordinates does not produce this effect.

Plots of magnetic conjunction between 17:23:20 UTC to 17:27:20 UTC of the payloads are shown in the Figure 61, where the difference in ILat in space and time are displayed.  $\text{ILat}\Delta\varphi$  is the latitudinal distance (in km) between the Low Flyer's footprint compared to the High Flyer's. The High Flyer leads the mission, so the plot begins with a positive  $\text{ILat } \Delta\varphi$  but the Low Flyer's footprint eventually overtakes it around 17:26:00 UTC. Similarly,  $\text{ILat } \Delta t$  is the lag time for the Low Flyer's footprint to reach the same ILat value as the High Flyer. A  $\Delta t = 0$  implies the payloads observe the same magnetic field lines at the same time, assuming insignificant variation in the longitudinal differences of the payload's footprints. The best magnetic alignment occurred at 17:25:50 UTC, which is approximately near apogee for both rockets as shown in Figure 58. Similarly, the ILong distance vs time is shown in Figure 62 with an identical interpretation but in the zonal direction. Notably, the delay time in longitude is not significantly meaningful since several longitudes are not crossed by both payloads until very large time delays occur. Finally, we show a projection of both payload trajectories along with their ILat and ILong paths at 100 km in Figure 63 to give an overview.

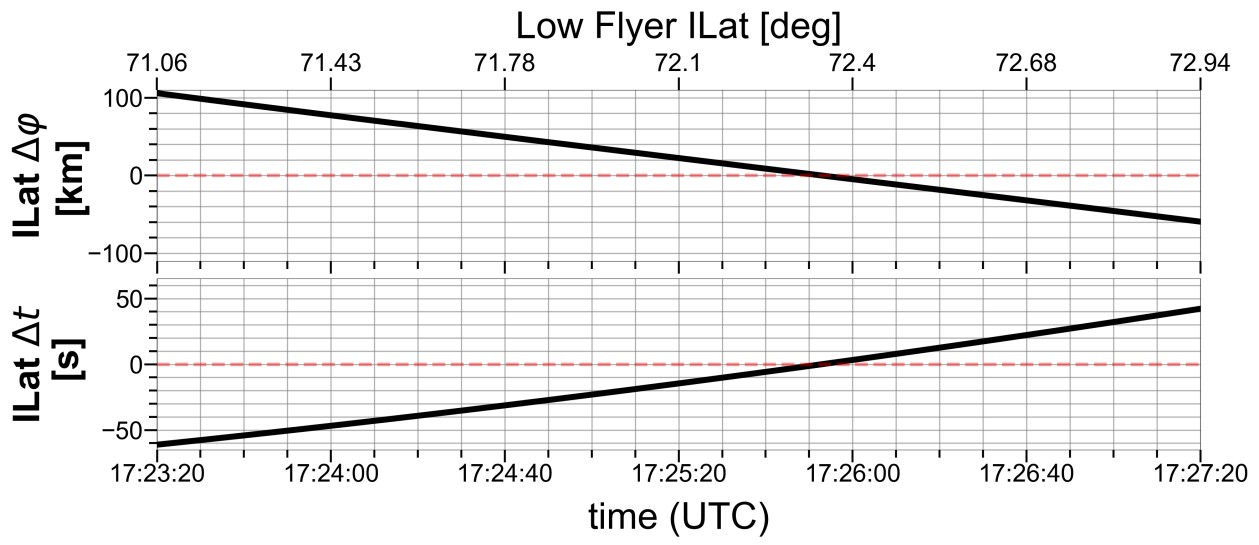


Figure 61. Magnetic conjunction between the payloads expressed in Ilat coordinates referenced to 150 km.  $\Delta\phi$  is the latitudinal distance between the payload footprints and ILat  $\Delta t$  is the lag time.

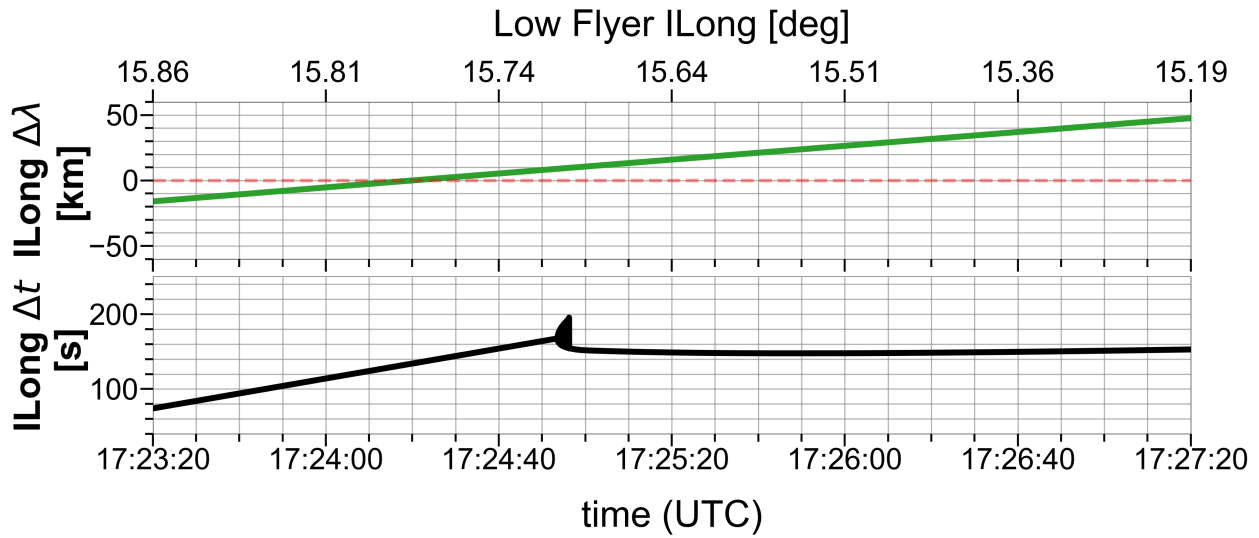


Figure 62. Magnetic conjunction between the payloads expressed in ILong coordinates referenced to 150 km.  $\Delta\lambda$  is the latitudinal distance between the payload footprints and ILong  $\Delta t$  is the lag time. Notably, the delay time in longitude is not significantly meaningful since several longitudes are not crossed by both payloads until very large time delays occur.

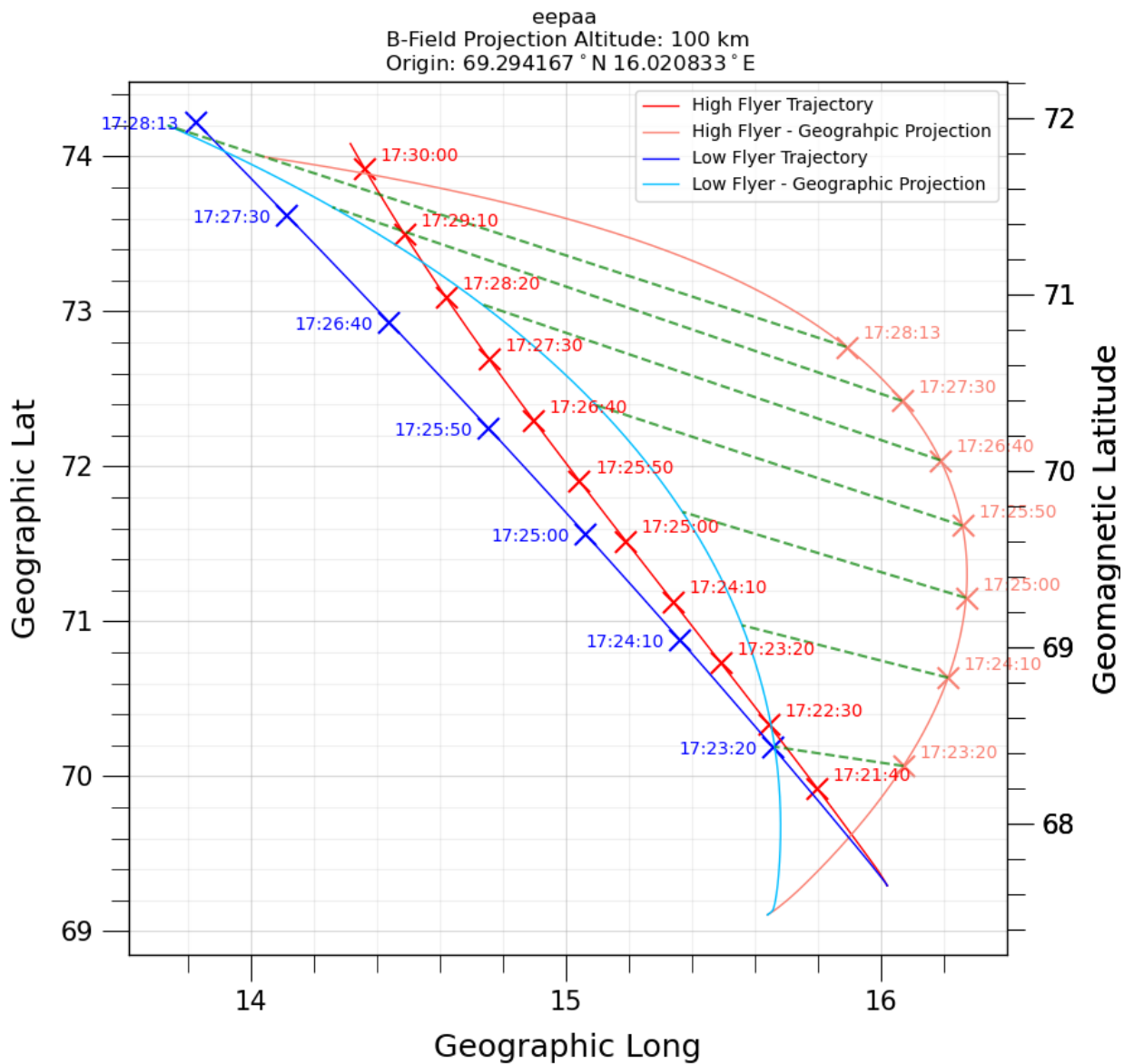


Figure 63. Magnetic conjunction between the payloads expressed in geographic coordinates Lat/Long for a projection of the magnetic field at 100km. The dark blue line is the Low Flyer Trajectory and its associated ILat/ILong coordinates are shown in lighter blue. The Higher Flyer trajectory is shown in red with it's ILat/ILong projection shown in orange. Select times are shown as "X" marks and a green line links the positions of the payloads here.

## **6.2 Performance and Issues**

As with most experimental scientific endeavors, this mission suffered a few mechanical and instrumental issues but was otherwise successful. The Low Flyer maintained minimal coning ( $0.35^\circ$  at 0.1 Hz) but the High Flyer experienced a deployment issue that manifested as strong coning ( $\sim 6.5^\circ$  at 0.05 Hz) between spin and velocity. The RingCore magnetometer data on the High Flyer suggested a minor impact during release of the nosecone due a sudden spike in magnetometer activity during this time, although this was never confirmed officially. This coning prevented continuous coverage of the High Flyer's EEPAA  $0^\circ$  and  $180^\circ$  pitch bins and introduced significant noise into the magnetometer data at the coning frequency and harmonics. Furthermore, the High Flyer's EFI data was deemed unusable as the booms failed to deploy. Additionally, an unwanted RC decay on the EEPAA's inner hemisphere on both payloads limited the detectable energy range to 28.22 eV - 13.7 keV, leaving 41 reliable energy channels. A similar issue occurred during the testing of ACE instrument on the SMEX mission called TRACERS wherein this problem was finally understood. The source of the RC decay was the voltage steps on the inner hemisphere that required 49 rising energy steps and 1 retrace-step to go from the highest voltage on the analyzer down to the lowest within 1 ms. The internal circuitry of the EEPAA was not capable of driving the voltage low enough during its allotted 1 millisecond and instead took 1 + 8 milliseconds to finally re-align with its setpoint voltage during each sweep. The TRACERS instrument fixed this by stepping up the voltage and then back down in a stair-step pattern. However, this issue could not be solved for ACES-II since it was discovered post-launch. These issues are illustrated in Figure 64. We note again that the gain within the swept Langmuir probe instrument on both payloads was set too large to resolve the characteristic curve, explained in detail in Chapter 5.6.

## **6.3 ESA Calibration**

A series of calibration steps are taken to ensure the quality of the flux measurements from the ESA detectors. Here we will focus on the EEPAA detector, although the following procedures

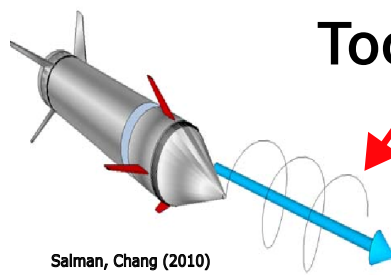
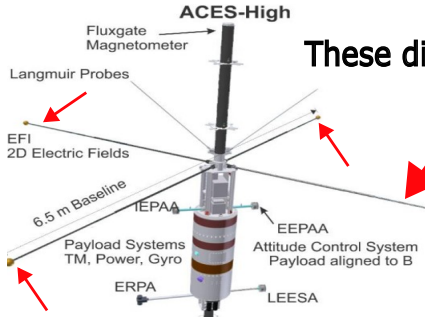
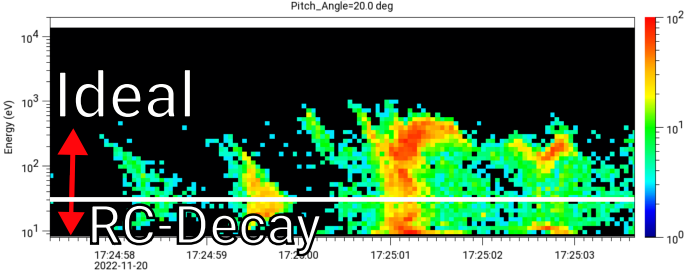
Issue	Description	Fixable?
Severe Rocket Coning (High Flyer)	 Too large <small>Salman, Chang (2010)</small>	Yes
EFI Booms Gearbox Failure (High Flyer)	 These did not deploy	No
EEPAA RC Decay	 Ideal RC-Decay	No

Figure 64. The three primary issues ACES-II suffered during flight.

apply for both the IEPAA and LEESA. The ESA detectors measure counts, for which Poisson statistics applies to the measurement: the number of measured counts occurs within a fixed interval of time where each count is determined independently from previous counts. For any particular time interval where  $N$  counts are measured, the error on that measurement is given by  $N \pm \sqrt{N}$ . Thus, a measurement of  $N=2$  represents  $\sqrt{N}/N = 70.7\%$  error. For this reason, the very first calibration step taken on the raw counts data for the EEPAA detector is to threshold away any datapoints with  $N \leq 2$  counts since the error in these measurements is essentially as large as the measurement itself. The next calibration step is to account for pitch angle misalignment.

On the EEPAA instrument there are pitch angle sectors  $\alpha_k = -10^\circ, \dots, 190^\circ$  that are defined

by the placement of the instrument's anodes used to collect particles only from a specific range of pitch angles e.g. pitch sector  $\alpha_2 = 10^\circ$  should only report fluxes with pitch angle  $10^\circ \pm 5^\circ$ . To improve the accuracy of the EEPAA data, an *in situ* calibration process is employed to ensure the validity of these pitch angle pads. For these sectors to be accurate requires the spin-axis of the rocket to be aligned to the geomagnetic field. However, variations in  $\vec{B}_{geo}$  may break this alignment briefly and cause incorrect reporting of fluxes from certain pitch angles sectors. The fix is simple: calculate the pitch angle at every EEPAA sweep and see if it falls outside of the  $\alpha_k \pm 5^\circ$  range of the pitch sector. If it does, then re-bin to the correct sector and average it with any existing data. To determine when this overlap occurs, we calculate the angle between velocity the unit vectors that are defined by the EEPAA instrument itself and the direction of  $\vec{B}_{geo}$ , given by the magnetometers. The pitch angle bins of the EEPAA represent the velocity vectors of the incoming particles and by taking the dot product between these unit vectors  $\hat{n}_k$  and  $\vec{B}_{geo}$  we can determine the *in situ* calculated pitch angle for each EEPAA pitch bin:

$$\alpha_k = \cos^{-1} \frac{\hat{n}_k \cdot \vec{B}_{geo}}{|\vec{B}_{geo}|} \quad (149)$$

As stated, if  $\alpha_k$  falls out of its designated pitch angle bin by  $> 5^\circ$  the data is re-binned and averaged with existing data.

Another calibration step is implemented to account for the variations in manufacturing and sensitivity of each pitch angle pad, which also addresses any degraded performance/variation by the charge-sensitive amplifier circuitry. In principle, if two EEPAA pitch angle pads are exposed to identical flux then they should report identical count values. If this not the case, it may be due to the reasons previously mentioned. We can use the previous calibration step of pitch angle mis-alignment to estimate the sensitivity differences between the pitch angle sectors since those data points represent two pitch angle pads observing electrons with the same incoming pitch angle. Specifically, we can determine a needed calibration factor to bring two EEPAA pitch angle pads into agreement by forming a set of datapairs each time a misalignment occurs. From there we

can use reduced chi square minimization/least-squares fitting techniques to gauging the needed calibration factors between pitch sectors. Data for the minimization is collected the same way as was done for the re-binning of pitch angles i.e. collect the pitch angles that deviated more than  $5^\circ$  from their pitch sector. We call these data values the “uncalibrated values”. The uncalibrated values will be compared to the “principle value”, which is the corresponding value in the pitch sector the uncalibrated value needs to be moved into. For example, suppose at time t and energy E, that a particular counts value is  $N(t, \alpha_1 = 0^\circ, E) = 10$  with a calculated pitch angle  $\alpha = 7.6^\circ$  from equation 149. Since  $|7.6^\circ - 0^\circ| > 5^\circ$  this value needs to be moved into the next pitch sector  $\alpha_2 = 10^\circ$  at time t and energy E, but there’s a value that already exists at position  $(t, \alpha_2, E)$  which we’ll say is  $N(t, \alpha_2 = 10^\circ, E) = 25$ . Here  $N = 10$  is the uncalibrated value and  $N=25$  is the principle value and we see the difference in counts is significant. We will label this data pair as  $(N_u, N_p)$  To collect the whole dataset for  $\chi^2$  we start by focusing on one pitch sector (the principle sector) at a time and search for all such data pair between all other pitch sectors, then move to a new principle sector. An example dataset for the High Flyer EPAA detector is given in Figure 65.

We assume the various differences between the detecting circuits on EPAA can be represented by a single multiplicative calibration factor, call it  $\kappa$ . To determine the value of this calibration factor, we use the reduced chi-square minimization/least-fitting formula:

$$\chi^2_v = \frac{1}{v} \sum_{i=1}^N \frac{(N_{p_i} - \kappa N_{u_i})^2}{\sigma_i^2} \quad (150)$$

where  $v$  is the degree of freedom,  $v = N - m$ .  $N$  is the total number of data pairs found between a uncalibrated and principle angle sector pair and  $m$  is the number of fitting parameters. Here  $v = N - 1$ . The data pairs  $N_{u_i}, N_{p_i}$  are the  $i^{th}$  uncalibrated and principle data point, respectively. The Poisson standard error in each measurement  $\sigma_i$  and is given by  $\sigma_i = \sqrt{\sigma_{u_i}^2 + \sigma_{p_i}^2}$  where  $\sigma_u, \sigma_p = \sqrt{N_u}, \sqrt{N_p}$ . In general, when  $\chi^2 \rightarrow 1$  the fit is good, when  $\chi^2 < 1$  the data is over-fit (i.e. too many free parameters) and when  $\chi^2 > 1$  the fit is poor. Note that this criteria along does not qualify for a full analysis to justify good fitting, and we refer the interested reader to Winkler, 1993 for further

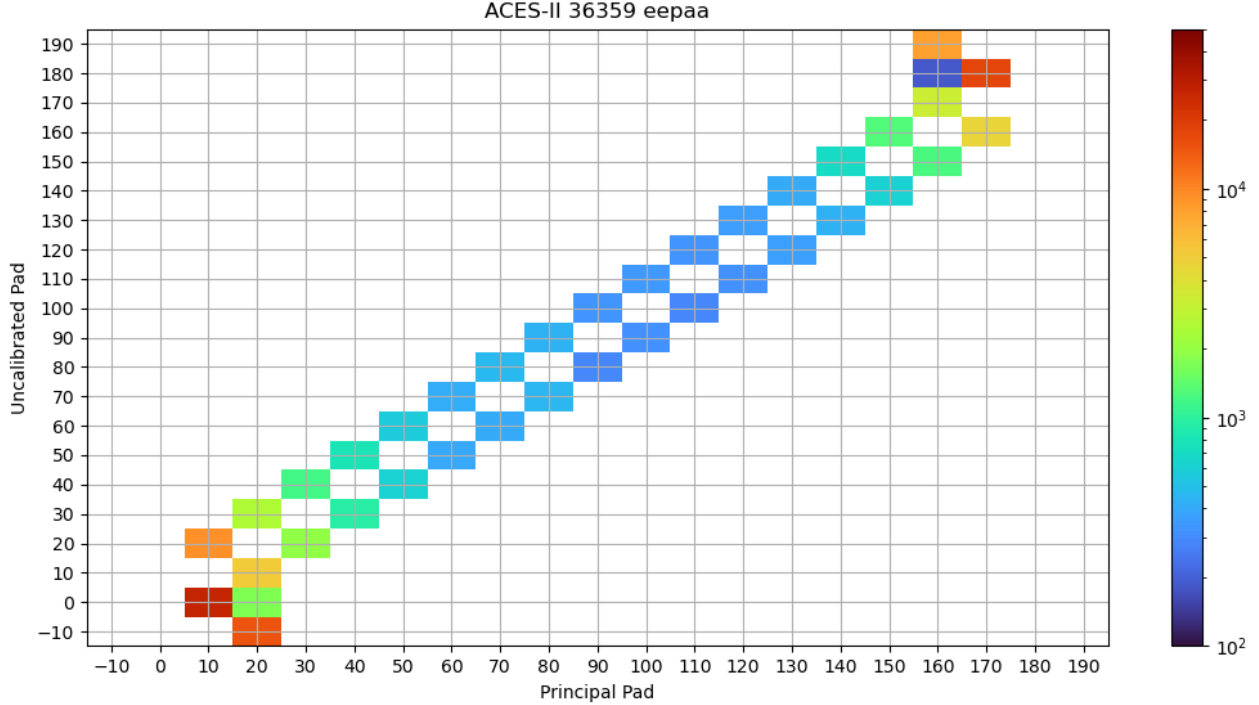


Figure 65. Plot showing the data pairs used in the High Flyer’s EEPAA detector. The principle pad represents a choice of EEPAA pitch angle sector. The uncalibrated pal values for a specific principle pad are the number of datapairs in other pitch angle sectors that need to be re-binned into that specific principle pad. The diagonal reports no values since each prinicpal pad has zero values that need to be re-binned to itself. This particular instrument had significant pitch angle mis-alignment due to the coning of the rocket.

details. For this work, we loop over many  $\kappa$  values until  $\chi^2$  is sufficiently close to 1.

The last complication to this calibration is the choice of which pitch sector should be the reference that all other sectors should calibrate to. Because any one chosen principle pad can have data pairs from multiple uncalibrated pads at the same time, there is a need for a primary reference to correct to. For example, principle pad  $\alpha_3 = 20^\circ$  may share data pairs with  $\alpha_0, \alpha_1$  and  $\alpha_2$ , but  $\alpha_3$  itself may share data points with  $\alpha_4$ . In this situation  $\alpha_0, \alpha_1$  and  $\alpha_2$  don’t share pairs with  $\alpha_4$  so the question becomes “which pad do you reference everything to?”. We decided the pitch sectors that had the most number of uncalibrated sector pairs where chosen as the reference pad. From this chosen pad, all other pads can reference to on another in a chain that terminates at our reference pad.

In addition to the raw counts, the energy steps of the EEPAA are calibrated to ensure their

accuracy. As previously discussed in Chapter 5.3 the theoretical energy response of the ESA depends upon its physical dimensions and the voltage set on the inner hemisphere. These parameters set the accepted energy measured by the detector but also are prone to error. To account for this, a known calibration source of electrons with narrow energies via a Faraday cup is applied and the response of the detectors is recorded. The step number vs. the log of the measured energy is plotted in Figure 66 and the fit between them was used to determine the true energy bins of the EEPAA.

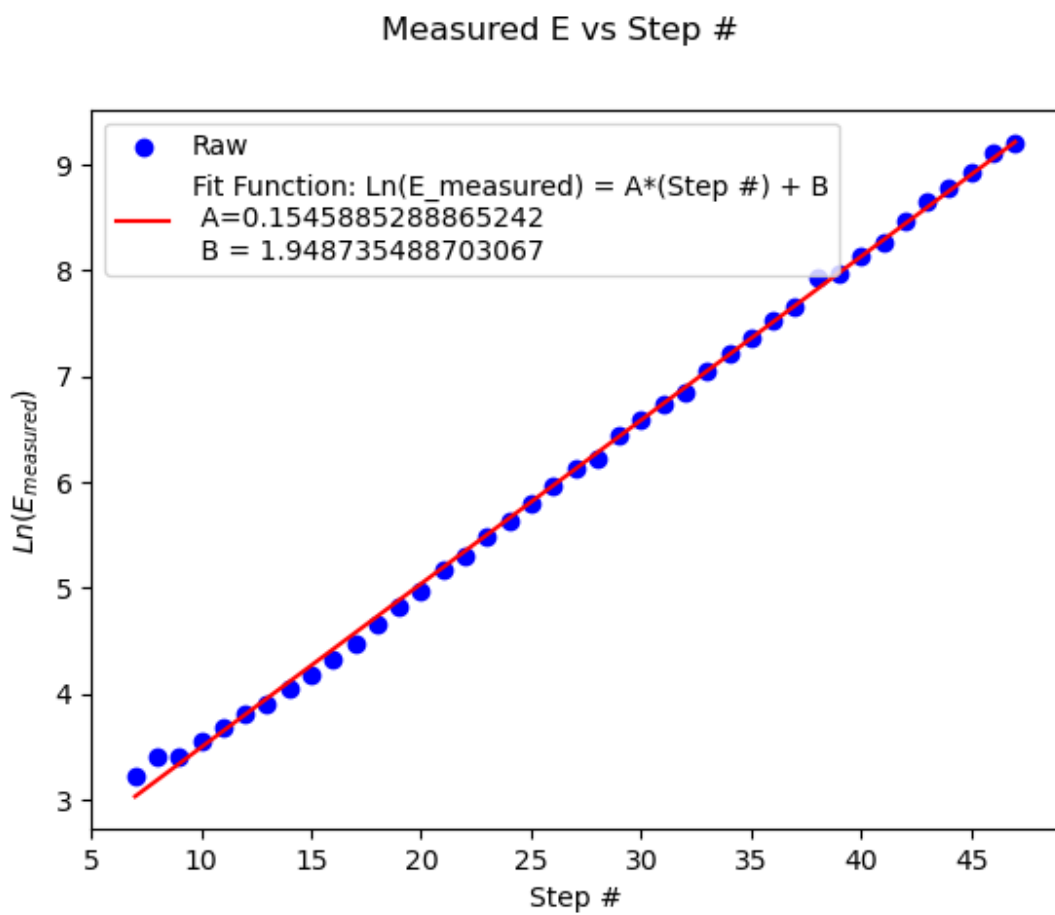


Figure 66. EEPAA Step number vs.  $\log E_{\text{measured}}$  response curve determined using a known electron source. For each step, a calibrated energy value can be determined and was used for the energy bins of the EEPAA detector.

## 6.4 B-Fields - Calibration and Despin

The procedure to convert raw ADC values from the telemetry to scientific measurements of the external magnetic field is a lengthy process that combines both ground-based pre-flight calibrations and in-flight performance. We will start by detailing the steps used by ACES-II, which have been detailed in published works by Greene et al., 2024 and Broadfoot et al., 2022. We will follow a top-level procedure from these two papers in this section for the calibration and despin methods used. We hope the following section is a cautionary tale against using separate clock timings for field measurements instead of syncing to the payload timings.

The first link in the calibration chain is to extract the raw ADC magnetometer and EFI values recorded by the rocket and send down via telemetry (TM) and ensure the time series are correct. Normally this step is omitted in most works since it isn't germane to the science, however ACES-II did not support a magnetometer dedicated to the ACS, which can drastically affect the timestamps of the data for this instrument. This incurs a penalty when attempting to align the ACS data to the magnetometer time series during the despin procedure which can introduce severe errors. For this reason, it is imperative the timestamps between the ACS and the magnetometer are aligned. The EFI instrument was sampled by the rocket TM so there were no temporal issues with this dataset at this stage. The RingCore magnetometer onboard ACES-II, however, sported its own internal clock system to ensure the sample rate of 128 samples/sec was guaranteed. However, only the data from the TM was sent down and any internal timeseries generated by the RingCore's FPGA was not available. This forces a calibration between the rocket's record of the magnetometer data and the known-to-exist (but unavailable) time series generated internally by the magnetometer itself. We will now discuss the methods used to solve this problem.

Since the 128 samples/s of the magnetometer was guaranteed, a new time series that's different from what is reported by the telemetry is constructed. We take the first timestamp given by the telemetry for its record of the magnetometer data and then increment time using our known sample rate for subsequent samples. The first issue to correct with this procedure was that the internal sampling rate of the magnetometer (128 samples/s) differed from the rocket's telemetry

sample rate of the RingCore (200 Hz), resulting in the occasional repeat value in the magnetometer samples. A housekeeping value was sent via telemetry to denote which value is the repeated one. This occurred in a frequency-beating pattern throughout the dataset and was removed. The next issue to correct was the true start time of the magnetometer compared to the telemetry. The initial value that was chosen to start the magnetometer times series comes the moment that TM values are recorded, which may be after the magnetometer itself began recording internally. Since the EFI instrument was synchronized to the rocket we can use the timings of events seen by the EFI and magnetometer to cross-calibrate the initial time value chosen. Five rocket timing events (second stage motor release, nose cone deployment, yo-yo despin, etc) are recorded in the magnetometer and EFI datasets and the times for these were plotted against each other. If the EFI and magnetometer time series had the same initial start time, this method would produce a line with unity slope and zero intercept. A linear fit between corresponding axes of each instrument gave a slope near  $m = 0.999986$  and intercept of around  $b = 0.03294$  seconds. The constant temporal shift of 32.94 ms was applied to the magnetometer time series and then the dataset was interpolated onto the rocket/EFI time. This puts the RingCore data onto a time series which can be despun effectively by attitude data into geophysical coordinates.

Now that the timings between instruments are corrected, we can begin to implement the calibrations on the ADC magnetometer values themselves. The calibration steps are as follows:

1. Apply scaling factor to ADC values to convert to pseudo-nano-tesla measurements (pre-flight calibration)
2. non-linearity response in instrument (pre-flight calibration)
3. near-zero correction (pre-flight calibration)
4. spin-up model geomagnetic field model into rocket frame
5. use least-squares regression to determine the primary physical calibration corrections in the equation  $B_{model} = R^{-1}A^{-1}S^{-1}(B_{pseudo} - O_{offset})$

## 6. use the attitude data to despin the magnetometer data

The first step is to determine the scaling function that converts raw ADC into nano-testla, a process which is done before launch. A known magnetic field is applied to the instrument along a particular axis via a  $\mu$  metal can, which can produce clean, stable DC magnetic fields along a particular axis of the can. For a series of known  $\vec{B}$  values that are linearly stepped, the resulting ADC value of the magnetometer is recorded. A conversion between  $\vec{B}$  and ADC value is made by fitting this dataset. This is called the “scaling factor” calibration which gives a value in nano-tesla, which is often called a “pseudo-nano tesla” value since many more calibrations must be done.

Ideally, the response of the RingCore should mirror the linearly stepped stimulus field, however internal detector electronics make this often not the case. Instead, an S-shaped curve often appears within the instrument response that must be removed in order to force the instrument into a linear response. The residuals of this process are shown in Figure 67 and a fifth order polynomial is chosen to completely characterize the non-linear aspects of the response. By subtracting this curve from the scaling factor corrected data, we get the “non-linearity” corrected data. Next, the magnetometer data may be off by a single scalar/offset value, which is most easily seen near  $\vec{B} = 0$  or “near-zero”. To calibrate this, the detector is again placed in the  $\mu$  can with a nulling field inside so that  $\vec{B} = 0$  approximately at the point of the magnetometer. If the magnetometer reads differently than  $\vec{B} = 0$  along the axes of interest, this implies either a near-zero offset in the magnetometer itself or the  $\mu$  can itself may have an offset. To isolate just the magnetometer’s offset, a measurement of the null-field is made  $B_1$  in the detector and then the magnetometer is spun  $180^\circ$  and another value is taken for that axis  $B_2$ . Since the  $\mu$  can’s offset hasn’t changed direction, the “near-zero” calibration offset for one axis is then calculated via

$$B_{offset} = \frac{B_1 + B_2}{2} = \frac{(B'_{offset} + B_\mu) + (B'_{offset} - B_\mu)}{2} \quad (151)$$

Repeating this for each axis gets the pre-flight “near-zero” correction of the magnetometer data.

After launch, the magnetometer data is fit to a geomagnetic field model in order to account

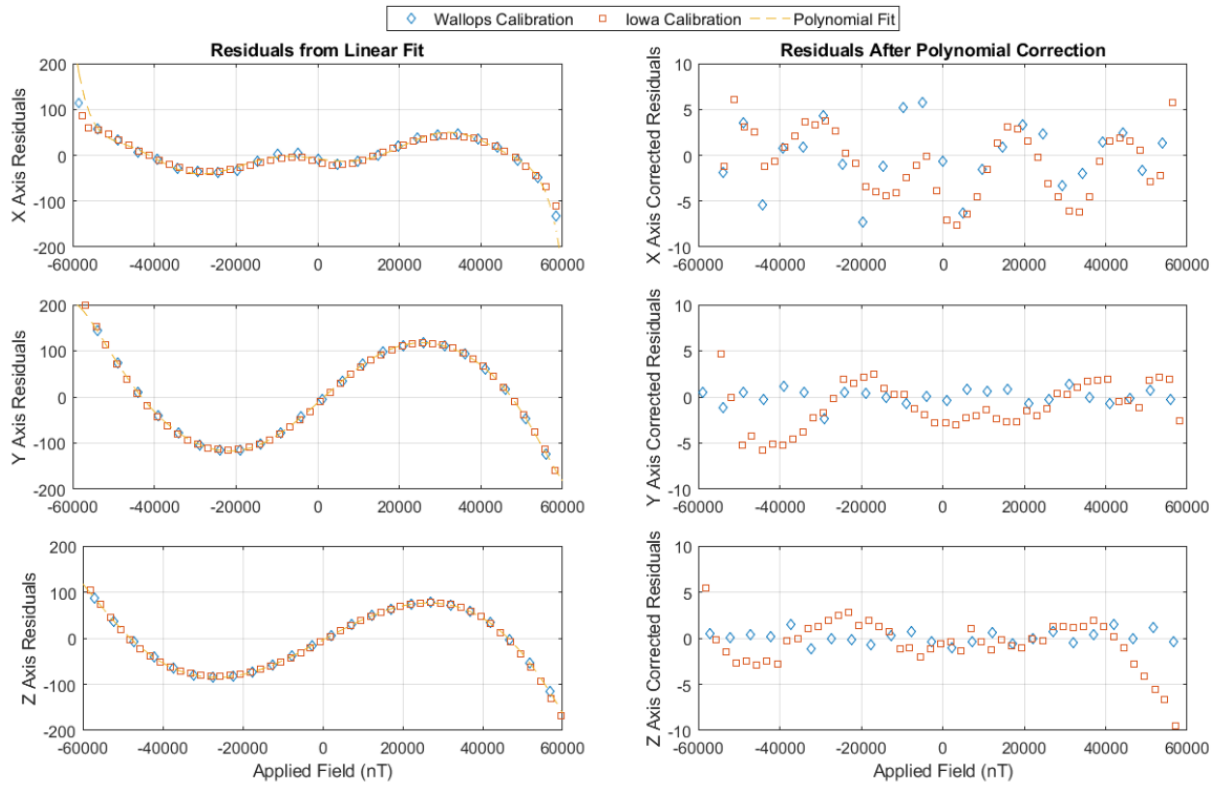


Figure 67. From Greene et al., 2024, used with permission. This data comes from the pre-flight calibrations of the Tesseract magnetometer which flew on the ACES-II Low Flyer. (left column) The S-shaped response residuals. These are derived from taking the ideal linear response of the external field and subtracting the actual response as measured by the detector. (Right column) the residuals of the actual detector response after a 5th-order polynomial was used to characterize the non-linear aspects of the detector response, and then subtract out the non-linearity.

for the various physical errors that arise from being mounted to a rocket body. To do this, the model field must be “spun-up” into the rocket frame. This requires a discussion of the spinning magnetometer frame and the transformation matrix provided by the attitude data to convert payload coordinates into geophysical coordinates. Recalling back to the coordinate system in Figure 48, the magnetometer has its own coordinate system within the rocket coordinates called the RingCore frame. This frame has axes XYZ and can be (ideally) transformed into the payload XYZ frame a singular  $90^\circ$  rotation about the RingCore Z-axis. In flight, the magnetometer spins at the rocket’s spin rate  $\omega_s$  and also the coning frequency (if present)  $\omega_c$ . This introduces coupled sinusoidal oscillations into the magnitude of the measured magnetic field  $|\vec{\mathbf{B}}|$  measured by the magnetometer, which is shown in Figure 68.

## Magnetometer Coordinates

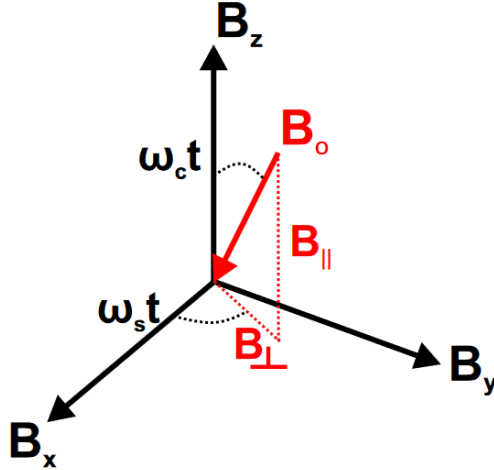


Figure 68. Fixed RingCore magnetometer frame that shows how the oscillations from the rocket spin and coning get introduced into the measurement of  $|\vec{B}|$ . Ideally, the Z-axis of the RingCore frame is perfectly aligned to  $|\vec{B}|$ . The most apparent frequency is the spin  $\omega_s$  and if rocket coning occurs  $\omega_c$  will also be seen in the spun data. This particular RingCore frame is also shown in Figure 48. Image from Kaepller, 2013, used with permission.

This spinning measurement in the RingCore frame can be represented as the vector

$$\vec{B}_{measured}(XYZ) = \begin{bmatrix} B_X \\ B_Y \\ B_Z \end{bmatrix} = \begin{bmatrix} |\vec{B}| \cos \omega_c t \cos \omega_s t \\ |\vec{B}| \cos \omega_c t \sin \omega_s t \\ |\vec{B}| \cos \omega_c t \end{bmatrix} \quad (152)$$

To despin these measurements into a geophysical coordinate system requires rotating the vector in equation 152 in the opposite direction of the payload motion. The Direction Cosine Matrix (DCM) from the attitude data is provided by Wallops Flight Facility (WFF) specifically for this purpose. The DCM is a real, 3x3 unitary ( $AA^T = AA^{-1} = A^{-1}A = A^TA = I$ ) matrix expressing the payload body frame axes column vectors in the coordinates of the local geodetic East, North, Up (ENU) reference frame. The ENU frame itself is an instance of the Earth-centered Earth-Fixed (ECEF) coordinate system. The application of this matrix to equation 152 results in a magnetic measurement in the ENU coordinates,  $\vec{B}_{ENU}$ :

$$\begin{bmatrix} B_E \\ B_N \\ B_U \end{bmatrix} = (DCM_{3x3}) \cdot \vec{\mathbf{B}}_{measured}(XYZ) = \begin{bmatrix} A_{11} & A_{12} & A_{13} \\ A_{21} & A_{22} & A_{23} \\ A_{31} & A_{32} & A_{33} \end{bmatrix} \begin{bmatrix} B_X \\ B_Y \\ B_Z \end{bmatrix} \quad (153)$$

where the  $A_n$  values are the elements of  $DCM_{3x3}$  and are defined for each sample in the attitude data. Typically the attitude data is sampled at lower cadences than scientific instruments, which requires interpolation of the  $A_n$  values. This can be a source of significant error if the time series for the attitude data and scientific instruments aren't carefully aligned. The DCM matrix in equation 153 can be used to convert ENU coordinates to payload frame ENU and vice versa through its inverse. We use the CHAOS-7 model to define a  $B_{geo-model}$  in ENU coordinates at every position and time using the attitude data, then apply the inverse transform  $DCM_{3x3}^T$  to spin-up this model field.

By using a least-squares regression on the spun magnetometer data to match the the spun-up model field, we can calibrate the magnetometer data for *in situ* scalar offsets, orthogonality, instrument sensitivity and rotation mis-alignment. This type of calibration accounts for the magnetometers noise due to proximity to ferromagnetic materials, other electronics noise and the dipole-like field generated by the payload's power supply. To start, we identify the regions in the magnetometer data where the rocket has undergone it's final yo-yo de-spin thereby entering the ballistic projectile portion of it's flight i.e. the “scientific region” where no additional rocket maneuvers are left. The spun-up model field will not display any perturbations due to auroral activity but the real *in situ* data will. This, however, is not an issue for calibrations if the size of the un-perturbed regions is comparatively large. As mentioned, there are four primary sources of calibration error that must be accounted for in order to bring the spun data into alignment with the spun model field. They are represented in the matrix equation

$$\vec{\mathbf{B}}_{model} = R^{-1} A^{-1} S^{-1} (\vec{\mathbf{B}}_{measured} - O) \quad (154)$$

where  $R^{-1}$  is the rotation correction,  $A^{-1}$  is the orthogonality correction,  $S^{-1}$  is the sensitivity

correction and  $O$  are the scalar offsets for each axis. Conceptually,  $R^{-1}$  represents errors that can be corrected via a 3D rotation caused by misalignment of the magnetometer axes to the payload axes during the mounting process. Similarly, if the magnetometer axes themselves are not perfectly orthogonal (e.g. due to manufacturing) this introduces cross-talk between instrument axes that can be corrected. The sensitivity (or gain) accounts for any differences a particular axes might have when exposed to the same stimulus as another axes. Finally, offsets  $O$  are additional scalar offsets that could not be account for in the pre-flight calibrations. In this analysis of equation 154, we assume that  $\vec{B}_{model}$  is correct and any large differences between our measured  $\vec{B}_{measured}$  are due to one of these corrections. Again, the aurora also introduces variations from  $\vec{B}_{model}$  but these effects aren't removed from calibration because they occur over relatively small time windows compared to the whole science region. The specific details of how to determine  $R^{-1}, A^{-1}, S^{-1}$  and  $O$  are not given here since this work was carried out by Broadfoot et al., 2022. The procedure essentially involves a QL matrix decomposition which extracts the  $R^{-1}, A^{-1}, S^{-1}$  terms as triangular matrices. In truth, directly solving only for the combined product  $H = R^{-1}A^{-1}S^{-1}$  and  $O$  is sufficient for this calibration, however the decomposition provides insight into whether the individual calibration terms are physical. Once the terms  $R^{-1}, A^{-1}, S^{-1}$  and  $O$  are known they are applied to  $\vec{B}_{measured}$  giving a fully calibrated magnetometer measurement.

The final step to despin the magnetometer is to interpolate the DCM onto the RingCore time series and apply it directly, as shown in equation 153. If coning is minimal, this should eliminate any spin-related oscillations that typically occur around 0.6 Hz and provide a DC  $\vec{B}_{geo}$  measurement that contains the auroral  $\Delta\vec{B}$  deflections and any AC signals. However, the coning for the High Flyer was significant and the techniques used to address this are discussed in section 6.7.

## 6.5 E-Fields - Calibration and Despin

As mentioned, the EFI probes on the High Flyer failed to deploy thus we will only briefly discuss the calibrations and de-spin for the Low Flyer EFI instrument. Because the Low Flyer exhibited controlled and minimal coning, the application of the DCM directly to the EFI data was sufficient to adequately despin the data after the DCM was interpolated onto the EFI timebase. Before this, the timestamps for this instrument were aligned via a scalar time offset to the fixed magnetometer timestamps from the previous section using identifiable payload events (nose-cone deploy, etc) seen by both instruments. This work was carried out primarily by R. Roglans from U.C. Berkeley.

The most important post-despin calibration step is to account for the induced electric field from the convection of the geomagnetic field across the probes. To account for this requires a Lorentz transformation from the rocket frame (primed) to the plasma rest frame (unprimed) using (Di Mare et al., 2024):

$$\vec{\mathbf{E}} = \vec{\mathbf{E}}' - \vec{\mathbf{v}}_{sc} \times \vec{\mathbf{B}}_{geo} \quad (155)$$

and  $\vec{\mathbf{B}} = \vec{\mathbf{B}}'$  for the non-relativistic limit  $\vec{\mathbf{v}}_{sc}/c \ll 1$ . The geomagnetic field is taken from a model of  $\vec{\mathbf{B}}_{geo}$  (IGRF) in this case. Despite the payload velocity of  $\sim 1$  km/s being quite low, not accounting for this correction can lead to significant DC offset in the measurements.

The double probe setup also has a few considerations worth mentioning that give perspective on the calibration of the measurements and why this technique is useful. Not all sources of error listed here were employed in the ACES-II mission. By construction the double probe technique eliminates a few sources of error with the measurements which we will briefly discuss both. Just like Langmuir Probes described in the previous section, the electric potential is a relative measurement which must have a reference voltage to compare against. In general, this is done with respect to the spacecraft chassis ground much like was done for Langmuir Probes:

$$V_m = V_{probe} - V_{SC} \quad (156)$$

where  $V_m$  is the voltage measured by the probe electronics,  $V_{probe}$  is the voltage at the spherical electrode and  $V_{SC}$  is the spacecraft chassis ground. Also similar to Langmuir Probes, the EFI probes in a plasma can charge to a floating voltage that would skew the measured value of  $V_m$  by a few volts, which is often significantly larger than signal of the physics of interest. If another probe is implemented, then difference of the two  $V_m$  measurements eliminates the floating problem via  $\Delta\Phi = V_{m1} - V_{m2} = V_{probe1} - V_{probe2}$ , which has no dependence on the spacecraft ground. Debye Sheath effects are also a source of issue, where the smaller the Debye sphere surrounding the probe the better. Here, the size of the probes themselves are engineered depending upon the environment they encounter, where the conditions of small Debye sheaths compare to the dimension of the probes dictate the size of electrode that should be used. The probes need to be far enough away from the spacecraft itself to avoid the sheath formed around the body of the chassis or cross-talk between other instruments. Photoemission of electrons from sunlight is another consideration since this produces a cloud of electrons round the sensor which can shield the probe voltage. Finally, the geometry of the probes should be as symmetric as possible to avoid systematic errors from sheath effects or charge build-up, however the conductive coating Aerodag is often sufficiently rugged to eliminate this concern.

## 6.6 E and B Fields - Field aligned Coordinates

A particularly useful set of coordinates for the magnetometers and EFI used on ACES-II are a set of field-aligned coordinates  $(\hat{e}, \hat{p}, \hat{r})$ , which align the basis vectors of our electric and magnetic fields data to a CHAOS-7 geomagnetic field model. An illustration of this system is shown in Figure 69. The new basis vectors are (1) the field aligned direction  $\hat{p}$  (2) the east-like direction  $\hat{e} = (\hat{p} \times \mathbf{R}_{sc})/|\hat{p} \times \mathbf{R}_{sc}|$ , where  $\mathbf{R}_{sc}$  is the earth-centered radius vector of the rocket and (3) the north-like coordinate  $\hat{r} = \hat{e} \times \hat{p}$ . This convention works when close to Earth. The transformation starts by interpolating the attitude data onto the RingCore time series and defining a  $\vec{\mathbf{B}}_{geo}$  from the CHAOS-7 model in ENU coordinates for each RingCore Epoch value. Next, the ENU RingCore data is rotated into the XYZ geodetic coordinate system (GEO) via the transformation:

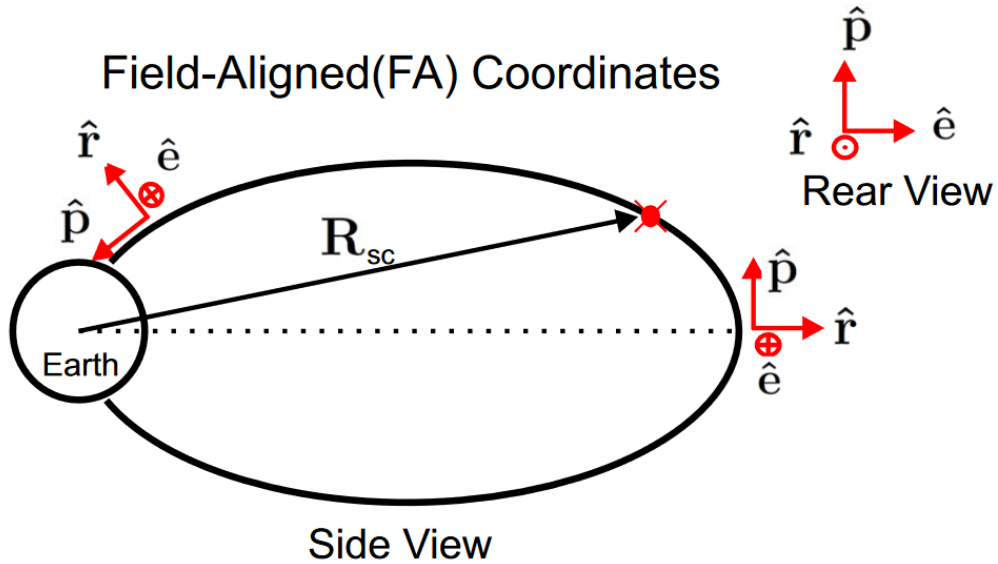


Figure 69. From Kaepller, 2013 and used with permission, defined and inspired from Eriksson et al., 2005. The three coordinates are  $\hat{e}, \hat{p}, \hat{r}$  and are approximately eastward, field aligned and approximately northward, respectively when at low altitudes. The radial vector  $\vec{R}_{sc}$  points to the spacecraft from the center of earth.

$$\begin{bmatrix} B_X \\ B_Y \\ B_Z \end{bmatrix}_{GEO} = \begin{bmatrix} -\sin(\lambda) & -\cos\lambda \sin\phi & \cos\lambda \cos\phi \\ \cos(\lambda) & -\sin\lambda \sin\phi & \sin\lambda \cos\phi \\ 0 & \cos\phi & \sin\phi \end{bmatrix} \begin{bmatrix} B_E \\ B_N \\ B_U \end{bmatrix}_{ENU} \quad (157)$$

for geodetic latitude  $\phi$  from the equator and longitude  $\lambda$ . The payloads position vector  $\vec{R}_{sc}$  is calculated in GEO coordinates using Earth's Radius  $R_E$  and the altitude  $z_{alt}$ , co-latitude  $\theta = 90 - \lambda$  and longitude of the payload via

$$\vec{R}_{sc} = \begin{bmatrix} |R_E + z_{alt}| \sin\theta \cos\lambda \\ |R_E + z_{alt}| \sin\theta \sin\lambda \\ |R_E + z_{alt}| \cos\theta \end{bmatrix}_{GEO} \quad (158)$$

expressed in kilometers. Now that the direction of the model  $\vec{B}_{geo}$  and the payload are within the same coordinate system, we can form a transformation matrix to convert from measured  $\vec{B}_{GEO}$  in equation 157 to field-aligned  $\vec{B}_{FA}$ . The final transformation is then

$$\begin{bmatrix} B_{\hat{p}} \\ B_{\hat{e}} \\ B_{\hat{r}} \end{bmatrix}_{FA} = \begin{bmatrix} \hat{e}_X & \hat{e}_Y & \hat{e}_Z \\ \hat{p}_X & \hat{p}_Y & \hat{p}_Z \\ \hat{r}_X & \hat{r}_Y & \hat{r}_Z \end{bmatrix} \begin{bmatrix} B_X \\ B_Y \\ B_Z \end{bmatrix}_{GEO} \quad (159)$$

where  $\hat{p} = \vec{\mathbf{B}}_{model}/|\vec{\mathbf{B}}_{model}| = (\hat{p}_X, \hat{p}_Y, \hat{p}_Z)$  for each point during the flight and the other vectors  $\hat{e}, \hat{r}$  are defined at the beginning of this section. The value of this transformation is that naturally field-aligned phenomena, such as Alfvén waves, should appear primarily in the  $B_{\hat{e}}, B_{\hat{r}}$  components, making the analysis simpler and more compelling. For any analysis of the AC signals within our RingCore data, the CHAOS-7 DC field was subtracted.

## 6.7 E and B Fields - Coning and Filtering

Filtering of the fields data was done separately for each payload since each payload experienced different amounts of spin and coning. As previously stated at the beginning of this chapter, the Low Flyer maintained minimal coning ( $0.35^\circ$  at 0.1 Hz) about the geomagnetic field but the High Flyer experienced a deployment issue that manifested as strong coning ( $\sim 6.5^\circ$  at 0.05 Hz). These values were determined by using the CHAOS-7 model  $\vec{\mathbf{B}}_{geo}$  and the z-axis of the RingCore magnetometer, which nominally points along the spin axis of the payload as shown in Figure 48. The primary science of this thesis is concerned with low frequency ( $< 10$  Hz) oscillations in the electric and magnetic field, thus excitation's in the RingCore or EFI data at the coning or spin frequencies (and harmonics) contribute significant noise to the interested frequency regime. Here we discuss how these effects were reduced and mitigated, particularly for the High Flyer data.

The first step was to apply a high pass filter to all available fields, removing large DC offsets. The exact same filter is applied to all data. A “forward-backward” technique is employed where the data is first filtered, then the data is flipped along the time-axis and filtered again to produce a zero phase offset from the filtering. After the DCM is applied to the calibrated Low Flyer RingCore data, residual spin tone is still observed as shown in the top panel of Figure 70. In order to preserve any low-frequency physical signal and ensure filter stability, a fourth order 0.7

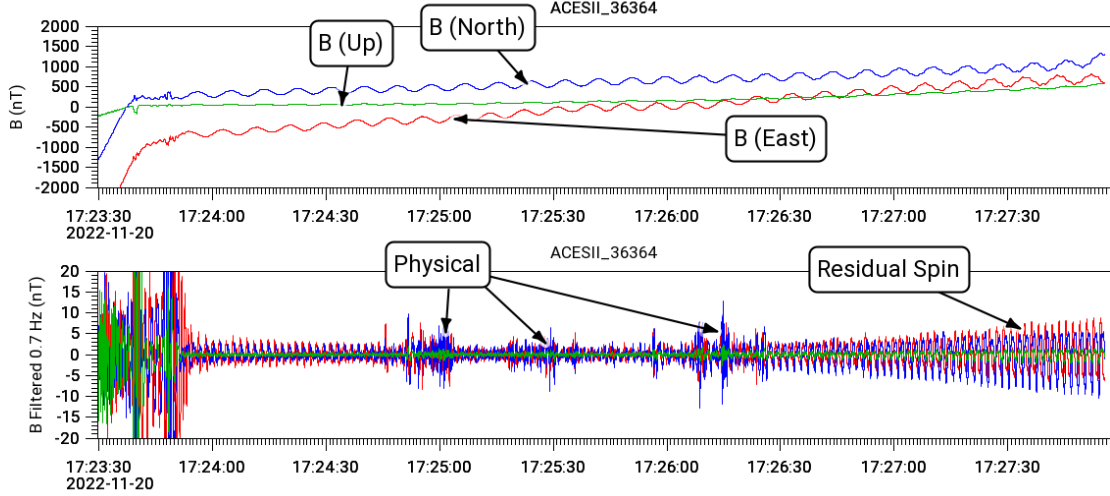


Figure 70. ACES-II Low Flyer calibrated ringcore data in ENU coordinates. (Top) RingCore data with  $\vec{B}_{geo}$  subtracted, leaving only residual spintone (bottom) 0.7 Hz, Highpass, Butterworth filtered data. Clear evidence of AC  $\delta B$  fluctuations can be seen in the filtered data near 17:24:50 UTC along with residual, low amplitude spin-tone.

Hz high pass Butterworth filter is applied to the dataset. This filter is designed to have a -3 dB gain response at 0.7 Hz that rolls-off at lower frequencies. This effectively damps all frequencies below 0.7 Hz and leaves the signal untouched above 1 Hz. The filter gain response is not a step function, so a small fraction of the spin-tone near 0.55 Hz still exists since this frequency is near our chosen 0.7 Hz. The Low Flyer data using this filter is shown in the bottom panel of Figure 70. Despite the filter, residual spin tone at 0.55 Hz is still observed however physical AC fluctuations can be seen throughout. Notably, the DCM is optimized for payload apogee, which is why the residual spin minimizes near 17:25:50 UTC since this is approximately when the Low Flyer reached it's highest altitude and worsens at other altitudes. This filter was applied to the HighFlyer RingCore, Low Flyer RingCore and EFI datasets.

The severe coning on the High Flyer RingCore data introduced significant power into the coning frequency and its harmonics, making the filtering process above significantly less effective. This problem is shown in Figure 71. An envelope of wave power that beats near 0.05 Hz is the result of coning, while the 0.55 Hz spin tone can largely still be seen. However, the excited harmonics of the coning (0.05 Hz, 0.1 Hz, 0.15 Hz, ...) contain significant power and produce

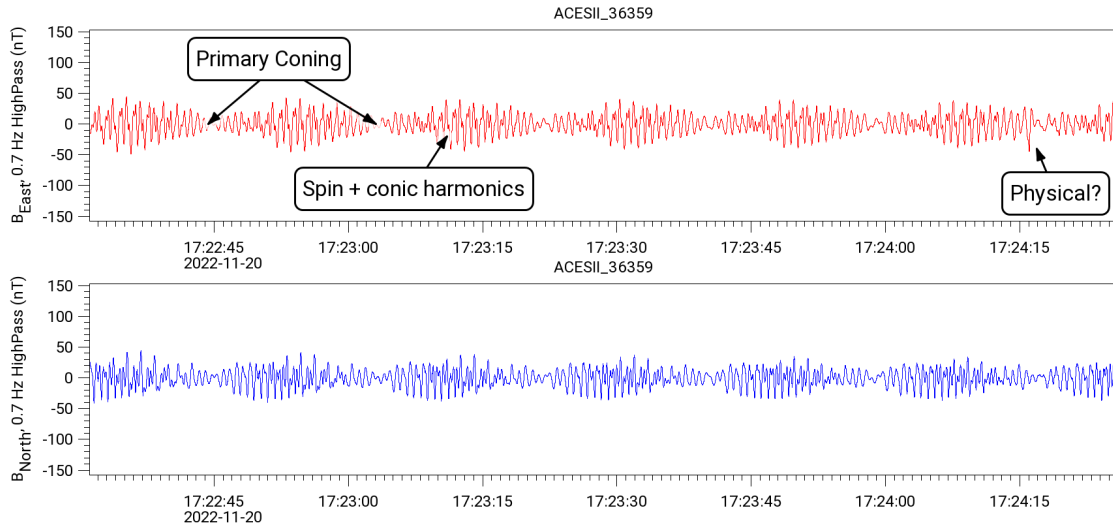


Figure 71. ACES-II High Flyer calibrated RingCore data in ENU coordinates with a 0.7 Hz, 4-th order Butterworth Highpass filter. Only the  $B_{East}$  (top) and  $B_{North}$  components are shown. Due to the coning and excited harmonics of the payload, the depin and filtered signal are still severely contaminated at low frequencies. This motivates the use of a new type of filtering.

a complex interference pattern within this envelope. Furthermore, it is difficult to discern any physical signal embedded within this interference since the amplitude of the spin/coning are larger than any possible signal itself. Only at the edge of the envelope can the possibility of a physical signal be observed, as indicated on the plot. Bandpass Butterworth filters are often the solution here, however, in order to ensure stability they must affect many frequencies at once, which doesn't allow for precise removal of the cone harmonics. To solve this problem requires a new filtering method which we will now describe.

## 6.8 E and B Fields - Multivariate Singular Spectrum Analysis (mSSA) Filtering

(The reference material for this section comes from Hassani et al., 2018, Finley et al., 2023 and a python tutorial found here: <https://www.kaggle.com/code/jdarcy/introducing-ssa-for-time-series-decomposition>)

The filtering technique termed multivariate Singular Spectrum Analysis (mSSA) is the multidimensional extension of the singular spectrum analysis (SSA) method for decomposing time series into “elementary” components. By using sufficient resolution and some guess-and-check, elementary components corresponding to the noise in the input can be isolated and removed with minimal impact to the original signal. This method has seen increasingly widespread application in the fields of Space Physics to solve the types of problems described herein. The foundational principles can be found in the reference material listed above.

Here we will describe SSA first and generalize it to mSSA later. The RingCore magnetometer is a time-series with an associated value at each point. This can be written for a single axis of the instrument  $B_i$  with length  $N$ , as

$$B_i = (f_0, f_1, f_2, \dots, f_N) \quad (160)$$

where  $f_i$  are the magnetic field values of the the axis  $B_i$ . The first step is to map the time series  $B_i$  to a sequence of multi-dimensional lagged vectors using a user-chosen, integer value “L” termed the *the window length*. The window length must be  $2 \leq L \leq N/2$  and we form “windowed” lagged vectors by taking samples of our time series of length L. We slide this window along the time

series, forming a column vector  $\mathbf{X}_i$  for each window:

$$\begin{aligned} X_0 &= (f_0, f_1, f_2, \dots, f_{L-1})^T \\ X_1 &= (f_1, f_2, f_3, \dots, f_L)^T \\ X_2 &= (f_2, f_3, f_4, \dots, f_{L+1})^T \\ &\vdots \\ X_{N-L} &= (f_{N-L}, f_{N-L+1}, f_{N-L+2}, \dots, f_{N-1})^T \end{aligned}$$

These vectors are formed into the L-*trajectory matrix* denoted by  $\mathbf{X}$ . This trajectory matrix looks like

$$\mathbf{X} = \begin{bmatrix} f_0 & f_1 & f_2 & \dots & f_{N-L} \\ f_1 & f_2 & f_3 & \dots & f_{N-L+1} \\ f_2 & f_3 & f_4 & \dots & f_{N-L+2} \\ \vdots & \vdots & \vdots & \ddots & \vdots \\ f_{L-1} & f_L & f_{L+1} & \dots & f_{N-1} \end{bmatrix} \quad (161)$$

This matrix is symmetric across the anti-diagonals. Matrices with this property are called *Hankel* matrices and this step is also referred to as “Hankel-izing” the data.

The next step is to decompose the trajectory matrix with singular-value decomposition (SVD) into its component eigenvectors. The SVD process breaks up the matrix  $\mathbf{X}$  into three matrices  $\mathbf{U}, \Sigma, \mathbf{V}^T$  in the form

$$\mathbf{X} = \mathbf{U}\Sigma\mathbf{V}^T \quad (162)$$

where  $\mathbf{U}$  is a  $L \times L$  unitary matrix of orthogonal left singular vectors,  $\Sigma$  is a  $L \times K$  rectangular diagonal matrix containing L singular values of  $\mathbf{X}$  and  $\mathbf{V}$  is a  $K \times K$  unitary matrix of the right singular vectors of  $\mathbf{X}$ . These definitions and their interpretations stem from the standard SVD process itself and deeper explanation of this are beyond the scope of this work. The point is that  $\mathbf{U}$  and  $\mathbf{V}$  form two orthonormal basis sets which span the column and row-space of the trajectory matrix. Consequently, the matrix  $\Sigma$  (containing the singular values  $\sigma_i$ ) can be used to determine

the relative importance of the eigentriple  $(U_i, \sigma_i, V_i)$  in the expansion of  $\mathbf{X}$

$$\mathbf{X} = \sum_{i=0}^{d-1} \sigma_i U_i V_i^T \quad (163)$$

where “d” is the rank of the trajectory matrix and  $U_i, V_i$  are the vectors of the  $i$ th columns of  $\mathbf{U}$  and  $\mathbf{V}$ . We can define the  $i$ th *elementary matrix* of  $\mathbf{X}$  as

$$\mathbf{X}_i = \sigma_i U_i V_i^T \quad (164)$$

The main takeaway here is that the various  $\mathbf{X}_i$  matrix contributions to the trajectory matrix are expressed through their associated singular value  $\sigma_i$ .

Formally, in order to reconstruct the the original time series  $B_i$ , the individual  $\mathbf{X}_i$  matrices must be converted into a Hankel matrix like equation 161 and then deconstructed into a time series. However, by construction the  $\mathbf{X}_i$  already are Hankel matrices. Proving this fact requires considerable details and we refer the reader to the provided sources for the formal proofs. Skipping to the end, the original time series can be uniquely determined by the sum

$$B_i = \sum_{i=0}^{d-1} \mathbf{X}_i \quad (165)$$

Thus far we have described the SSA process, which applies to a single dimension. To expand this technique to multi axes we must couple the mSSA process together for three dimensions. Simply performing SSA on each individual axis is analogous to filtering the components of a magnetometer dataset with different filters. Luckily, accounting for this is easy. For three time series of equal length N:

$$E_i = \{e_1, e_2, e_3 \dots e_N\} \quad (166)$$

$$N_i = \{n_1, n_2, n_3 \dots n_N\} \quad (167)$$

$$D_i = \{d_1, d_2, d_3 \dots d_N\} \quad (168)$$

we can form the *combined trajectory matrix* by creating the Hankel Matrix for each individual time series and then forming them together like:

$$\mathbf{X}_{mSSA} = \begin{bmatrix} e_1 & e_2 & \dots & e_{N-L} & n_1 & n_2 & \dots & n_{N-L} & d_1 & d_2 & \dots & d_{N-L} \\ e_2 & e_3 & \dots & e_{N-L+1} & n_2 & n_3 & \dots & n_{N-L+1} & d_2 & d_3 & \dots & d_{N-L+1} \\ \vdots & \vdots \\ e_{L-1} & e_L & \dots & e_{N-1} & n_{L-1} & n_L & \dots & n_{N-1} & d_{L-1} & d_L & \dots & d_{N-1} \end{bmatrix} \quad (169)$$

performing the same steps for SSA on the above matrix. Notably, the formation of the mSSA trajectory matrix this way is called the “Horizontal” formulation (H-mSSA), and several authors on the subject recommend the “vertical” formulation (V-mSSA). We recognize this difference, however for the purposes of demonstration equation 169 is enough.

How do we use this in practice? The  $\mathbf{X}_i$  matrices are Henkel matrices that can be converted into their own time series using the chosen window length. These sub-signals are equal in length to the original signal are the *principle components*  $F_i$  of the original time series  $B_i$ , which contains specific frequency information of the original signal. The sum of all  $F_i$  will perfectly recover  $B_i$ ,

$$B_i = \sum F_i \quad (170)$$

however some of the  $F_i$  may be associated with unwanted signal (noise) which can be left out during the reconstruction of  $B_i$ . This is the “filter” part of this technique and it allows us to be more selective with what frequencies are removed from the original signal. To implement this, we appeal to the python library *pymssa* found here: <https://github.com/kieferk/pymssa>, which takes the chosen window length parameter  $L$  and the 3 components of the RingCore magnetometer as inputs.

The result of an example mSSA filter applied to a subsection of the Low Flyer’s RingCore data is shown in Figure 72. The untouched, original signal of the Low Flyer’s  $B_E$  component is shown as “Orig”. Principle components  $F_2, F_3, F_4$  are also shown as examples of what individual

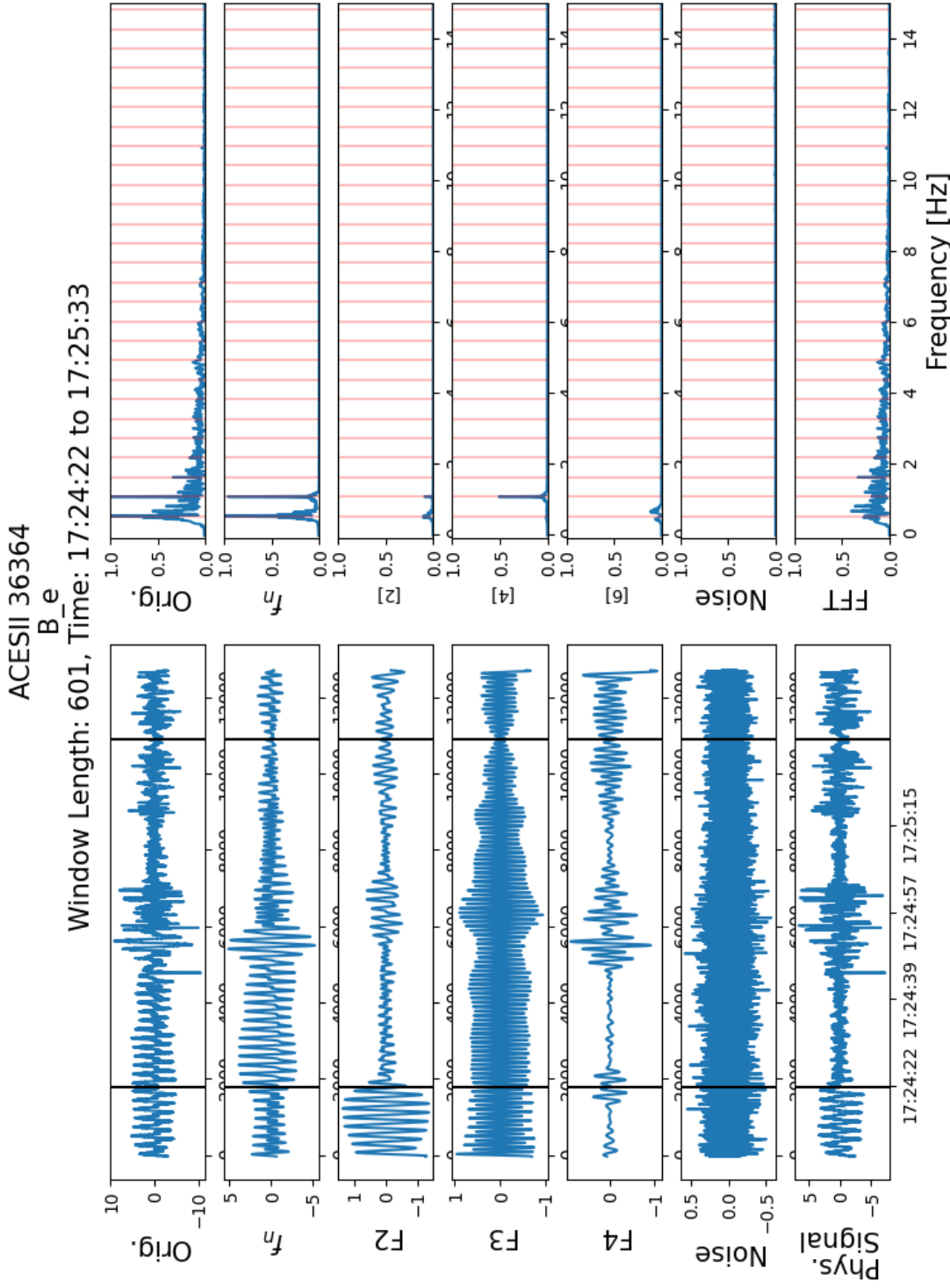


Figure 72. Example using mSSA on the Low Flyer's RingCore  $B_E$  component, used to isolate residual spin-tone in the signal. (Left Column) The original waveform (Orig.), the identified principle components  $F_2, F_3, F_4$  identifiable broadband noise and the resultant signal after reconstruction (Phys. Signal). The black lines denote where 20% of the data has been mirrored in order to avoid mSSA edge effects in the reconstructed signal. This extra data is not included in the final reconstruction. (Right Column) The FFT of each of the waveforms on the left, with red lines denoting the spin harmonics of the payloads. See texts for details.

components look like. The Fourier transform for each of these is shown in the right column, with the spintone (and harmonics) of the rocket denoted with red line. Here, the principle component  $F_3$  is heavily aligned with a harmonic of the spintone based on its FFT whereas  $F_2$  and  $F_4$  are nearer to true physical signal. By plotting each principle component and identifying by eye which are most associated with puretone-noise we can identify which  $F_n$  should not get reconstructed into the overall signal. What is shown in Figure 72 is only for one axes, however if the same type of noise is present in all three axes then the same set of  $F_n$  that identify the noise will work on the other axes. By combining all the identified harmonic signals, we plot their isolated waveform as  $f_n$  in Figure 72. The window length for this particular filter was  $L = 601$ . Higher window lengths offer more components to investigate which improves frequency isolation of the filter, however this comes with the price of steep computational costs and ambiguity in the resulting output since more sub-signals results in less statistical significance to each.

Two mitigation techniques are implemented to avoid large errors in the reconstructed signal. First, to improve the frequency resolution without increasing the window length we can subdivide our RingCore data into chunks and apply the mSSA process on each sub-time series. There are no issues with this so long as the same sets of principle components are removed from all subsets. Second, the removal of certain principle components from the reconstruction will introduce error at both ends of the time series. To mitigate this, the original data is mirrored by 20% of its total length on either end, a step that is commonplace in several filtering applications. The original endpoints are denoted by black bars in Figure 72 and outside these bars represents the mirrored data which is removed before reconstruction of the signal. By doing this, only the mirrored data experiences the edge effects from the removal of components and these sections are later removed.

The result of this more advanced filtering technique is a physical signal that has been selectively (and narrowly) damped in frequency space at the coning and spin frequency. The “Phys. Signal” waveform in Figure 72 is the result for the Low Flyer’s RingCore. This achieves a much greater isolation of the noise signal compared to standard analog or digital filters. Naturally, some of the true wave form’s amplitude is lost in this process as well as some introduced phase shift.

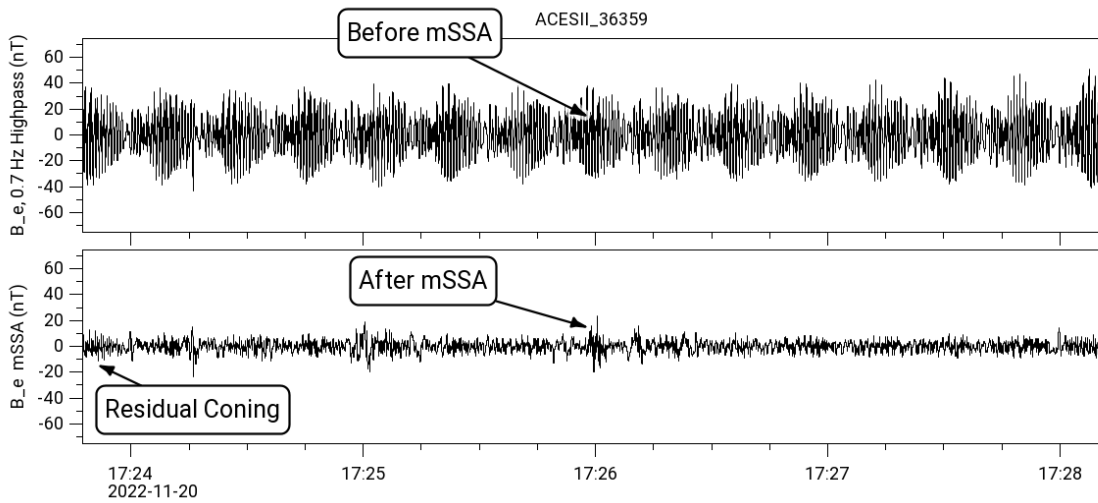


Figure 73. High Flyer RingCore  $B_E$  data. (top) 0.7 Hz, High Pass Filtered (Bottom) Same data, but after the mSSA process is applied to remove spin and coning harmonics. Physical signal is now able to be distinguished at the point labelled “After mSSA”.

As far as we can surmise, this is unavoidable. Nonetheless, the deviations from the true physical signal are small compared to the impact other filtering techniques may have. The process described above is repeated for the Low Flyer’s EFI instrument and the High Flyer’s RingCore data that was shown in Figure 71. In particular, Figure 73 shows the before-and-after of the mSSA process on the High Flyer RingCore data, which highlights the usefulness of this technique.

## 6.9 Langmuir Probe Calibration

In order to employ the ion saturation current via equation 142 the fixed Langmuir probe data must be converted from engineering units to current  $I$ . To do this, several resistor values were chosen and applied (in series) to the probe, with the full -5V probe bias across the resistor. The resulting ADC value is recorded and using Ohm’s Law for current we generate a calibration dataset. A curve is then fitted to this data convert between ADC and amperes. Resistor values 500 M $\Omega$ , 250 M $\Omega$ , 100 M $\Omega$ , 50M $\Omega$ , 10 M $\Omega$  and 5 M $\Omega$  are chosen to produce small currents that represent possible *in situ* values. A log amplifier is implemented on the circuitry to ensure small current values can still be detected as an ADC value, thus the fit of the calibration data is plotted as  $\ln(I_{cal})$  vs ADC. An example of this fit for the High Flyer fixed probe is shown in Figure 74.

This fitted expression is inverted and used to convert ADC to current.

After determination of the *in situ* current, the ion plasma density is calculated from the ion saturation current via equation 142 which requires knowledge of the average thermal velocity of the ions in  $v_{th} = \sqrt{k_B T_i / m_i}$ . Unfortunately, this parameter is entirely unknown to the ACES-II mission since the available ESA detectors energy range is too large to detect thermal ions and were not modified to handle the enormous flux this would produce. Instead, we approximate this parameter using the Tromsø EISCAT radar dataset but take only a slice in altitudes which correspond to our rocket's altitudes. An example of these profiles for the plasma density is shown in Figure 75. Doing this shows an ion temperature that remained approximately constant at  $T_i = 0.1$  eV throughout the entire ACES-II flight. Here we are less interested in any fine details due to the alignment of the EISCAT data, which naturally introduces errors in our measurement of  $n_i$ . Using this value of  $T_i$  and the ion saturation current we can estimate  $n_i$  throughout the entire flight.

The determination of  $n_i$  introduces errors which, again, must be corrected using the available EISCAT data. To do this, we scale the *in situ*  $n_i$  to radar density profiles by identifying iono-

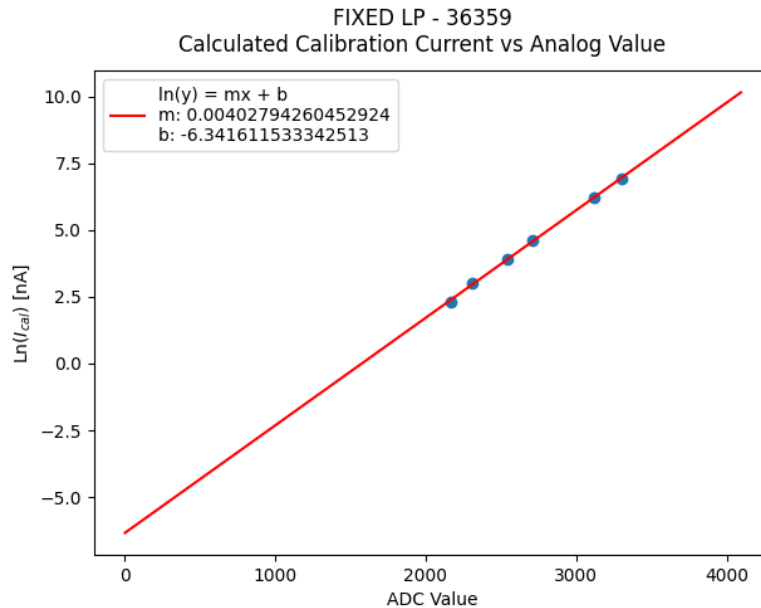


Figure 74. Calibration curve used to convert Langmuir Probe ADC values into current, I. The circuit was designed with a logarithmic respond to input current in order to response to a large range of input current values, hence the circuit response linearly to  $\ln(I_{cal})$  vs ADC.

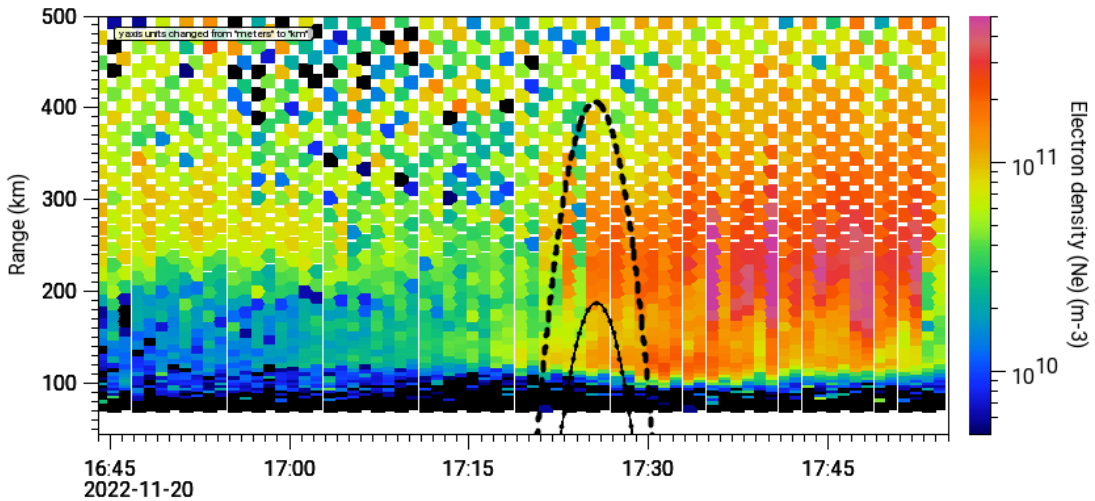


Figure 75. Example showing the path the ACES-II mission took through the Tromsø EISCAT dataset. The particular parameter plotted here is the plasma density. Each available EISCAT parameter was sampled at the altitude and time corresponding to the ACES-II attitude data for comparison to *in situ* data. The ambient ion temperature indicated an average value of  $T_i = 0.1$  eV from this method, which is used to determine the ion saturation current in the Langmuir probes.

spheric E-Region crossings (large enhancements of plasma density around 120 km) in the up-leg journey for both payloads. These E-Region peaks are observed by both payloads and ideally, both rockets observed similar E-Regions so the scaling value is the same. The approximate E-Region density seen by both payloads near 120 km was  $n_i = 9 \times 10^4 \text{ cm}^{-3}$ . It is found that a factor of 1/70 was required for the Low Flyer data to match this peak value, whereas a value of 1/36 was required for the High Flyer's. A single multiplicative scalar value of 1/50 for both payloads was chosen to average any systematic error between the two instruments since their design was identical and shouldn't produce different responses to the same E-region. The result of this process is shown in Figure 76 for both payloads with the nighttime E-region crossings identified on the up-leg journey. These datasets are used to calculate the local Alfvén speed in Chapter 7.5, which is insensitive to small multiplicative factors in plasma density. Despite this, caution must be given since a single-point calibration like we've done has been shown to produce erroneous plasma density scaling when considering density values further away from the single calibration point (Baker

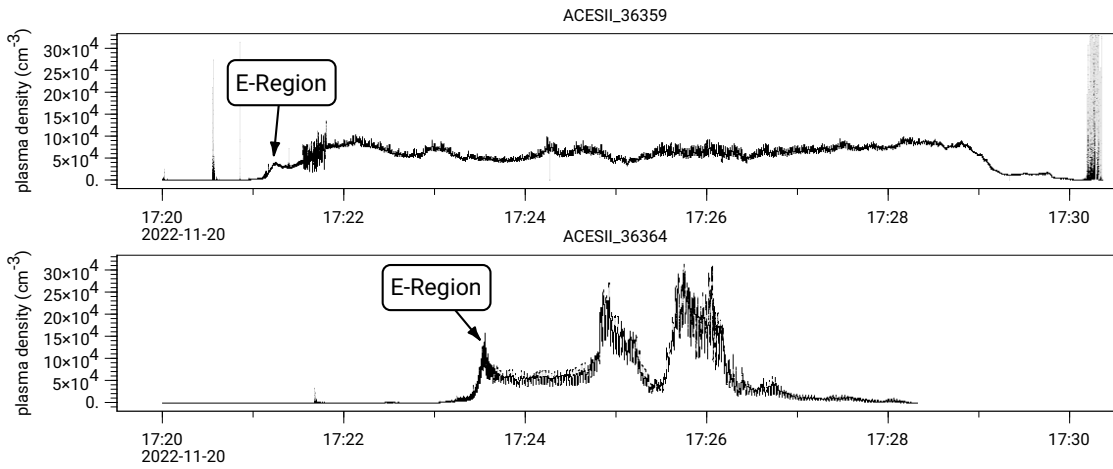


Figure 76. Post-processed Langmuir Probe data using the peak density of E-Region seen by both Flyers as indicated by the EISCAT data. A multiplicative factor of 1/50 is applied to both the High Flyer and Low Flyer's dataset to average out any systemic error since both instruments saw approximately the same E-Region but reported different density values. The LP circuitry was identical for both payloads.

et al., 1985). Thus, we emphasize that this dataset is used only as a "rough" determination of the absolute plasma density and the magnitude of any reported values should be interpreted as such.

## CHAPTER 7: RESULTS AND ANALYSIS

This chapter and the following contain the bulk of the scientific work for the ACES-II sounding rocket mission. Here, we present an overview of the processed data, interpret the physics in the context of a multi-payload dataset and begin to analyze the suprathermal electron bursts that ACES-II observed and were described in Chapter 4.6. The bursts reported here provide some of the first *in situ* evidence for numerically modelled predictions in the previous decades. In particular, section 7.7 of this chapter details the overall objective of this scientific work and how ACES-II is uniquely able to discuss the impacts of a changing source population. This data and its presentation will closely follow the associated paper on this topic (Feltman et al., 2024).

### 7.1 Data Overview

As previously mentioned in Chapter 6.1, ACES-II successfully launched two payloads into a post-dust auroral arc. By plotting the datasets in ILat and ILong we can align the arc-crossings by both payloads as a first step. If the same arc was passed by both payloads, then the ILat/ILong alignment should place the arc around the same spot for both datasets. Figure 77(a) and 77(d) shows electron differential energy flux averaged over all pitch angles for both rockets plotted against ILat. Typical quasi-static inverted-V signatures are observed throughout, with a “primary” inverted-V region between  $72.1^\circ$  and  $72.6^\circ$  ILat in both flyer’s electron data. These features are accompanied by a lesser flux of degraded primaries and secondaries that span energies below the quasi-static flux Evans, 1974. Fewer inverted-V signatures are observed by the Low Flyer, however the same primary inverted-V appears along the same ILats, as expected through magnetic alignment. The other auroral arcs seen in the High Flyer do not appear as strongly in the Low Flyer dataset. Figure 77(b) and 77(e) shows the filtered fields data for component pairs  $\delta B_e, \delta E_r$  on both payloads. Pocked throughout the data are regions of magnetic activity both inside and outside inverted-V features. The *in situ* plasma density is shown in Figure 77(c) and (f) for the High/Low Flyers respectively. There is a general trend between the datasets where the plasma

density grows wherever an inverted-V signature is present, as expected. This effect is most apparent in the Low Flyer. The analysis of the Pedersen and Hall currents from these inverted-Vs to answer the questions of the ACES-II mission is still on-going work. Instead we will focus on a relatively small region embedded in the aurora which showed evidence of suprathermal electron burst (STEB) activity.

The ILats between  $71.9^\circ$  and  $72.05^\circ$  on the High Flyer displayed evidence of STEB features coincident with magnetic fluctuations. Despite the larger noise floor in the magnetic data due to mSSA filtering, a clear localized enhancement of magnetic activity can be seen in the region termed the “Dispersive Region” in Figure 78. Here the fluctuations in  $\delta B_e, \delta B_r$  occurred mainly in the components perpendicular to  $\vec{B}_{geo}$ . On the same Dispersive Region ILats near  $72^\circ$ , the Low Flyer saw scant particle flux but did record strong electric and magnetic field fluctuations near the equatorward edge of its observed primary inverted-V. Similar perturbations are observed on the poleward edge near  $72.7^\circ$  ILat. Despite being on the same ILats, these perturbations are not interpreted as being associated with the Dispersive region and are the subject of another work by K. Greene (submitted as of this writing). Ideally, the Low Flyer observed the same field lines as the High Flyer when the High Flyer was in the Dispersive region. Given the lack of any particle flux on the Low Flyer, this may have not been the case. By using the  $\Delta$ ILat data from Figure 61 we estimate (assuming no longitudinal dependence) the Low Flyer’s Footprint was 40 km away and 20 s behind the High Flyer’s footprint when the High Flyer crossed the Dispersive region. This suggests the time delay between the payloads was too large to expect conjunctive spatial measurements. Indeed, if the Alfvén waves that caused the Dispersive Region were present at the Dispersive Region ILats then they would pass to the lower altitudes very quickly. The Low Flyer could only see them if it was on the same field lines as the High Flyer since they have parallel speeds of order  $10^5$  m/s and parallel wavelengths near 500 km (Schroeder et al., 2021). These waves would not persist long enough for our payloads to observe if there was a significant time delay. This motivates re-alignment of the data in time. Figure 77 (b) and (e) shows the time-conjugate regions boxed in black between the High Flyer’s dispersive region and the time-associated dataset in the Low

Flyer. The new Low Flyer time-aligned dataset displays significant electric and magnetic activity coincident with some electron flux ( $< 10^7 \text{ cm}^{-2} \text{ str}^{-1} \text{ s}^{-1}$ ). In the next section we will zoom into these time-aligned Dispersive Regions.

## 7.2 The Dispersive Region

The zoomed-in view of the temporally aligned, black boxed regions from Figure 77 for both Flyers is shown in Figure 78. The differential energy flux is plotted in panels 78(a) and (e) as energy-time spectrograms at pitch angle  $\alpha = 10^\circ$  and pitch angle vs. time spectrograms between  $0^\circ$  to  $180^\circ$  for energies 28 to 988 eV in panels (b) and (f). Coverge loss due to coning of the High Flyer are seen as white patches in the  $0^\circ$  and  $180^\circ$  bins for Figure 78(b).

The High Flyer EEPAA data shows the Dispersive Region starting at 17:24:56 UTC and lasting  $\sim 11.5$  seconds over a cross track distance of 11.5 km (calculated from a cross-track payload velocity of  $\sim 1$  km/s). Several dispersed STEB events occur both outside and coincident with an inverted-V feature near 17:25:01 UTC. The STEBs are field-aligned in pitch angle ( $\alpha < 40^\circ$ ), high-to-low energy dispersions with a peak energy equal to or less than the nearest inverted-V. The bursts near 17:24:58 UTC repeat with an average frequency of 1.1 Hz, similar to reports from previous studies (Arnoldy et al., 1999; Chaston, Bonnell, Carlson, Berthomier, et al., 2002; Lynch et al., 1999; Lynch et al., 2012; McFadden et al., 1987; Wu et al., 2021). The High Flyer  $\delta B_e$  in panel 78(c) and associated power spectral density (7/8 overlap, Hanning) in 78(d) reveal low frequency (1-6 Hz)  $\delta B_e = \pm 5$  nT activity in the vicinity of the STEBs starting around 17:24:58 UTC and persisting through the entire dispersive region.

At nearly the same time, the Low Flyer saw unclear, burst-like electron features coincident with in-phase, low frequency electric and magnetic field perturbations. The electron data in panels 78(e) and (f) show three faint flux signatures that share similar lifetimes and field-aligned bias to the events in Figure 78(a). If these are low altitude STEB events, only the high energy component should be observed. Work by Semeter et al., 2005 modeled ionization profiles for various electron beams during typical nighttime polar atmospheres and found 100 eV electron flux drops off near

190 km and 500 eV electrons near 150km (Figure 79). This is consistent with our faint signatures that have energies  $100 \text{ eV} < E < 600 \text{ eV}$ . The Low Flyer's  $\delta B_e$ ,  $\delta E_r$  components coincident with the bursts are plotted in Figure 78(g) and (h). Similar to the High Flyer, the Low Flyer observed low frequency (1-8 Hz)  $\delta B_e = \pm 5 \text{ nT}$  activity for 10s, starting at 17:24:54 UTC. The AC electric field component  $\delta E_r$  is clearly in phase with the AC magnetic field, indicative of propagating plasma waves.

The start of the electric/magnetic fluctuations on both flyers is separated by 4 seconds, for which both datasets share similar frequency content ( $< 8 \text{ Hz}$ ) and total lifetime ( $\sim 10$  seconds). One possible explanation is that the same source of wave activity produces the waves at the Low Flyer and then propagates into the path of the High Flyer 4 seconds later. In section 7.4 we evaluate the spatial requirements for this explanation.

# ACES-II Flight

HF: 17:23:51 to 17:27:06 UTC

LF: 17:24:41 to 17:26:31 UTC

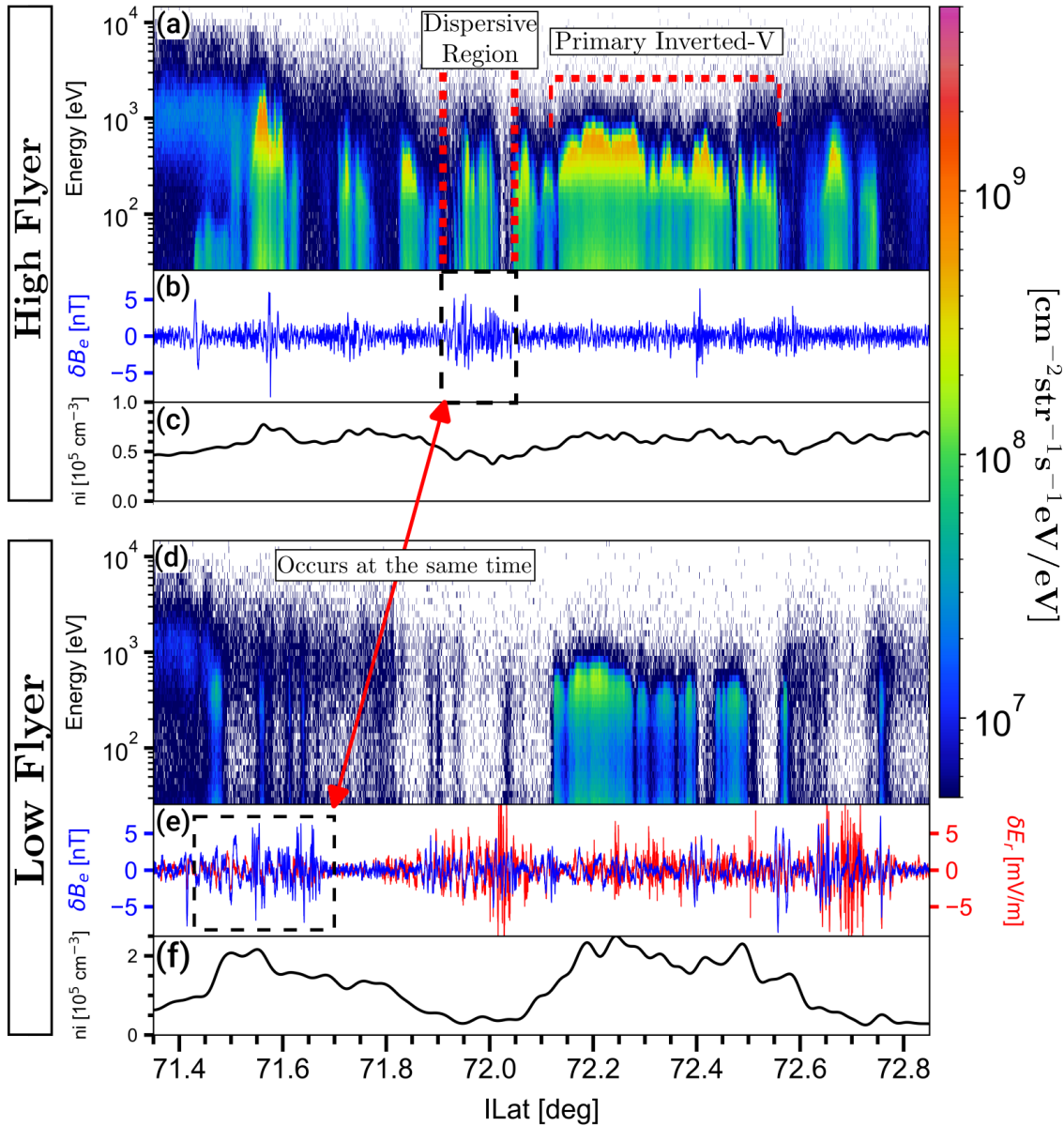


Figure 77. Overview of the EEPAA electron spectra, fields data and plasma density for both payloads plotted vs ILat. (a) Averaged differential energy flux over all pitch angles. (b) 0.7 Hz highpass filtered  $\delta B_e$ ,  $\delta E_r$  component pairs. No electric field measurements for the High Flyer are available. Additional filtering via mSSA was applied to the High Flyer's magnetic fields data to remove rocket coning. (c) 0.3 Hz Lowpass filtered plasma density to remove spin and wake effects. Panels (d) to (f) follow similar format for the Low Flyer. A "primary" inverted-V signature between  $72.1^\circ$  to  $72.55^\circ$  ILat is seen by both payloads. A "Dispersive" region that contained several STEB events is seen conjunctive with  $\delta B_e$  fluctuations in the High Flyer dataset.

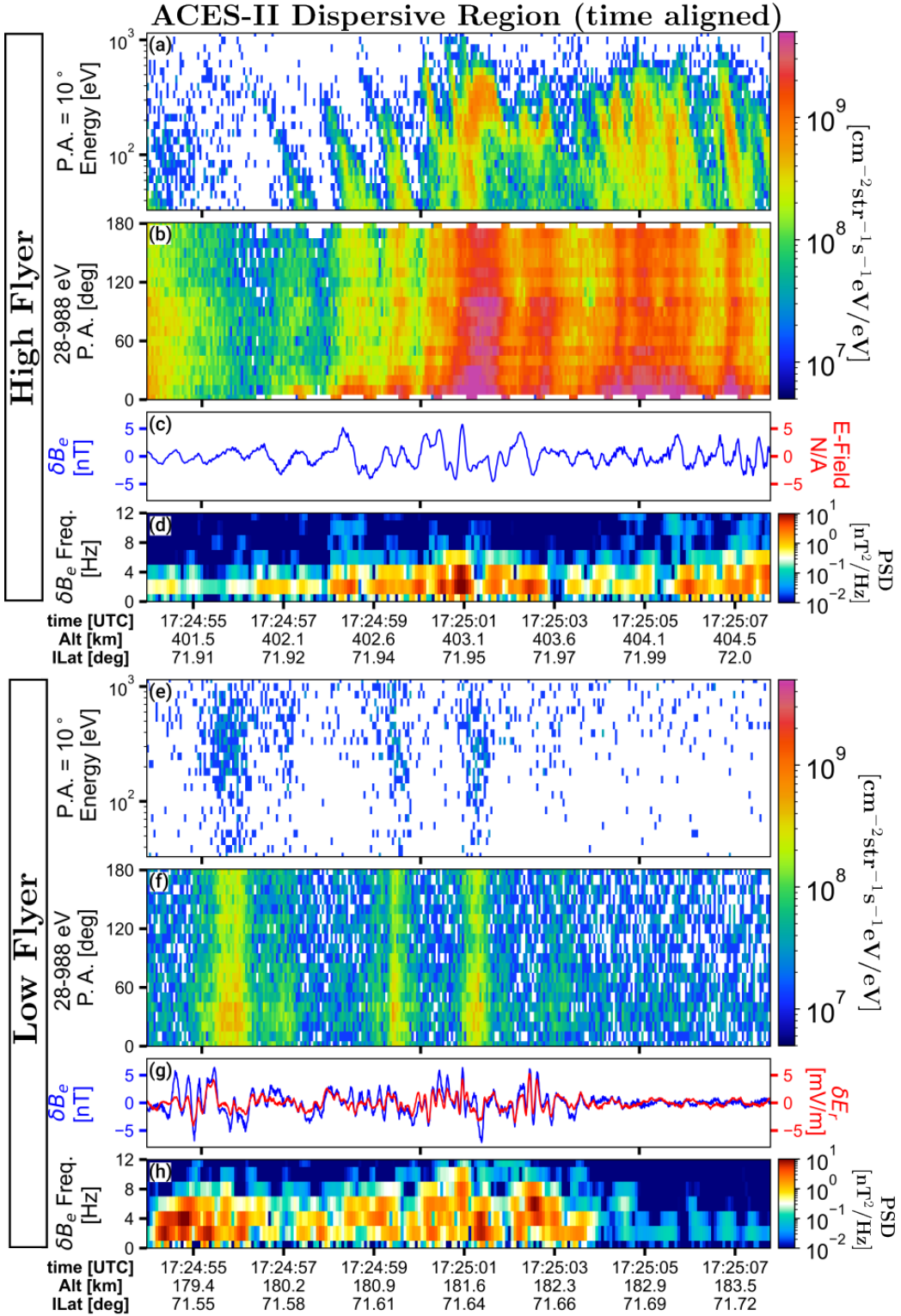


Figure 78. Time-aligned data during the High Flyer's Dispersive Region. EEPAAs differential energy flux (a) energy-time spectrograms at  $10^\circ$  pitch angle and (b) Pitch Angle vs time for 28 eV to 988 eV. (c) Filtered  $\delta B_e$  and  $\delta E_r$  component pairs. (d) Power spectral density of  $\delta B_e$  at 7/8 hanning overlap. Panels (e) to (h) follow similar format for the Low Flyer. Both datasets show burst-like electron signatures coincident with low-frequency magnetic fluctuations.

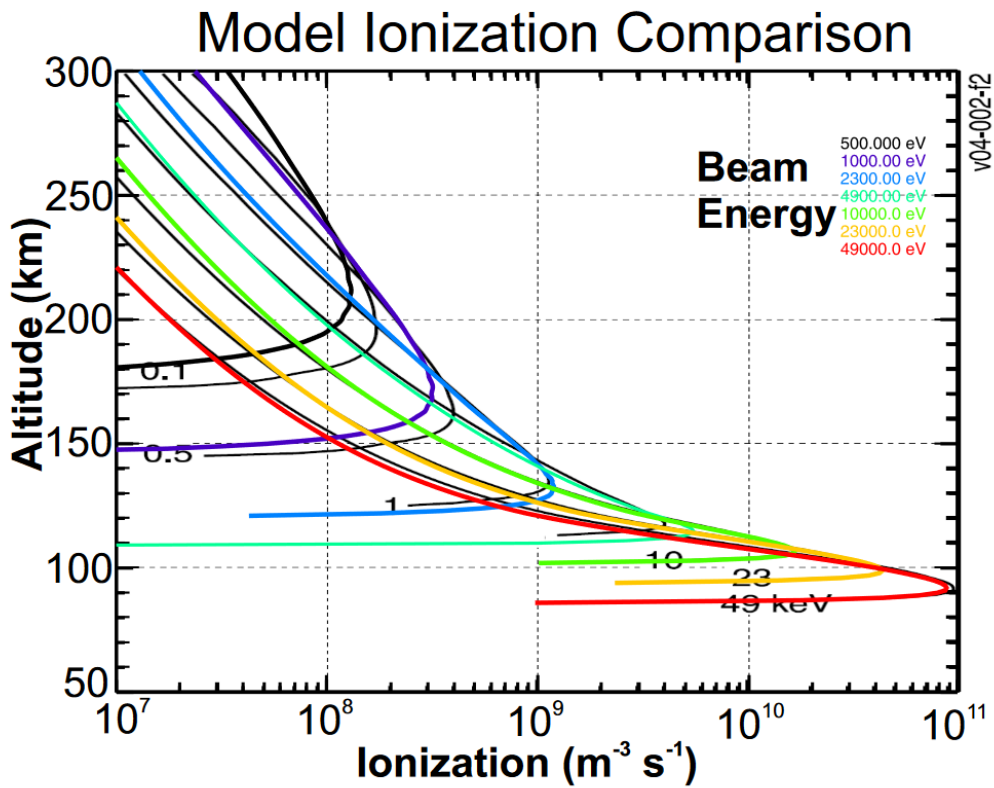


Figure 79. From Kaepller, 2013. The comparison of altitude vs. ionization profiles for two identical models, one from Kaepller, 2014 (colored) and the other from Semeter et al., 2005 for various input beams of electrons in a model nighttime ionosphere. For our work, we care about the observation that flux for electrons below 500 eV sharply falls off below 180 km. This provides a possible explanation for why we might only see the high-energy component in the Low Flyer bursts if they are STEBs. This is because the Low Flyer was at 180 km when it saw its bursts in Figure 78 so energies below 500 eV would have been stopped at higher altitudes.

### **7.3 Uniqueness of the Measurements - Criteria to Investigate a Changing Source Population**

The dataset of the High Flyer electrons in Figure 78 is exciting because it fulfills the requirements in order to address a numerically modelled prediction. Simulations of Alfvén waves passing through various electron velocity distributions relating to auroral physics often try to (a) determine the specific parameters required to reproduce observations from spacecraft or (b) set-up a model ionosphere and estimate the impact variations in the Alfvén wave parameters have on the resultant electron dispersions (Andersson et al., 2002; Chaston, Bonnell, Peticolas, et al., 2002; L.-J. Chen et al., 2005a; C. A. Kletzing, 1994; C. A. Kletzing et al., 2001; Tanaka et al., 2005). However, the impact of changing source population, not the wave, still remains less explored. This is likely because it's uncommon for two nearly-identical Alfvén waves to pass within a region of two different resonant source populations and still be observed from one spacecraft. In this way, we wish to explore keeping the accelerating waves identical but now change the resonant source population to see how this impacts the resultant STEBs.

Variations in the source population temperature, density or electron energy spread can drastically affect the resultant STEB electron flux and peak energy. Auroral field lines are commonly filled with (a) a cold ionospheric component near 1 eV, (b) inverted-V auroral electrons at keV energies (c) secondary/degraded primary backscatter from the inverted-V beam that fill sub-keV energies and (d) a suprathermal plasma sheet source of hundreds of eV (C. A. Kletzing et al., 2003). An Alfvén wave passing through these distributions would produce considerably different electron traces. One of the few studies to explore the effect of a changing source population were the simulations by L.-J. Chen et al., 2005a, which introduced more “high energy” backscattered electrons as well as more “low energy” backscatter and secondary electrons into their simulated inverted-V distribution. Here, “high energy” refers to electrons with energies just below the inverted-V energy but above 1 keV and Low-energy means energies below 100 eV. In Figure 80 we show this simulation result by L.-J. Chen et al., 2005a, where panel (a) shows two dispersion traces beneath their inverted-V for an enhanced number of high-energy backscatter electrons. The data in this panel is not similar to our data in Figure 78(a), however in panel (b) they show the same waves interacting

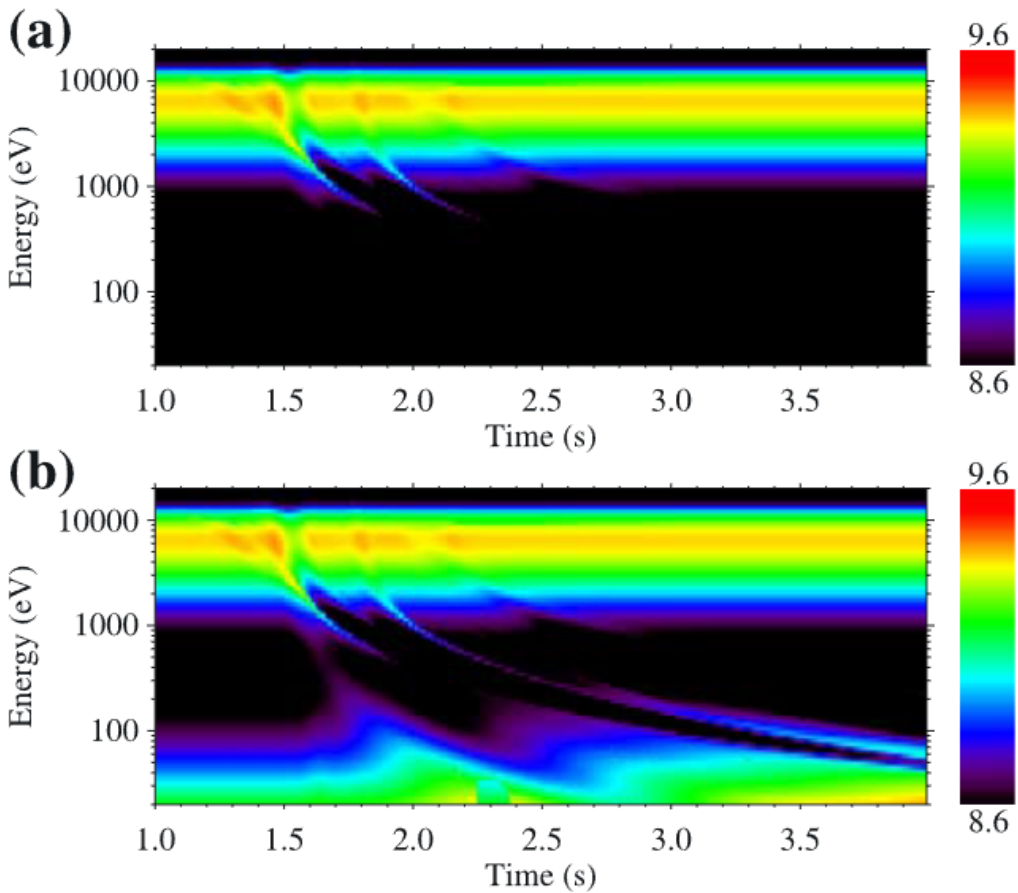


Figure 80. Figure 14 from L.-J. Chen et al., 2005a which used Alfvén waves to generate electron dispersions with different source distributions. An inverted-V style distribution is simulated with 5 keV energies at  $2 R_E$  with some addition of “high energy” backscattered electrons as well as “low energy” backscatter and secondary electrons. Here, “high energy” refers to electrons with energies just below the inverted-V energy but above 1 keV. Low-energy means energies below 100 eV. An Alfvén wave is passed to create dispersion traces and the wave starts at  $4 R_E$ ,  $E_{\perp} = 40$  mV/m and  $k_{\perp}c/\omega_{pe} = 1$  when the wave launches. (a) The effect of adding higher levels of high-energy backscatter electrons and (b) adding more low-energy backscatter and secondary electrons.

with an inverted-V with an enhanced number of low-energy backscatter and secondaries. The data here starts to look similar to our STEBs in Figure 78(a) at the low energies. In particular, the low-energy dispersion traces ( $E < 400$  eV) in panel (b) show the same behaviour as our STEBs: the highest energies in the STEBs show the lowest flux values whereas the lowest energies show the highest flux. Additionally, the highest energy electrons arrive before the lower energy electrons. This is contrary to panel (a) where the highest energies in the STEBs also display the highest fluxes and decrease in flux at lower altitudes. This analysis is one of the few studies to consider this question in some detail and they concluded the amplitude of the wave parallel electric field together with the source electron population determines the intensity of their STEBs.

To investigate how a changing source population affects STEB development *in situ* requires a unique arrangement of events that isolate the changing phenomenon. An ideal measurement would be for a source of Alfvén waves to launch identical waves that map inside and outside of inverted-V precipitation that can be observed in one pass of a spacecraft. Under this arrangement, the accelerating waves are spatially localized enough to argue that they originate from a similar source and observed differences in STEBs are primarily due to changes resonant source population. Previous rocket studies rarely meet these requirements for several reasons. Bursts are often seen entirely outside or inside inverted-V precipitation (Arnoldy et al., 1999; C. A. Kletzing et al., 1994; Lynch et al., 1999 or are single events Tanaka, 2005). Inverted-V precipitation may not be present (Lynch et al., 2012) or the payload wasn't capable of measuring Alfvén waves (Tanaka, 2005). Satellites have also reported repetitive STEBs near inverted-Vs but also are unable to address this question for the same reasons above or the question simply isn't considered (Andersson et al., 2002; Asamura et al., 2009; Chaston, Bonnell, Carlson, McFadden, Strangeway, et al., 2003; Chaston, Bonnell, Peticolas, et al., 2002).

For these reasons, the ACES-II is an exciting opportunity to explore the effects of a changing source population because Figure 78 has shown STEB events that fit the criteria we set above. Furthermore, ACES-II was equipped with sufficient electron, wave and plasma density measurements to resolve wave frequencies, in-phase relationships, amplitudes and time-delays between

electrons in STEB dispersions accurately. The remainder of this thesis is dedicated to showing how different source populations were likely responsible for the differences in peak energy and differential number flux intensities between our STEB events in 78(a).

## 7.4 Cross-Payload Interpretation

The first step to analyzing the STEB events is to prove the magnetic perturbations seen in panel Figure 78(c) and (g) are Alfvénic. To do this, we analyze the spatial distances between the rockets' field measurements, prove the Low Flyer's measurements are Alfvénic then argue that the perturbations seen by both flyers should be similar types of plasma waves. If the perturbations came from a single source (call it  $\delta B_{\perp}$ ), then the  $\sim 4$  s observation delay of  $\delta B_{\perp}$  between the flyers may come from the transverse movement of the source structure at significantly higher altitudes in the magnetosphere. Essentially, we are saying the electric and magnetic perturbations seen by both flyers in Figure 77 come from the same overall structure. Here, the spatial separation between payloads and source transverse velocity determines the delay. This is not unfounded since previous studies have reported along-arc movement of rayed aurora that produce repetitive electron bursts similar to our observations (Lynch et al., 2012; Wu et al., 2021). The top panel of Figure 81 illustrates the spatial position of the rockets during the Dispersive Region, along with their respective geomagnetic field lines mapped to 150 km (boxed in green). The bottom panel depicts a 2D slice at 150 km altitude viewed from above showing the paths the magnetic footprints of each rocket in time (dashed arcs). The times and distances when magnetic perturbations were first observed by each payload are noted.

As shown in the bottom panel of Figure 81, the  $\delta B_{\perp}$  source produces waves along the geomagnetic field of various scale lengths and traverses the distance between the rockets by moving transverse to  $\vec{\mathbf{B}}_{geo}$ . This 2D slice in ILat/ILong shows the paths both rocket's geomagnetic field-line footprints follow along the rocket's trajectories at higher altitudes. We label two specific moments in time with cross-circles: The first moment the Low Flyer sees  $\delta B$  perturbations in its data that last  $\sim 11$ s at 17:24:54 UTC and second, the moment the High Flyer sees its  $\delta B$  perturbations

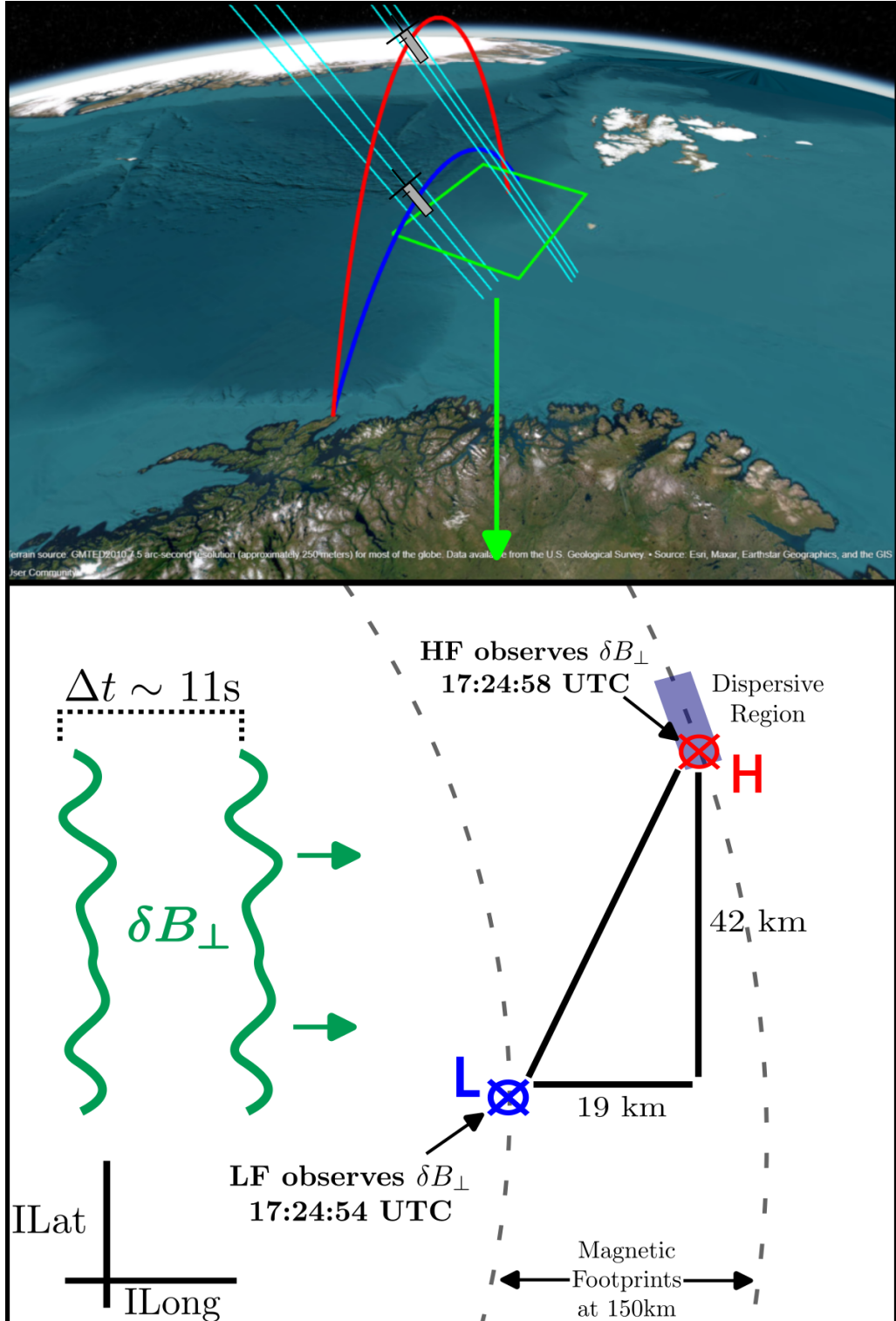


Figure 81. Schematic showing the projections of the geomagnetic fields during the Dispersive Region for both flyers. The green box represents the plane of ILat/ILong at 150 km. A zoomed-in version of this plane is provided in the bottom panel, which connects the fluctuations seen by both rockets to an assumed  $\delta B_{\perp}$  source moving transverse to  $\vec{B}_{geo}$ . To match observations, the along-arc source structure must move approximately 4.75 km/s eastward.

within the Dispersive Region starting at 17:24:58 UTC. To match the delay in perturbations seen by both payloads,  $\delta B_{\perp}$  would need to travel 19 km within 4 seconds with a corresponding velocity of 4.75 km/s at 150 km. This assumes  $\delta B_{\perp}$  is latitudinally extended enough to cover the 42 km distance between payloads. Typically, imager data could support this observation however the ASI integration time was 30s, which is too long to resolve the 4 second delay of our observations. Our value of 4.75 km/s is similar to previous studies. Wu et al., 2021 estimated rayed arc movement of 4 km/s longitudinally, with latitudinal extend of 10-20 km for repetitive bursts associated with 0-8 Hz electromagnetic fluctuations seen by the e-POP satellite. The Cascades-2 sounding rocket used THEMIS keograms of rayed arcs to determine 8.5 km/s along-arc motion of their rays (Lynch et al., 2012). From these we argue the plausibility that the fluctuations first seen by the Low Flyer and 4 seconds later by the High Flyer are connected to a similar source of plasma waves. In the next section we show these perturbations to be Alfvénic.

## 7.5 Alfvén Waves on the Low Flyer

Often the first consideration for analyzing waves on a moving platform is the effect of the Doppler Shift for the observed frequencies. This occurs if the payload has some component of its velocity parallel to the wavefront of the wave. The relationship between observed frequencies  $\omega_{sc}$  and the true frequency of the phenomena in its frame  $\omega$  is given by

$$\frac{\omega_{sc}}{k} = \frac{\omega}{k} + \frac{\vec{k} \cdot \vec{V}_{sc}}{k} \quad (171)$$

where  $\vec{k} = k_{\perp} \hat{e}_{\perp} + k_{\parallel} \hat{e}_{\parallel}$  is the angular wave number vector of the wave,  $\vec{V}_{sc}$  is the spacecraft velocity vector and  $k = 2\pi/\lambda$  is the magnitude of the wave vector. This type of correction is primarily useful for spacecraft with large velocities, such as satellites with speeds above 7 km/s. For the Alfvén waves we're interested in, their phase velocity is predominately along Earth's geomagnetic field so that  $\vec{k} \cdot \vec{V}_{sc} = k_{\parallel} V_{sc\parallel}$ . The “Up” component in ENU coordinates of our payload velocities is a good enough alignment to  $\vec{B}_{geo}$  for our demonstrative purposes here and is plotted in Figure 82.

We see the “parallel” component of our rockets’ velocity to  $\vec{\mathbf{B}}_{geo}$  is at most  $V_{sc\parallel} \sim 1$  km/s for both rockets in the Dispersive Region of the flight. The phase velocity of the Alfvén waves we’re inter-

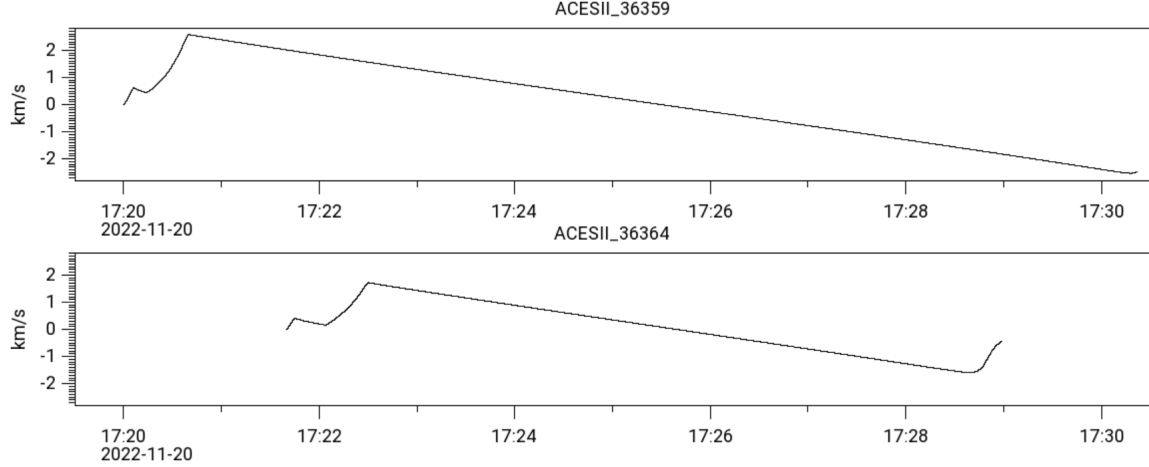


Figure 82. Up component in ENU coordinates of rockets’ payload velocity. The High Flyer is shown in the top panel and the Low Flyer in the bottom panel. Values are converted into ENU from the ECEF velocities given in the attitude data.

ested in is given in equation 82, where the typical velocity for Alfvén waves at altitude around 100 km - 500 km is of order  $\sim 4000$  km/s and the parallel wavelengths can be hundreds of kilometers, say  $\lambda_{\parallel} \sim 500$  km (Schroeder et al., 2021) and the perpendicular wavelengths are near  $\lambda_{\perp} = 2$ km in the ionosphere (Lynch et al., 2012; Wu et al., 2021). Inserting our values into equation 171 we see:

$$\frac{\omega_{sc}}{k} = \frac{\omega}{k} + \frac{\sqrt{\lambda_{\perp}^2 + \lambda_{\parallel}^2}}{\lambda_{\parallel}} V_{sc\parallel} = (4000 \text{ km/s}) + \frac{\sqrt{(2\text{km})^2 + (500\text{km})^2}}{500\text{km}} (2\text{km/s}) \approx 4002 \text{ km/s} \quad (172)$$

Clearly, we see  $\omega/k \gg \frac{k \cdot V}{k}$  and we do not need to consider Doppler effects. The frequencies observed by our payloads should then be considered representative of the true wave frequency. This is usually true for rockets due to their low payload velocities, although not universally true.

Next we show the in-phase perturbations seen by the Low Flyer are Alfvén waves. The lack of High Flyer EFI measurements prohibits confirmation of Alfvénic activity associated with our STEB events, but by analyzing the Low Flyer’s fields data we can connect our observations. A closer look at the Low Flyer’s filtered fields data are shown in Figure 83 for three intervals: (1) A

quiet region early in the flight (2) a subsection from the temporal alignment from Figure 78 and (3) an ILat-aligned region when the Low Flyer crossed the ILats of the Dispersive Region. These regions were chosen to characterize the background noise, determine the type of plasma waves seen during the High Flyer's pass of the Dispersive Region and observe the Dispersive regions' ILats at a lower altitude, respectively.

Figure 83(a)-(c) show the filtered electric  $\delta E_r$  and magnetic field  $\delta B_e$  perturbations for all regions. The quiet region's AC fields appear out of phase and at approximately  $\pm 2$  mV/m and  $\pm 2$  nT. These values are considered an upper limit on the  $f < 2$  Hz noise since the de-spin procedure is optimized for payload apogee, while the quiet region's data was taken minutes before this point. The latter two region's AC fields appear in-phase and the  $\delta E_r, \delta B_e$  fluctuations are of order  $\pm 5$  mV/m and  $\pm 5$  nT. Panels 83(d)-(f) show the instantaneous field-aligned Poynting flux ( $\delta \vec{S}_p$ ) calculated via  $\delta \vec{S} = \delta \vec{E} \times \delta \vec{B}/\mu_0$  with positive values directed towards the Earth. We only show  $\delta \vec{S}_p$  since the perpendicular components displayed negligible flux by comparison for all regions considered. The peaks in Figure 83(e) for the temporally aligned region are higher frequency and mostly between 0.007 erg/cm<sup>2</sup>s to 0.03 erg/cm<sup>2</sup>s. The ILat-aligned region peaks share similar magnitudes between 0.015 erg/cm<sup>2</sup>s to 0.02 erg/cm<sup>2</sup>s.

The frequency spectra in panels 83(g)-(i) and the E/B ratios in panels 83(j)-(l) indicate the existence of low-frequency MHD Alfvén waves. The MHD wave phase speed (red line in panels 83(j)-(l)) is given by  $V_A = B/\sqrt{\mu_0 \rho_m}$  for mass density  $\rho_m = \sum [C]_i n_i m_i$ , where EISCAT ion concentrations for atomic oxygen,  $[C]_{O^+} = n_{O^+}/n_{total}$  and combined concentrations for heavier ions,  $[C]_{NO+, O2+, N2+} = (n_{NO+} + n_{O2+} + n_{N2+})/n_{total}$  are used to calculate  $\rho_m$  with the LP total plasma density  $n_{total}$ . Each of the three region in Figure 83 indicated an EISCAT average ion temperature of 0.08 eV, *in situ* plasma density near  $10^5$  cm<sup>-3</sup> and magnetometer  $|B| \simeq 5 \times 10^{-5}$  T. The average EISCAT ion concentrations for O<sup>+</sup> were 0.84, 0.57, 0.48 and 0.16, 0.43, 0.52 for heavier ions in each region. The MHD speeds are determined over each time range and averaged. The waves in panels 83(j) and (l) are MHD since the kinetic correction to equation 83 that depends upon electron skin depth tends towards unity at the Low Flyer's altitude. For example, realistic

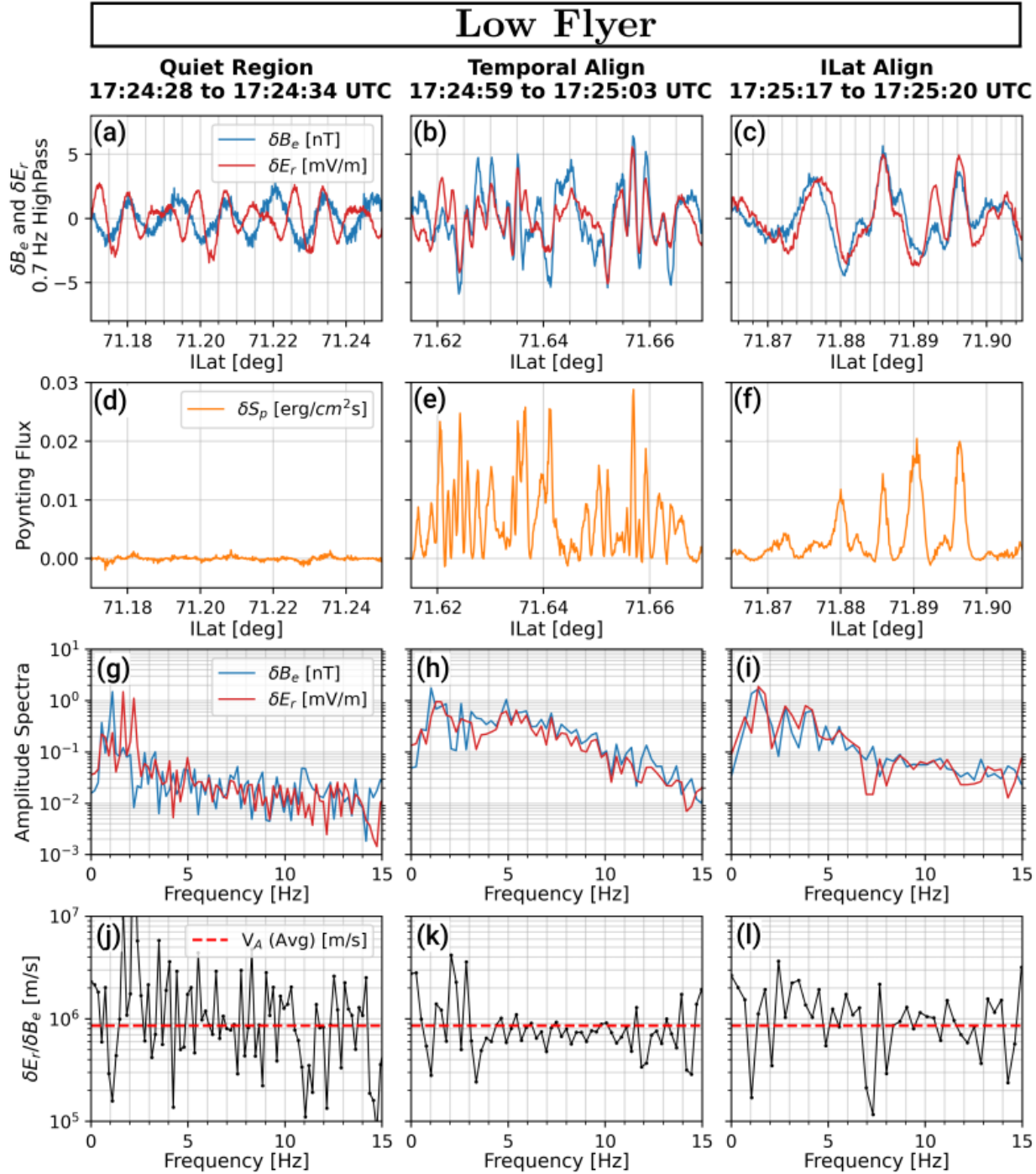


Figure 83. Low Flyer's fields instruments data. (Left Column) Pre-auroral quiet region. (Middle Column) Temporally aligned data when the High Flyer was intercepting the Dispersive region. (Right Column) ILat footprint of the Dispersive Region seen by the Low Flyer 20s after the High Flyer passed above. (a-c) 0.7 Hz Highpass filtered electric and magnetic fields. (d-f) Field-aligned Poynting Flux. Positive values are Earthward. (g-i)  $\delta B_e$ ,  $\delta E_r$  frequency spectra. (j-l) electric-to-magnetic field E/B ratio (black) compared to local average MHD Alfvén speed (red).

wave parameters at these altitudes are  $\omega_{wave} = 3$  Hz,  $\lambda_{\perp} = 2$  km which produce kinetic contribution  $k_{\perp}^2 \lambda_e^2 = 2.8 \times 10^{-9} \ll 1$  using our estimates. For our data, the quiet interval shown in Figure 83(g) suggests  $3 \times 10^{-2}$  mV/m is the upper limit where signal becomes indistinguishable from noise at  $f > 3$  Hz, so we interpret measurements above this limit as significant. The temporal region amplitudes in panel 83(h) persists above this limit up to 13 Hz. Here, strong agreement between the *in situ* MHD Alfvén speed can be seen between 4 - 13 Hz in panel 83(k). Similarly, the Ilat region approaches this limit near 12 Hz with good (but lesser) agreement to the MHD speed around 5 and 10 Hz. The quiet region's E/B ratio in panel 83(j) shows little meaningful agreement to its predicted wave velocity.

We interpret these observations as low frequency downward propagating MHD Alfvén waves in the temporally aligned and Ilat aligned regions. In particular, the time-aligned region shows the clearest agreement to downward propagating 4 to 13 Hz Alfvén waves. By invoking the arguments made in section 7.4 about the similarity of the perturbations and the cross-payload spatial connection, we conclude that the magnetic perturbations seen in the High Flyer coincident with its STEBs are likely Alfvén waves from a similar source as seen by the Low Flyer.

## 7.6 Source Altitude: Time-of-Flight

Now that we have a connection to Alfvén waves for our STEB events, we start to consider the how changes in STEB source population affect the resultant electron dispersion with our *in situ* data. We focus on the first five STEBs in the beginning of the Dispersive Region shown in Figure 78(a) since these satisfy the criterion we set in chapter 7.3 i.e. a spatially localized source of nearly identical Alfvén waves which map within and outside of inverted-V precipitation. Here, we spend time distinguishing STEB electrons from auroral inverted-V precipitation and then estimate their source altitudes through time of flight methods. By determining the altitudes from which our STEB electrons came from we can analyze which resonant populations may have existed at these altitudes.

A zoomed-in portion of High Flyer EEPAA differential energy flux data from Figure 78(a)

involving five STEBs events near an inverted-V is shown in Figure 84. All times are given in seconds from High Flyer's launch at 17:20:00 UTC. Panel 84(a) shows averaged pitch angles slices  $-10^\circ < \alpha < 10^\circ$  for repetitive bursts, separated approximately 1 second apart. A narrow, low energy ( $100 \text{ eV} < E < 200 \text{ eV}$ ) inverted-V starts near 300.55s followed by another, broader inverted-V starting at 300.95s ( $100 \text{ eV} < E < 600 \text{ eV}$ ). STEB event S1, S2 and S3 are observed several seconds away from the nearest inverted-V whereas events S4 and S5 are coincident. Three equally spaced slices in time are denoted by lines for S2, S3, S4 and S5 and  $(v_\perp, v_\parallel)$  velocity space slices are plotted in sub-panels 84(b) to (e). The bursts are identified by inhabiting the most field-aligned pitch angles, starting broad in pitch angle ( $10^\circ < \alpha < 50^\circ$ ) then becoming field-aligned at later times/lower energies. Meanwhile, inverted-V precipitation distinguishes itself by intense flux broadly distributed over pitch angles  $-10^\circ < \alpha < 110^\circ$  (labeled with dot-dashed arcs in the velocity-space subpanels) across many high-energy channels which does not retreat to lower energies in time.

Traditionally, estimating the source altitude for accelerated STEB particles is done using a time of flight (TOF) cross-correlation analysis on the equation

$$\Delta t = z_{src} \left( \frac{1}{v_{slow}} - \frac{1}{v_{fast}} \right) = \frac{z_{src}}{\Delta v} \quad (173)$$

where the observed delay time,  $\Delta t$ , is calculated from the parallel component of an energy channel  $v_{fast}$  and combinations of the other energy channels,  $v_{slow}$  for a specific pitch angle bin. This method assumes a single source altitude  $z_{src}$  above the rocket and the peak in the cross-correlation analysis (in time) between  $v_{fast}, v_{slow}$  determines  $\Delta t$  (Andersson et al., 2002; C. A. Kletzing et al., 1994; McFadden et al., 1987; Paschmann et al., 1983; Tanaka, 2005). A linear fit between  $\Delta t$  and  $\Delta 1/v$  gives a slope equivalent to  $z_{src}$ .

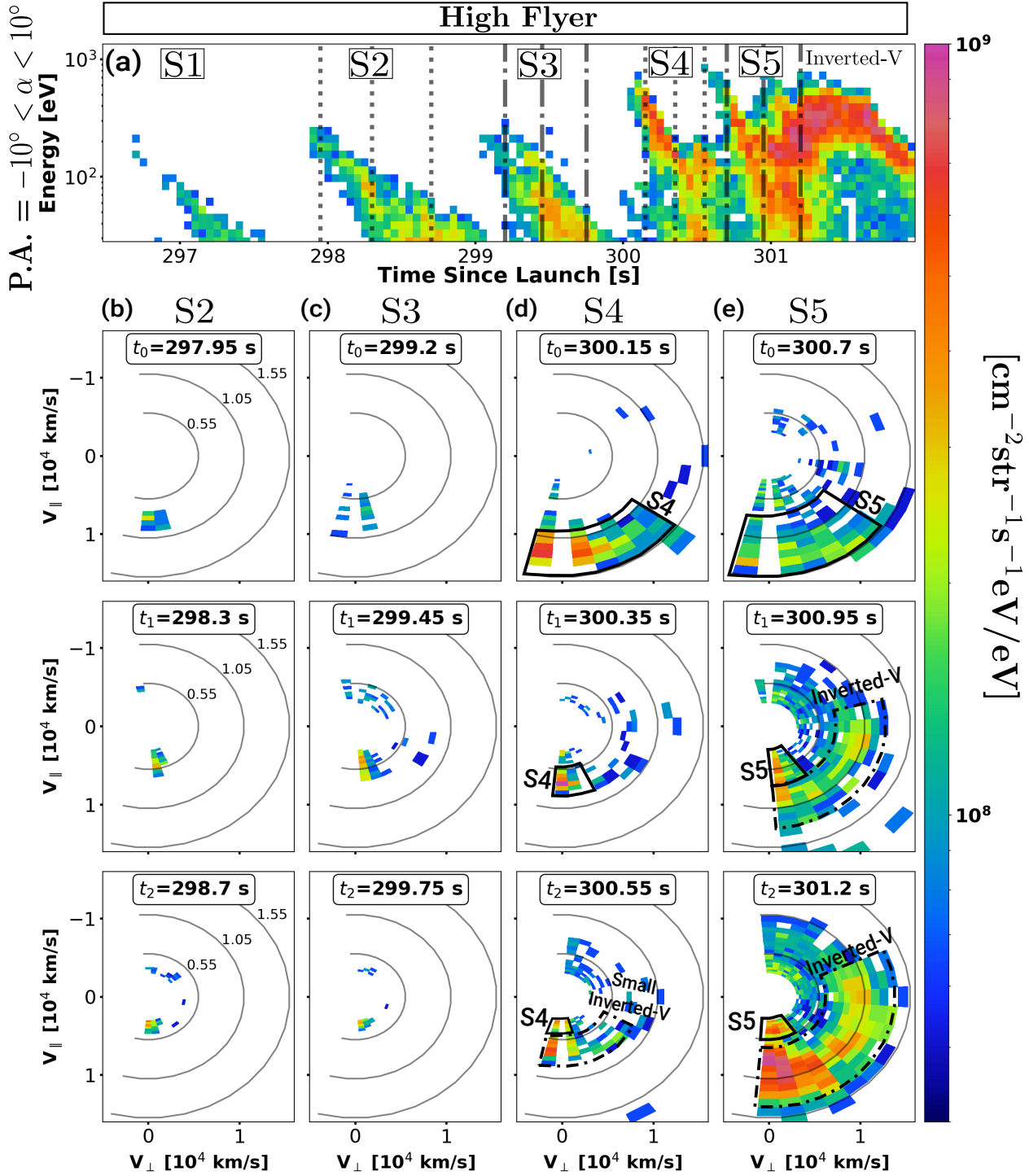


Figure 84. High Flyer EEPAA differential energy flux for five STEB events which precede an inverted-V in the Dispersive Region. Panel (a) shows the energy-time counts spectrogram for  $-10^\circ < \alpha < 10^\circ$  averaged bins. Black lines indicate slices in time shown in  $(v_{\parallel}, v_{\perp})$  velocity space subpanels (b), (c), (d) and (e). Examples of STEB (solid) vs. inverted-V (dot-dashed) electrons are provided in panels (d) and (e). These events coincident with inverted-V precipitation (S4, S5) show higher peak energy and flux compared to those outside.

Here we will provide additional details on how the TOF method actually works. TOF can be done using STEB electrons on an energy vs. time dataset for one pitch or a pitch angle vs. time dataset for a specific energy. We employ the first method since the pitch angle dispersion of a STEB is often affected by the mirror force in unwanted ways. The first step in our TOF cross-correlation technique is to apply a 4-count threshold on the raw EEPAA counts, which removes data with  $\Delta N/N = 50\%$  error. The second step is to isolate a subset of EEPAA raw-counts data that contains a STEB at a particular pitch angle. In Figure 85 we show STEB 5 at pitch angle  $\alpha = 10^\circ$  before and after it was isolated by eye. Choosing pitch angles close to  $0^\circ$  removes the impact of the mirror force which improves the accuracy of determining source altitudes. This STEB in particular overlapped with an inverted-V on the right-hand-side of the bottom panel which leaves ambiguity in which pixels represent STEB electrons or not. Luckily, the TOF process is primarily concerned with the distribution of peak counts along the diagonal elements of a dispersion trace (more on this later) so removing values from the edges of a dispersion trace will not significantly affect the overall TOF method. The isolation step is primarily useful for removing data not associated with the STEB or energy channels with low counts that can drastically skew the cross-correlation analysis in the next step.

After isolation, a cross-correlation analysis is applied to determine the  $\Delta t$  between combinations of energy channels. Figure 86 details how this process works: a particular energy channel is chosen as  $v_{fast}$  and all combinations of this channel and those below it in energy  $v_{slow}$  are cross-correlated to determine the lag-time between the peaks in the energy vs. time datasets. The python function “correlate” from the `scipy.signal` library is used for this step. Essentially, the process involves taking two slices out of the energy vs. time datasets in the top panel of Figure 86. Two example slices (colored in red and green in the top panel) are shown in the middle panels called  $v_{fast}$  Counts and  $v_{slow}$  counts. From here, the 2D datas are shifted in time and mathematically convoluted using the definition of the correlation “z” for two d-dimensional arrays “x” and “y”:

$$z[k] = (x * y)(k - N + 1) = \sum_{l=0}^{\|x\|-1} x_l y_{l-N+1}^* \quad (174)$$

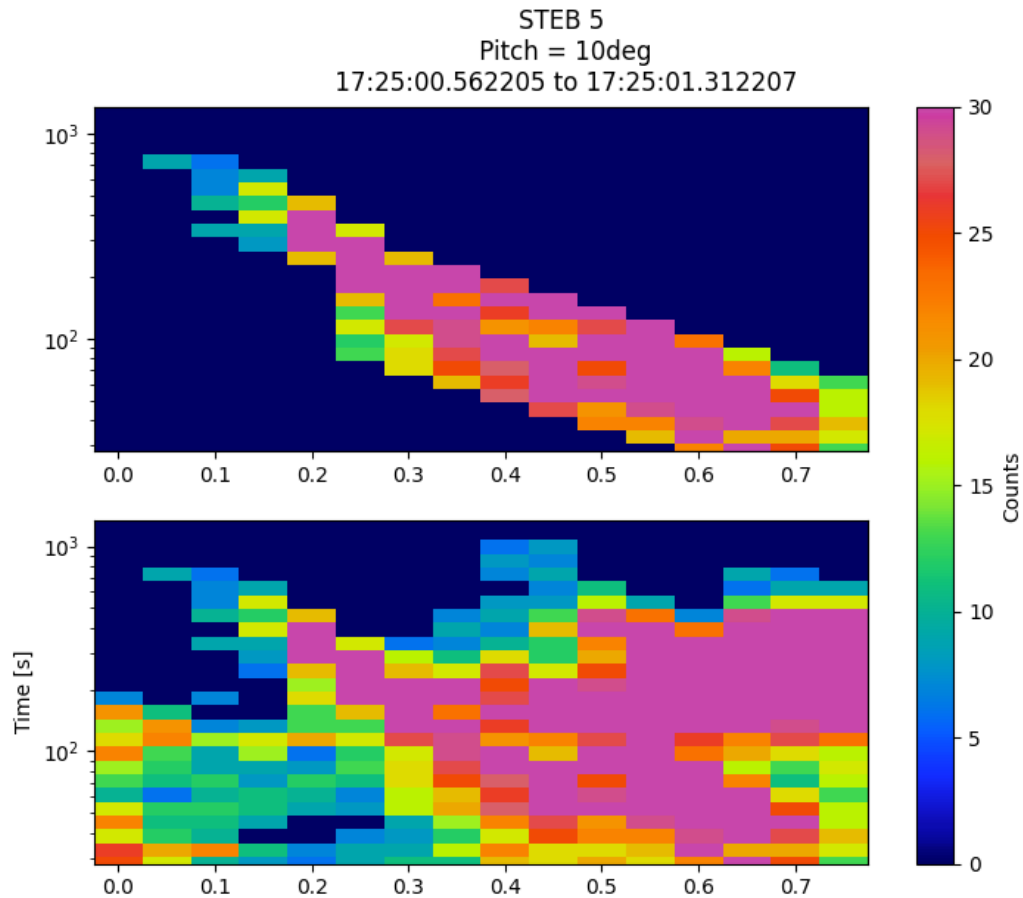


Figure 85. Example of the type of isolation used for all STEBs in our study. STEB 5 is displayed here which partially overlapped with an inverted-V on the right-hand-side. The top panel shows the isolation of the STEB and the bottom panel is the raw counts data. The cross-correlation process primarily cares about the peak counts along the diagonal of the STEB so the removal of the inverted-V on the edges will not significantly affect the TOF results.

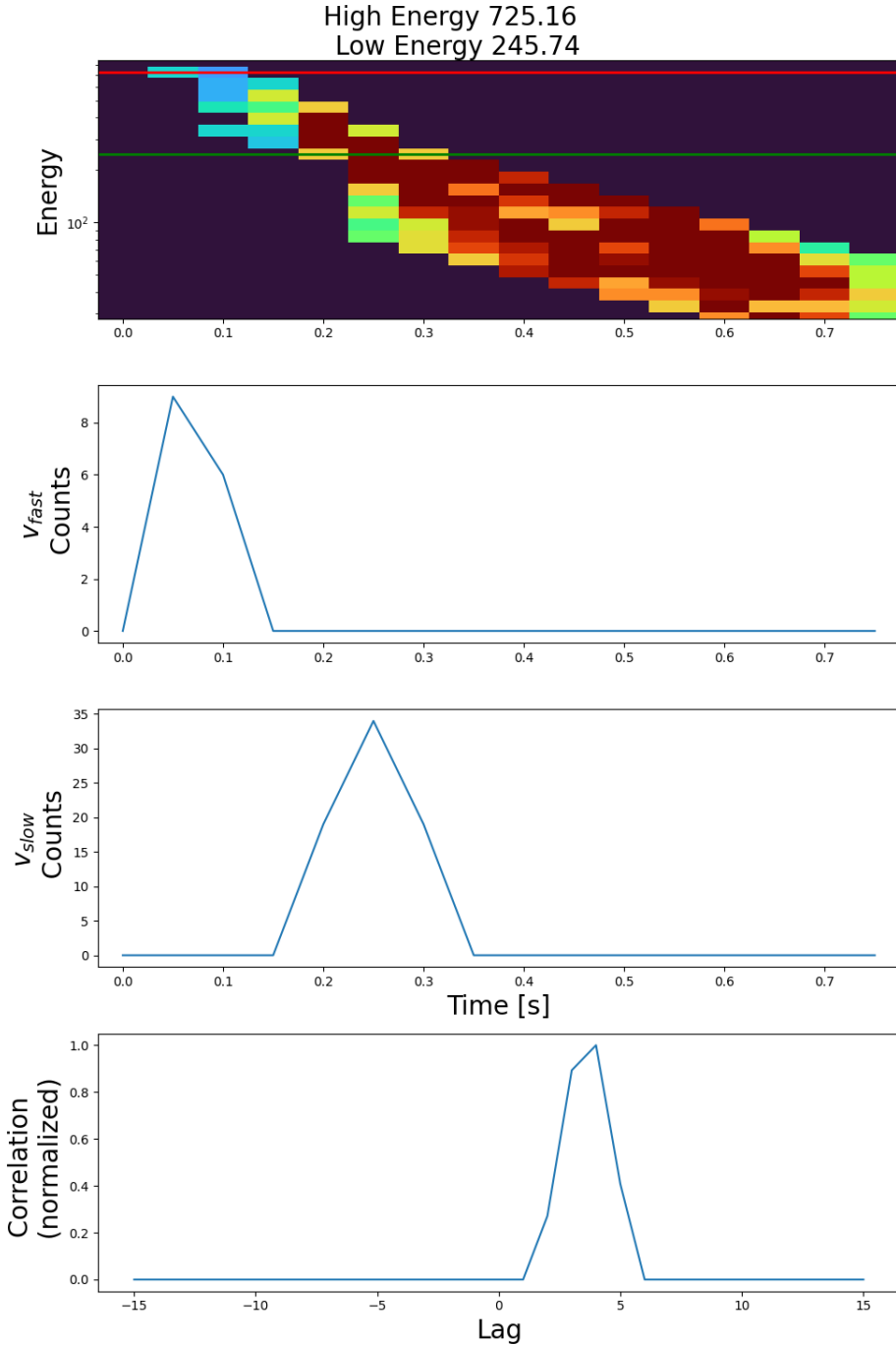


Figure 86. Example of the cross-correlation technique used on STEB 5 to determine the  $\Delta t$  values between all combinations of energy channels. For each possible combination, one channel is labelled  $v_{fast}$  and another is labelled  $v_{slow}$ . The time series are convolved and summed to produce a single correlation value. (Top panel) STEB 5 raw counts data after isolation. Green and red lines denote the  $v_{slow}$  and  $v_{fast}$  time series, respectively. (Second panel) The red-line  $v_{fast}$  time series plotted as raw counts vs. time. (Third panel) The green-line  $v_{fast}$  time series plotted as raw counts vs. time. (Bottom panel) The correlation value between our example  $v_{fast}$  and  $v_{slow}$ . The peak in the correlation is assumed to correspond to the arrival time delay between STEB electrons at these energies.

for  $k = 0, 1, \dots, ||x|| + ||y|| - 2$  where  $||x||$  is the length of the time series  $x$ ,  $N = \max(||x||, ||y||)$  and  $y_m$  is 0 when  $m$  is outside the range of  $y$ . Conceptually, we are taking the time series  $v_{fast}$  counts and shifting it a single unit in time (50 ms in this case because it's the EEPAA temporal resolution) and multiplying the values in the shift  $v_{fast}$  dataset by their counterparts in  $v_{slow}$  (i.e. a convolution), then summing this multiplication. As the peaks in the individual time series start to overlap, the correlation value grows until a maximum is reached and then falls back down as the peaks stop overlapping. The peak in the correlation itself (bottom panel of Figure 86) is assumed to be the time delay between electrons arriving at the EEPAA detector for a given energy. This  $\Delta t$  time delay value is calculated by determining the number of timesteps required to reach the peak correlation value and multiplying by the EEPAA dataset temporal resolution. Notably, this process is primarily sensitive to where the peak in the 2D slices occurs, not at the edges far away from this peak. This is the reason the TOF process is insensitive to removing the inverted-V signal back in Figure 85.

The correlation process results in a new dataset that can be fit to estimate source altitude. The pairs of energy channels in 86 can be converted into a new x-axis variable called  $1/\Delta v$  via

$$\frac{1}{\Delta v} = \frac{1}{v_{fast}} - \frac{1}{v_{slow}} \quad (175)$$

and the new y-axis variable is the previously determined  $\Delta t$  value. By applying this method to each of our STEBs we can estimate a source altitude from equation 173. However, this equation assumes a single source altitude for STEB electrons in equation 173, which inherently misrepresents the Alfvén wave-particle acceleration process, which is known to occur over thousands of kilometers due to decreasing phase velocity (Andersson et al., 2002; Chaston, Bonnell, Carlson, Berthomier, et al., 2002; L.-J. Chen et al., 2005a; Tanaka et al., 2005). Thus  $z_{src}$  from equation 173 is only considered a heuristic that will underestimate the true source altitude, which is really a range of altitudes instead of a single value. Alternatively, another TOF fit was presented by Tanaka, 2005

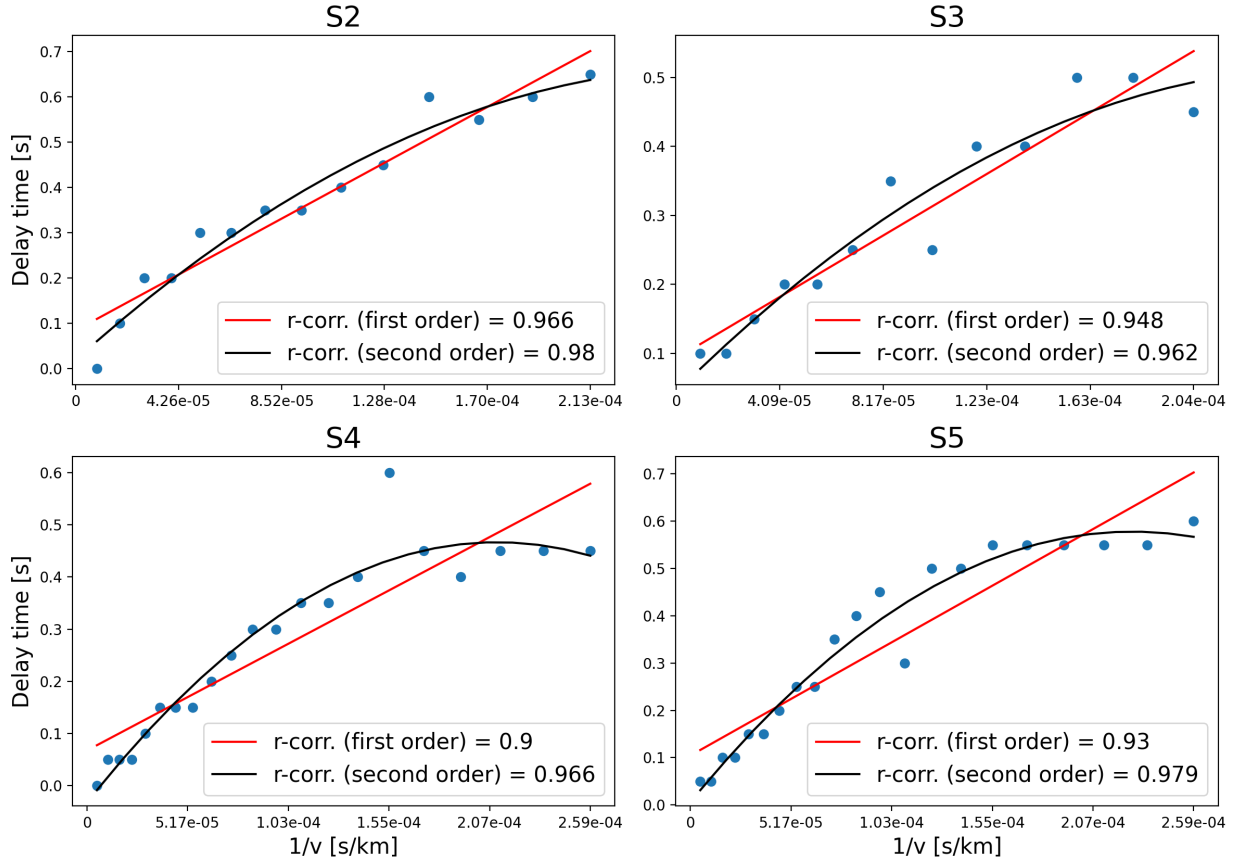


Figure 87. Time of Flight (TOF) comparison plots for STEB events S2, S3, S4, S5 using a traditional linear, single-source altitude fit and a polynomial fit from Tanaka, 2005. In every case considered here, the Pearson correlation for the polynomial fit outperforms the linear fit and events S4 and S5 clearly indicate the genuine quadratic nature of the data. The fit parameters and source altitudes are listed in Table 1.

which used a second-order polynomial of the form

$$\Delta t = a_0 + \frac{a_1}{\Delta v} + \frac{a_2}{\Delta v^2} \quad (176)$$

where  $a_0, a_1, a_2$  are constants. In a subsequent numerical simulation of STEBs by Tanaka et al., 2005, the fit constants were shown to be sensitive to variations in the perpendicular scale length  $\lambda_{\perp}$  of the accelerating wave. This is more representative of the underlying physical process compared to equation 173 since changing the wave parameters in the simulation should change the types of electrons that resonate with the wave and therefore the arrival times of the electrons (i.e.  $\Delta t$ ).

However a model to directly relate equation 176 to  $\lambda_{\perp}$  was not provided and they justified their usage of equation 176 primarily on the shape of their  $\Delta t$  vs.  $1/\Delta v$  dataset. In particular, Tanaka, 2005 argued that 35% of their STEB events are clearly better fit by the second order model and the remaining 65% of events were indefinite between the linear and polynomial model. In Figure 87 we show the  $\Delta t$  vs.  $1/\Delta v$  data for our STEBs in ACES-II for events S2 to S4 and similar to Tanaka, 2005, we found the polynomial fit in equation 176 was more representative of our dataset than linear fits for all events considered. The Pearson-correlation coefficient is used to determine the quality of the fits. Coefficient “r” values close to one indicate a strong, positive correlation. In Figure 87 we calculate the r-correlation coefficient between the measured  $\Delta t$  values from the cross-correlation process and the theoretical  $\Delta t$  values of our two fits using the linear and the polynomial  $a_0, a_1, a_2$  in equation 173 and 176 with our  $1/\Delta v$  values. Here we see that the underlying dataset itself appears non-linear and that the polynomial fit appears more representative of the true data instead of doing a better job fitting just because more fit parameters are allowed, hence the r-correlation coefficients for all fits appear closer to 1 for the polynomial form.

The principle advantage of equation 176 is that Tanaka, 2005 argued the derivative of equation 176 with respect to  $1/\Delta v$  represents a source altitude as a function of  $1/\Delta v$ . This allows us to estimate a range of source altitudes for our STEB electrons,  $z_{src}$ (second order), based upon the energy of the observed electrons. Neither equation 173 nor equation 176 precisely model the source altitudes of our STEBs, however the polynomial fit altitudes compare reasonably well to modelled source altitudes presented by Tanaka et al., 2005. We chose the  $\alpha = 10^{\circ}$  bin for all STEBs in our analysis. The results of both linear and polynomial TOF techniques with their associated correlation coefficients are shown in Table 1.

The TOF analysis from Table 1 indicates two powerful observations: (1) The distributions associated with our STEB electrons are likely ionospheric or accelerated inverted-Vs and (2) that slowing inertial Alfvén Waves (IAWs) were likely responsible for our STEB events and produced higher energy electrons at higher altitudes. By using the derivative of equation 176 with our polynomial coefficients and the minimum/maximum energies of our STEBs we estimate the source

Parameter	S2	S3	S4	S5	unit
Time to Disperse	1.45	0.955	0.64	0.749	s
$E_{min}$	28.22	28.22	28.22	28.22	eV
$E_{max}$	245.74	210.54	725.16	846.39	eV
$z_{src}$ (first order)	2722	2400	1977	2402	km
r-corr. (linear)	0.966	0.948	0.900	0.93	—
$a_0$	$3.89 \times 10^{-2}$	$1.54 \times 10^{-2}$	$-3.243 \times 10^{-2}$	$1.366 \times 10^{-2}$	s
$a_1$	$4.67 \times 10^3$	$4.33 \times 10^3$	$4.733 \times 10^3$	$4.85 \times 10^3$	km
$a_2$	$-9.11 \times 10^6$	$-9.29 \times 10^6$	$-1.12 \times 10^7$	$-9.86 \times 10^6$	$\text{km}^2/\text{s}$
r-corr. (second order)	0.980	0.962	0.966	0.979	—
$z_{src}$ (second order)	2731 to 4672	2432 to 4330	1828 to 4733	2252 to 4850	km

Table 1. Results of the TOF analysis for four events preceding an inverted-V near 17:25:00 UTC in the High Flyer EEPAA data. The source altitudes above the payload,  $z_{src}$ , can be added to the altitude at measurement (400 km) to get true altitude.

region is between 2000 km and 5000 km altitude for most of our events. The EISCAT radar indicated a maximum ion temp near 1000 K (0.09 eV) at 700 km during the Dispersive Region, which likely doesn't significantly deviate up to  $1R_E$ . At higher altitudes ( $> 2R_E$ ) the hot plasma sheet with ( $T_i \sim 300$  eV, and  $n = 0.5 \text{ cm}^{-3}$  (C. A. Kletzing et al., 2001; C. A. Kletzing et al., 2003) can raise the average plasma temperature, but the ionosphere provides much of the plasma density in our region of interest. Model estimates of nighttime ionospheric density at high latitudes from 2000 km to 5000 km are between  $10^3 \text{ cm}^{-3} > n_i > 10^1 \text{ cm}^{-3}$  (L.-J. Chen et al., 2005a; C. A. Kletzing et al., 1994; C. A. Kletzing et al., 1998; Schroeder et al., 2021), which suggests an ion plasma beta  $\beta_i$  between  $6.50 \times 10^{-7} > \beta_i > 3.95 \times 10^{-8}$  for a 1 eV ion temperature plasma in a dipole magnetic field. This cold and low density ionospheric plasma very likely satisfies a purely atomic oxygen  $\beta_i < m_e/m_i = 3.43 \times 10^{-5}$  limit for these waves to be IAWs in our acceleration region. Furthermore, these altitudes are below the typical peak in Alfvén phase velocity which occurs around  $1R_E$  for nighttime conditions (Chaston, Petricolas, et al., 2003; L.-J. Chen et al., 2005a; C. A. Kletzing et al., 2001). Below this peak, the Alfvén phase velocity monotonically decreases. Thus the highest energy electrons must have been accelerated at the highest resonant wave speeds i.e. at the higher altitudes and vice versa. From this we say that IAW were likely responsible for our STEB features between 2000 km to 5000 km altitude.

## 7.7 The effects of a changing source population: Key Observations

From the previous sections we have shown our STEBs on the Higher Flyer to very likely be associated with Alfvén waves and estimated the region of acceleration occurred between 2000 to 5000 km above the rocket observation. This analysis helps us determine which distributions should be present at the source altitudes. In this section we finally arrive at the heart of our analysis: showing the effect of changing the source population during IAW acceleration. By itself, the data in Figure 84(a) illustrates the primary observation of this thesis: STEB events near/within inverted-V precipitation show increased peak energy and differential flux due to an enhanced source population. This is best explained by two observations: (i) the inverted-V supplies a greater number of resonant electrons (primaries, secondaries, degraded primaries) than the ambient plasma sheet (thereby increasing STEB flux); and (ii) that these electrons resonate with the wave at higher energies (thereby increasing peak STEB energy). Some of the enhanced resonant population can even be seen in panel 84(a) with energy fluxes  $\geq 10^8 \text{ cm}^{-2}\text{str}^{-1}\text{s}^{-1}\text{eV/eV}$  of primary/secondary/degraded electrons seen within the inverted-V, which should map via the mirror force to our resonant altitudes at 2000 km to 5000 km (Bennett et al., 1983; Evans, 1974).

To illustrate this point, Figure 88(a) shows a 2D slice of the parallel component of the distribution function  $f(\mathbf{v}_{\parallel})$  for three populations that *may* exist throughout the 2000 - 5000 km altitudes. They are the accelerated inverted-V electrons (blue), the backscattered/secondary electrons produced by the inverted-V (magenta) and the ambient plasma sheet background (red). Spatially, the inverted-V and backscatter/secondary populations are separate from the ambient plasma sheet electrons, however we display them together to compare the effect of a similar acceleration process. The plasma sheet population is drawn as a Maxwellian and the inverted-V as a half-Maxwellian accelerated by a quasi-static potential (Banks et al., 1974; Evans, 1974; Kaepller, 2014). The backscatter/secondary electron distribution curve is drawn close to a thermal population but with greater flux at lower energies and a sustained, high energy tail close to the inverted-V similar to the model by Evans, 1974. Theoretically, a discontinuity between the backscatter/secondaries and the inverted-V exists but this is usually smoothed out by a detector in actual measurement (Evans,

1974). Each of these distribution shapes are discussed in more detail in section 4.4. Here, the exact values for these distributions are not important since we’re primarily interested in the general shapes and relative maximum energies these distributions should have.

If the same accelerating IAW passes through these altitudes, its parallel electric field will “snip off” a portion of these distributions when the parallel electron velocity falls within the resonance bands (black dotted lines in Figure 88(a)) centered around the phase velocity  $\omega/k$  (see Chapter 4.5). As the wave propagates to lower altitudes, the phase speed decreases due the exponential plasma density while the resonance window shrinks due to the diminishing contribution of the kinetic term  $k_{\perp}^2 \lambda_e^2$  that controls the parallel electric field amplitude (Stasiewicz et al., 2000, see Chapter 2.8). Figure 88(b) shows the same distributions at the end of resonant acceleration where the wave has modified  $f(v_{\parallel})$  to produce STEBs. For the STEB with a plasma sheet source (green curve in Figure 88(b)), resonance begins at the highest parallel thermal velocity and the resulting dispersion trace grows in accordance with its thermal spread of velocities. For the STEB produced from the inverted-V and backscatter/secondaries (orange curve in 88(b)), resonance begins at much higher energies due to the electron velocities from the quasi-static potential. The total number of electrons (area under STEB curve) is also greater due to the existence of the backscatter/secondary populations, a population unavailable to the ambient plasma sheet. This produces a STEB with higher peak energy and average differential number flux vs. energy (herein referred to as “flux intensity”) and shows how STEBs are enhanced by the inverted-V, even for the same accelerating wave. In truth, the wave accelerates only a small window of velocities at each altitude and the electron distributions at each altitude will have a small part of it missing instead of the entire distribution missing the high-energy portion as we have drawn in Figure 88. Nonetheless, the key ideas are communicated.

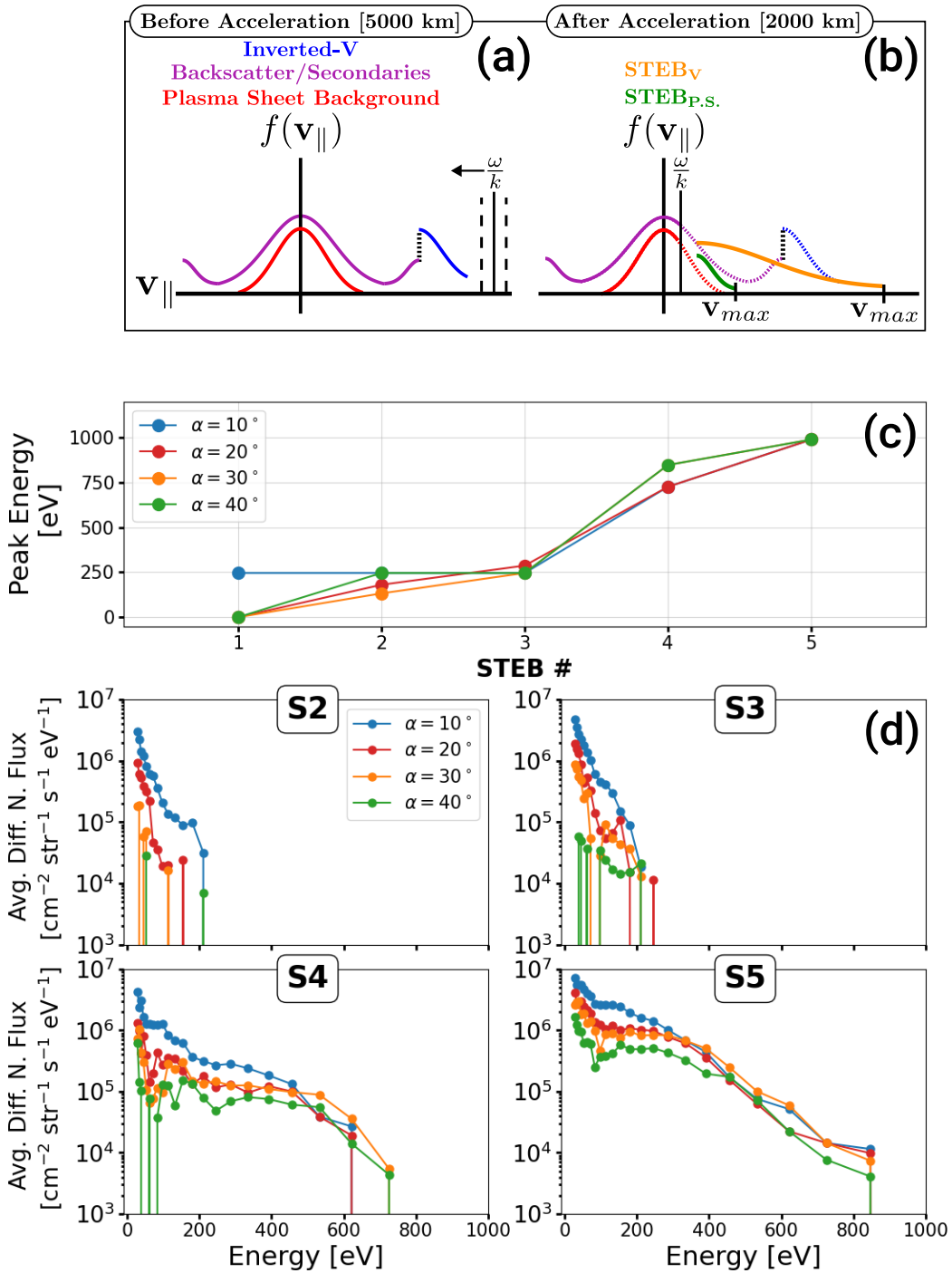


Figure 88. (a) 2D Illustration of the parallel distribution function  $f(v_{\parallel})$  for an inverted-V/backscatter population and an ambient plasma sheet source at high altitude before IAW resonance. (b) The effect of the same IAW passing through both distributions to produce a pair of STEBs with different peak energies and number flux. (c) Peak energy and (d) Averaged differential number flux over energy for choice STEB events in Figure 84.

By using the same EPAA data from Figure 84(a), we can show the characteristic differences of peak energy and flux intensity directly. In Figure 88(c) we plot the peak energy of our five STEB events for pitch angles  $10^\circ < \alpha < 40^\circ$ . Event S1 had no data for pitch bins  $> 10^\circ$  above the 4-count threshold applied earlier, hence it reports a null peak energy here. Here, the peak energy of events which coincide with the inverted-V ( $> 750$  eV) is over three times the peak energies of those events outside the inverted-V ( $< 250$  eV). Additionally, events S1, S2, S3 all report similar peak energies at similar pitch angles, which is also the case for events S4 and S5 together. If the IAW between our events are the same, the strong similarity of the peak energies for S1 to S3 suggest these shared a lower-energy resonant electron source population compared to S4, S5. Likewise, the higher peak energies of events S4 and S5 indicate these had a source that provided electrons at much greater parallel energies than the colder, background plasma sheet. These observations match the illustration in Figure 88(a) and (b) which shows the  $v_{max}$  for the plasma sheet STEB being much lower than the  $v_{max}$  for the inverted-V STEB.

The average flux intensity vs. energy across  $10^\circ < \alpha < 40^\circ$  for S2 to S4 are shown in Figure 88(d). This is calculated by averaging the differential number flux at each energy channel in a dispersion trace for a particular pitch angle. Here, S2 and S3 display the expected behavior of a thermal plasma sheet population, as shown by the red curve in Figure 88(a), accelerated by an IAW; a near exponential rise in flux intensity (linear-like region on a log plot) at the lower energy bins ( $E < 200$  eV) without a high energy component, as shown by the green curve in Figure 88(b). As depicted by Figure 88(a) and (b), the highest energies in the S2, S3 flux intensities come from the highest resonant thermal electrons and the exponential rise comes from the underlying (assumed) Maxwellian shape of the distribution. In contrast, S4 and S5 show the expected behavior of the backscattered and secondary electrons arising from the precipitating inverted-V electrons and backscatter, as illustrated by the purple curve in Figure 88(a), that are accelerated by a similar IAW: a much broader distribution of accelerated electrons up to a much higher peak energy, as shown by the orange curve in Figure 88(b). Events S3 and S4 have elongated flux intensities which start at higher energies and transition to a nearly exponential rise at  $E < 200$  eV. A plateau-like

behavior between  $200 < E < 400$  eV is seen in S4 and S5 as well as a drop-off in flux to below  $10^5$  [ $\text{cm}^{-2}\text{str}^{-1}\text{s}^{-1}\text{eV}^{-1}$ ] after  $E > 400$  eV. If the accelerating IAWs are the same for all our events, the lack of a high energy component for S2 and S3 suggests the underlying source population limited their peak energies. Additionally, the overall higher flux levels for S4, S5 compared to S2, S3 suggest a greater availability of resonant electrons for the former.

The observations of S4, S5 also fit the illustration in Figure 88 and may represent some additional features which we can speculate on. The exponential rise in S4 and S5 at the low energies should come from the exponential backscatter/secondary population. As shown in Chapter 4.4, the amount of additional electrons from these low energies that are produced by the inverted-V often display higher differential number fluxes than the high-energy peak representative of the quasi-static accelerated thermal distributions (inverted-V). This may explain why the peak fluxes for S4, S5 in the exponential region below  $E < 200$  eV show greater flux intensities than the assumed thermal populations that make up S2, S3. Next, the high-energy roll-off for S4, S5 at  $E > 500$  eV possibly represents the exponential decay in inverted-V electrons. The electrons that are accelerated at higher energies get more spread out in energy than the lower energies because the  $\Delta KE$  is greater, as given by the change in energy expression derived by C. A. Kletzing, 1994 in chapter 4.5. Finally, the plateau region that exists in the middle of S4, S5 may be the smoothed-over transition from inverted-V electrons to high-energy backscatter that also exhibits a plateau-like behaviour in differential number flux as seen by the EPAA detector. Finally, the comparison between S4 and S5 shows the later, higher energy STEB with generally larger flux intensities than the former. This may be due to S4 being coincident with a lower flux, lower peak energy inverted-V compared to S5's inverted-V as indicated in Figure 84(a). Without numerical models we cannot quantitatively evaluate this further and instead conclude that the general shape of the flux intensities in S4, S5 could reasonably be consistent with the illustration in Figure 88.

In summary, the interpretation of the STEBs in Figure 84(a) outside or coincident with inverted-V precipitation as coming from different resonant source populations is supported by their peak energy and average differential number flux vs. energy. We have connected the shapes

of the flux intensity graphs to the shapes of the underlying distributions we expect from Section 7.6 and found them consistent with our illustration in Figure 88(a) and (b). Notably, we have assumed similar accelerating waves produced these STEBs based on the spatial arguments of section 7.4 and their Alfvénic nature in section 7.5.

## 7.8 Other Explanations - Variation in Wave Parameters and Pitch Angle

In the previous section we assumed the accelerating IAWs were identical and that the differences between the STEBs behaviours were caused by different resonant source populations. Conceivably, this may not be true if there exists significant variation in the IAWs themselves while the underlying resonant populations are similar. It's worth qualitatively speculating on the expected impact from the wave frequency  $\omega$ , wave amplitude and perpendicular scale length  $\lambda_{\perp}$ .

Models like Tanaka et al., 2005 have shown the wave frequency could affect the flux intensities in Figure 88(d) by lowering the average number flux per energy. Physically, lowering the frequency spreads the wave energy over larger distances and the extended parallel electric field affects a greater number of altitudes at the same time. This increases the time between the first and last electrons seen within a STEB at a specific energy. Figure 78(a) showed S4, S5 as narrow features with short dispersion times ( $<1$  s) coincident with 1-5 Hz fluctuations and events S1, S2 and S3 as wider bursts, with longer dispersion times ( $\geq 1$  s) associated with 1-3 Hz frequencies. The lower frequencies associated with S2, S3 may have caused their average flux intensities in Figure 88(d) to appear lower than if they shared the same frequencies with S4, S5. However, Tanaka et al., 2005 indicates the difference of a few Hz produces a minimal impact and likely doesn't account for the factor of ten differences in flux intensity seen in Figure 88(d) between these STEBs.

Next, the wave amplitude can significantly affect the peak energy and flux intensity by directly affecting the resonance bands in equation 122. Increasing this parameter increases the wave parallel electric field and thereby the peak potential  $\phi_p$ . This causes the wave to interact with more electrons overall and at higher energies (Chaston, Bonnell, Peticolas, et al., 2002; L.-J. Chen et al., 2005a; Tanaka et al., 2005; Watt et al., 2006). The analog to the wave amplitude is

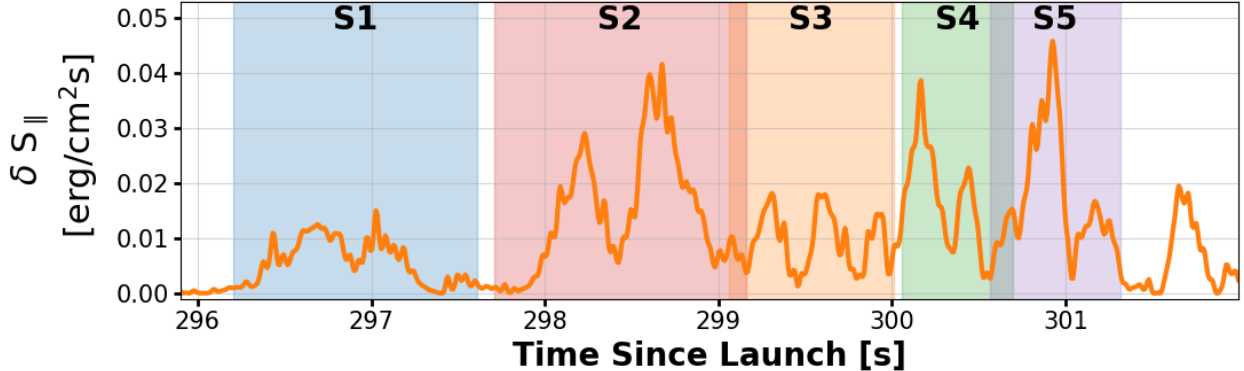


Figure 89. High Flyer Poynting Flux during the same time range as Figure 84 in the Dispersive Region. Flux values are estimated from  $\delta S_{\parallel} \sim V_A \delta B_{\perp}^2 / \mu_0$  and the duration of each STEB is colored and labelled.

the wave Poynting flux  $\delta S_{\parallel}$ , which cannot be determined directly for the High Flyer. Instead, an approximation to  $\delta S_{\parallel}$  using the magnetic field and *in situ* plasma density is made:

$$\delta S_{\parallel} \sim \frac{\delta B_{\perp}^2}{\mu_0} V_A \quad (177)$$

where  $\delta B_{\perp}^2 = \delta B_r^2 + \delta B_e^2$  and  $V_A$  is the local MHD Alfvén speed. In Figure 89 we plot  $\delta S_{\parallel}$  in the Dispersive Region with colored regions denoting the temporal duration of our STEBs. Despite the filtering done in Chapter 5.2, the relative magnitudes between peaks in  $\delta S_{\parallel}$  should still be representative of the unfiltered signal. Good agreement in time between the observed peaks in  $\delta S_{\parallel}$  and the duration of our bursts is seen, with the peaks occurring 0.25 to 0.5 seconds after the first high energy STEB electrons. Notably, any electrons accelerated by the wave should arrive first since these particles necessarily reflect and emerge ahead of the slowing wave. If a causal relationship between our STEBs and these  $\delta S_{\parallel}$  peaks exists, additional processes must be present. We posit two possibilities: (1) the wave did not fully accelerate electrons to the local phase speed at interaction or (2) resonant deceleration occurred. Explanation (2) has even been simulated by C. A. Kletzing et al., 2001, who showed waves arriving 0.2 seconds after the first high energy STEB electrons but within the dispersion trace. From this we argue the possibility that the peaks in  $\delta S_{\parallel}$  are causally correlated to our STEBs.

Despite the temporal agreement, there is a lack of correlation between  $\delta S_{\parallel}$  and the peak energy or flux intensity for our bursts. Event S2 is associated with a  $0.04 \text{ erg/cm}^2\text{s}$  peak, which is nearly the same as for S4 and S5, but S2 exhibits one third the peak STEB energy. Furthermore, S2 displays considerably lower flux intensity in Figure 88(d) compared to S4, S5 for any pitch angle. In these respects, event S2 is closer to event S3 even though S3 has less than half the associated wave power. That S2, S4 and S5 share similar associated wave powers but exhibit considerably different characteristics suggests the limiting factor was the source population being unable to supply enough high energy resonant electrons. Conversely, S4 and S5 have similar peak energies, flux intensities and share similar peak  $\delta S_{\parallel}$  as expected from similar waves accelerating a similar source. These observations suggest our STEB events were insensitive to factors of 2 to 4 changes in wave power, which is more consistent with the illustration in Figure 88(a) and (b) than the possibility that the differences in  $\delta S_{\parallel}$  for our events produced the differences in peak energy and flux intensity.

Finally, the perpendicular scale length  $\lambda_{\perp} = 2\pi/k_{\perp}$  also affects the peak energy and flux intensity of the STEBs. For example, lowering the initial  $\lambda_{\perp}$  of the IAW lowers the overall phase velocity  $\omega/k$  in Figure 88(a) via equation 114 but also expands its resonance bands due to an enhanced wave parallel electric field amplitude (Stasiewicz et al., 2000). Estimating  $\lambda_{\perp}$  directly is challenged by the rocket's cross-track velocity of 1 km/s and the STEB lifetimes of  $\sim 1$  s since previous studies report  $\lambda_{\perp}$  for STEBs in the ionosphere between 2 - 5 km (Lynch et al., 2012; Tanaka et al., 2005). As a heuristic attempt, the TOF polynomial coefficients in Table 1 can be fitted to the simulated  $a_2$  vs  $\lambda_{\perp}$  data in Figure 14 from Tanaka et al., 2005, which gives  $\lambda_{\perp}$  for events S2 to S5 in the ionosphere as 4.6 km, 4.05 km, 1.43 km, and 2.8 km, respectively. If these values are even approximately true, we would expect S2, S3 to have higher peak energies than S4,S5 if the source populations weren't the limiting factor since a higher  $\lambda_{\perp}$  implies a generally higher phase velocity. This is contrary to observation. Furthermore, the previous analysis of the  $\delta S_{\parallel}$  peaks suggests that the enhanced resonance bands for S4, S5 due to their  $\lambda_{\perp}$  values plays a minimal role in determining their peak energies and fluxes compared to the effect of an underlying

source population. From these observations we suggest the variation in our heuristic  $\lambda_{\perp}$  values are insufficient to explain the STEB behavioral differences.

In addition to wave parameters, we can look at variations in the median pitch angle to see if this parameter confirms our previous conclusions. In Figure 90 we show the median pitch angle for each energy-time pixel. The calculation excludes the  $-10^{\circ}, 0^{\circ}, 180^{\circ}$  and  $190^{\circ}$  bins due to inconsistent coverage and an additional 4-count threshold was implemented to remove points with  $\Delta N/N = 50\%$  error (colored as white). Dashed black lines help focus on the measurements for STEBs S4 and S5 as well as the inverted-V (dotted) that overlaps with S5. Events S1 to S3 are strongly field aligned with all median pitch angles near  $10^{\circ}$  whereas S4 and S5 reach above  $50^{\circ}$  at the higher energies. Furthermore, the most field-aligned electrons arrive first for S4 and S5. These observations may be explained by several possibilities: (1) the change in parallel kinetic energy for lower energies being more significant in how it affects their pitch angle compared to higher energies. (2) the highest energy STEB electrons are produced at the highest altitudes, allowing the mirror force to act longer and grow the pitch angles of these electrons and (3) events S1, S2, S3 come from the same source populations while S4, S5 come from individually different but similar source populations. As an example for possibility (1), a 20eV electron with  $\alpha = 50^{\circ}$  that gains 10 eV of parallel energy has a new pitch angle of  $\alpha = 40.4^{\circ}$  whereas a 500 eV particle at  $50^{\circ}$  than gains 150 eV has a new pitch angle  $\alpha = 43.5^{\circ}$ . These energy gains are the approximate values from the simulation by Tanaka, 2005. In this view, the low energies are more affected in pitch angle thereby displaying median pitch around  $10^{\circ}$  but the high energies are less affected. For explanation (2), this comes directly from the description of the mirror force in Chapter 2.2. Possibility (3) suggests that the waves which produced S1 to S3 were similar and passed through similar distributions, which may be supported by the ambient plasma sheet being a distribution that doesn't have much spatial variation on the scales of a few kilometers whereas the inverted-V distributions for S4 and S5 are highly variable over these distances. These observations serve to corroborate the interpretations of Chapter 7.6 and 7.7, wherein the highest energy electrons would come from higher altitudes and our STEB events S1 to S3 may be connected to a similar source

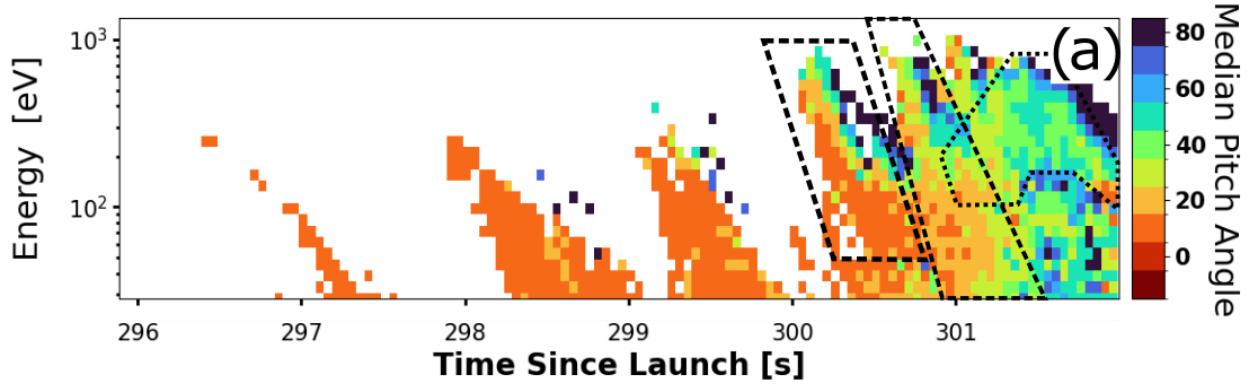


Figure 90. High Flyer EEPAA counts median pitch angle vs time since launch. Dashed black lines are provided to help distinguish S4, S5 from nearby inverted-V pixels.

poplution.

Without modeling we can only speculate on these possibilities, and conceivably various combinations of  $\delta S_{||}$  and  $\lambda_{\perp}$  could have conspired to create our STEBs, although the arguments here suggest this is unlikely. Notably, we have ignored energy loss by the wave during acceleration that may have coincidentally produced STEBs with similar  $\delta S_{||}$  peaks. We have also omitted the possibility of wave energy loss from reflections off the ionosphere since none of the available field measurements indicated significant phase differences between components.

## 7.9 Summary

The particle and fields instruments from the ACES-II sounding rockets observed identifiable dispersive electron signatures coincident with wave activity at nearly the same time while flying through the high-latitude post-dusk auroral region. The low frequency ( $< 8$  Hz) electromagnetic activity is shown to be Alfvénic on the Low Flyer and inferred as Alfvénic on the High Flyer due to the similarity of frequencies, field-aligned nature, known connection to suprathermal electron bursts as well as our interpreted spatial connection. A unique dataset of electron bursts is presented which shows electron bursts inside and outside regions of inverted-V precipitation. A case study involving these electrons showed the dispersions were likely accelerated from low-frequency inertial Alfvén waves between 2000 km - 5000 km altitude. Dispersive features coincident with inverted-V precipitation displayed higher peak energies and broader average differential number

flux vs. energy than those outside. Estimates for the accelerating wave parameters are given and qualitatively analyzed to eliminate the possibility that changes in Poynting Flux, frequency or perpendicular scale length are sufficient to explain these behavioral differences. This constitutes *in situ* evidence for STEB peak energy and flux enhancements due to resonant acceleration with primary inverted-V and secondary/backscatter electron populations. This provides observational support for similar conclusions made by L.-J. Chen et al., 2005a in their modeling of dispersion traces using Alfvén waves.

## CHAPTER 8: MODELING

The results of the Chapter 7 were based upon the idea that the waves that accelerated our STEB electrons were approximately similar and did not vary enough to explain the behavioral differences of our dispersions. This was argued by the electron observations themselves and any available electric and magnetic fields data coincident with the STEBs. Two key points arose from this analysis: (1) the peak energies of the STEBs were too different to come from the same source population and (2) the shapes of the differential number flux vs. energy curves don't match for similar energy channels. In this chapter, we model the distributions that created our STEBs in more detail and demonstrate these key points directly. We show that under reasonable assumptions of our accelerating waves, the conclusions of the previous chapter are supported by this work. The efforts presented here are ongoing and have yet to be published.

### 8.1 Model Description

The first step in our model is to calculate an Inertial Alfvén Wave speed profile. This will be used to estimate which range of particle velocities should undergo wave-particle resonance at any given altitude. The next step is to fit the inverted-V data within the Dispersive Region in order to model the accelerated magnetospheric electron distributions at various altitudes. Finally, we can use the approximated source altitudes of TOF from Chapter 7.6 to estimate the required peak potential our IAW must have had in order to reproduce our STEBs.

The equations which describe our IAW were derived in Chapter 2.8. The phase velocity of the IAW is given by

$$\left(\frac{\omega}{k_{\parallel}}\right)^2 = V_A^2 \frac{(1 - \omega^2/\omega_{ci}^2)(1 + k_{\perp}^2 \rho_i^2)}{(1 + k_{\perp}^2 \lambda_e^2)} \quad (178)$$

for wave frequency  $\omega$ , parallel scale length  $k_{\parallel} = 2\pi/\lambda_{\parallel}$ , MHD Alfvén velocity  $V_A = B/\sqrt{\mu_0 \rho_m}$ , mass-weighted mass density  $\rho_m = \sum n_i m_i$ , magnetic field  $B$ , ion cyclotron frequency  $\omega_{ci} = qB/m_i$ , perpendicular scale length  $k_{\perp} = 2\pi/\lambda_{\perp}$ , ion Larmor radius  $\rho_i = mv_{\perp}/qB$ , electron skin depth  $\lambda_e = c/\omega_{pe}$ , speed of light  $c$  and electron plasma frequency  $\omega_{pe} = (ne^2/m_e \epsilon_0)^{1/2}$ . This expression

is valid in regions where  $\beta_i < m_e/m_i$  and the electrons are cold,  $\omega/k_{\parallel} > v_{th,e}$ . The last required piece for the IAW is the resonance band for electrons with velocity parallel to the wave  $v_{\parallel,e}$ , which was given in Chapter 4.5:

$$\frac{\omega}{k_{\parallel}} - \sqrt{\frac{2e\Phi_{max}}{m_e}} < v_{\parallel,e} < \frac{\omega}{k_{\parallel}} + \sqrt{\frac{2e\Phi_{max}}{m_e}} \quad (179)$$

where the left inequality corresponds to wave-particle acceleration and the right inequality deceleration.

### 8.1.1 Geomagnetic Field

The first geophysical parameter we model is the geomagnetic field  $\vec{B}_{geo}$ . To do this we follow a single magnetic field line to higher altitudes. Alfvén waves move approximately along a constant L-Shell value down to the Earth since they move so quickly parallel to  $\vec{B}_{geo}$  that they do not deviate very much from the geomagnetic field lines they were produced on. For the ACES-II mission, the Dispersive region occurred near  $L = 8.7$  and by fixing this value we can estimate a geomagnetic latitude for any altitude using the L-Shell equation:

$$\lambda(r) = \arccos \sqrt{\frac{r}{L}} \quad (180)$$

where  $\lambda(r)$  is the geomagnetic latitude at altitude “r” (in units of  $R_E$ ) at a chosen L-Shell value. The geomagnetic longitude of the dispersive region does not change with altitude, thus we can convert our values into geodetic Lat/Long/Alt and feed them into the CHAOS-7 (Finlay et al., 2020) model to determine a  $|\vec{B}_{geo}|(z)$  altitude profile along a specific L-Shell. In Figure 91 we show  $|\vec{B}_{geo}|$  and  $\nabla|\vec{B}_{geo}|$  for  $L=8.7$ . A red line is added for the altitude where the ACES-II High Flyer observed the Dispersive Region.

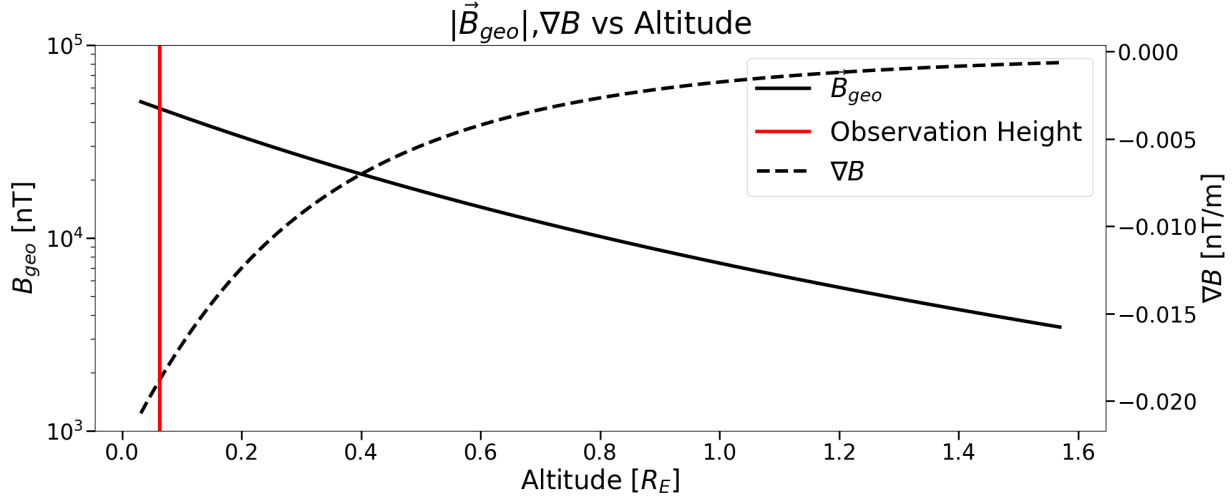


Figure 91. (Top) The model  $|\vec{B}_{geo}|$  for a specific L-Shell of  $L=8.7$ . (Bottom) Calculated gradient in magnetic field  $\nabla|\vec{B}_{geo}|$  used later in magnetic mirroring.

### 8.1.2 Perpendicular Scale Length

The first wave parameter we model is the perpendicular scale of the wave over altitude,  $k_{\perp}(z)$ . Conceptually, a wave propagating along a geomagnetic field line is extended some distance  $\lambda_{\parallel}$  along the field line and some distance  $\lambda_{\perp}$  across the field line. The generator of these waves is considered to be far out in the magnetosphere, which launches waves with some initial  $\lambda_{\perp}$  at some frequency  $\omega$ . The perpendicular scale size of the wave compresses due to the converging field lines of Earth, reducing  $\lambda_{\perp}$ . In Figure 92 we show how  $k_{\perp}$  will change as the wave approaches the ionosphere. The key mechanism which drives this is the assumption of constant magnetic flux through the wave being preserved:

$$\vec{B} \cdot \vec{A} = \lambda_{\perp}^2 B = \text{const.} \quad (181)$$

This allows us to estimate how  $\lambda_{\perp}$  should evolve over distance. If we set  $k_{\perp 0}$  as the scale size of the wave in the Ionosphere with magnetic field  $B_I$ , we can estimate  $k_{\perp}(z)$  at any higher altitude

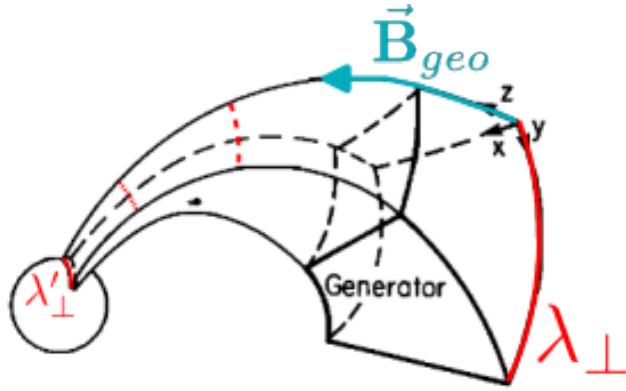


Figure 92. Adapted from Lysak, 1985. As the geomagnetic field lines of Earth coalesce, the  $k_{\perp}$  of the wave shrinks to maintain constant magnetic flux.

$B_M(z)$  through the magnitude of the magnetic field:

$$k_{\perp}(z) = k_{\perp 0} \sqrt{\frac{B_M(z)}{B_I}} \quad ; \quad \lambda_{\perp}(z) = \lambda_{\perp 0} \sqrt{\frac{B_I}{B_M(z)}} \quad (182)$$

For a choice value of  $\lambda_{\perp 0}$  in the ionosphere and a series of geomagnetic field values  $B_M(z)$ , we can determine the altitude profile of  $k_{\perp}(z)$ . By using  $B_M = |\vec{B}_{geo}|$  from our geomagnetic field model we show the  $\lambda_{\perp}(z), k_{\perp}(z)$  profiles for  $\lambda_{\perp 0} = 3.5$  km in Figure 93.

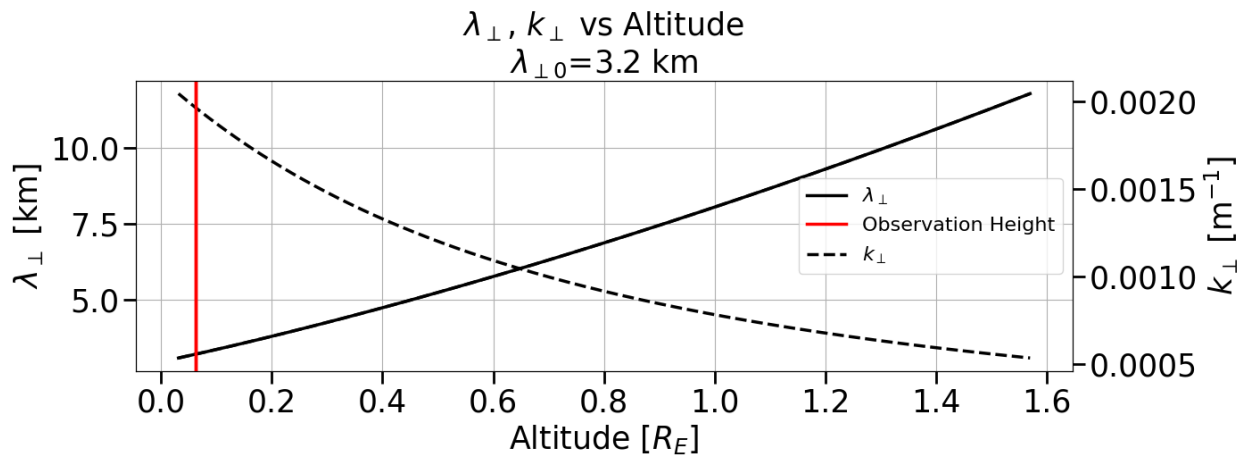


Figure 93. Model  $\lambda_{\perp}(z), k_{\perp}(z)$  for a chosen ionospheric value of  $\lambda_{\perp 0} = 3.5$  km

### 8.1.3 Plasma Density, Ion Mass And Skin Depth

Our plasma density profile is an empirically determined density profile from C. A. Kletzing et al., 1998 between 1000 km to 8000 km above 60° invariant latitude that's dominated by cold ionospheric plasma (L.-J. Chen et al., 2005a; C. A. Kletzing et al., 1994; C. A. Kletzing et al., 1998; Schroeder et al., 2021). It's given by

$$n_e(z) = n_0 e^{-(z-z_0)/h} + n_1 z^{-1.55} \quad (183)$$

where  $n_0 = 6 \times 10^4 \text{ cm}^{-3}$ ,  $n_1 = 1.34 \times 10^7 \text{ cm}^{-3}$ ,  $z_0 = 318 \text{ km}$  and  $h=383 \text{ km}$ . From this, we can also model the ion composition vs altitude by assuming quasi-neutrality in equation 183,  $n_e(z) \approx n_i(z)$ . This assumes all ion densities are dominated by singly ionized states. Above 2000 km the ambient plasma is mostly dominated by  $\text{H}^+$ , but below this  $\text{O}^+$  is the dominant species. To reflect this transition, a hyperbolic tangent function from Schroeder et al., 2021 is used:

$$\frac{n_O}{n_i} = \frac{1}{2} \left[ 1 - \tanh \left( \frac{z - z_i}{h_i} \right) \right] \quad (184)$$

where  $z_i = 2370 \text{ km}$  and  $h_i = 1800 \text{ km}$ . This allows the effective ion mass at any altitude to be calculated as  $m_i = (n_H m_H + n_O m_O) / n_i$  where the total ion density is  $n_i = n_H + n_O$ . Finally, the electron skin depth is calculated directly from the plasma density via

$$\lambda_e = c / \omega_{pe} = \left( \frac{c^2 \epsilon_0 m_e}{n e^2} \right)^{1/2} \quad (185)$$

and shown in Figure 96.

### 8.1.4 Ion Terms And Kinetic Corrections

As mentioned in Chapter 7, the Ion terms in equation 178 are generally negligible for our low-frequency waves in a cold plasma. Nevertheless, we provide the expressions used. The mass-weighted Ion larmor frequency is calculated directly from  $\omega_i = qB/m_i$  using our model  $|\vec{\mathbf{B}}_{geo}|$ ,

weighted ion mass vs altitudes  $m_i$  and  $q = +|e|$  for our singularly charged ions. The Larmor radius is given by  $\rho_i = v_{\perp}/\omega_i$  and estimates for  $v_{\perp}$  come from the thermal velocity of the ion plasma,  $v_{th,i} = \sqrt{k_B T_i/m_i}$ . A temperature vs altitude profile is required for this, which comes from Schroeder et al., 2021:

$$T_i(z) = T_1 e^{z/h_0} + T_0 \quad (186)$$

where the parameters  $T_0 = 1$  eV and  $T_1 = 0.0135$  eV and  $h_0 = 2000$  km.

With these pieces we can evaluate each of the terms in the phase velocity of equation 178. In Figure 97 we show an example set of kinetic corrections by assuming a 4 Hz Alfvén wave with ionospheric  $\lambda_{\perp 0} = 3.5$  km. The MHD Alfvén velocity is shown in the top left, the inertial term  $(1 + k_{\perp}^2 \lambda_e^2)$  in the top right, the ion Larmor radius term  $(1 + \rho_i^2 k_{\perp}^2)$  in the bottom left and the finite frequency effect  $(1 - \omega^2/\omega_{ci}^2)$  in the bottom right. Each term is plotted up to 10,000 km and only the Inertial term displays meaningful deviation from unity. This difference is apparent in the MHD vs. IAW phase speed shown in Figure 98 which gives the MHD velocity in solid red and the IAW velocity in solid blue. From these profiles we can now estimate  $\omega/k_{\parallel}$  at any altitude. This will allow us to consider the resonance condition in equation 179 after we estimate the types of electron distributions that should exist at different altitudes.

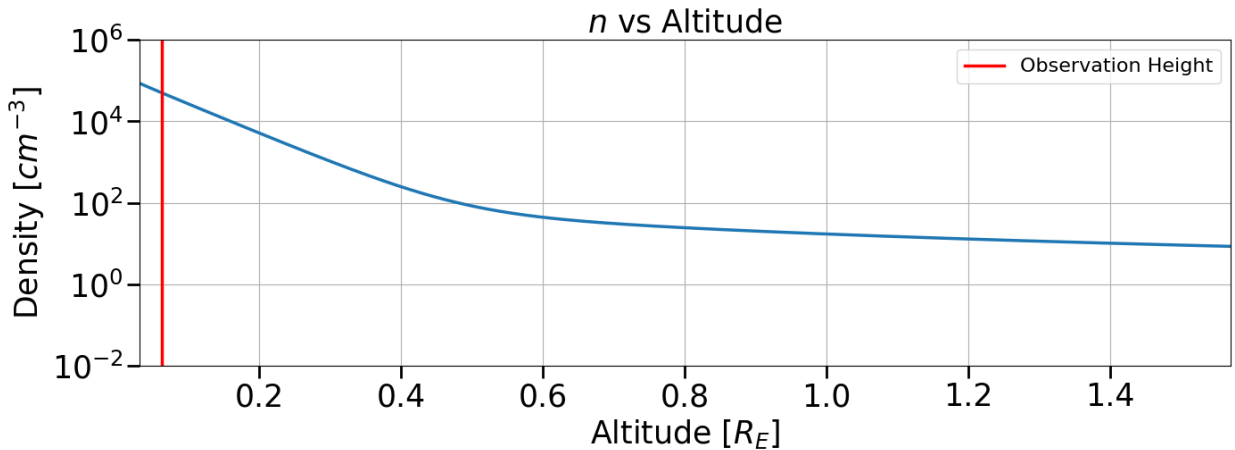


Figure 94. Model electron plasma density for the high latitude auroral zone. Based on the work from C. A. Kletzing et al., 1998.

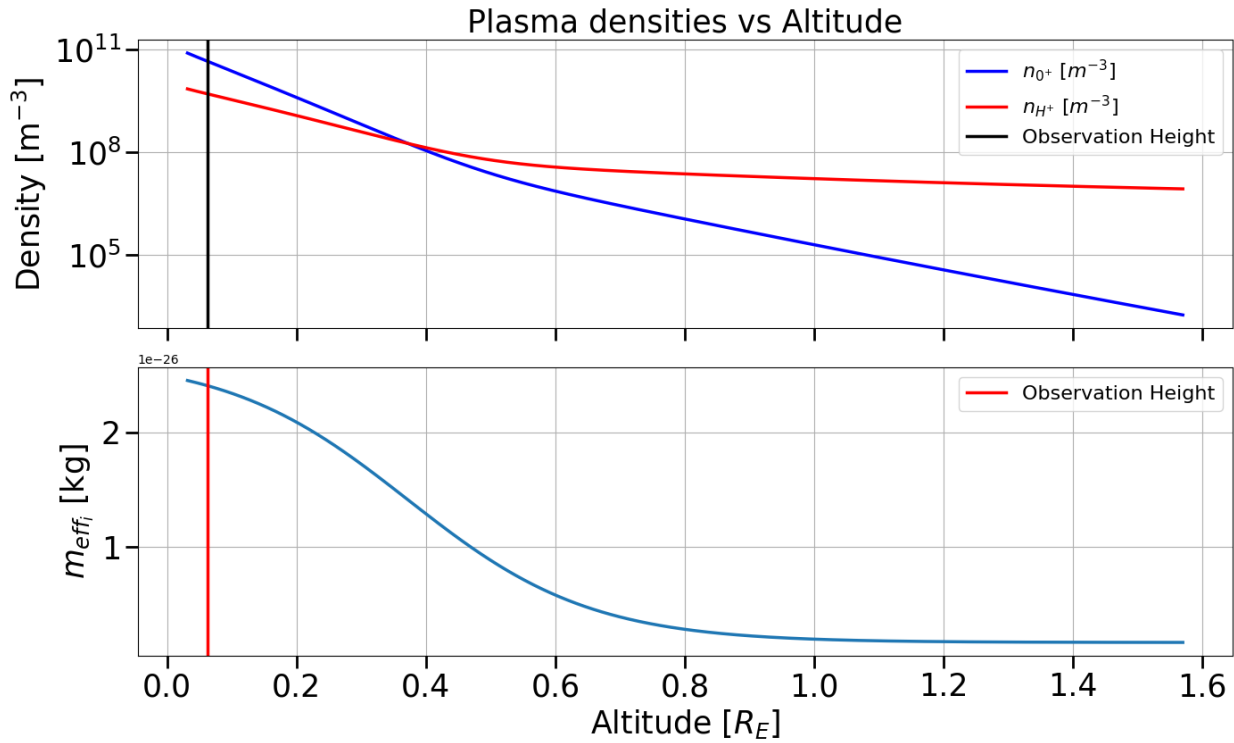


Figure 95. (Top) Ion compositions as given by equation 184. (Bottom) Effective ion mass calculated from  $m_i = (n_H m_H + n_0 m_0) / n_i$ .

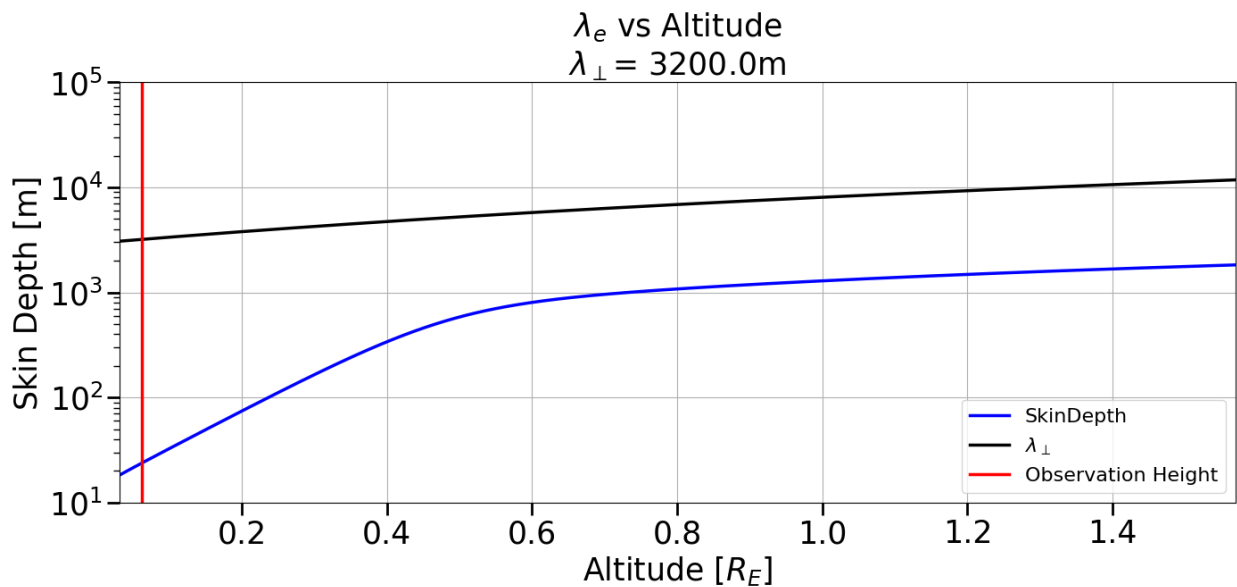


Figure 96. Model of Electron Skin Depth. An example  $\lambda_\perp(z)$  profile is also plotted for comparison on the  $k_\perp^2 \lambda_e^2$  term.

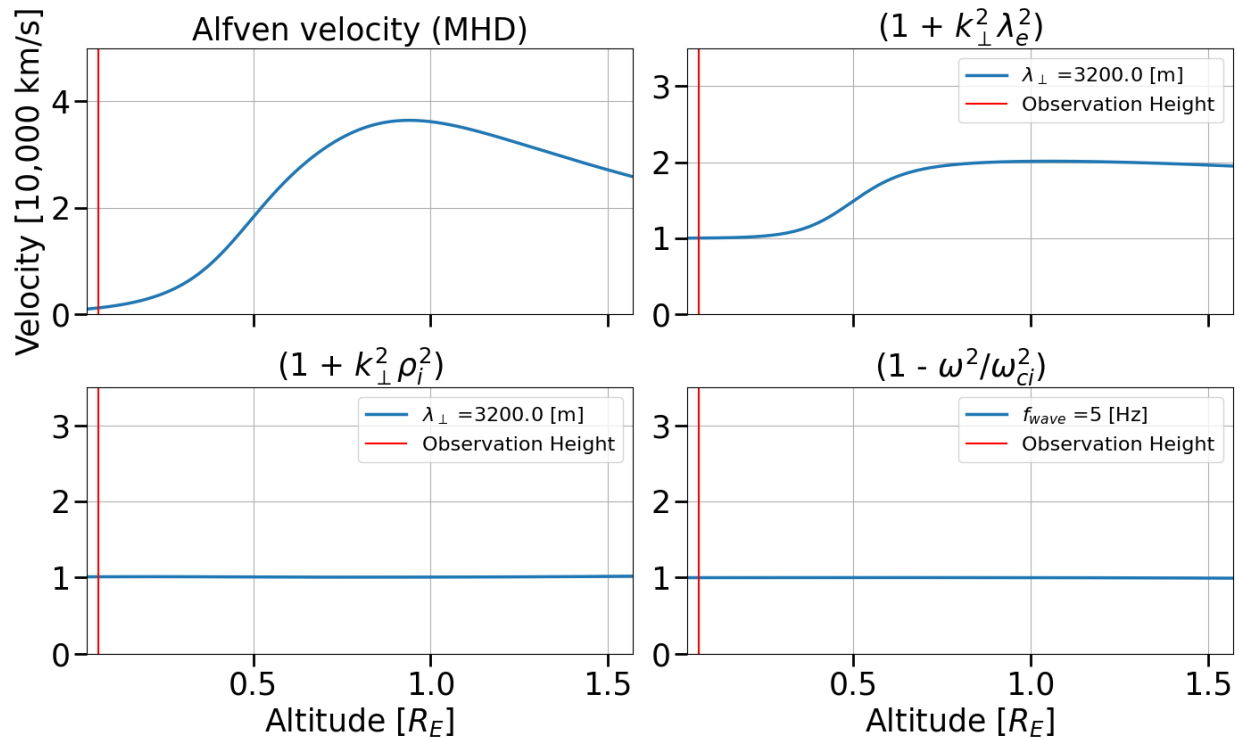


Figure 97. Model kinetic corrections to the Alfvén phase velocity vs altitude. (Top left) MHD Alfvén speed  $V_A = B/\sqrt{\mu_0 \rho_m}$  (Top Right) Electron inertia term  $(1 + k_{\perp}^2 \lambda_e^2)$  (Bottom left) Ion Larmor radius term  $(1 + \rho_i^2 k_{\perp}^2)$  (Bottom right) Finite Frequency term  $(1 - \omega^2/\omega_{ci}^2)$ . Only the inertial term meaningfully contributes at these altitudes due to the cold electrons/ions and low frequencies involved ( $f < 10$  Hz)

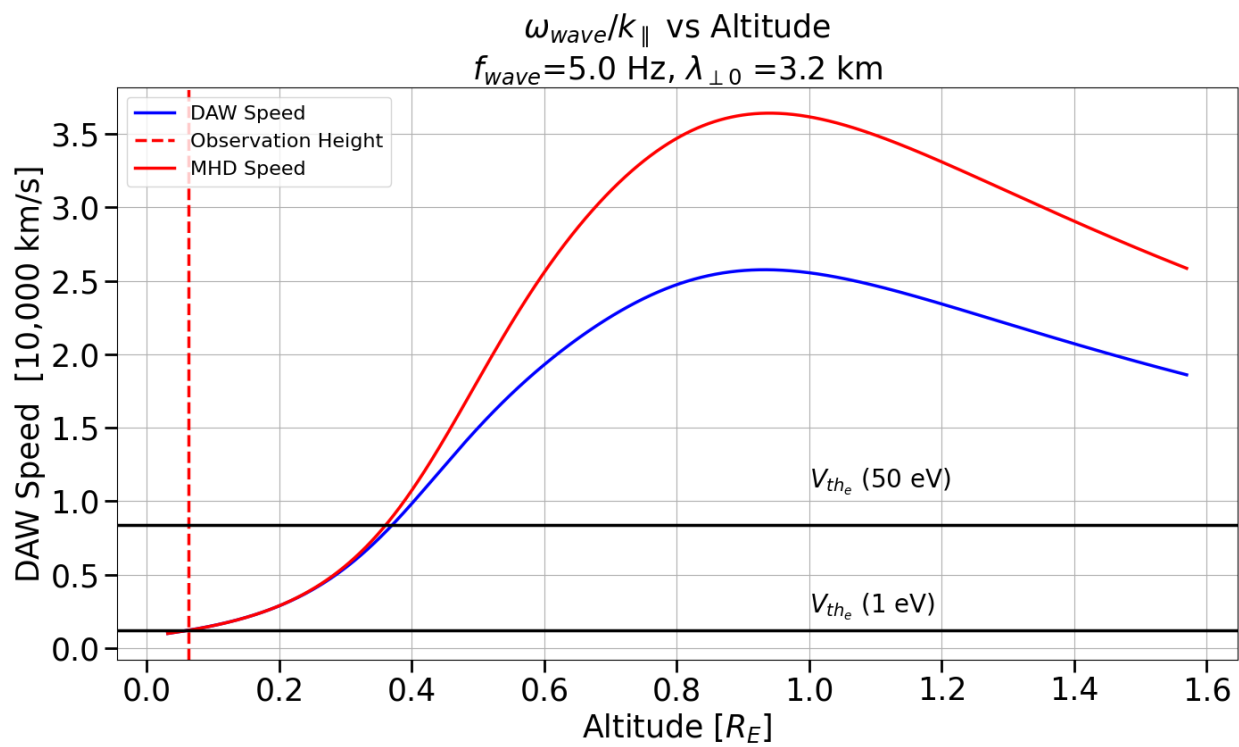


Figure 98. Model Alfvén wave phase velocities. (Solid Red) MHD Alfvén Velocity (Solid Blue) Inertial Alfvén Wave velocity with  $f = 4 \text{ Hz}$  and  $\lambda_{\perp 0} = 3.2 \text{ km}$  in the ionosphere. Example thermal velocities for a  $T_e = 1 \text{ eV}$  and  $50 \text{ eV}$  electron plasma are provided for reference when considering resonance.

## 8.2 Fitting the Inverted-V

Here we will leverage concepts discussed in Chapter 4 to fit the inverted-V electron distributions near our STEB events. This allows us to estimate the Maxwellian plasma parameters in the pre-accelerated plasma sheet. As discussed previously, the differential number flux  $j_N(E, \alpha)$  vs energy plots of inverted-V electrons in the ionosphere contain information regarding (1) the quasi-statically accelerated distributions at high altitude and (2) the amount of backscatter/secondary flux produced from the primary beams of electrons. Conceptually, a thermal population that has been accelerated by a quasi-static potential  $V_0$  should appear in a differential flux vs. energy plot as a peak in flux starting at the energy  $V_0$  that decays exponentially at higher energies. This is because the low-energy core of the distribution have energies  $E_{core} \ll V_0$  and appear at the energy of  $V_0$ . The exponential decay that follows is just the same underlying Maxwellian distribution, but now shifted upwards in energy by  $V_0$ . From this insight, we can devise a routine to estimate the plasma density  $n$ , electron temperature  $T_e$  and accelerating potential  $V_0$  from our ACES-II High Flyer data. We will choose field-aligned bins for our data since these are the least affected by magnetic mirroring which could shift differential number flux values to higher pitch angles, thereby affecting our fitting.

The fitting process starts by identifying the peak value in the  $j_N(E, \alpha)$  vs.  $E$  plots that are above a threshold energy in the High Flyer EEPAA's data near STEB 5 at 17:25:00 UTC. We interested in where the peak in  $j_N(E, \alpha)$  occurs at energies  $E > 100$  eV since this energy corresponds to the quasi-static potential  $V_0$ . Our routine considers only peaks with  $E \geq 140$  eV and checks 8 sweeps of the EEPAA detector for pitch angles  $10^\circ < \alpha < 30^\circ$ . All data above this energy threshold are considered part of the accelerated Maxwellian, which are fitted to

$$j_N(E, \alpha) = \left( \frac{2E}{m_e^2} \right) n \left( \frac{m}{2\pi k_B T_e} \right)^{3/2} \exp \left\{ -\frac{E + V_0}{m_e k_B T_e} \right\} \quad (187)$$

where  $E$  is the energy channel of the EEPAA,  $T_e$  is the temperature of the electron plasma and  $V_0$  is the quasi-static potential and  $n$  is the plasma density. We have written equation 187

in S.I. units however we will report all values in electronvolts and  $\text{cm}^{-3}$ . Notably, the isotropic nature of a Maxwellian distribution leads to no dependence on the pitch angle  $\alpha$  for  $j_N(E, \alpha)$ . The Marquart-Levenberg (ML) fitting routine called “curve fit” from the python library “scipy” was used to perform the fits. For this type of fitting, an initial “guess” of the expected fit parameters is made and the ML fitting procedure iteratively adjusts the guess until a minimum between the fit and data is achieved. Parameter “bounds” are implemented which constrain the fitting procedure to specific ranges that can be chosen for each parameter.

In Figure 99 we show an example of this process. The top plot is the EEPAA differential number flux  $\alpha = 30^\circ$  bin and the data that represents the inverted-V is boxed with a dotted black

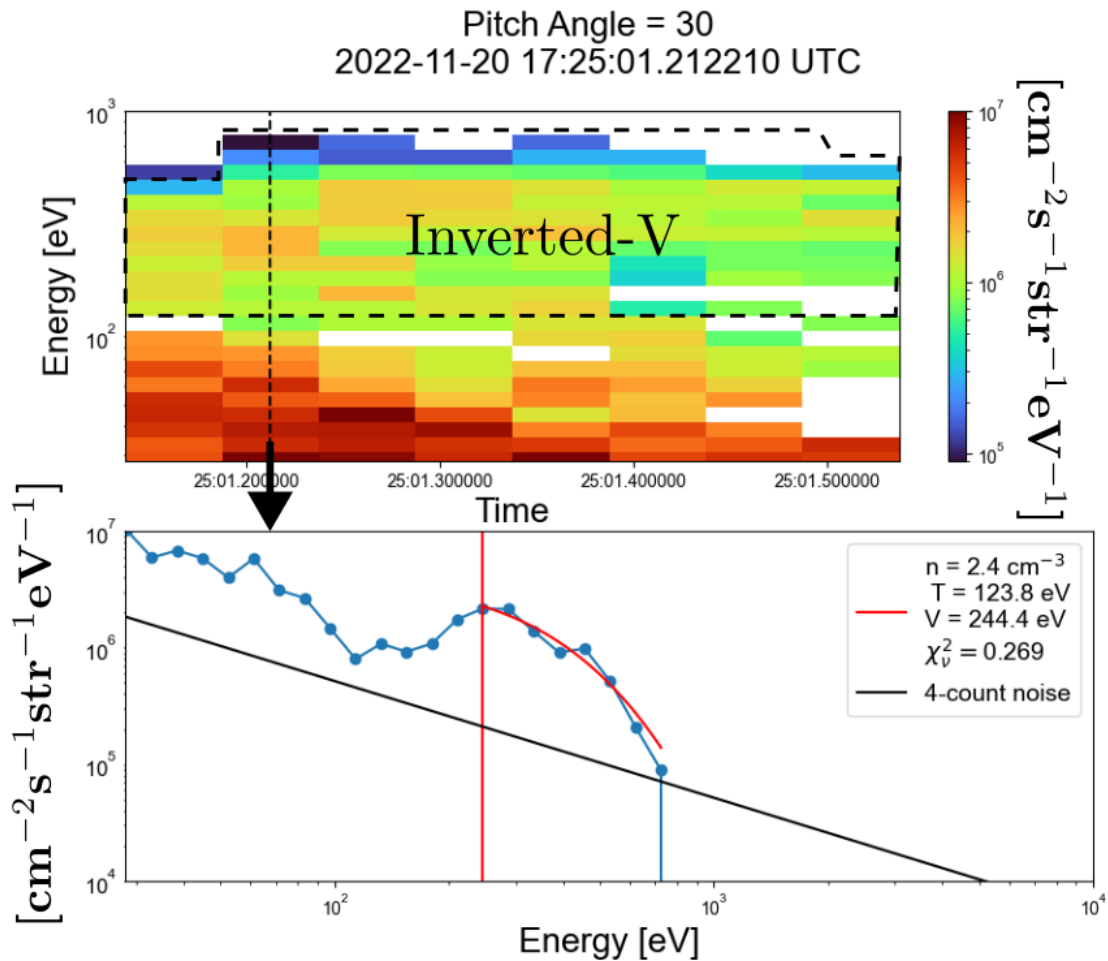


Figure 99. Example of fitting routine done on the ACES-II High Flyer EEPAA data to estimate the plasma parameters of the plasma sheet Maxwellian. See text for details.

line. A vertical dotted line represents the slice in  $j_N(E, \alpha)$  data shown on the bottom panel. In the bottom panel, the peak in  $j_N(E, \alpha)$  is shown with a vertical red line representing the value for  $V_0$  and the exponential red line is the Maxwellian fit. A black, 4-count noise baseline is plotted to determine data points with significant error. In this example, the fit predicts a Maxwellian with  $n = 2.4\text{cm}^{-3}$ ,  $T_e = 123.8\text{eV}$  and  $V_0 = 244.4\text{eV}$ . To evaluate the goodness of our fit, a reduced ChiSquared fitting statistic is calculated for our data using the same form as described in Chapter 6.3. The error values for each  $j_N(E, \alpha)$  are calculated by determining the standard deviation from the nearest 3 energy sweeps (in time) on either side of a particular  $j_N(E, \alpha)$  sweep.

We perform this fitting routine for a total of eight EEPAA sweeps near the inverted-V close to STEB event S5. In Figure 100 we plot the result of our fits for the  $\alpha = 10^\circ$  pitch bin. Red lines in each plot indicate the average value. Previous reports from the Hydra satellite of *in situ* data for the plasma sheet electrons that reach auroral field line suggest a density between 0.01 to 1  $\text{cm}^{-3}$  and a temperature between 50 eV to 200 eV is reasonable for plasma sheet electrons C. A. Kletzing et al., 2003. The average temperature value for all our fits is near  $T_e \sim 130$  eV and our average density across all pitch angles is  $n \sim 2.5 \text{ cm}^{-3}$ . The  $\chi^2$  values themselves are close to unity, indicative of a good fit and each fit was visually confirmed to look appropriate, however we caution any interpretation beyond this since no additional deeper analysis was done to verify a good fit in a statistical sense (see for more details Press et al., 2007). The discrepancy between our plasma density and the expected plasma density  $n < 1 \text{ cm}^{-3}$  may be the result of the initial guess and bounds used in the Marquart-Levenberg fitting. For example, the shape of the Maxwellian function is sensitive to both the plasma density and temperature, thus finding a unique fit to a set of points requires heavy constraints on these parameters. For our purposes, the “rough” fits we have performed are sufficient since we are mostly interested in the spread of velocities (temperature) of our plasma sheet distributions, not so much the amplitude (density). Improvements to our fitting procedure will not have meaningful impact on our illustrative results since the plasma temperature would have to change significantly ( $\Delta T_e > 100$  eV) after improving the fit for this to matter, which is unlikely. Additional details can be found in Kaepller, 2014.

## Pitch = 10

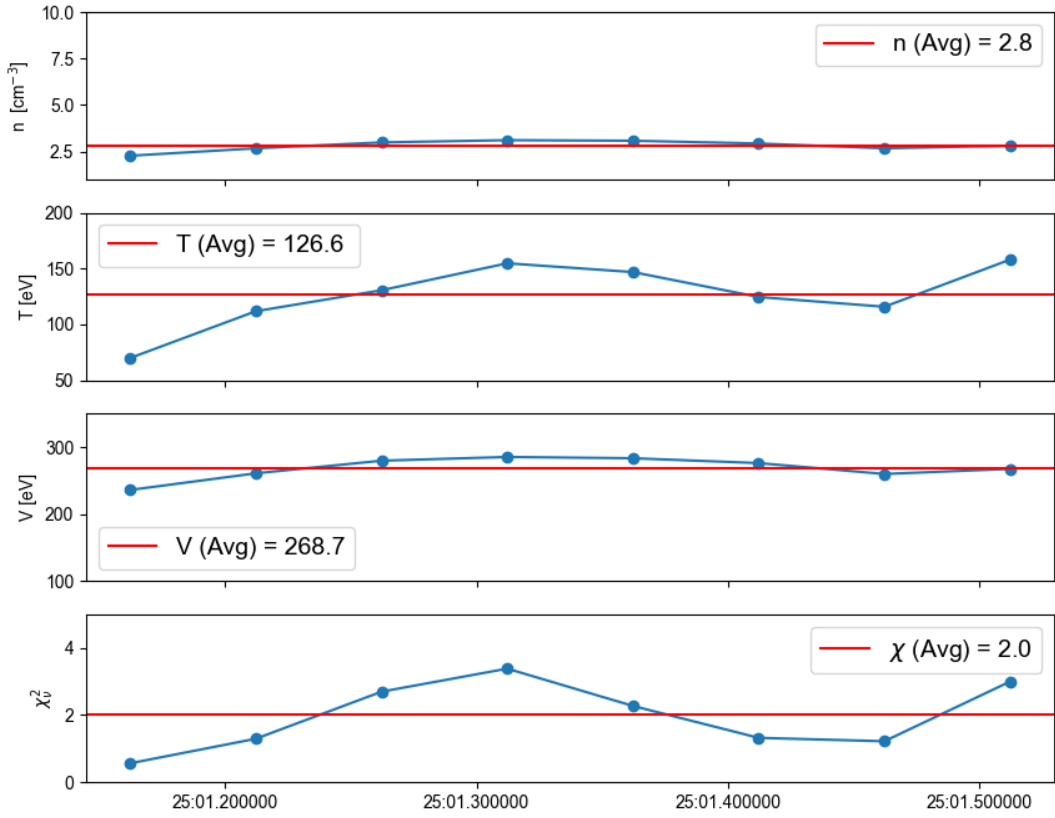


Figure 100. Average values for the  $\alpha = 10^\circ$  pitch bin for 8 sweeps of EEPAA data in the inverted-V near STEB event S5.

### 8.3 Model Distributions and Mapping

In this section, we use our model to represent the resonant populations that likely created our STEB events. We use the distribution parameters described in the previous section and map them to different altitudes through the conservation of the first adiabatic invariant and Louisville's Theorem. The details of this phase space mapping were covered in Chapter 4.4. We then discuss how the IAW resonance bands are implemented

The ambient plasma sheet is the assumed source population for STEB event S1, S2 and S3 in the High Flyer EEPAA dataset shown in Figure 84. In the previous section we have modelled

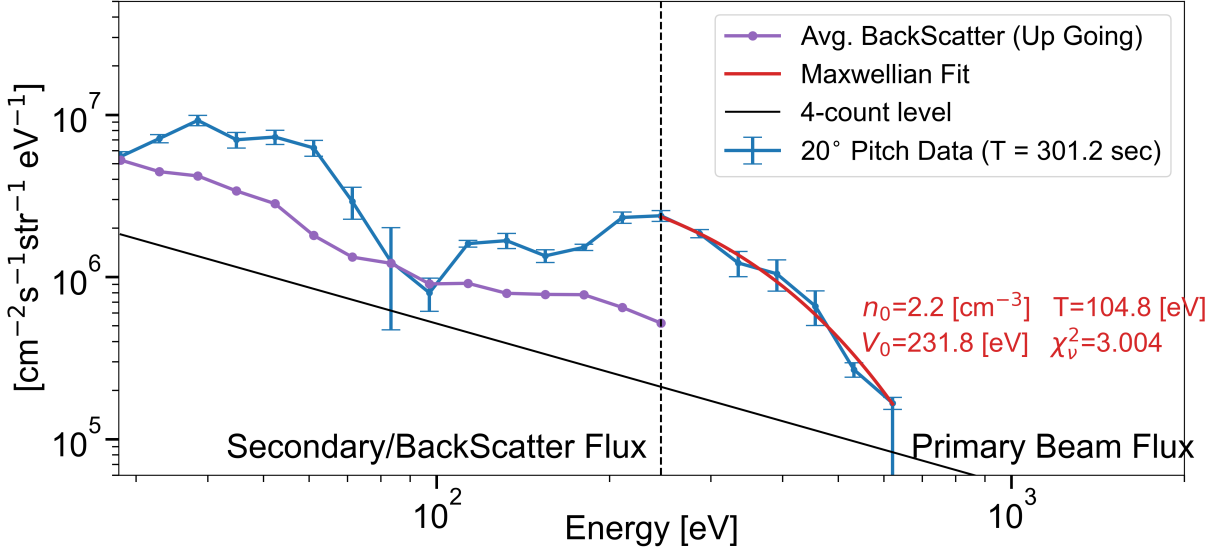


Figure 101. Slice in differential number flux used for the modelling of the ambient plasma sheet.

the distribution of plasma sheet electrons that would have been accelerated by the inverted-V near STEB 5. We take these parameters as decently accurate descriptions of the un-accelerated plasma sheet distribution that existed along the geomagnetic field lines for STEB events S1 to S3. We start our modelling by choosing the best inverted-V parameters to describe our Maxwellian. The chosen data (blue line in Figure 101) was taken at  $t = 301.2\text{ s}$  and  $20^\circ$  pitch due to its proximity to STEB S5 and identifiable peak in differential number flux. The fit parameters indicate a Maxwellian with plasma density  $n = 2.2 \text{ cm}^{-3}$ , temperature  $T_e = 105 \text{ eV}$  and accelerating potential  $V_0 = 232 \text{ eV}$  at a  $\chi_v^2 = 3$  level. A grid in velocity space is generated and assigned a  $f(\vec{v}_\perp, \vec{v}_\parallel)$  Maxwellian distribution value. The velocity grid is transformed to different altitudes by the physics that transforms the velocities of the (un-primed) point  $v_{\perp,i}, v_{\parallel,i}$  to the (primed)  $v'_{\perp,i}, v'_{\parallel,i}$  point at a new altitude. The value of the distribution function in the pre-transformed coordinates is unchanged and simply carried to the new coordinates. In our case, an initial distribution is created at a starting altitude of  $z_0$  and mapped to different altitudes via the mirror force. We choose a starting altitude of  $z_0 = 6000 \text{ km}$  since this altitude is typically where electrons are released from acceleration (Bennett et al., 1983). To realistically model this distribution along an undisturbed geomagnetic field line, we assume any particles that reach 100 km altitude will be lost, thereby introducing a loss-cone into

our plasma sheet distribution. Furthermore, the peak energy of the distribution simulated by the model is capped by the peak energy seen by the EEPAA detector minus the accelerating parallel potential. This represents the peak thermal energy of the non-accelerated Maxwellian. In Figure 102 we show an example of this plasma sheet model mapped to 6000 km, 2500 km and 400 km.

The modelling of the inverted-V distribution is similar to the ambient plasma sheet but with a few differences. The same plasma sheet Maxwellian distribution is created at 6000 km but no loss cone is introduced since a continuous stream of electrons are injected into the ionosphere from the aurora, which fills these missing regions. Next, the velocity space is transformed in parallel velocity by the quasi-static potential  $V_0$ . Only the portion of the Maxwellian with pitch angles  $|\alpha| \leq 90^\circ$  are relevant since any other pitch angles do not get accelerated by the parallel potential. In addition to the Maxwellian, a secondary/backscatter population is added to represent these lower-energy electrons which also populate the inverted-V field lines. These additional electrons are assumed to be isotropically produced at the ionosphere (Evans, 1974) so 5 EEPAA sweeps centered at  $t=301.2\text{s}$  from  $100^\circ < \alpha < 170^\circ$  are averaged into a single  $j_{N,\text{seconday}}(E)$  curve for energies below the  $V_0$  energy. This secondary/backscatter flux curve is shown as a purple line in Figure 101. As described by Evans, 1974, this secondary flux of electrons will travel back to the quasi-static parallel potential and get reflected back towards the ionosphere. Thus, in modeling the inverted-V distributions we add an isotropic distribution of  $j_{N,\text{seconday}}(E, \alpha)$  at 400 km moving up the field line, map these distributions to higher altitudes through the mirror force and then flip the direction of the parallel velocity since this distribution will contain approximately equal components moving upward and downward. In Figure 103 we show this secondary population of downgoing flux along with the classic “banana” distribution of the inverted-V.

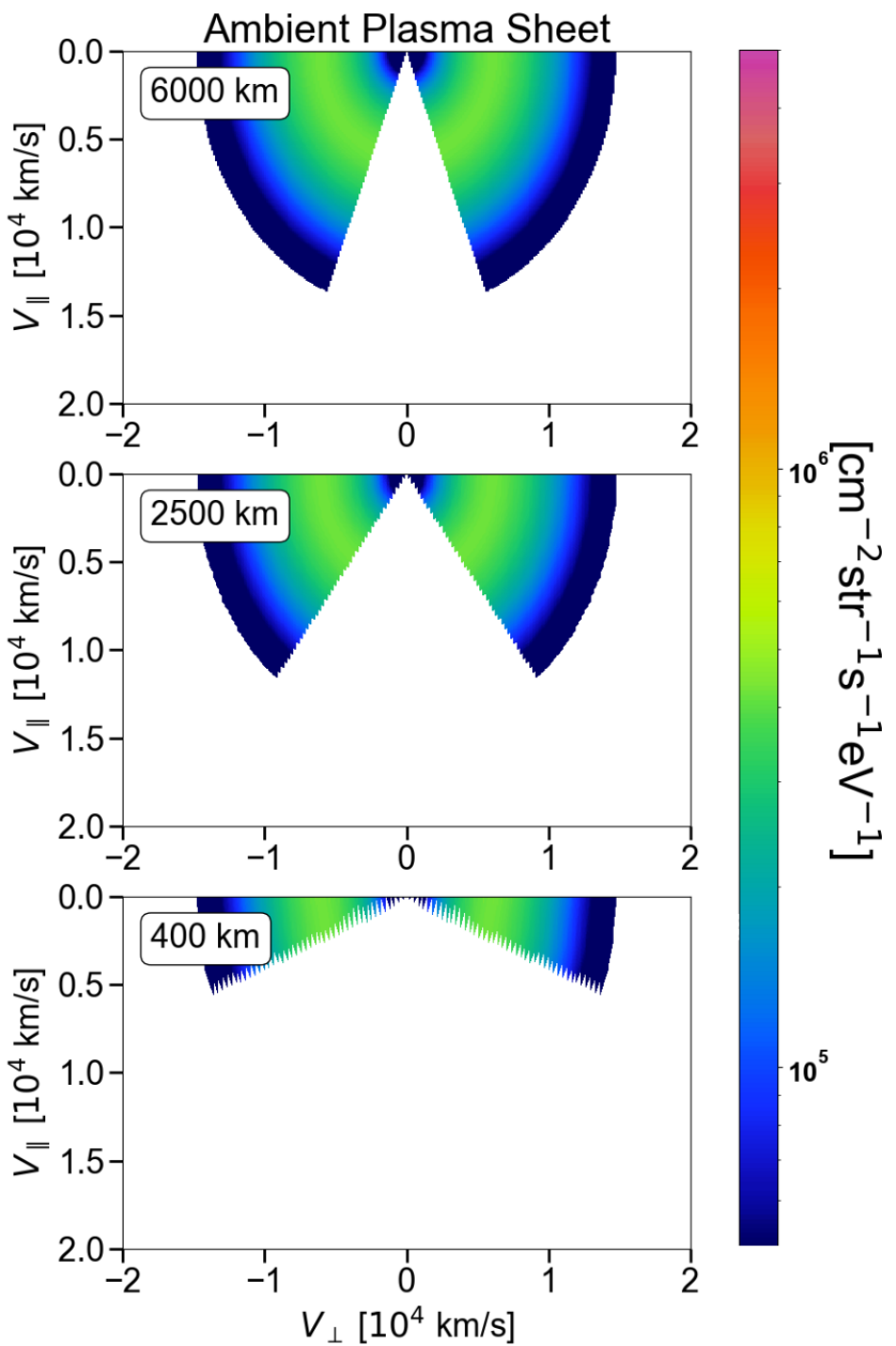


Figure 102. Plots in velocity space vs differential number flux for modelled ambient plasma sheet that likely produced with S1, S2, S3 mapped to three example altitudes. The distribution is a Maxwellian with  $n = 2.2 \text{ cm}^{-3}$  and temperature  $T_e = 105 \text{ eV}$  which were fitted from the Inverted-V nearest to STEB event S5.

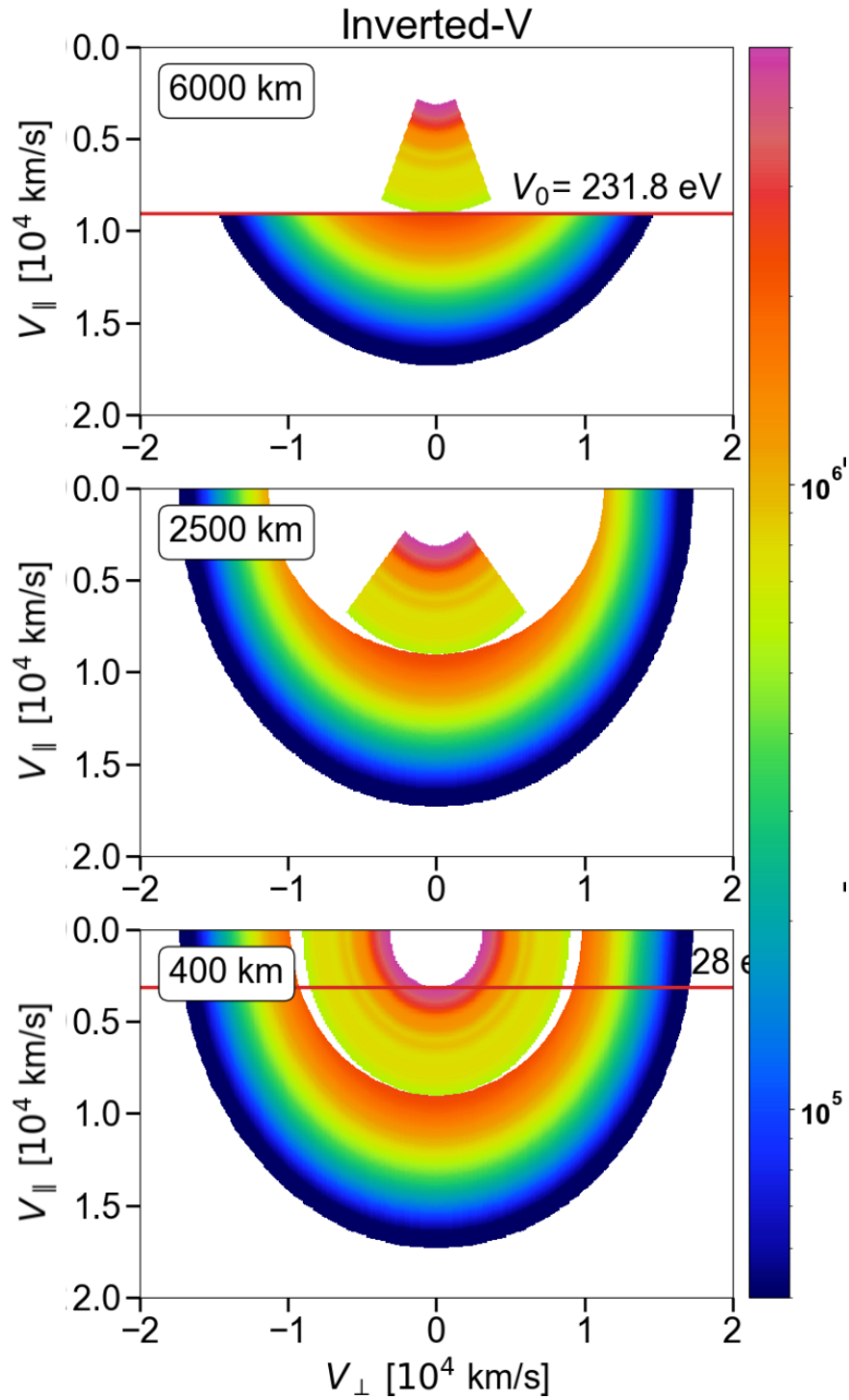


Figure 103. Plots in velocity space vs differential number flux for modelled inverted-V that likely produced STEB event S4 and S5 mapped to three example altitudes. The distribution is a Maxwellian with  $n = 2.2\text{cm}^{-3}$ , temperature  $T_e = 105\text{ eV}$  and quasi-static potential  $V_0 = 232\text{ eV}$  which were fitted from the Inverted-V nearest to STEB event S5. The mirror force causes a “banana” shape to occur in the inverted-V.

## 8.4 Calculating the Wave Potential $\Phi$

In this section, we use our model to represent the resonant populations that likely created our STEB events in order to corroborate the conclusions of Chapter 7. To do this, we will assume our modelled ambient plasma sheet population corresponds to the source electrons for STEB event S2 while our modelled inverted-V distribution represents the electrons for STEB S5. We will then model an Alfvén phase speed profile and consider the necessary peak wave potential  $\Phi_{max}$  required to match our source altitudes from TOF determined in Chapter 7.6. From this we will show that the greater peak energy and differential number flux in S5 is explained primarily by the differences in our model distributions and not variation in wave parameters.

In order to evaluate  $\Phi_{max}$  in the resonance condition, we need a suitable choice of  $\lambda_{\perp 0}$  in the ionosphere since we use the IAW phase velocity (equation 178) in the limit where only the  $k_{\perp}^2 \lambda_e^2$  kinetic term matters. In Chapter 7.8,  $\lambda_{\perp}$  was determined for our STEB events to have an average value of  $\lambda_{\perp} = 3.2 \pm 1.42$  km using a heuristic fitting method. We will first assume the same  $\lambda_{\perp 0}$  value for both IAWs passing through S2 and S5 source distributions since the observed Alfvén waves in Chapter 7.8 appeared insensitive to variations in wave parameters. Later we will readjust this parameter to their exact values and consider any differences.

After using our  $\lambda_{\perp 0}$  to determine an Alfvén speed profile, we can determine the  $\Phi_{max}$  required to match our TOF observations at a few key altitudes. The source population data in Table 1 from Chapter 7.6 indicates two important altitudes during the IAW acceleration process: (1) The approximate source altitude for the lowest energies of our STEBs occurred near 2500 km and (2) The approximate source altitude for the highest energies of our STEBs occurred near 5000 km. From these, we can estimate  $\Phi_{max}$  by solving equation 179 using the value of the IAW speed  $\omega/k_{\parallel}$  at that altitude and the highest/lowest parallel electron velocity  $v_{\parallel,e}$ :

$$\Phi_{max} = \frac{m_e}{2e} \left( \frac{\omega}{k_{\parallel}} - v_{\parallel,e} \right)^2 \quad (188)$$

The question is now: If the IAW are the same, from which distribution should the  $v_{\parallel,e}$  be chosen

to estimate  $\Phi_{max}$ ? Because STEB S4 and S5 were directly coincident with inverted-V electrons this means we have greater confidence these STEBs came from resonant auroral electrons whereas some inference must be used to assume a plasma sheet source for S1 to S3. Thus we will solve for  $\Phi_m$  in the inverted-V case and assume the same  $\Phi_m$  occurred in the plasma sheet since we have assumed identical waves.

In Figure 104 we show the results of this process with the Alfvén wave phase speed profiles in the top panel and our distributions at different altitudes in the bottom panels. The gray resonance bands in the bottom panels of Figure 104 represent the range of velocities between  $\omega/k_{\parallel} - \sqrt{2e\Phi_{max}/m_e} < v_{\parallel,e} < \omega/k_{\parallel}$  where the IAW can accelerate electrons. The solid black horizontal line represents  $\omega/k_{\parallel}$  and the horizontal dotted black line is  $\omega/k_{\parallel} - \sqrt{2e\Phi_{max}/m_e}$ . At each altitude, we estimate a value for  $\Phi$  based on our TOF information that puts constraints on the possible true value of  $\Phi_{max}$ . For example, at 6000km no electrons were resonant according to TOF so a maximum possible wave potential (call it  $\Phi_p$ ) is calculated between the highest  $v_{\parallel,e}$  in the inverted-V distribution and the wave phase velocity here (indicated by the rightmost red dot in the IAW phase speed profile) via equation 188. Performing this calculating results in  $\Phi_p \leq 343$  eV, which is near the 100's of eV potentials commonly observed for transverse waves near  $1 R_E$  (Chaston, 2006). The identical calculation is performed at 5000 km where TOF analysis indicated IAW acceleration just begins, resulting in a  $\Phi_{max} = 268$  eV. Finally, at the point where IAW resonance ends near 2500 km the EEPAA data suggests STEB electrons with energies at the lowest energy channel (28 eV) were abundant for S5. This means the wave must have accelerated electrons with at least as much energy in order to observe 28 eV electrons in our STEB in the first place. This defines an estimate for a minimum potential which we calculate to be  $\Phi_{min} \geq 113$  eV. In reality  $\Phi_{min}$  is greater than 113 eV since electrons have to start at lower energies than 28 eV to be accelerated up to 28 eV. However,  $\Phi_{min}$  should not be so large as to resonate with the cold ionospheric plasma near 1 eV, as this would short out the wave. Using our values, the true peak wave potential for our

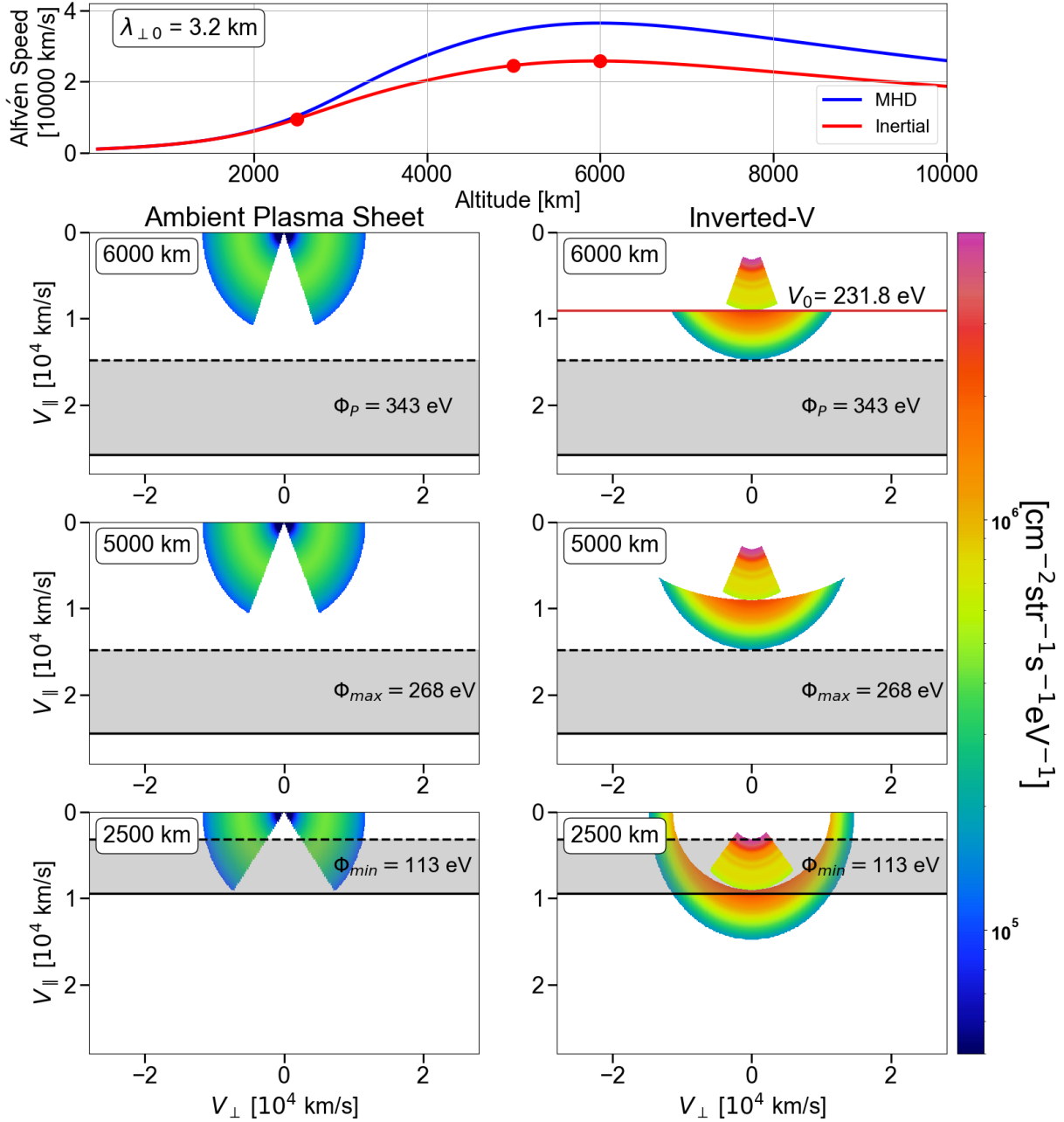


Figure 104. (Top Panel) Modelled Alfvén speed profile for an ionospheric perpendicular wavelength  $\lambda_{\perp 0} = 3.2$  km. The value of the ionospheric perpendicular scale is chosen as an average from the heuristic fits in Chapter 7.6. (Bottom Panels) Ambient Plasma Sheet and inverted-V distributions mapped to different altitudes under the mirror force. IAW resonance bands for acceleration are shown as gray bars. At 6000 km, TOF indicates no resonance occurred so a maximum possible wave potential  $\Phi_p$  is calculated. When resonance starts around 5000 km, the required  $\Phi_{max}$  must have been near 268 eV. When resonance ends near 2500 km, an estimate for the minimum wave potential was  $\Phi_{min} = 113$  eV to reproduce our STEB data. This plot demonstrates why STEBs S2, S3 have lower peak energies and differential number fluxes.

waves throughout the entire acceleration process should have been approximately between

$$128 \text{ eV} < \Phi_{wave} < 343 \text{ eV} \quad (189)$$

It may confuse the reader that the amplitude of the wave potential should change, however some of the wave energy is expended during acceleration and the parallel electric field of the IAW diminishes over distance due to the decreasing contribution of the kinetic term  $k_\perp^2 \lambda_e^2$  (see Figure 97). This model does not represent a self-consistent way to estimate  $\phi$ ,  $\lambda_{\perp 0}$  or the most accurate Alfvén speed profile to reproduce our STEBs. Nevertheless, it will illustrate our point.

## 8.5 Results

From Figure 104 we make clear that under realistic assumptions of our accelerating wave and distributions that the inverted-V population should resonate at higher energies and produce STEBs with greater electron flux than the plasma sheet for the same wave. In particular, the S2 ambient plasma sheet energies are too low at 5000 km to be able to begin resonate with this wave with a significant difference in wave energy required to make up the gap. This is somewhat inconsistent with the S2 TOF source altitudes which suggest 5072 km as the altitude for its highest energy electrons. However, our TOF values are only considered approximate and may not be appropriate when discussing the difference of several hundred kilometers. Instead, our TOF is useful for a general picture on scales of thousands of kilometers but should be not considered perfectly representative of the source altitude distribution. At 5000 km, the highest energies of the inverted-V electrons begin to get accelerated. Since the Alfvén phase velocity only decreases with decreasing altitude, this implies the IAW accelerated auroral electrons here form the highest energies of our STEB events. Thus, these energies will be higher than the ambient plasma sheet when its electrons start to resonate. Here we have shown how the peak energy of the STEBs with inverted-V source electrons will be higher energy than the ambient plasma sheet electrons similar to Chapter 7, however this modelling work makes these points more accurately.

At 2500 km the Alfvén wave stops resonating as indicated by TOF, which is likely due to the diminishing parallel electric field of the wave. As previously noted, the parallel electric field of the IAW diminishes over distance due to the decreasing contribution of the kinetic term  $k_{\perp}^2 \lambda_e^2$ . Until this happens, the wave  $E_{\parallel}$  does begin to accelerate the plasma sheet and inverted-V electron at similar resonant energies, however the spectral shapes of the distributions makes the resultant STEB flux different. The flux intensities in the ambient plasma sheet for a given energy are lower than their inverted-V counterpart. Furthermore, the electron flux in the intermediate energies between the highest and lowest resonant electrons are much higher in the inverted-V due to the backscatter/secondaries. The expectation is that inverted-V STEBs should show meaningful number flux across many energy bands whereas the plasma sheet thermal population STEB should suddenly appear at its peak energy and grow only in accordance with its thermal spread. These observations are identical to Figure 88 in Chapter 7.7, however they have now been shown with greater detail due to the inclusion of modelled inverted-V distributions from our data. We will not elaborate further since these points were made in Chapter 7.7.

## 8.6 Summary

A model of the ambient plasma sheet and inverted-V distributions is developed from fitting the High Flyer's EEPAA data near STEB event S5. The ambient plasma sheet is interpreted as the source population for the lower peak energy, lower differential number flux vs. Energy events S1, S2 and S3 whereas the inverted-V is understood as the source population for S4 and S5. The model shows that under reasonable estimates for the Inertial Alfvén Wave speed profile and the source altitudes from the Time-of-flight, that the same conclusions from Chapter 7.7 are observed: the peak energies and higher differential number fluxes for events S4 and S5 likely came from a change in resonant source population instead of variations in accelerating wave parameters. Additional work in the form of numerical modeling is required to prove this point in more detail.

## CHAPTER 9: SUMMARY, CONCLUSIONS AND FUTURE WORK

### 9.1 Summary & Conclusions

Two sounding rocket successfully launched 100 seconds apart from Andøya, Norway on Nov. 20th, 2022 in a post-dusk discrete auroral arc. The data from the mission indicates the same arc was crossed near the apogee of both rockets, with one payload intercepting the arc at 400 km and another at 180 km. High energy electron differential number flux, magnetic field and electric field measurements are made by both payloads *in situ* and provide a high resolution dataset through the simple geometry of a discrete arc. Data from the high-energy electron electrostatic analyzers on the High Flyer indicated the existence of many time-dispersed electron signatures on the equatorward edge of an auroral arc, which was termed the “Dispersive Region”. This region displayed evidence of the intensification of suprathermal electron bursts due to auroral precipitation. Due to the lack of electric field measurements, an analysis on the time-conjugate data between both payloads revealed the existence of Alfvén waves seen by the Low Flyer at nearly the same time these bursts were observed on the High Flyer. An argument based on the movement of Alfvén wave signatures in the ionosphere from previous studies provides a plausible connection between the High Flyer’s electron bursts and the Low Flyer’s Alfvén waves.

A case studying involving a subset of suprathermal bursts from the Dispersive Region revealed a pair of bursts that fall outside auroral precipitation and another pair that fall within it. The outside and coincident pairs are both interpreted due to resonantly accelerated electrons with Inertial Alfvén waves, but from different sources of electrons. The latter bursts displayed greater peak energies by more than a factor of three and enhancements in differential number flux vs. energy by greater than an order of magnitude across many more energies. The pair that doesn’t appear with auroral electrons are assumed to come from an ambient plasma sheet source population whereas the pair of bursts coincident with the inverted-V come from auroral inverted-V electrons. Under these assumptions, the behavior of the suprathermal burst pairs are explained through the resonance bands of the Alfvén waves using the expected shape of the wave speed profile throughout the al-

titudes of resonant acceleration. The general shapes of the accelerated plasma distributions that make up the plasma sheet and inverted-V are discussed to illustrate how the resonance bands from the same accelerating wave should produce the observed differences in our suprathermal bursts. The alternative explanation that the observed differences between the bursts are due to variation in the accelerating waves is explored through a speculative analysis of the available wave parameters in the ionosphere, which shows this possibility to be unlikely. Finally, a model of the auroral environment between 0 to  $1.6 R_E$  in altitude is presented to further elucidate the form of the accelerated plasma distributions. Under reasonable assumptions for the Alfvén wave resonance process, the model corroborates the conclusions in more detail that the source population themselves are the likely explanation for the peak energy and differential flux differences between the bursts.

## 9.2 Future Work

While the general idea of our suprathermal burst behavior may be explained through the observational analysis presented here, significant work needs to be done to quantitatively verify our interpretation. The modeling work we have presented is a starting point that's primarily illustrative, but does not currently simulate the wave-particle interaction. To achieve better results requires a thorough Alfvén wave propagation numerical model which can accurately reproduce our observational features, akin to the work by Chaston, Bonnell, Peticolas, et al., 2002; L.-J. Chen et al., 2005a; Tanaka et al., 2005. With such a simulation, the plasma sheet and inverted-V populations can be reproduced in detail and variations in accelerating Alfvén waves can be explored. In particular, confirming the time-alignment between our High Flyer burst events and our estimated poynting flux helps to discern which suprathermal electrons may be accelerated by the wave and which are decelerated. Finally, performing this work would help to catalog the behaviours of suprathermal bursts due to changes in source population, an exploration which the literature has not extensively investigated.

In addition to providing numerical support to the conclusions of this dissertation, a simulation of our suprathermal bursts allows us to explore many other common auroral features. The

focusing of pitch angles into the loss cone due to Alfvén wave-particle resonance and the subsequent study of the observed pitch angles within our time-dispersed events at the ionosphere may reveal embedded information that can be used in spacecraft data. This analysis would be done under various environmental conditions to gauge the impact on pitch angle for suprathermal electrons. Next, modeling the altitude of the inverted-V and the widening of auroral pitch angles when compared to our data may provide a means to estimate the altitude where the inverted-V is located based on ionospheric measurements; for which, to this authors knowledge, no reliable method exists.

Finally, the primarily science goals of the ACES-II mission itself should be investigated with similar analysis to Kaepller, 2014. The field-aligned currents which form the auroral electrojet are often inferred or modelled, and providing *in situ* measurements of these values helps constrain future work in these areas. The study of ionospheric conductivity has applications not only for the greater magnetospheric-ionospheric community itself, but even in the study of Alfvén waves. Conductivity gradients play a role in ionospheric feedback instabilities are mediated through Alfvén waves. Alfvén waves which propagate into the ionosphere can reflect and become trapped in a resonator between the conductive atmosphere and the high altitude magnetosphere due to the steep gradient in Alfvén phase speed. Not only these, but suprathermal bursts of the kind we have described offer a means for the magnetosphere to deposit energy into the ionosphere, thus studies on the energy deposition of these bursts should be compared to the joule heating estimates from typical auroral processes. In summary, Alfvén wave measurements within the ionosphere offer a menagerie of avenues to probe the interesting physics which couples the large-scale magnetosphere to small-scale ionospheric electrodynamics.

## APPENDIX A: DERIVING THE PLASMA WAVE EQUATION

The response of a conductive medium to an Alfvén wave is akin to the analysis of a light wave without assuming vacuum conditions. Maxwell's equations provide the *microscopic* fields within the material which has an anisotropic conductivity tensor  $\vec{\sigma}$ . The macroscopic Ampere's Law for microscopic free current  $\vec{J}_f$  is

$$\nabla \times \vec{H} = \mu_0 \vec{J}_f + \mu_0 \frac{\partial \vec{D}}{\partial t} \quad (190)$$

The macroscopic *magnetizing field*  $\vec{H}$  is

$$\vec{H} = \frac{1}{\mu_0} \vec{B} - \vec{M} \quad (191)$$

and the macroscopic Displacement Field  $\vec{D}$

$$\vec{D} = \epsilon_0 \vec{E} + \vec{P} \quad (192)$$

These fields are connected to the *macroscopic* bound current density  $\vec{J}_b$  within the material and *macroscopic* polarization  $\vec{P}$ :

$$\vec{J}_b = \nabla \times \vec{M} + \frac{\partial \vec{P}}{\partial t} \quad (193)$$

If we assume the linear relationship  $\vec{J}_f = \vec{\sigma} \cdot \vec{E}$ , then we can insert equations 191, 192 and 193 into equation 190 to get

$$\frac{1}{\mu_0} \nabla \times \vec{B} = \vec{\sigma} \cdot \vec{E} + \epsilon_0 \frac{\partial \vec{E}}{\partial t} \quad (194)$$

Using Faraday's Law to eliminate  $\vec{B}$  and a Fourier transformation of  $\vec{E}$  gets us the *plasma wave equation*:

$$\vec{n} \times (\vec{n} \times \vec{E}) + \vec{\epsilon} \cdot \vec{E} = 0 \quad ; \quad \vec{\epsilon} \equiv \epsilon_0 \left( \vec{I} + \frac{i}{\epsilon_0 \omega} \vec{\sigma} \right) \quad (195)$$

where we have defined the wave index of refraction vector by  $\vec{n} = \frac{c}{\omega} \vec{k}$  and the *dielectric tensor*  $\vec{\epsilon}$ .

## APPENDIX B: PROVE EQUATION 125

The inner and outer hemispheres of a top-hat ESA are separated by a thin  $\Delta r = r_{out} - r_{in}$  with the inner hemisphere having a set potential,  $V_{set}$ , and the outer hemisphere being tied to spacecraft ground, 0V so that  $\Delta V = V_{out} - V_{in} = -V_{set}$ . Particles enter the radial electric field,  $\vec{E} \approx \Delta V / \Delta r \hat{r}$ , and become centripetally accelerated to the anode. The path that particles who reach the anode taken is approximately  $r_p = r_{out} - \Delta r / 2$ . If we set our origin to the center of the inner hemisphere and consider radially outward as positive, then the energy of the particle in  $\vec{E}$  is

$$E_{permitted} = \frac{1}{2}mv^2 + q\Delta V$$

We can determine  $v^2$  by looking at force balance:

$$\vec{F}_{net} = \frac{q\Delta V}{\Delta r} \hat{r} = \frac{mv^2}{r_p} \hat{r} \implies v^2 = \frac{qr_p}{m} \frac{\Delta V}{\Delta r}$$

The values for  $\Delta r$  and  $r_{out}$  on ACES-II are 0.055" and 0.945" respectively. This makes  $r_{out}/\Delta r \gg 1$  and thus we derive the permitted energy equation as was shown in the text (values taken from the TRACERS/ACE Level 4 Requirements document on 12/16/2021): Putting these together gives us

$$E_{permitted} = \frac{q\Delta V}{2} \left[ \frac{r_p}{\Delta r} + 2 \right] = -\frac{qV_{set}}{2} \left[ \frac{r_{out}}{\Delta r} + \frac{3}{2} \right] \approx -\frac{qV_{set}r_{out}}{2\Delta r}$$

Fringing effects of the electric field near the entrance to the inner hemisphere region can occur and were ignored here. Additionally, the energy resolution of detector is derived from the geometry via

$$\gamma = \frac{\Delta E}{E} = \frac{E(r_{out}) - E(r_{in})}{E} = \frac{\Delta r}{r_{out}} \quad (196)$$

since  $\gamma$  depends on the detector's geometrical parameters we can see it is a constant.

## APPENDIX C: HALL AND PEDERSEN CONDUCTIVITY

Take the x-axis to point towards the north pole, y-axis pointing west and z-axis pointing away from earth. Precipitating charge will be modelled as two species MHD fluid in the neutral's frame that experiences a constant geomagnetic field magnitude  $\vec{B} = B_0(-\hat{z})$ . The ionosphere here is a weakly ionized plasma so we concern ourselves mostly with ion-neutral and electron-neutral collisions. Let there be an  $\vec{E}$  embedded within the ionosphere in the altitude range of 90 to 120km. The steady state two fluid collisional MHD equations for species 's' applied to the above situation is:

$$m_s n_s v_{sn} \vec{u}_s = q_s n_s [\vec{E} + \vec{u}_s \times \vec{B}]$$

Where  $m_s$  as species mass,  $v_{sn}$  is the species-neutral collisions frequency,  $q_s$  is charge and  $u_s$  is the fluid speed. Using  $\vec{J}_s = q_s n_s \vec{u}_s$  we can rewrite the above expression:

$$\vec{J}_s = \sigma_0 \vec{E} + \frac{\sigma_0}{n_s q_s} \vec{J}_s \times \vec{B} \quad (197)$$

Where we have defined the classical conductivity as  $\sigma_{0s} = n_s q_s^2 / m_s v_{sn}$ . For a generalized  $\vec{E} = (E_x, E_y, E_z)$  we can decouple equation (197) into its components:

$$\begin{aligned} J_x &= \frac{1}{1 + \sigma_{0s}^2 B_0^2 / n_s^2 q_s^2} \left[ \sigma_{0s} E_x - \frac{\sigma_{0s}^2 B_0}{n_s q_s} E_y \right] \\ J_y &= \frac{1}{1 + \sigma_{0s}^2 B_0^2 / n_s^2 q_s^2} \left[ \sigma_{0s} E_y + \frac{\sigma_{0s}^2 B_0}{n_s q_s} E_x \right] \\ J_z &= \sigma_{0s} E_z \end{aligned}$$

This can be rewritten in terms of the sign-dependant particle gyro frequency  $\Omega_s = q_s B_0 / m_s$ :

$$\sigma_{0s}^2 B_0^2 / n_s^2 q_s^2 = \left( \frac{n_s q_s^2}{m_s v_{sn}} \right)^2 \frac{B_0^2}{n_s^2 q_s^2} = \left( \frac{\Omega_s}{v_{sn}} \right)^2$$

$$\sigma_{0s} = \frac{n_s q_s}{B_0} \left( \frac{\Omega_s}{v_{sn}} \right)$$

Thus, our Ohm's law equation  $\vec{J}_s = \sigma_s \cdot \vec{E}$  can be written in terms of the conductivity tensor for a species  $\sigma_s$ :

$$\vec{J}_s = \begin{pmatrix} \sigma_{Ps} & -\sigma_{Hs} & 0 \\ \sigma_{Hs} & \sigma_{Ps} & 0 \\ 0 & 0 & \sigma_{0s} \end{pmatrix} \cdot \vec{E} \quad (198)$$

Where  $\sigma_P, \sigma_H$  are defined to be the Pedersen and Hall conductivities:

$$\sigma_{Ps} = \frac{n_s q_s}{B_0} \left[ \frac{v_{sn}/\Omega_s}{1 + (v_{sn}/\Omega_s)^2} \right] \quad \sigma_{Hs} = \frac{n_s q_s}{B_0} \left[ \frac{1}{1 + (v_{sn}/\Omega_s)^2} \right] \quad (199)$$

We want to characterize the ionospheric currents, so we sum over both species  $\vec{J} = \vec{J}_i + \vec{J}_e$  which amounts to summing the conductivities. Assuming quasi-neutrality ( $n_e \approx n_i = n$ ) we get:

$$\sigma_P = \sigma_{Pi} + \sigma_{Pe} = \frac{ne}{B_0} \left[ \frac{v_{in}/\Omega_i}{1 + \frac{v_{in}^2}{\Omega_i^2}} + \frac{v_{en}/\Omega_e}{1 + \frac{v_{en}^2}{\Omega_e^2}} \right] \quad (200)$$

$$\sigma_H = \sigma_{Hi} + \sigma_{He} = \frac{ne}{B_0} \left[ \frac{1}{1 + \frac{v_{en}^2}{\Omega_e^2}} - \frac{1}{1 + \frac{v_{in}^2}{\Omega_i^2}} \right] \quad (201)$$

In the current connection region, the ion-neutral mobility coefficient,  $\kappa_i = \Omega_i/v_{in}$ , nears order unity but  $\kappa_e$  is usually large. This approximation simplifies  $\sigma_P, \sigma_H$  to:

$$\sigma_P \approx \frac{ne}{B_0} \left[ \frac{v_{in}/\Omega_i}{1 + \frac{v_{in}^2}{\Omega_i^2}} + \frac{v_{en}}{\Omega_e} \right] \quad (202)$$

$$\sigma_H \approx -\frac{ne}{B_0} \frac{1}{1 + \frac{\Omega_i^2}{v_{in}^2}} \quad (203)$$

## APPENDIX D: PROVE EQUATION 91

The current flowing into the connection region as FACs are assumed to close through the ionosphere. Consider the region where downward FACs convert into the Hall and Pedersen currents, which move in the x-y plane (as shown in red on Fig 24). The height-integrated ionospheric currents and their directions can be given in reference to the mapped electric field,  $\vec{E}_\perp$ , which is perpendicular to the geomagnetic field

$$\vec{J}_\Sigma = \vec{J}_P + \vec{J}_H = \Sigma_P \vec{E}_\perp - \Sigma_H \hat{b} \times \vec{E}_\perp \quad (\text{B.1})$$

By current continuity we relate the downward FAC current,  $\vec{j}_\parallel$  to  $\vec{J}_\Sigma$  by

$$\vec{j}_\parallel = -\nabla_\perp \cdot \vec{J}_\Sigma = -\nabla_\perp \cdot (\Sigma_P \vec{E}_\perp) + \nabla_\perp \cdot (\Sigma_P \hat{b} \times \vec{E}_\perp) \quad (\text{B.2})$$

If we assume a spatial dependence in x-y plane for  $\Sigma_P, \Sigma_H$ , and assume that any spatial variations in the geomagnetic field are small i.e.  $\nabla \times \vec{B} = -\frac{\partial \vec{B}}{\partial t} = 0$ , then we can rearrange the right side of B.2 using these assumptions and some vector identities. We will short-hand  $\nabla_\perp$  to  $\nabla$  without loss of generality. B.2 becomes:

$$\begin{aligned} \vec{j}_\parallel &= -\nabla \cdot (\Sigma_P \vec{E}_\perp) + \nabla \cdot (\Sigma_P \hat{b} \times \vec{E}_\perp) \\ &= -\Sigma_P (\nabla \cdot \vec{E}_\perp) - \vec{E} \cdot (\nabla \Sigma_P) + \nabla \cdot (\Sigma_P \hat{b} \times \vec{E}_\perp) \\ &= -\Sigma_P (\nabla \cdot \vec{E}_\perp) - \vec{E} \cdot (\nabla \Sigma_P) + \left[ \nabla \times (\Sigma_H \hat{b}) \cdot \vec{E}_\perp - \cancel{(\nabla \times \vec{E}_\perp) \cdot \Sigma_H \hat{b}}^0 \right] \\ &= -\Sigma_P (\nabla \cdot \vec{E}_\perp) - \vec{E} \cdot (\nabla \Sigma_P) + \left[ \Sigma_H \cancel{(\nabla \times \hat{b})}^0 \cdot (\nabla \Sigma_H) \times \hat{b} \right] \cdot \vec{E}_\perp \\ &= -\Sigma_P (\nabla \cdot \vec{E}_\perp) - \vec{E} \cdot (\nabla \Sigma_P) - \hat{b} \cdot [\nabla \Sigma_H \times \vec{E}_\perp] \end{aligned}$$

## REFERENCES

- Andersson, L., Ivchenko, N., Clemons, J., Namgaladze, A. A., Gustavsson, B., Wahlund, J.-E., Eliasson, L., & Yurik, R. Y. (2002). Electron signatures and alfvén waves. *Journal of Geophysical Research: Space Physics*, 107(A9), SMP 15–1-SMP 15–14. <https://doi.org/https://doi.org/10.1029/2001JA900096>
- Arnoldy, R. L., Moore, T. E., & Cahill Jr., L. J. (1985). Low-altitude field-aligned electrons. *Journal of Geophysical Research: Space Physics*, 90(A9), 8445–8460. <https://doi.org/https://doi.org.proxy.lib.uiowa.edu/10.1029/JA090iA09p08445>
- Arnoldy, R. L., Lynch, K. A., Austin, J. B., & Kintner, P. M. (1999). Energy and pitch angle-dispersed auroral electrons suggesting a time-variable, inverted-v potential structure. *Journal of Geophysical Research: Space Physics*, 104(A10), 22613–22621. <https://doi.org/https://doi.org/10.1029/1999JA900219>
- Asamura, K., Chaston, C. C., Itoh, Y., Fujimoto, M., Sakanoi, T., Ebihara, Y., Yamazaki, A., Hirahara, M., Seki, K., Kasaba, Y., & Okada, M. (2009). Sheared flows and small-scale alfvén wave generation in the auroral acceleration region. *Geophysical Research Letters*, 36(5). <https://doi.org/https://doi.org.proxy.lib.uiowa.edu/10.1029/2008GL036803>
- Atkinson, G. (1970). Auroral arcs: Result of the interaction of a dynamic magnetosphere with the ionosphere. *Journal of Geophysical Research (1896-1977)*, 75(25), 4746–4755. <https://doi.org/https://doi.org.proxy.lib.uiowa.edu/10.1029/JA075i025p04746>
- Baker, K., LaBelle, J., Pfaff, R., Howlett, L., Rao, N., Ulwick, J., & Kelley, M. (1985). Absolute electron density measurements in the equatorial ionosphere. *Journal of Atmospheric and Terrestrial Physics*, 47(8-10), 781–789. [https://doi.org/10.1016/0021-9169\(85\)90054-6](https://doi.org/10.1016/0021-9169(85)90054-6)
- Banks, P. M., Chappell, C. R., & Nagy, A. F. (1974). A new model for the interaction of auroral electrons with the atmosphere: Spectral degradation, backscatter, optical emission, and

- ionization. *Journal of Geophysical Research*, 79(10), 1459–1470. <https://doi.org/10.1029/JA079i010p01459>
- Baumjohann, W. (1982). Ionospheric and field-aligned current systems in the auroral zone: A concise review. *Advances in Space Research*, 2(10), 55–62. [https://doi.org/10.1016/0273-1177\(82\)90363-5](https://doi.org/10.1016/0273-1177(82)90363-5)
- Bennett, E. L., Temerin, M., & Mozer, F. S. (1983). The distribution of auroral electrostatic shocks below 8000-km altitude. *Journal of Geophysical Research*, 88(A9), 7107. <https://doi.org/10.1029/JA088iA09p07107>
- Bonnell, J. W., Mozer, F. S., Delory, G. T., Hull, A. J., Ergun, R. E., Cully, C. M., Angelopoulos, V., & Harvey, P. R. (2008). The Electric Field Instrument (EFI) for THEMIS. *Space Science Reviews*, 141(1-4), 303–341. <https://doi.org/10.1007/s11214-008-9469-2>
- Borovsky, J. E. (1993). Auroral arc thicknesses as predicted by various theories. *Journal of Geophysical Research: Space Physics*, 98(A4), 6101–6138. <https://doi.org/10.1029/92JA02242>
- Broadfoot, R. M., Miles, D. M., Holley, W., & Howarth, A. D. (2022). In situ calibration of the Swarm-Echo magnetometers. *Geoscientific Instrumentation, Methods and Data Systems*, 11(2), 323–333. <https://doi.org/10.5194/gi-11-323-2022>
- Burch, J., Fields, S., & Heelis, R. (1979). Polar cap electron acceleration regions. *Journal of Geophysical Research: Space Physics*, 84(A10), 5863–5874. <https://doi.org/10.1029/JA084iA10p05863>
- Cameron, T., & Knudsen, D. (2016). Inverse electron energy dispersion from moving auroral forms. *Journal of Geophysical Research: Space Physics*, 121(12), 11, 896–11, 911. <https://doi.org/10.1002/2016JA023045>
- Carlson, C., Curtis, D., Paschmann, G., & Michel, W. (1982). An instrument for rapidly measuring plasma distribution functions with high resolution. *Advances in Space Research*, 2(7), 67–70. [https://doi.org/10.1016/0273-1177\(82\)90151-X](https://doi.org/10.1016/0273-1177(82)90151-X)

- Chaston, C. C. (2006). Ulf waves and auroral electrons. *Magnetospheric ulf waves: Synthesis and new directions* (pp. 239–257). American Geophysical Union (AGU). <https://doi.org/https://doi-org.proxy.lib.uiowa.edu/10.1029/169GM16>
- Chaston, C. C., Bonnell, J. W., Carlson, C. W., Berthomier, M., Peticolas, L. M., Roth, I., McFadden, J. P., Ergun, R. E., & Strangeway, R. J. (2002). Electron acceleration in the ionospheric Alfvén resonator. *Journal of Geophysical Research: Space Physics*, 107(A11). <https://doi.org/10.1029/2002JA009272>
- Chaston, C. C., Bonnell, J. W., Carlson, C. W., McFadden, J. P., Ergun, R. E., & Strangeway, R. J. (2003). Properties of small-scale alfvén waves and accelerated electrons from fast. *Journal of Geophysical Research: Space Physics*, 108(A4). <https://doi.org/https://doi-org.proxy.lib.uiowa.edu/10.1029/2002JA009420>
- Chaston, C. C., Bonnell, J. W., Carlson, C. W., McFadden, J. P., Strangeway, R. J., & Ergun, R. E. (2003). Kinetic effects in the acceleration of auroral electrons in small scale Alfvén waves: A FAST case study. *Geophysical Research Letters*, 30(6), 2002GL015777. <https://doi.org/10.1029/2002GL015777>
- Chaston, C. C., Bonnell, J. W., Peticolas, L. M., Carlson, C. W., McFadden, J. P., & Ergun, R. E. (2002). Driven Alfvén waves and electron acceleration: A FAST case study. *Geophysical Research Letters*, 29(11). <https://doi.org/10.1029/2001GL013842>
- Chaston, C. C., Peticolas, L. M., Bonnell, J. W., Carlson, C. W., Ergun, R. E., McFadden, J. P., & Strangeway, R. J. (2003). Width and brightness of auroral arcs driven by inertial alfvén waves. *Journal of Geophysical Research: Space Physics*, 108(A2). <https://doi.org/https://doi.org/10.1029/2001JA007537>
- Chaston, C. C., Carlson, C. W., McFadden, J. P., Ergun, R. E., & Strangeway, R. J. (2007). How important are dispersive alfvén waves for auroral particle acceleration? *Geophysical Research Letters*, 34(7). <https://doi.org/https://doi.org/10.1029/2006GL029144>
- Chen, F. (2016). *Introduction to plasma physics and controlled fusion*. <https://doi.org/10.1007/978-3-319-22309-4>

- Chen, L.-J., Kletzing, C. A., Hu, S., & Bounds, S. R. (2005a). Auroral electron dispersion below inverted-v energies: Resonant deceleration and acceleration by alfvén waves. *Journal of Geophysical Research: Space Physics*, 110(A10). <https://doi.org/https://doi.org/10.1029/2005JA011168>
- Chen, L.-J., Kletzing, C. A., Hu, S., & Bounds, S. R. (2005b). Auroral electron dispersion below inverted-V energies: Resonant deceleration and acceleration by Alfvén waves [eprint: <https://agupubs.onlinelibrary.wiley.com/doi/pdf/10.1029/2005JA011168>]. *Journal of Geophysical Research: Space Physics*, 110(A10). <https://doi.org/https://doi.org/10.1029/2005JA011168>
- Collinson, G. A., Dorelli, J. C., Avanov, L. A., Lewis, G. R., Moore, T. E., Pollock, C., Kataria, D. O., Bedington, R., Arridge, C. S., Chornay, D. J., Gliese, U., Mariano, A., Barrie, A. C., Tucker, C., Owen, C. J., Walsh, A. P., Shappirio, M. D., & Adrian, M. L. (2012). The geometric factor of electrostatic plasma analyzers: A case study from the Fast Plasma Investigation for the Magnetospheric Multiscale mission. *Review of Scientific Instruments*, 83(3), 033303. <https://doi.org/10.1063/1.3687021>
- Council, N. R. (2004). *Understanding the sun and solar system plasmas: Future directions in solar and space physics*. The National Academies Press. <https://doi.org/10.17226/11188>
- Di Mare, F., & Howes, G. G. (2024). New regime of inertial alfvén wave turbulence in the auroral ionosphere. *Phys. Rev. Lett.*, 133, 045201. <https://doi.org/10.1103/PhysRevLett.133.045201>
- Dors, E. E., & Kletzing, C. A. (1999). Effects of suprathermal tails on auroral electrodynamics. *Journal of Geophysical Research: Space Physics*, 104(A4), 6783–6796. <https://doi.org/10.1029/1998JA900135>
- Eriksson, P. T. I., Blomberg, L. G., Walker, A. D. M., & Glassmeier, K.-H. (2005). Poloidal ulf oscillations in the dayside magnetosphere: A cluster study. *Annales Geophysicae*, 23(7), 2679–2686. <https://doi.org/10.5194/angeo-23-2679-2005>

- Evans, D. S. (1968). The observations of a near monoenergetic flux of auroral electrons. *Journal of Geophysical Research (1896-1977)*, 73(7), 2315–2323. <https://doi.org/https://doi.org/10.1029/JA073i007p02315>
- Evans, D. S. (1974). Precipitating electron fluxes formed by a magnetic field aligned potential difference. *Journal of Geophysical Research (1896-1977)*, 79(19), 2853–2858. <https://doi.org/https://doi.org.proxy.lib.uiowa.edu/10.1029/JA079i019p02853>
- Feltman, C., Howes, G. G., Bounds, S. R., Miles, D. M., Kletzing, C. A., Greene, K., Broadfoot, R., Bonnell, J., & Roglands, R. (2024). Evidence for suprathermal electron burst intensification due to inverted-v precipitation. *ESS Open Archive*. <https://doi.org/10.22541/essoar.172345563.32584220/v1>
- Finlay, C. C., Kloss, C., Olsen, N., Hammer, M. D., Tøffner-Clausen, L., Grayver, A., & Kuvshinov, A. (2020). The CHAOS-7 geomagnetic field model and observed changes in the South Atlantic Anomaly. *Earth, Planets and Space*, 72(1), 156. <https://doi.org/10.1186/s40623-020-01252-9>
- Finley, M. G., Broadfoot, R. M., Shekhar, S., & Miles, D. M. (2023). Identification and removal of reaction wheel interference from in-situ magnetic field data using multichannel singular spectrum analysis [e2022JA031020 2022JA031020]. *Journal of Geophysical Research: Space Physics*, 128(2), e2022JA031020. <https://doi.org/https://doi.org.proxy.lib.uiowa.edu/10.1029/2022JA031020>
- Frank, L. A., & Ackerson, K. L. (1971). Observations of charged particle precipitation into the auroral zone. *Journal of Geophysical Research (1896-1977)*, 76(16), 3612–3643. <https://doi.org/https://doi.org/10.1029/JA076i016p03612>
- Gjerloev, J. W., & Hoffman, R. A. (2000). Height-integrated conductivity in auroral substorms: 1. Data. *Journal of Geophysical Research: Space Physics*, 105(A1), 215–226. <https://doi.org/10.1029/1999JA900354>

- Goertz, C. K., & Boswell, R. W. (1979a). Magnetosphere-ionosphere coupling. *Journal of Geophysical Research: Space Physics*, 84(A12), 7239–7246. <https://doi.org/10.1029/JA084iA12p07239>
- Goertz, C. K., & Boswell, R. W. (1979b). Magnetosphere-ionosphere coupling. *Journal of Geophysical Research*, 84(A12), 7239. <https://doi.org/10.1029/JA084iA12p07239>
- Greene, K., Bounds, S. R., Broadfoot, R. M., Feltman, C., Hisel, S., Kraus, R. M., Lasko, A., Washington, A., & Miles, D. M. (2024). First in situ measurements of the prototype tesseract fluxgate magnetometer on the aces-ii-low sounding rocket. <https://api.semanticscholar.org/CorpusID:268296254>
- Hasegawa, A. (1976). Particle acceleration by MHD surface wave and formation of aurora. *Journal of Geophysical Research*, 81(28), 5083–5090. <https://doi.org/10.1029/JA081i028p05083>
- Hassani, H., & Mahmoudvand, R. (2018). *Singular Spectrum Analysis*. Palgrave Macmillan UK. <https://doi.org/10.1057/978-1-37-40951-5>
- Hershkowitz, N. (2013). “*how langmuir probes work,*” in *plasma diagnostics. discharge parameters and chemistry, chap.3* (Vol. 1). Academic Press.
- Hudson, M. K., & Mozer, F. S. (1978). Electrostatic shocks, double layers, and anomalous resistivity in the magnetosphere. *Geophysical Research Letters*, 5(2), 131–134. <https://doi.org/10.1029/GL005i002p00131>
- Ivchenko, N., Marklund, G., Lynch, K., Pietrowski, D., Torbert, R., Primdahl, F., & Ranta, A. (1999). Quasiperiodic oscillations observed at the edge of an auroral arc by auroral turbulence 2. *Geophysical Research Letters*, 26(22), 3365–3368. <https://doi.org/10.1029/1999GL003588>
- Johnson, F., & Dessler, A. (1961). *Satellite Environment Handbook*. Stanford University Press. <https://books.google.com/books?id=CezEAAAIAAAJ>
- Johnstone, A. D., & Winningham, J. D. (1982). Satellite observations of suprathermal electron bursts. *Journal of Geophysical Research: Space Physics*, 87(A4), 2321–2329. <https://doi.org/10.1029/JA087iA04p02321>

- Kaeppler, S. R. (2014). Observations in the *E* region ionosphere of kappa distribution functions associated with precipitating auroral electrons and discrete aurorae. *Journal of Geophysical Research: Space Physics*, 119(12). <https://doi.org/10.1002/2014JA020356>
- Kaeppler, S. R. (2013). *A rocket-borne investigation of auroral electrodynamics within the auroral-ionosphere* (Doctor of Philosophy). University of Iowa. <https://doi.org/10.17077/etd.vqmju27g>
- Kaufmann, R. L., Walker, D. N., & Arnoldy, R. L. (1976). Acceleration of auroral electrons in parallel electric fields. *Journal of Geophysical Research*, 81(10), 1673–1682. <https://doi.org/10.1029/JA081i010p01673>
- Kelly, M. C. (2009). *The Earth's Ionosphere: Plasma Physics and Electrodynamics, Second Edition*.
- Kletzing, C. et al. (1983). Evidence for electrostatic shocks as the source of discrete auroral arcs. *Journal of Geophysical Research*, 88(A5), 4105. <https://doi.org/10.1029/JA088iA05p04105>
- Kletzing, C. A. (1994). Electron acceleration by kinetic Alfvén waves. *Journal of Geophysical Research*, 99(A6), 11095. <https://doi.org/10.1029/94JA00345>
- Kletzing, C. A., & Torbert, R. B. (1994). Electron time dispersion. *Journal of Geophysical Research: Space Physics*, 99(A2), 2159–2172. <https://doi.org/10.1029/93JA01745>
- Kletzing, C. A., Berg, G., Kelley, M. C., Primdahl, F., & Torbert, R. B. (1996). The electrical and precipitation characteristics of morning sector Sun-aligned auroral arcs. *Journal of Geophysical Research: Space Physics*, 101(A8), 17175–17189. <https://doi.org/10.1029/96JA00294>
- Kletzing, C. A., Mozer, F. S., & Torbert, R. B. (1998). Electron temperature and density at high latitude. *Journal of Geophysical Research: Space Physics*, 103(A7), 14837–14845. <https://doi.org/10.1029/98JA00962>

- Kletzing, C. A., & Scudder, J. D. (1999). Auroral-plasma sheet electron anisotropy. *Geophysical Research Letters*, 26(7), 971–974. <https://doi.org/https://doi-org.proxy.lib.uiowa.edu/10.1029/1999GL900092>
- Kletzing, C. A., & Hu, S. (2001). Alfvén wave generated electron time dispersion. *Geophysical Research Letters*, 28(4), 693–696. <https://doi.org/10.1029/2000GL012179>
- Kletzing, C. A., Scudder, J. D., Dors, E. E., & Curto, C. (2003). Auroral source region: Plasma properties of the high-latitude plasma sheet. *Journal of Geophysical Research: Space Physics*, 108(A10). <https://doi.org/https://doi-org.proxy.lib.uiowa.edu/10.1029/2002JA009678>
- Kletzing, C. A., Thuecks, D. J., Skiff, F., Bounds, S. R., & Vincena, S. (2010). Measurements of Inertial Limit Alfvén Wave Dispersion for Finite Perpendicular Wave Number. *Physical Review Letters*, 104(9), 095001. <https://doi.org/10.1103/PhysRevLett.104.095001>
- Knight, S. (1973). Parallel electric fields. *Planetary and Space Science*, 21(5), 741–750. [https://doi.org/10.1016/0032-0633\(73\)90093-7](https://doi.org/10.1016/0032-0633(73)90093-7)
- Liang, J., Shen, Y., Knudsen, D., Spanswick, E., Burchill, J., & Donovan, E. (2019). E-pop and red line optical observations of alfvénic auroras. *Journal of Geophysical Research: Space Physics*, 124(6), 4672–4696. <https://doi.org/https://doi-org.proxy.lib.uiowa.edu/10.1029/2019JA026679>
- Lin, C. S., & Hoffman, R. A. (1979). Characteristics of the inverted-v event. *Journal of Geophysical Research: Space Physics*, 84(A4), 1514–1524. <https://doi.org/https://doi-org.proxy.lib.uiowa.edu/10.1029/JA084iA04p01514>
- Lynch, K. A., Pietrowski, D., Torbert, R. B., Ivchenko, N., Marklund, G., & Primdahl, F. (1999). Multiple-point electron measurements in a nightside auroral arc: Auroral turbulence ii particle observations. *Geophysical Research Letters*, 26(22), 3361–3364. <https://doi.org/https://doi.org/10.1029/1999GL900599>

- Lynch, K. A., Hampton, D., Mella, M., Zhang, B., Dahlgren, H., Disbrow, M., Kintner, P. M., Lessard, M., Lundberg, E., & Stenbaek-Nielsen, H. C. (2012). Structure and dynamics of the nightside poleward boundary: Sounding rocket and ground-based observations of auroral electron precipitation in a rayed curtain: CASCADES2 RAYS. *Journal of Geophysical Research: Space Physics*, 117(A11), n/a–n/a. <https://doi.org/10.1029/2012JA017691>
- Lyons, L. R. (1981). Discrete aurora as the direct result of an inferred high-altitude generating potential distribution. *Journal of Geophysical Research: Space Physics*, 86(A1), 1–8. <https://doi.org/10.1029/JA086iA01p00001>
- Lyons, L. R. (1999). Association between geotail plasma flows and auroral poleward boundary intensifications observed by canopus photometers. *Journal of Geophysical Research: Space Physics*, 104(A3), 4485–4500. <https://doi.org/https://doi-org.proxy.lib.uiowa.edu/10.1029/1998JA900140>
- Lysak, R. L. (1985). Auroral electrodynamics with current and voltage generators. *Journal of Geophysical Research: Space Physics*, 90(A5), 4178–4190. <https://doi.org/10.1029/JA090iA05p04178>
- Lysak, R. L. (1991). Feedback instability of the ionospheric resonant cavity. *Journal of Geophysical Research: Space Physics*, 96(A2), 1553–1568. <https://doi.org/https://doi.org/10.1029/90JA02154>
- Lysak, R. L., & Carlson, C. W. (1981). The effect of microscopic turbulence on magnetosphere-ionosphere coupling. *Geophysical Research Letters*, 8(3), 269–272. <https://doi.org/https://doi.org/10.1029/GL008i003p00269>
- Lysak, R. L., & Lotko, W. (1996). On the kinetic dispersion relation for shear Alfvén waves. *Journal of Geophysical Research: Space Physics*, 101(A3), 5085–5094. <https://doi.org/10.1029/95JA03712>
- M. Kivelson, C. R. (1995). *Introduction to space physics*. Cambridge University Press.

- Marklund, G., Karlsson, T., & Clemons, J. (1997). On low-altitude particle acceleration and intense electric fields and their relationship to black aurora. *Journal of Geophysical Research: Space Physics*, 102(A8), 17509–17522. <https://doi.org/https://doi.org/10.1029/97JA00334>
- McFadden, J. P., Carlson, C. W., & Boehm, M. H. (1986a). Field-aligned electron precipitation at the edge of an arc. *Journal of Geophysical Research: Space Physics*, 91(A2), 1723–1730. <https://doi.org/https://doi-org.proxy.lib.uiowa.edu/10.1029/JA091iA02p01723>
- McFadden, J. P., Carlson, C. W., & Boehm, M. H. (1986b). Field-aligned electron precipitation at the edge of an arc. *Journal of Geophysical Research: Space Physics*, 91(A2), 1723–1730. <https://doi.org/https://doi-org.proxy.lib.uiowa.edu/10.1029/JA091iA02p01723>
- McFadden, J. P., Carlson, C. W., Boehm, M. H., & Hallinan, T. J. (1987). Field-aligned electron flux oscillations that produce flickering aurora. *Journal of Geophysical Research: Space Physics*, 92(A10), 11133–11148. <https://doi.org/https://doi.org/10.1029/JA092iA10p11133>
- McIlwain, C. E. (1960). Direct measurement of particles producing visible auroras. *Journal of Geophysical Research*, 65(9), 2727–2747. <https://doi.org/10.1029/JZ065i009p02727>
- McIlwain, C. E. (1961). Coordinates for mapping the distribution of magnetically trapped particles. *Journal of Geophysical Research (1896-1977)*, 66(11), 3681–3691. <https://doi.org/https://doi-org.proxy.lib.uiowa.edu/10.1029/JZ066i011p03681>
- Merlino, R. L. (2007). Understanding Langmuir probe current-voltage characteristics. *American Journal of Physics*, 75(12), 1078–1085. <https://doi.org/10.1119/1.2772282>
- Miles, D. M., Bennet, J. R., Mann, I. R., & Millling, D. K. (2013). A radiation hardened digital fluxgate magnetometer for space applications. *Geoscientific Instrumentation, Methods and Data Systems*, 2(2), 213–224. <https://doi.org/10.5194/gi-2-213-2013>

- Mozer, F. S., Carlson, C. W., Hudson, M. K., Torbert, R. B., Parady, B., Yatteau, J., & Kelley, M. C. (1977). Observations of Paired Electrostatic Shocks in the Polar Magnetosphere. *Physical Review Letters*, 38(6), 292–295. <https://doi.org/10.1103/PhysRevLett.38.292>
- Nagatsuma, T., Fukunishi, H., Hayakawa, H., Mukai, T., & Matsuoka, A. (1996). Field-aligned currents associated with alfven waves in the poleward boundary region of the nightside auroral oval. *Journal of Geophysical Research: Space Physics*, 101(A10), 21715–21729. <https://doi.org/https://doi-org.proxy.lib.uiowa.edu/10.1029/96JA01797>
- NOAA Center For Environmental Information, N. G. D. (2006). Usdoc/noaa/nesdis/ncei-definition of the ionospheric regions (structures). <https://www.ngdc.noaa.gov/stp/IONO/ionostru.html>
- O'Brien, B. J. (1970). Considerations that the source of auroral energetic particles is not a parallel electrostatic field. *Planetary and Space Science*, 18(12), 1821–1827. [https://doi.org/10.1016/0032-0633\(70\)90015-2](https://doi.org/10.1016/0032-0633(70)90015-2)
- Palmroth, M., Grandin, M., Sarris, T., Doornbos, E., Tourgaidis, S., Aikio, A., Buchert, S., Clilverd, M. A., Dandouras, I., Heelis, R., Hoffmann, A., Ivchenko, N., Kervalishvili, G., Knudsen, D. J., Kotova, A., Liu, H.-L., Malaspina, D. M., March, G., Marchaudon, A., ... Yamauchi, M. (2021). Lower-thermosphere–ionosphere (lti) quantities: Current status of measuring techniques and models. *Annales Geophysicae*, 39(1), 189–237. <https://doi.org/10.5194/angeo-39-189-2021>
- Paschmann, G., Papamastorakis, J., Sckopke, N., Haerendel, G., & Shelley, E. G. (1983). Altitude and structure of an auroral arc acceleration region. *Journal of Geophysical Research: Space Physics*, 88(A9), 7121–7130. <https://doi.org/https://doi-org.proxy.lib.uiowa.edu/10.1029/JA088iA09p07121>
- Press, W. H., Teukolsky, S. A., Vetterling, W. T., & Flannery, B. P. (2007). *Numerical recipes 3rd edition: The art of scientific computing* (3rd ed.). Cambridge University Press. [http://www.amazon.com/Numerical-Recipes-3rd-Scientific-Computing/dp/0521880688/ref=sr\\_1\\_1?ie=UTF8&s=books&qid=1280322496&sr=8-1](http://www.amazon.com/Numerical-Recipes-3rd-Scientific-Computing/dp/0521880688/ref=sr_1_1?ie=UTF8&s=books&qid=1280322496&sr=8-1)

- Robinson, R. M., Winningham, J. D., Sharber, J. R., Burch, J. L., & Heelis, R. (1989). Plasma and field properties of suprathermal electron bursts. *Journal of Geophysical Research: Space Physics*, 94(A9), 12031–12036. <https://doi.org/https://doi.org/10.1029/JA094iA09p12031>
- Russell, C. T., Luhmann, J. G., & Strangeway, R. J. (2016). *Space physics: An introduction*. Cambridge University Press.
- Russell, C., Luhmann, J., & Strangeway, R. (2016). *Space physics: An introduction*. Cambridge University Press. <https://books.google.com/books?id=HaBODAAAQBAJ>
- Schroeder, J. W. R., Skiff, F., Kletzing, C. A., Howes, G. G., Carter, T. A., & Dorfman, S. (2016). Direct measurement of electron sloshing of an inertial alfvén wave. *Geophysical Research Letters*, 43(10), 4701–4707. <https://doi.org/https://doi-org.proxy.lib.uiowa.edu/10.1002/2016GL068865>
- Schroeder, J. W. R., Skiff, F., Howes, G. G., Kletzing, C. A., Carter, T. A., & Dorfman, S. (2017). Linear theory and measurements of electron oscillations in an inertial Alfvén wave. *Physics of Plasmas*, 24(3), 032902. <https://doi.org/10.1063/1.4978293>
- Schroeder, J. W. R., Howes, G. G., Kletzing, C. A., Skiff, F., Carter, T. A., Vincena, S., & Dorfman, S. (2021). Laboratory measurements of the physics of auroral electron acceleration by Alfvén waves. *Nature Communications*, 12(1), 3103. <https://doi.org/10.1038/s41467-021-23377-5>
- Semeter, J., & Kamalabadi, F. (2005). Determination of primary electron spectra from incoherent scatter radar measurements of the auroral *E* region. *Radio Science*, 40(2), 2004RS003042. <https://doi.org/10.1029/2004RS003042>
- Sharp, R. D., Johnson, R. G., & Shelley, E. G. (1979). Energetic particle measurements from within ionospheric structures responsible for auroral acceleration processes. *Journal of Geophysical Research: Space Physics*, 84(A2), 480–488. <https://doi.org/10.1029/JA084iA02p00480>

- Stasiewicz, K., Bellan, P., Chaston, C., Kletzing, C., Lysak, R., Maggs, J., Pokhotelov, O., Seyler, C., Shukla, P., Stenflo, L., Streltsov, A., & Wahlund, J. (2000). Small scale alfvenic structure in the aurora. *Space Science Reviews*, 92(3-4), 423–533. <https://doi.org/10.1023/a:1005207202143>
- St f nt, R. J. (1970). Alfv n Wave Damping from Finite Gyroradius Coupling to the Ion Acoustic Mode. *The Physics of Fluids*, 13(2), 440–450. <https://doi.org/10.1063/1.1692938>
- Su, Y.-J., Jones, S. T., Ergun, R. E., & Parker, S. E. (2004). Modeling of field-aligned electron bursts by dispersive alfv n waves in the dayside auroral region. *Journal of Geophysical Research: Space Physics*, 109(A11). <https://doi.org/https://doi-org.proxy.lib.uiowa.edu/10.1029/2003JA010344>
- Tanaka, H. (2005). High time resolution measurement of multiple electron precipitations with energy-time dispersion in high-latitude part of the cusp region. *Journal of Geophysical Research*, 110(A7), A07204. <https://doi.org/10.1029/2004JA010664>
- Tanaka, H., Saito, Y., Asamura, K., & Mukai, T. (2005). Numerical modeling of electron energy-time dispersions in the high-latitude part of the cusp region. *Journal of Geophysical Research: Space Physics*, 110(A5). <https://doi.org/https://doi.org/10.1029/2004JA010665>
- Temerin, M., Boehm, M. H., & Mozer, F. S. (1981). Paired electrostatic shocks. *Geophysical Research Letters*, 8(7), 799–802. <https://doi.org/10.1029/GL008i007p00799>
- Torbert, R. B., & Mozer, F. S. (1978). Electrostatic shocks as the source of discrete auroral arcs. *Geophysical Research Letters*, 5(2), 135–138. <https://doi.org/10.1029/GL005i002p00135>
- Watt, C. E. J., Rankin, R., Rae, I. J., & Wright, D. M. (2005). Self-consistent electron acceleration due to inertial alfv n wave pulses. *Journal of Geophysical Research: Space Physics*, 110(A10). <https://doi.org/https://doi-org.proxy.lib.uiowa.edu/10.1029/2004JA010877>

- Watt, C. E. J., Rankin, R., Rae, I. J., & Wright, D. M. (2006). Inertial Alfvén waves and acceleration of electrons in nonuniform magnetic fields. *Geophysical Research Letters*, 33(2), 2005GL024779. <https://doi.org/10.1029/2005GL024779>
- Winkler, J. R. (1993). Numerical recipes in C: The art of scientific computing, second edition. *Endeavour*, 17(4), 201. [https://doi.org/10.1016/0160-9327\(93\)90069-F](https://doi.org/10.1016/0160-9327(93)90069-F)
- Wu, J., Knudsen, D. J., Shen, Y., & Gillies, D. M. (2021). E-pop observations of suprathermal electron bursts in the ionospheric alfvén resonator [e2020JA028005 2020JA028005]. *Journal of Geophysical Research: Space Physics*, 126(2), e2020JA028005. <https://doi.org/10.1029/2020JA028005>